INHIBITION OF PITTING ON CARBON STEEL

Ismarullizam Mohd Ismail

Submitted in accordance with the requirements for the degree of

Doctor of Philosophy

The University of Leeds
Faculty of Mechanical Engineering

October, 2011

Acknowledgements

First and foremost, I would like to acknowledge God Almighty for blessing me with health, strength and motivation to persevere through this journey.

I am extremely grateful to my supervisor, Professor Anne Neville for her constant guidance and encouragement and for her unique way of teaching that always served to motivate and extrapolate my skill and knowledge, making me enthusiastic towards my research and making me a better researcher. I also express my special thanks to my co-supervisor Dr. Xinming Hu for his guidance, encouragement and ability to lend a hand whenever I need his support.

I would like to express my gratitude to University of Leeds, England and Baker Hughes for their project funding, especially to Wai Mok, Jeremy Moloney, Chris Gamble, Vladimir Jovancicevic and Sunder Ramachandran for the discussion, guidance and support during this studies. I would also like to acknowledge MARA (Malaysian Government Student Department) for their support during my studies.

I am grateful to the present and past members of iETSI Research Group especially Rick, Michael, Azzura, Khalid, Kuldeep, Abinesh, John, Penny, Juan, Akbar, Benissa, Violette, Wendy, Eleftheria, Nasser, Nassim, Laura, Shariar, Jane, Hui, Louise, James, Ike, Thibaut, Feth-Allah and Faisal Reza for the discussion and friendships. I also would like thanks the iETSI staff Graham Jakeman, Ron Cellier, John Groves, Jackie Kidd, Fiona Slade, Andy Barnett, Dr. Nik Kapur, Dr. Chun Wang, Dr.Thomas Liskiewicz and Dr. Ardian Morina for their guidance and support. Special thanks Adrian Eagles, John Harrington and Richard Walshaw for their support and guidance in using the surface analysis equipment.

I would like to express my appreciation and dedicate this work to my beloved wife, Jullyza Teoh and my daughters Aisyah and Balqis for their love, motivation, constant patience, encouragement and always on my side during this studies. Special thanks to my family back home; my parents Mohd Ismail and Norakin and my in-laws Hassan Teoh and Junaidah and my brothers and sisters for their love and support.

"Life is a Journey....."

Abstract

Carbon dioxide and hydrogen sulphide pitting related failures are a prime concern in oil and gas internal pipelines. Often, these types of failure have a great impact on safety and environmental matters and can cause severe financial consequences to the operator.

Chemical inhibitors have been used to provide effective protection for the asset whether it is due to localised corrosion or general corrosion. More often than not, the operating conditions determine the type of corrosion product film produced on the carbon steel and in turn influence the type of corrosion inhibitor to provide effective protection for the asset.

In order to develop superior localised corrosion inhibitors, a better understanding of the mechanisms of the action and interaction of pitting and the corrosion products are required. An extensive study on the corrosion film, pitting growth and inhibition of pitting corrosion of carbon steel X65 in sweet and sour conditions has been carried out using electrochemical methods and various post test surface analysis techniques. The results revealed that both phosphate ester and imidazoline inhibitors showed excellent performance to stop pit propagation in sweet conditions if the optimum concentration is applied.

An *in-situ* monitoring technique for assessing real and artificial pit growth on X65 carbon steel surfaces in sweet and sour conditions has been developed to investigate the inhibitor action on the pits and surrounding corrosion films. Assessments of the surface chemistry around the pits by FTIR analysis revealed that there are two different mechanisms focused on inhibiting pitting corrosion. The first mechanism revealed that the inhibitor adsorbs at the pit site and is absent on the surrounding film and the second mechanism revealed that the inhibitor adsorbs both on the pit site and on the surrounding films.

Table of Contents

List of Figures

List of Tables

Abbreviations

AP	Artificial Pit
ASTM	American Society for Testing and Material
AISI	American Iron and Steel Institute
AFM	Atomic Force Microscopy
BSE	Backscattered Electrons
EDX	Energy Dispersive X-ray Analysis
E_{corr}	Free corrosion potential
F	Faraday's constant
FTIR	Fourier Transform InfraRed spectroscopy
FIB	Focused Ion Beam
h	Hour
i_{corr}	Corrosion current density
min	Minute
NP	Natural Pit
OSPAR	Convention for the Protection for the Marine Environment of North-East Atlantic
ppm	Parts per million
ppb	Parts per billion
pH	Level of acidity or alkalinity
R_p	Polarization resistance
SEM	Scanning Electron Microscope
SE	Secondary Electrons
SCE	Saturated Calomel Electrode
s	Second
T	Temperature
V	Velocity
XRD	X-Ray Diffraction
XPS	X-Ray Photoelectron Spectroscopy

Chapter 1 Introduction

1.1 Overview of oilfield corrosion as a global challenge

Carbon dioxide and hydrogen sulphide-related corrosion failures in internal oil and gas pipelines represent a very serious and costly problem [1-5]. The first recorded carbon dioxide and hydrogen sulphide corrosion problems were reported in the United States oil and gas industry in the 1940s [2, 4, 5]. In order to meet the growth of energy demand, oil and gas exploration moved from shallow water to deep water and is now moving to super deep water and ultra deep water explorations to obtain the resources [6]. Furthermore, much of the existing production infrastructure is operating beyond the original design life and many new locations are being explored that were previously considered to be out of limits [6, 7]. This creates significant challenges to operating pipelines in these environments and moreover transporting the production fluids will require higher reliability and improved corrosion control, especially in ageing facilities [6, 7]. The advancement in technology to maintain oil and gas production pipelines is a very attractive economic strategy and needs proper planning [8, 9]. According to Koch et al. the average corrosion related cost in the United States of America is estimated to be about $7 billion including monitoring, replacing and maintaining the assets [10]. This corrosion cost study clearly reveals that the technological advancement demands many new improved technologies to better understand the corrosion control strategies in technical and nontechnical areas. Corrosion control requires significant expenditure while the payoff includes increased public safety, reliable performance, maximised asset life, environmental protection and more cost effective operations in the long run [10].

1.2 Carbon steel X65 pipeline operation in oilfield industry

Most pipelines operate under acidic gas environments which in oilfield terminology, can be regarded as sweet or sour conditions. Reservoir environments containing measurable amounts of hydrogen sulphide (down to 0.5ppm) are classified as sour conditions and reservoirs free from hydrogen sulphide are classified as sweet conditions [11]. These acidic gases dissolve in mixtures of hydrocarbons and aqueous fluids produced from the reservoir [11]. Typically, the operating conditions are more

aggressive when these acidic gases dissolve in the produced fluids that originate from the geological formation or injected water coming from a distant water injection well to maintain the reservoir pressure to sweep oil towards the production well, as shown in Figure 1-1 [12-14]. The produced hydrocarbons and fluids will be transmitted from the offshore platform to the onshore refinery through transmission pipelines mostly made from carbon steel X65.

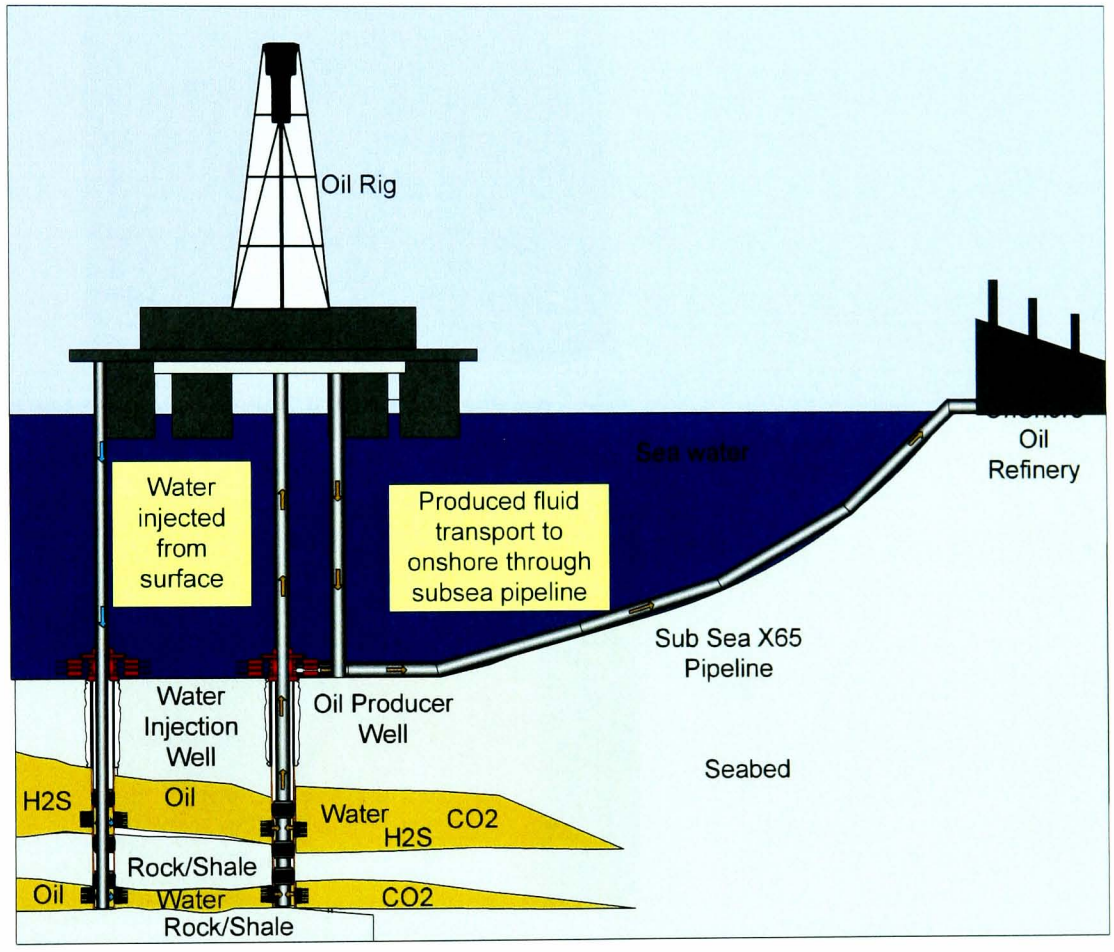

Figure 1-1: X65 Carbon steel pipeline transporting production fluid from offshore to onshore facilities.

One of the main failures of this X65 pipeline is through localised corrosion especially pitting and general corrosion problems, as shown in Figure 1-2 [15, 16]. Weakening of the pipeline by corrosion will reduce the resistance of pipeline to external forces and will accelerate the material and fabrication weaknesses, which lead to service failure as a result of leaking, as shown in Figure 1-3. Most of the failures are repeated because the pitting mechanism in sweet and sour conditions is not widely understood [6, 13, 17, 18]. Pipeline failures due to internal corrosion can

occur in almost any part of the pipeline system and it is imperative that the corrosion inhibitor deployed can give good protection to the inside of the entire system [19, 20].

Figure 1-2: Localised corrosion in pipeline [16]

Figure 1-3: Leaking in subsea pipeline due to internal corrosion [16]

Generally, pitting corrosion is difficult to quantify in the field or the laboratory due to its discrete and random nature. Localised corrosion monitoring in oil and gas production is difficult because either larger sections of pipeline need to be inspected or selected sections of a pipeline have to be monitored [21].

1.3 Carbon steel pitting in sweet environments

Internal pipeline corrosion processes depend on the service of the pipeline and operating parameters of the services [22]. Sweet corrosion services are caused by the

presence of carbon dioxide dissolved in the fluids and is also called carbonic acid corrosion [23]. Major operational parameters that influence sweet corrosion in the field are pressure, temperature, water cut, water composition, flow rate and the presence of solids [23]. Carbon dioxide gas is a highly soluble gas compared to other mineral acids in the sweet system and the acid formed can discharge electrons on the surface of the metal in several ways [23, 3, 5]. Sweet corrosion can result in a very high corrosion rate and the mode of attack could often be localised attack [5]. The surface of the pipe is usually covered with iron carbonate film but local breakdown of the film can occur and normally the damage is most severe at the bottom of the pipe where water layers preferentially form [23, 3, 5]. The corrosion control programme at the facility employs corrosion inhibitors to provide corrosion control to ensure high productivity [22, 23]. Concerns over the ability of the inhibitor to protect the pipelines against localised corrosion have been raised as the inhibitor dose is based on general corrosion. General corrosion is a safe form of corrosion because it is readily measurable and controlled in the field. However, localised attack results from small variations in operational conditions and is difficult to locate and measure [23].

1.4 Carbon steel pitting in sour environments

Sour corrosion is caused by hydrogen sulphide in the fluids. Hydrogen sulphide is a highly toxic and corrosive gas and it is soluble in hydrocarbons and water [23, 24]. In sour environments, hydrogen sulphide reacts with the surface of the metal to form adherent iron sulphide films, which are protective but can break down to reveal bare steel. This breakdown occurs because of the nature of the iron sulphide film to change its form from initial mackinawite which converts to another sulphide form and this reaction changes the density of the film and results in cracking of the film [23, 24]. The bare steel will form a galvanic couple with the iron sulphide film and can cause rapid pitting attack. Severe localised corrosion can occur in production pipelines with high hydrogen sulphide content [22, 25]. Such corrosion can cause failures in a time period as short as a few months if not mitigated [21]. Conversely, some high sour production systems have not experienced a significant number of failures due to localised corrosion. This is because of the difference in severity observed between similar producing systems, which could be due to the presence of iron sulphides and/or elemental sulphur, which is known to accelerate localised

corrosion [21]. In mildly sour systems, the films formed may be a mixture of iron carbonate and iron sulphide. The protectiveness of iron sulphide film is good but the stability of the film is generally affected by the salinity, temperature and metallographic details [22, 23].

1.5 Inhibition of corrosion in oilfield industry

The successful application of X65 carbon steel in oil and gas transmission pipelines in sweet and sour conditions depends mostly on protective corrosion product films [26, 27]. Although this film formation can be accelerated by using corrosion inhibitors it will depend on the operating conditions they are designed to protect. Often, corrosion inhibitors are used as the solution for avoiding further corrosion damage but obviously understanding the corrosion mechanism is very important to resolve the problem [28]. Introducing a new chemical into a field is a complex process, which involves many operational considerations as well as careful planning from the conception stage to successful deployment [16]. One important aspect of overall improvement plans is to initiate a laboratory test programme to evaluate the new inhibitors, which may offer higher corrosion inhibition performance [29]. Specific test programmes have been designed to study the behaviour of pitting and the interaction between the inhibitor and pitting corrosion, which is a critical performance requirement to ensure continuous integrity of the pipelines [16]. Another important consideration in selecting the inhibitor is the compatibility when mixing with other chemicals in the system and various operational parameters. With more environmental regulations, public sensitivity to leakages and significant financial penalty, this will ensure that more effort is required to achieve the corrosion management objectives. In order to develop superior corrosion inhibitor products to better protect different parts of the pipeline system, particularly against pitting corrosion, a better understanding of the interaction between chemicals and the surface films is required. Before this can be achieved, a better understanding of the characteristics of the film formation and pitting process under sweet and sour conditions is needed.

1.6 Objectives of the research

Sweet and sour pitting related failures are a prime concern in oil and gas internal pipelines. Often, these types of failure have a great impact on the safety and environmental matters and can cause severe financial consequences to the operator. Chemical inhibitors have been used to provide effective protection for the asset against both localised corrosion and general corrosion. In order to develop superior localised corrosion inhibitors a better understanding of the mechanisms of the action and interaction of pitting and the film are required. An extensive study on the inhibition of pitting corrosion of carbon steel X65 in sweet and sour conditions has been carried out using electrochemical and post test surface analysis techniques.

The objectives of this study are:

- The development of a laboratory methodology to produce reproducible films in sweet and sour systems.
- The development of a methodology to initiate and grow pits in a reproducible manner.
- The investigation of *in-situ* monitoring techniques to study localised breakdown.
- The evaluation of the mechanisms of the action and efficiency of localised corrosion inhibitors.

In order to achieve the objectives of the study, the results section is structured to comprise four main chapters:

- Investigation of sweet and sour surface film.
- Natural pitting growth in sweet and sour environments.
- *In-situ* monitoring of pit growth and the effect of inhibition under sweet conditions.
- *In-situ* monitoring of pit growth and the effect of inhibition under sour conditions.

The results obtained in this study show the mechanism of the action of the inhibitor to withstand pitting corrosion in sweet and sour conditions.

1.7 Scope of work

The scope of work in the first year was to study the methodology to produce reproducible films in sweet and sour systems and investigate using various surface analysis techniques to study the generated films. At the same time, the work also focused on developing an *in-situ* monitoring technique rig for localised breakdown and the design of the corrosion sour rig. In the second year, the natural growth of pitting in sweet and sour environments was investigated and the sweet corrosion inhibitor performance was evaluated on natural pits. In the third year, the corrosion inhibitor performance was evaluated on artificial pits with *in-situ* monitoring techniques in sweet and sour environments and *ex-situ* FTIR analysis.

1.8 Outline of the thesis

The thesis is presented in eleven chapters:

Chapter 2 is the basic theory of corrosion discussing electrochemical reaction, the kinetics and thermodynamics of corrosion and classification of type of corrosion with emphasis on pitting corrosion.

Chapter 3 presents the review of the literature on corrosion in sweet and sour environments. The reviews are related to mechanism, corrosion films, operating parameters and a summary of current research status with a focus on pitting corrosion. The review also covers the development of *in-situ* techniques, artificial pit and surface analysis techniques.

Chapter 4 presents the design and development of the *in-situ* monitoring rig and sour rig. This also covers the safety and operational procedure to operate the sour rig.

Chapter 5 presents the experimental techniques describing the sample preparation, techniques, experimental rigs, methods and procedures used in this study. The post-test examination is also explained in this chapter.

Chapter 6 presents the experimental results from the investigation on sweet and sour surface films. The corrosion film is generated and the film is further investigated using various surface analysis techniques.

Chapter 7 presents the experimental results from natural pit studies in sweet and sour conditions. The pits are generated and the pit depth measurements are obtained by post-test analysis with surface profilometry. Sweet corrosion inhibitors are also evaluated on natural pits.

Chapter 8 presents the experimental results from the *in-situ* monitoring technique on artificial pits under sweet conditions. The sweet corrosion inhibitor is evaluated and the pit depth measurement is obtained by post-test analysis with a surface profilometry. Further FTIR analysis is also carried out to investigate the corrosion inhibitor mechanisms.

Chapter 9 presents the experimental results from the *in-situ* monitoring technique on artificial pits under sour conditions. The sour corrosion inhibitor is evaluated and the pit depth measurement is obtained by post-test analysis with a surface profilometry. Further FTIR analysis is also carried out to investigate the corrosion inhibitor mechanism.

Chapter 10 presents a detailed discussion of the experimental results, comparing the work in this thesis with other reports in the literature and establishing the differences and contributions of this study. The principal sections in this chapter relate to sweet and sour film investigation and the effects associated with the film protectiveness and film breakdown. This chapter also discusses the formation of pitting in sweet and sour corrosion from the perspective of pitting depth and the effect on corrosion rate. Moreover it also discusses the individual inhibitor component mechanisms on the film and pitting area in sweet and sour environments.

Chapter 11 presents the conclusions made from the study and focuses on the contribution of the current work to the existing knowledge. This chapter also suggests the industrial applications of this work and future work for further understanding of pitting corrosion inhibitor mechanisms.

Chapter 2 Fundamental theory

2.1 Corrosion

Corrosion is the degradation of a material through the reaction with its environment [5, 14, 30-36]. Corrosion is subdivided into dry, wet and hot type corrosion for metals and non-metals. The process of corrosion occurs at the surface of the material, which is destructive or beneficial for the material depending on its application [31]. The science and art of corrosion engineering are intended to control or prevent corrosion damage on the material economically and safely [30, 32].

2.2 Electrochemical reactions of aqueous corrosion

Aqueous corrosion is the reaction of the material at the interface with the electrolyte of the material where the anodic dissolution and the cathodic reduction take place, which is the domain of metallurgists and physicists [31, 32]. The anodic reaction or oxidation involves a loss of electron metal by an increase in valence [30, 33]. Simultaneously, a cathodic reaction or reduction process decreased in valence charge consumes the electrons generated from the anodic process. This leads to the basic corrosion principle, which states that the rate of oxidation is equal to the rate of reduction. All parts of a metal surface during the corrosion process are anodic and cathodic alternately over a period of time in which both reactions are mutually dependent upon each other [30, 33, 34].

The anodic and cathodic reaction when iron is immersed in water or seawater with the presence of oxygen is as follows [30]:

$$Fe \rightarrow Fe^{2+} + 2e \qquad 2\text{-}1$$

$$O_2 + 2H_2O + 4e \rightarrow 4OH^- \qquad 2\text{-}2$$

Sodium and chloride ions in the solution do not participate in the reaction, which makes the overall reaction as:

$$2Fe + O_2 + 2H_2O \rightarrow 2Fe^{2+} + 4OH^- \rightarrow 2Fe(OH)_2 \qquad 2\text{-}3$$

Ferrous hydroxide precipitated from the solution is unstable in an oxygenated solution and is oxidised to ferric salt, which makes the final product of familiar rust [30]:

$$2Fe(OH)_2 + H_2O + \tfrac{1}{2}O_2 \rightarrow 2Fe(OH)_3 \qquad 2\text{-}4$$

2.3 Thermodynamics of corrosion reactions

The thermodynamics of corrosion are influenced by the chemical and electrochemical processes of the surface and interfacial energy of the material [31, 32, 34, 35]. The energy of the reaction is described by the change in their internal energy or enthalpy. The equilibrium electrode potential when concentrations of all reactions are maintained at unit activity are termed as half-cell standard potentials [30]. In any electrochemical reaction, the most negative or active half-cell tends to be oxidised and the most positive or noble half-cell tends to be reduced [31, 32, 34, 35]. The potential difference can be measured with a reference electrode quoted on a scale relating to the electrode. The potential difference between two reactions arises from the thermodynamics of the electrode reaction involved [31, 32]. The equilibrium potentials of an electrode reaction may include the formation of protecting insoluble salts or other compounds, which may also lead to corrosion protection. The reduction will proceed until the potentials of the two reactions are equal [31, 32, 35]. In order to account for all the likely corrosion phenomena, it is necessary to know what products are possible [31].

2.4 Free energy

The change in free energy ΔG is a measurement of the work capacity available from a system. A negative change in free energy accompanying the transition of a system from one state to another indicates a loss in free energy and also the spontaneous reaction direction of the system [30-33]. The system will transform to its lowest energy state if no external forces act on it. A positive change in free energy indicates that the transition represents an increase in energy and requires the addition of energy to the system. The change in free energy is a state function and independent of the reaction path [30, 31].

2.5 Kinetics of corrosion reactions

In order to produce a change in the electrode reaction so that the current density in one direction is greater than in the other direction, the potential of the electrode must change from the equilibrium value [30-32]. The change is referred to as polarisation. The relationship between the change and the value of the net current density is represented by a polarisation curve. The shape of polarisation curve is composed of three separate effects: activation polarisation requirements, concentration effects and resistance effects [30].

2.6 Polarisation

Polarisation can be defined as the displacement of electrode potential resulting from a net current or the deviation from equilibrium potential [30]. Electrochemical polarisation is divided into two different types: activation polarisation and concentration polarisation [30-36]. Activation polarisation refers to an electrochemical process controlled by the reaction sequence at the metal-electrode interface. This is the process of reduction of any species on a metal surface [30-33]. The absorbed or attached species on the surface will transfer the electron resulting in a reduction of the species. Concentration polarisation refers to electrochemical reactions controlled by the diffusion in the electrolyte [30, 31]. Concentration polarisation generally predominates when the concentration of the reducible species is small [30, 31]. At low reaction rates, activation polarisation usually controls whereas at higher reaction rate, concentration polarisation becomes controlling, as shown in Figure 2-1.

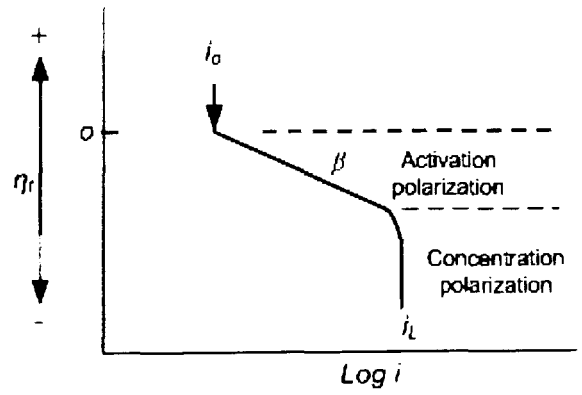

Figure 2-1: Combined polarisation curve-activation and concentration polarisation [30].

The behaviour of the metal can be divided into three main regions: active, passive and transpassive, as shown in Figure 2-2 [30]. In the active region, the material behaviour will be identical to that of a normal metal. A slight increase in the oxidising power of the solution causes a rapid increase in corrosion rate [30, 31]. This process will lead to the addition of oxidising agents added and a sudden decrease in corrosion rate corresponding to the beginning of a passive region. With increasing oxidising power, a very high concentration of oxidisers will reach a stage where the corrosion rate will increase again. At this stage the behaviour of the metal reaches a transpassive region [30-33].

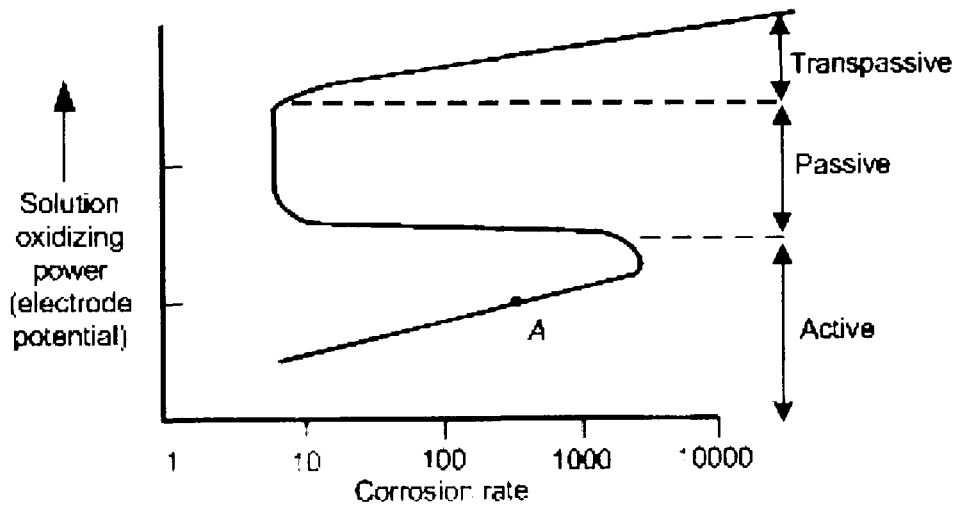

Figure 2-2: Corrosion characteristics of active-passive metal as a function of the solution oxidising power (electrode potential) [30].

2.7 Mixed potential electrodes

In mixed potential theory, any electrochemical reaction can be divided into two or more partial oxidation and reduction reactions and there can be no net accumulation of electric change during an electrochemical reaction [30, 31]. A mixed electrode is an electrode or metal sample in contact with two or more oxidation-reduction systems. The corrosion behaviour of iron in dilute hydrochloric acid solution represents two reactions, which are iron dissolution and hydrogen evolution, as shown in Figure 2-3 [30].

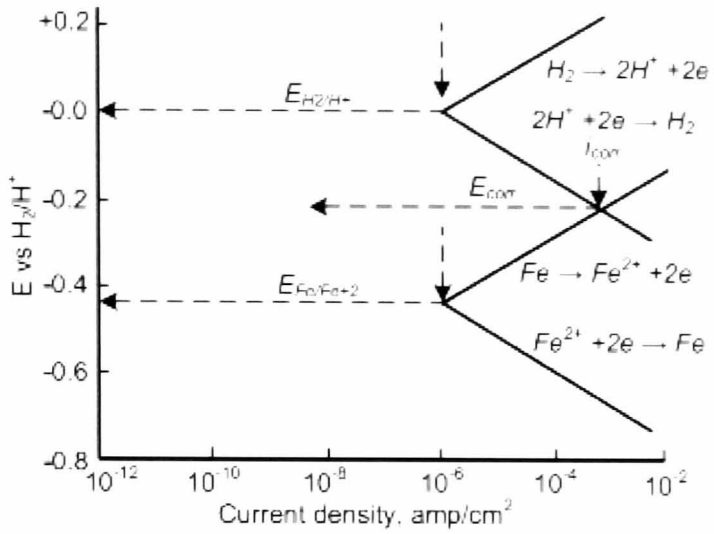

Figure 2-3: Schematic representation of electrode kinetic behaviour of pure iron in acid solution [30].

2.8 DC Linear polarisation test method

The mixed potential theory forms the basis for linear polarisation techniques to determine the corrosion rate. Figure 2-4 shows a typical three electrode cell submerged in an electrolyte for electrochemical corrosion tests. The potentiostat shifts the OCP of the working electrode and measure the respective current [36]. Changing an electrode potential from its OCP is referred to as polarization [36].

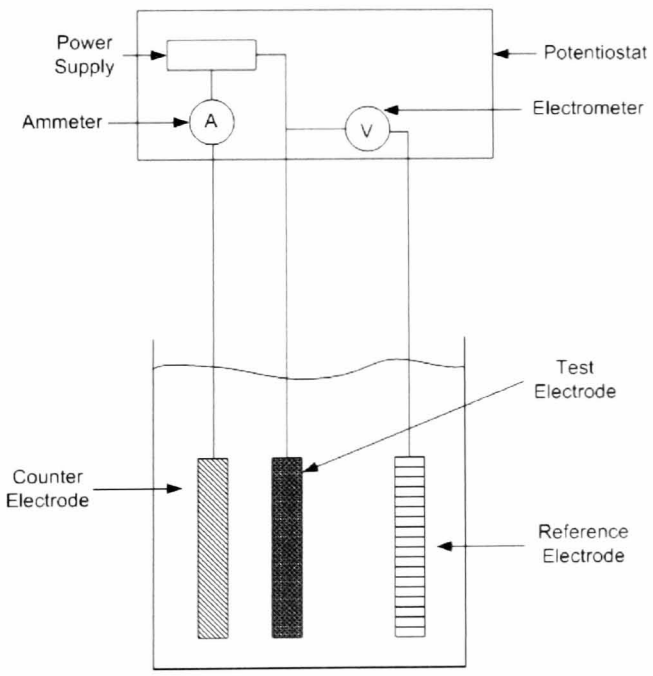

Figure 2-4: Three electrode test cell schematic [36].

Within 10mV more noble or more active than the corrosion potential, it is observed that the applied current density is a linear function of electrode potential [30, 36]. The corrosion potential is used as an overvoltage reference point. The plot of overvoltage versus applied anodic and cathodic current is shown on a linear scale, as in Figure 2-5. The plot represents the first 20mV linear polarisation of the curve related to the kinetic parameters of the system, as in [30, 36] where β_a and β_c are tafel slopes of the anodic and cathodic reactions, respectively, and term $\Delta E/\Delta i$ is given in $\Omega.cm^2$. Stern and Geary developed a mathematical relationship between corrosion resistance and corrosion current for linear polarisation, as follows [30, 36].

$$\frac{\Delta E}{\Delta i} = \frac{\beta_a \beta_c}{2.3(i_{corr})(\beta_a + \beta_c)} \qquad 2\text{-}5$$

The slope of a linear polarisation curve $\Delta E/\Delta i$ is controlled mainly by i_{corr} and is relatively insensitive to a change in beta value. An error in obtaining the correct beta value from the tafel slope could affect the i_{corr} value. The beta value should be taken from the test electrode that is in a steady state and compensated for the solution resistance [30]. In this study, localised corrosion kinetics and solution chemistry could have an effect on obtaining an accurate beta value for the experiments. By assuming the worst case scenario, an anodic and cathodic beta value of 0.12 volts is chosen to represent the average of all corrosion systems, which may be used to calculate the corrosion rate in this study by simplified equation [30, 36].

$$\frac{\Delta E}{\Delta i} = \frac{0.026}{i_{corr}} \qquad 2\text{-}6$$

Corrosion rate can be converted to MPY by the following equation [36]

$$MPY = i_{corr}(A)\left({}^{1}/_{\rho}\right)(\varepsilon) \qquad 2\text{-}7$$

Where:

A is a combination of several conversion terms 1.2866 $x10^5$ (equivalents.sec.mils/Coulombs.cm.years)

I_{corr} is corrosion current density Amps/cm^2 (1 Amp = 1 Coulomb/sec)

ρ is iron density 7.86 g/cm^3

ε is equivalent weight for iron 27.56g/equivalent

Corrosion rate can be converted from MPY to mm/yr using the following equation

$$^{mm}/_{yr} = MPY \times 0.0254 \qquad 2\text{-}8$$

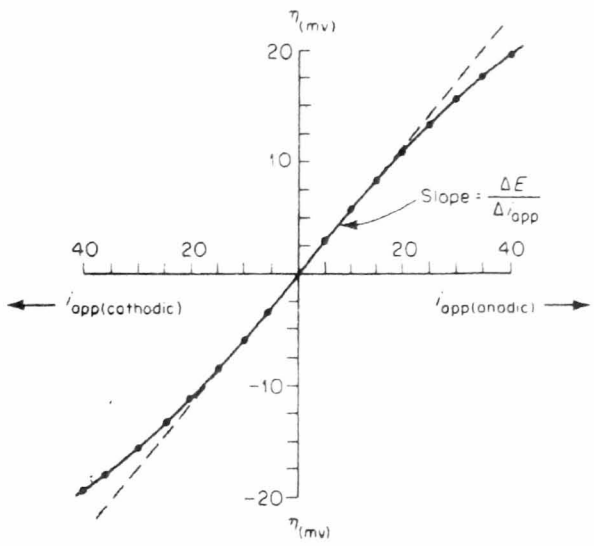

Figure 2-5: Applied-current linear polarisation curve. [30]

2.9 Type of corrosion

2.9.1 General corrosion

General corrosion or uniform attack is the most common form of corrosion. It can be characterised by a chemical or electrochemical reaction that proceeds uniformly over the entire exposed surface or over a large area [30-36]. The failure of the uniform corrosion can be identified by metal loss and the metal becoming thinner and eventually failing. The life of the equipment can be accurately estimated on the basis of a comparatively sample test [30-36].

2.9.2 Galvanic corrosion

Galvanic corrosion may happen when two dissimilar metals are involved and are in contact and immersed in an aqueous environment [30, 32]. The potential difference between them will initiate attack on the less noble of the two metals at a

corrosion rate largely dependent upon the surface reactions of the two metals. The less resistant metal becomes anodic and the more resistant metal becomes cathodic; usually the cathodic metal corrodes very little or not at all in this type of coupling [30, 32].

2.9.3 Crevice corrosion

Crevice corrosion or deposit corrosion is an intensive localised corrosion occurring within crevices and other shielded areas on a metal surface exposed to a corrosive medium [30-36]. This type of attack is related to small volumes of stagnant solution in which the excess of the working fluid is limited, and is usually caused by holes, gaps, lap joints and surface deposits [30, 32]. Deposits that may produce crevice corrosion are usually sand, dirt, corrosion products and other solids, which act as a shield and create a stagnant condition under them [30, 32].

2.9.4 Intergranular corrosion

Intergranular corrosion is related to grain boundary effects in which the grain interfaces are very reactive, which causes a localised attack at and adjacent to the grain boundaries with relatively little corrosion of the grains [30, 32]. This can come from impurities at the grain boundaries, enrichment of one of the alloying elements or depletion of one of these elements in the grain boundaries area, which can cause a loss of strength [30].

2.10 Pitting corrosion

Most of the corrosion phenomena are related to the formation of a film on the surface of the metal [5, 20, 30, 31, 37]. Under certain conditions, these film passivity layers may be destroyed locally, which leads to special corrosion phenomena like pitting corrosion, crevice corrosion and stress corrosion craking [31]. Pitting is a form of extremely localised attack resulting in small or large diameter holes or cavities in the metal with the surface diameter about the same as or less than the depth [30, 31, 37].

2.10.1 Mechanisms of pitting corrosion

Pits initiate when the rate of metal dissolution is momentarily high at one particular point and the chloride ions will migrate to this point. The presence of aggressive anions within the electrolyte cause localised attack on most passivated metals and alloys leading to the formation and growth of corrosion pits [30, 31]. Initiation or the early growth stage of pits results in rather unstable conditions due to repassivation. Most pitting failure is caused by chloride and chloride containing ions, which increase the metal dissolution. The adsorption of Cl^- through a passive film surface to the metal/oxide interface causes the build up of metal chloride at the interface, leading to film thinning [30, 31]. The adsorption, complexation and thinning of the passive film lead to a complete breakdown of the film, as shown in Figure 2-6 [30, 31]. Chloride ions are adsorbed on the oxide surface and form a complex with the surface cations. High solubility of the complex would enhance the dissolution and cause a local thinning of the passive film, which then leads to local depassivation and film breakdown [30, 31].

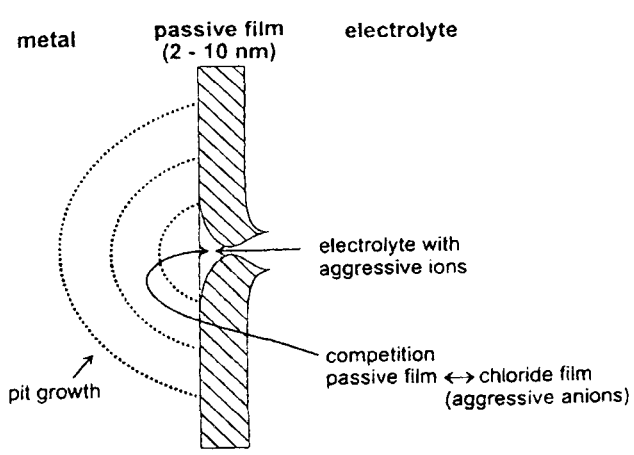

Figure 2-6: Mechanisms of film breakdown [31]

The presence of chloride could prevent repassivation of locally depassivated surfaces and, ultimately, causes pitting [31]. Dissolution will increase because of mechanical stress at a defect or random variation in the composition of the solution. Pitting is more likely to occur on etched or ground surfaces than on polished surfaces but pits forming on a polished surface are larger and penetrate more rapidly than those on a rough surface [30, 31].

2.10.2 Pitting shape and growth

Most pitting develops and grows downward from a horizontal surface, usually in the direction of gravity. The dense concentrated solution within a pit is necessary for its continuing activity and is a direct result of the autocatalytic nature of pitting [30, 37]. Pits often start with a small polygonal form and change to a hemispherical form when the precipitation of corrosion products occurs [31]. The surface of hemispherical pits may be rough depending on the formation of low solubility deposits during their growth [31, 37].

2.10.3 Evaluation of pitting damage

Pits are difficult to measure quantitatively and compare because of the varying depth, size and number of pits that may occur. The conventional weight loss test cannot be used for evaluation or comparison because the metal loss is very small and does not indicate the depth of penetration [30, 38]. The measurement of maximum pit depth as a function of exposed area would be a more reliable way of expressing pitting corrosion, since it is the deepest pits that will cause failure [30, 37].

2.11 Corrosion inhibitors

Corrosion inhibitors are a class of chemical substances that decrease the corrosion rate when present in the corrosion system in sufficient concentration without significantly changing the concentration of any other corrosive agents [31, 39]. The inhibitor can modify the surface layer by precipitation, pore plugging and enhanced film growth by the corrosion potential remaining unchanged and decreasing the corrosion rate [31]. Some surface active agents may act as inhibitors by providing an inhibition due to film formation and adsorption on the metal surface, interface or on the porous corrosion layer [31, 40]. Various types of corrosion inhibitor have been used for different applications. Generally, corrosion inhibitors can be classified as [31]:

Anodic, cathodic and mixed inhibitors

Organic and inorganic inhibitors

Oxidising and non-oxidising inhibitors

Interface (2D) and interphase (3D) inhibitors, according to thickness of formed layer

Oil field, cooling water, descaling and acid cleaning inhibitors.

Inhibitors may act on both cathodic and anodic partial electrode reaction. The cathodic inhibitor shifts the corrosion potential in the negative direction and forms an insulating layer, while the anodic inhibitor causes a change in the positive direction and forms a passive layer [31, 40]. Some mixed type inhibitors provide protection by blocking the whole surface and control the charge transfer or mass transport on the surface [30, 31, 40].

Chapter 3 Literature review

3.1 Sweet corrosion in carbon steel

The successful application of X65 carbon steel in oil and gas transmission pipelines in sweet and sour conditions depends mostly on the production of a protective corrosion product film [41-43]. The wide variety of operational environments and production fluids present vast challenges to operators to maintain transmission pipelines. Carbon dioxide is usually present in the fluid produced, which is a highly mineralised medium containing ions of chloride, carbonate, bicarbonate, sulphide, calcium, magnesium, sodium, potassium and iron [11, 14]. The presence of this element in its aqueous phase can result in very high corrosion rates in which the attack often leads to localised corrosion [5, 44]. Carbon dioxide corrosion in oil and gas pipelines is effected by a number of factors including supersaturation, temperature, solution pH, carbon dioxide partial pressure and sweet corrosion film [3, 5, 44-48].

3.1.1 Electrochemistry of sweet corrosion

Carbon dioxide gas is not corrosive by itself at normal temperatures but corrosive if dissolved in the aqueous phase [5]. Carbon dioxide gas dissolved in water generates carbonic acid [5, 13, 29, 47- 50].

$$CO_2 + H_2O \Leftrightarrow H_2CO_3 \qquad 3\text{-}1$$

The anodic dissolution for the iron in acid solution [2, 29, 47-49]:
Anodic reaction:

$$Fe \rightarrow Fe^{+2} + 2e^{-} \qquad 3\text{-}2$$

The cathodic process of mild steel in the solution is dominated by the diffusion of hydrogen ion reduction at pH 2 - 4 and the reduction of HCO_3^- and H_2CO_3 becomes important when the pH increases to pH 4 - 7 [5, 29, 45, 47-49, 51]:

Cathodic reactions:

At a lower pH

$$2H^+ + 2e^- \rightarrow H_2 \qquad 3\text{-}3$$

At a higher pH

$$2H_2CO_3 + 2e^- \rightarrow H_2 + 2HCO_3^- \qquad 3\text{-}4$$

$$2HCO_3^- + 2e^- \rightarrow H_2 + 2CO_3^{2-} \qquad 3\text{-}5$$

Direct reduction of water

$$2H_2O + 2e^- \rightarrow H_2 + 2OH^- \qquad 3\text{-}6$$

When the concentration of Fe^{2+} and CO_3^{2-} ion exceed the solubility limit of solid iron carbonate precipitates the formation of the carbonate film takes place [29, 47, 48, 49, 50, 51].

$$Fe^{2+} + CO_3^{2-} \rightarrow FeCO_3 \qquad 3\text{-}7$$

$$Fe^{2+} + 2HCO_3^- \rightarrow Fe(HCO_3)_2 \qquad 3\text{-}8$$

$$Fe(HCO_3)_2 \rightarrow FeCO_3 + CO_2 + H_2O \qquad 3\text{-}9$$

The electrochemical reaction would deposit a corrosion scale on the surface of the carbon steel which can be protective or non-protective depending on the microstructure and characteristics of the film [3, 5, 13, 29, 49, 50].

3.1.2 Effect of supersaturation

Supersaturation plays an important role in the formation and stability of iron carbonate film. High supersaturation accelerates the film formation and improves the stability and protectiveness of the film [5, 49, 52, 53]. High supersaturation of Fe^{2+} and CO_3^{2-}, which are released from the steel surface by corrosion and those coming from bulk solution, form an iron carbonate layer on the carbon steel surface [47, 52-54]. High supersaturation can be generated by increasing the bicarbonate and iron concentration to accelerate the film formation process [20]. Nesic et al. found that the higher Fe^{2+} concentration plays an important role in reducing the corrosion rate, as

shown in Figure 3-1 [20]. At high supersaturation, the corrosion rate has less effect on the corrosion layer accumulation rate of iron carbonate [50]. High supersaturation cannot be sustained for a long time at high temperature, as accelerated precipitation will tend to rapidly revert to a thermodynamic equilibrium [3]. At low supersaturation, which is typical for field conditions, the corrosion layer accumulation rate for iron carbonate is strongly affected by the corrosion rate of steel [47, 55, 56].

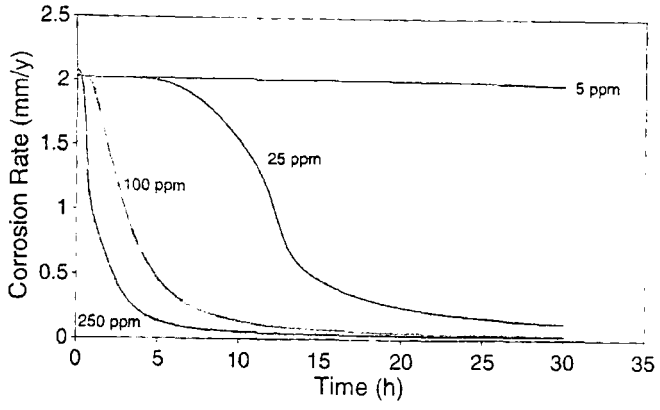

Figure 3-1: Predicted effect of Fe^{2+} concentration on the corrosion rate for T = 80°C, pH 6.6, P_{CO2}=0.54 bar and V = 1m/s [20]

3.1.3 Effect of temperature

Temperature accelerates all the processes in corrosion involving electrochemistry, chemical and transportation [3, 57, 58]. The change of temperature is important to film stability because it may affect the solubility and change the behaviour of the film [5, 59]. An increase in temperature also leads to increased supersaturation by rapidly accelerating the kinetics of precipitation to form a protective film to reduce the corrosion rate [3, 5, 58]. At temperatures higher than 60°C, the solubility of iron carbonate in the solution decreases and high supersaturation can lead to high precipitation [3, 5]. The temperature strongly affects the characteristics and morphology of the film by improving the protectiveness, which virtually reduces the film porosity and increases the adhesion and hardness of the film [5]. Iron carbonate is more stable at a temperature of 60°C - 90°C and becomes denser, and therefore, more protective over time [49, 59]. Figure 3-2 shows that the increase in temperature accelerates the formation of the protective film process, and, therefore, increases the surface coverage due to the higher precipitation rate [20, 49]. An iron carbonate film will also form at low temperature if the pH and dissolved iron

carbonate concentration in bulk is high [5, 54]. However at a lower pH, increasing the temperature will increase the corrosion rate due to the precipitation of non-protective films, which have a porous structure [5].

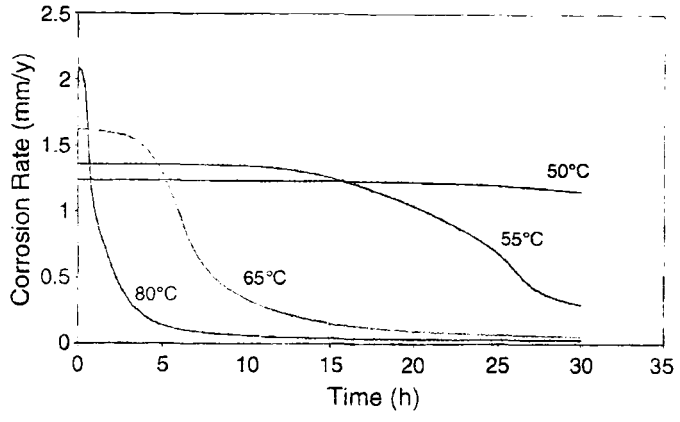

Figure 3-2: Predicted effect of temperature on the corrosion rate for pH 6.6, P_{CO2}=0.54 bar, C_{Fe2+} = 250ppm, and V = 1m/s [20]

3.1.4 Influence of pH

The solution pH plays an important role thereby affecting supersaturation, which influences the formation of a protective film and has a direct effect on the corrosion rate [3, 5]. Increasing the pH favours high supersaturation, which in turn, increases the film's precipitation rate [12, 41, 53]. Increasing the pH will reduce the solubility of the Fe^{2+} product, which leads to the probability of generating a protective iron carbonate film. As an example, at pH 4 - 5 the solubility of Fe^{2+} reduces 5 times and is even lower at a higher pH 5 - 6, which reduces the solubility of Fe^{2+} by 100 times [5, 17, 41].

The pH of saturated carbon dioxide condensed water is typically around pH 4 or less [3]. Figure 3-3 shows that the corrosion rate reduces when the pH increases to pH 6.6 [20]. The cathodic reaction dominates by H^+ reduction at low pH < 4.5 and HCO_3^- and H_2CO_3 control cathodic reaction at pH > 5, which lead to more protective films [19, 41, 51].

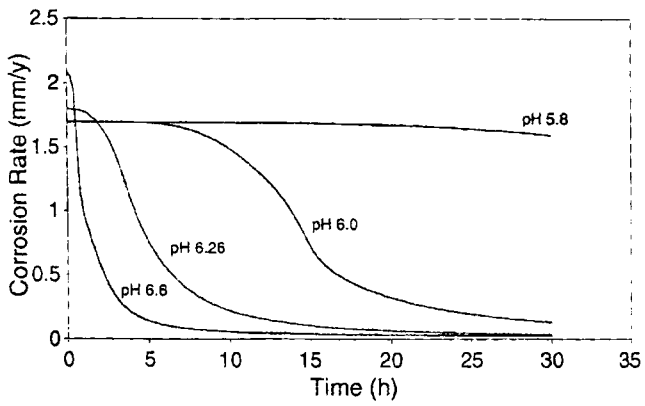

Figure 3-3: Predicted effect of pH on the corrosion rate for T=80°C, P_{CO2}=0.54 bar, C_{Fe2+} = 250ppm, and V = 1m/s [20]

3.1.5 Influence of carbon dioxide pressure

Carbon dioxide partial pressure will increase the carbon dioxide corrosion rate in the absence of a protective film [3]. However, when the conditions are favourable for the formation of a protective film, higher carbon dioxide partial pressure will lead to an increase in bicarbonate and carbonate ion concentration [20]. This condition will lead to higher supersaturation, which accelerates precipitation and film formation [3, 44].

3.2 Sweet corrosion films

There are many types of surface film that form on carbon steel during the carbon dioxide corrosion process. They can generally be divided into four main classes – transparent films, iron carbide films, iron carbonate films and iron carbonate plus iron carbide films [2, 3, 5,29]. All these films are different in thickness, structure and morphology, which lead to different corrosion rates and levels of protectiveness [5, 46, 60].

The precipitation kinetics of the film influences the nucleation and particle growth of the film. The protectiveness of the film will increase with exposure time and once the film formed is protective, it will remain protective even at lower supersaturation [5]. The protective film may be weakened by high chloride concentrations and by the presence of organic acid due to the reduction in the film's stability [41, 44, 56, 57].

The formation and protectiveness of the film also depends on the characteristics of the carbon steel microstructure, heat treatment and alloying element contents [5, 13, 48, 61, 62, 63]. The differences are mainly because of the build-up of carbide on the corroded steel surface, which can increase the corrosion rate due to galvanic corrosion between bare metal and Fe_3C [5, 29]. The anchoring effect of the carbide phase is also the main factor influencing the adhesion of the iron carbonate film structure [29, 64]. The pearlitic/ferrite microstructure has a carbide structure, which provides a good framework for the build up of protective carbonate film, however, the quenched and tempered steel and ferritic steel with low carbon content does not offer the integrated framework due to the finely distributed carbide structure [5, 48, 62-64].

3.2.1 Transparent films

Transparent film is a class of protective film that can form with very low ferrous ion concentration but is not considered as a thermodynamically stable solid carbon dioxide corrosion product. This film, with less then 1μm thickness, can only be observed at room temperature and will form faster by reducing the temperature below the ambient temperature [5]. Auger electron spectroscopy shows that the rough proportion of iron to oxygen ion in the film is 1:2 and does not show any carbonate [5].

3.2.2 Iron carbonate film

When the concentration of Fe^{2+} and CO_3^{2-} ions exceeds the solubility limits, iron carbonate precipitation take places on the surface of the material [47, 54]. Iron carbonate slows down the corrosion process by covering the metal surface and, thus, creates a diffusion barrier for the species involved in the corrosion process [3, 47, 65]. The protectiveness of iron carbonate films depends primarily on the precipitation rate of the film and the corrosion rate of the steel. Whether a protective film forms or not depends on the structure and morphology of the film and the thermodynamics and kinetics of the corrosion process [5]. A dense and protective film forms if the precipitation rate of the film exceeds the corrosion rate [3, 29].

3.2.3 Iron carbide film

Iron carbide is another species that can be generated on the surface under carbon dioxide environments [3, 5, 29, 64]. The corrosion process from the surface enriches the iron carbide in the film. Fe_3C is left behind from the corrosion process and differs from the formation of the $FeCO_3$ corrosion product layers [29]. Fe_3C is generally not effective in reducing the corrosion rate due to the film structure and morphology of the layers [5, 29, 64]. Fe_3C layers generally have poor contact and bonding at metal surfaces with some unfilled regions between the surfaces. This structure makes the surface fragile and porous which leads to its unprotective nature [5, 29].

3.2.4 Iron carbonate plus iron carbide film

Mixed iron carbonate and iron carbide film is the most common film found in carbon dioxide corrosion on the surface of carbon steel. The structure and protectiveness of the film is dependent on the iron carbonate film precipitations, as shown in Figure 3-4 [29]. The corrosion film appears to contain a double layer as iron carbonate film grows on the surface and the steel surface corrodes under the film continuously creating a void between the film and the surface, which is called the film undermining [20, 29, 51]. The void will then be filled with ongoing precipitation as soon as the void is created. Dense and protective films will form if the rate of precipitation at the steel surface equals or exceeds the rate of corrosion undermining. However, a porous and unprotective film will be created if the rate of corrosion undermining is faster than the precipitation that can fill the voids [13, 20, 29].

This process will generate three types of films, which are fully protective film, semi protective film and unprotective film, depending on the corrosion process that takes place [64]. The film can also change with time until it becomes a fully protective film to reduce the corrosion rate [64]. The protective film is sometimes very thin but still protective, and, vice versa, the film can be very thick but unprotective [20]. Figure 3-5 shows the dense and porous layer of film on the steel surface [3, 29].

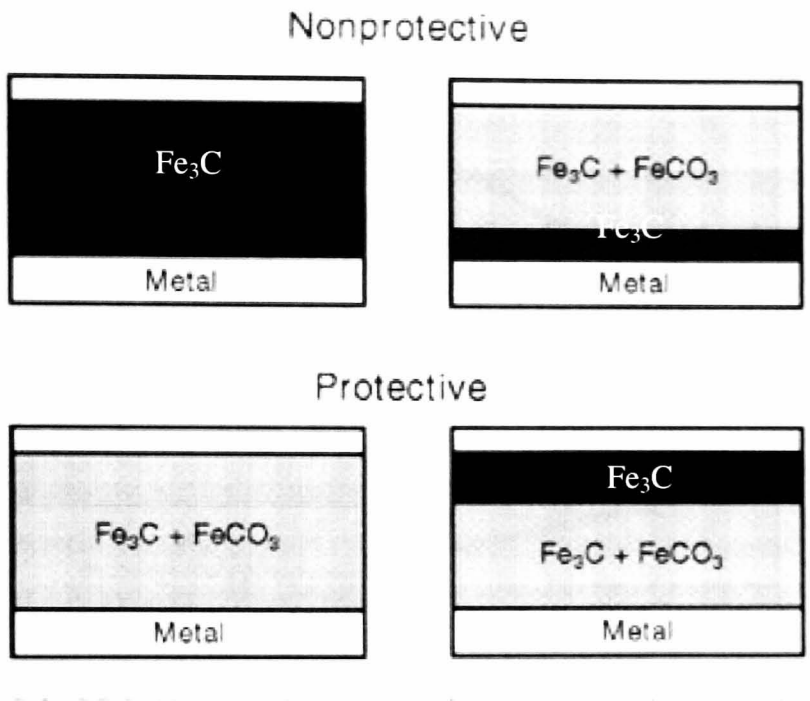

Figure 3-4: Morphologies observed for protective and unprotective corrosion layers [29]

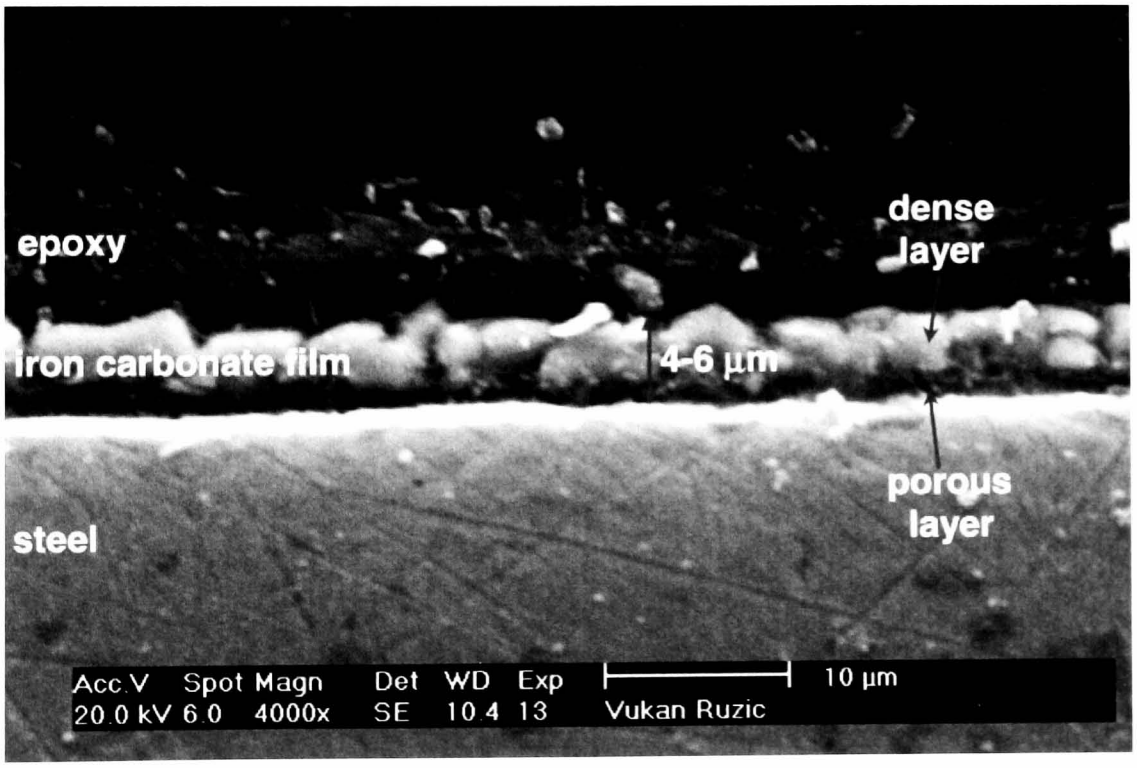

Figure 3-5: SEM image of a cross section of a steel specimen including iron carbonate scale. Exposed for 10h at T=80°C, pH = 5.6, P_{CO2}=0.54 bar, C_{Fe2+} = 250 ppm, and V = 1 m/s [20]

3.3 Sweet pitting corrosion on carbon steel

Carbon Steel X65 pipelines used in the oil and gas industry are frequently out of service due to localised corrosion attack and most of the failures cannot be fully explained by applying the principle of localised corrosion on stainless steel [17, 66, 67]. During the oil and gas transportation, water is separated and concentrates in the lower part of the pipeline, which makes that area the hot spot of localised corrosion [68]. Three types of localised corrosion are generally detected in carbon steel pipelines of which the most severe is pitting corrosion, followed by crevice corrosion and mesa attack [5, 44, 66]. Most of the carbon steel pipeline failures have a low general corrosion rate down to less then 0.1mm/yr but less than scale pitting defects [9].

3.3.1 Pitting corrosion failure

Pitting corrosion can occur over the full range of operating conditions – under stagnant to moderate flow conditions [5, 44, 67]. Pitting corrosion initiates due to the transient change in the environmental conditions like an increase in chloride ion concentration, temperature and partial pressure of CO_2 [41, 69-71]. Chloride ion content is important in localised corrosion because it largely affects the ionic strength and, thus, the supersaturation level of the solution [11, 17, 56, 67]. Temperature is another parameter that influences the pitting process; generally, most of the pitting is likely to occur in sweet pipelines at a temperature range of 70 - 90^{o}C [48].

The surface finish and microstructure of carbon steel can also influence the pitting process. A rougher surface generally provides more occluded geometries around sites, which can be the pit initiation sites, especially metastable pits [72]. Pits are likely to initiate at metallurgical discontinuities in the steel such as grain boundaries, pearlitic colonies and banded phases [73].

The pitting corrosion process for stainless steel can be divided into three sequences or steps – initiation by breakdown of passive film, initiation by metastable pits growth and stable growth pits [74]. The pits distribution is generally composed of three main populations, which are very small pits mainly dead pits or pits that are late

to initiate; pits that are formed from metastable pitting and pits that are formed by super stable pitting [75].

3.3.2 Pit initiation in sweet conditions

The initiation stage of pitting starts with the breakdown of iron carbonate films that largely depend on the undissolved cementite layer in the film morphology [62]. When there are flaws in the iron carbonate film content, or it is porous or has other imperfections located at the interface between the base material and scale, it will result in further destruction in the local cells at the site followed by localised attack [62, 63]. This will develop an aggressive local chemistry at the corroding site, which leads to cracking the iron carbonate layer [5, 54, 63, 72, 74].

Galvanic coupling between the steel and undissolved iron carbide layer provides local acidification in the aqueous solution that is trapped within the porous film [29]. This leads to a situation where a temporary local anode appears and unbalances the local equality between the anodic and cathodic current [29]. The corresponding reaction would enhance the protectiveness of the deposit formed and leads to the random nature of the pits nucleation [29]. Most of the film failure coincides with the underlying pit, where the pits grow under the porous corrosion film due to local cell mechanism [5, 8, 76, 77].

3.3.3 Metastable pits

The pitting nucleation stage is a very quick process and can occur within a very short time of exposure [70, 78]. The presence of a cover or salt film cover of the pits was found, which helps to maintain the aggressive local chemistry within the pits [72, 79, 80]. The pit cover will eventually collapse and the pit must be in an environment that favours propagation in order to become a stable pit, however, metastable pits are unlikely to become extreme and may terminate the growth whilst still in metastable pits [72, 74, 78, 81]. The pit growth is a self sustained process and would also contribute to hinder the dissolution at the bottom of the pit as a result of $FeCO_3$ precipitation. The pit may also grow spherically until a certain radius, followed by the opening of the pit mouth and lateral growth [28, 82]. The pit may continue to grow sufficiently large and sometimes the growth rate will accelerate the

autocatalytic process; the final pit depth depends on the pit growth rate and its initiation timing [15]. The pit may grow in various sizes and shapes, as shown in Figure 3-6; however, the true depth is the main parameter that leads to failure [22, 38].

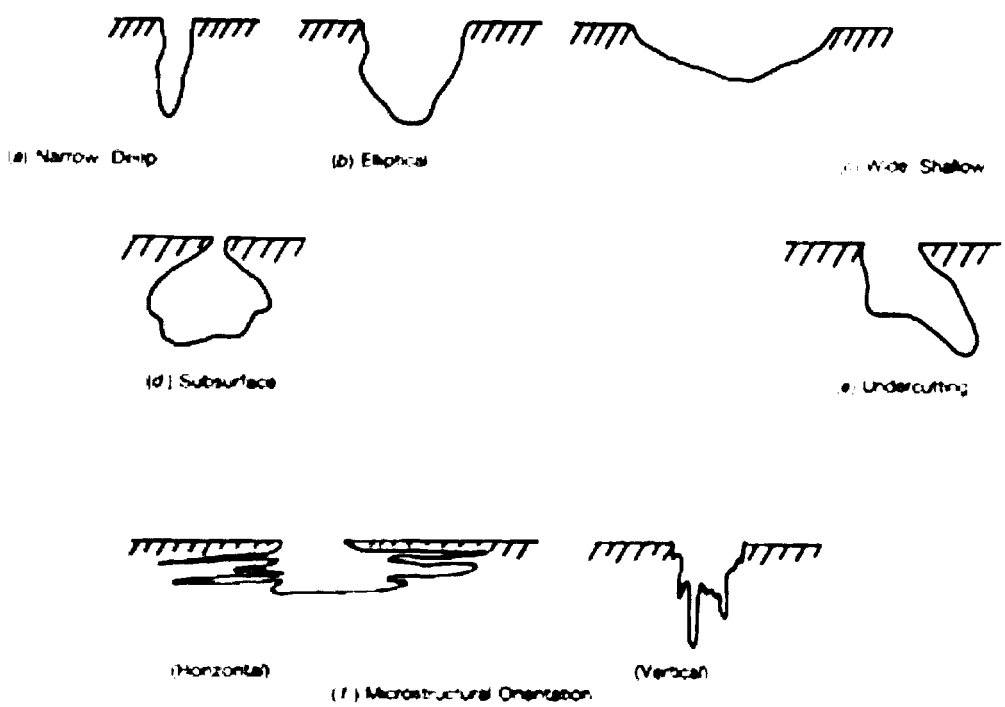

Figure 3-6: Variations in the cross-sectional shape of pits [38]

3.3.4 Stable pits

Pits that continue to grow can be quite large when the pit depth provides the boundary depth necessary for diffusion control [78]. The rapid growth of a uniform pit cover layer decreases the pH inside pits, which might be as low as zero, and, which is attributed to the increase in chloride concentration to reach the saturated level inside the pits [17, 79, 83]. Once the pit is engaged in stable growth, the local chemistry inside the pits becomes more corrosive and the bulk solution and solution within the pits become acidic and have a high concentration of Fe^{2+} and Cl^- [68, 79, 83]. The salt film covering the pit helps to maintain the harsh conditions inside the pit and limits access to the pitting surface by surfactant molecules [72, 79]. This harsh condition makes it difficult to stop the dissolution of supersaturation compared with the conditions when the pits are at the initiation stage [72, 79, 84].

3.3.5 Pit propagation in sweet environments

Pit propagation under CO_2 corrosion is mainly influenced by the difference between the iron carbonate film and the bare steel surface [50, 15, 85, 86]. Pits that grow underneath a corrosion product layer made up predominantly from iron carbonate may start the growth with small pits and merge with neighbouring pits to form larger pits [50]. Stable pit propagation will occur when a stable difference in corrosion potential is established between the anode and the cathode and the condition is close to saturation with respect to iron carbonate film when no dissolution or precipitation is expected [50, 86]. Solution conditions need to be maintained at a favourable condition in order for the pits to continue to propagate [50, 85]. One of the key factors that determine propagation of the pits is found to be the supersaturation of iron carbonate where the iron ion and carbonate ion concentration affect the solubility of the iron carbonate product [50]. The kinetics of iron carbonate film is another important factor to maintain the favourable conditions [25]. Pitting propagation could possibly take place when moderately protective iron carbonate forms, which is typically at a temperature between 50°C and 90°C, and pH 5.5 to pH 6.6, as shown in Figure 3-7 [25, 50, 87, 88]. A higher chloride concentration increases the solubility of the iron carbonate film making it more difficult to form a protective iron carbonate and more likely to result in pitting propagation [50, 15, 28, 88].

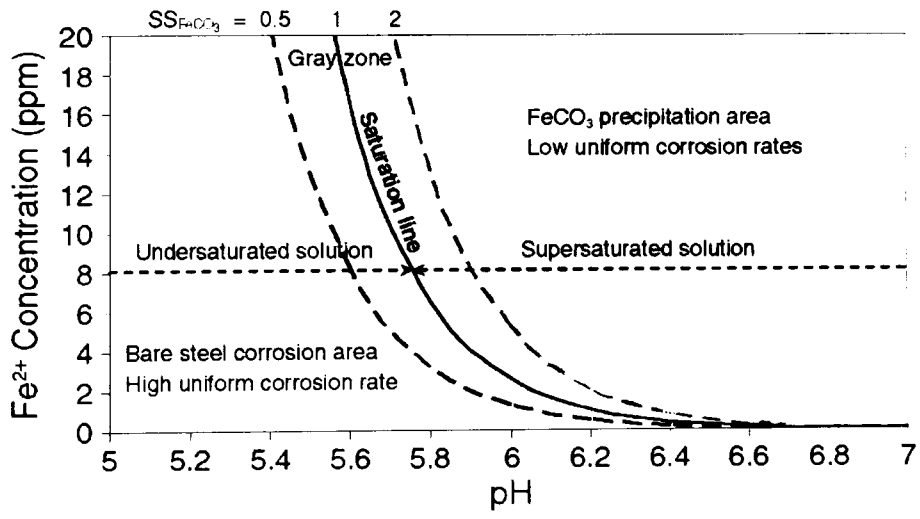

Figure 3-7: Calculated pH effect on solubility of $FeCO_3$ and the grey zone at T=80°C, PCO_2=0.53bar, 1% NaCl [50]

Pit propagation is not a continuous process and may stop if the protective iron carbonate film starts to re-form on the surface, however, if the solution conditions remain favourable, rapid pit propagation may continue until the point of line failure [15, 50]. Pitting corrosion can best be explained by establishing the relationship between the corrosion rate and the depth of the pit [22, 89].The absolute maximum pit depth was found to be a function of both the period of exposure and area of exposure [70].

3.4 Sweet corrosion inhibitors

Corrosion inhibitors are widely used in the oil and gas industry to protect the pipelines in sweet and sour environments [6, 16, 27, 90]. Sweet corrosion inhibitors are often a blend of an actively adsorbing chemical typically consisting of amines, imides, imidazolines, salt of nitrogenenous molecules, nitrogen quaternaries and many others depending on the application [47, 48, 91, 92]. Corrosion inhibitors are influenced by its pH buffering ability, surface activity and film forming barrier properties [60, 79]. Corrosion inhibitors mainly comprise two processes that start with adsorption of the inhibitor leading to inhibition of the anodic reaction and the second process, which leads to a reduction in the corrosion rate through inhibition of the cathodic reaction [3, 91, 93-95].

The inhibitor molecule structure actually changes the electrochemical reaction rates by influencing the mass transfer of reactants or reaction products or simply blocks parts of the active surface area [91, 95]. The more the inhibitor molecules are adsorbed and cover the surface of the metal, the more the active corrosion site is blocked and the remaining corrosion reaction that occurs is from areas that are inhibitor free [93, 95-97].

The synergy between the iron carbonate and inhibitor offer corrosion protection. Depending on the type of sweet inhibitor, the iron carbonate may change the crystalline morphology of the film to become more protective [98-100]. Some inhibitors hamper the growth of iron carbonate and some inhibitors stop the growth of iron carbonate [98-100]. Sweet corrosion inhibitors are also capable of preventing underscale corrosion and pitting corrosion if suitable doses are applied [9, 60, 101].

High performance inhibitors usually lower the general corrosion rate to 0.1mm/yr without incurring any pitting attack [6, 102, 103]. However, most localised corrosion inhibitors provide protection in terms of pitting attack but usually reduce the amount of general corrosion [102, 103].

3.4.1 Imidazoline inhibitor

Imidazoline is a nitrogen based organic surfactant that is commonly used to protect mild steel in oil and gas wells and pipelines from carbon dioxide and hydrogen sulphide corrosion [104]. The generalised structure of imidazoline is shown in Figure 3-8. Imidazoline is typically prepared from a long chain fatty acid and a polyamine that is dissolved in an aromatic solvent and dispersed with glycolic acid and hexylene glycol [91, 92]. Depending on the concentration, imidazoline is fairly soluble in CO_2 containing brine and influences the bonding of molecules with iron [90,91,104]. The surfactant molecules in the solution will form an adsorbed surfactant monolayer or bilayer on the metal surface [105]. The inhibitor film formation could be explained by the increase in bilayer cohesive energy with the hydrocarbon chain to provide a barrier to water and chloride ingress [98, 105]. Imidazoline inhibitor is also found to interact with Fe^{2+} creating a Fe complex and decreases the corrosion rate by preventing the growth of iron carbonate [98].

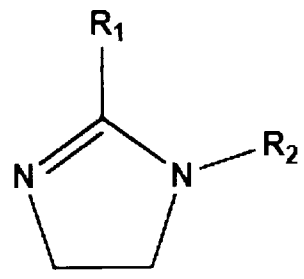

Figure 3-8: Generalised structure of saturated straight chain imidazolines [98]

3.4.2 Phosphate ester inhibitor

Phosphate ester type inhibitors are a reaction product of ethoxylated, propoxylated or butoxylatedalchohols or phenols with a phosphating agent [92]. Phosphate esters are green corrosion inhibitors and are biodegradable and safe for organisms that inhabit the general corrosion in oil and gas wells and pipelines [92, 106]. The generalised structure of phosphate ester is shown in Figure 3-9. The

reaction of phosphate esters with nitrogen base inhibitors could provide suitable inhibition for localised corrosion [92, 106]. Phosphate esters are used to complex with Fe^{2+} and Fe^{3+} to form insoluble iron phosphate, which prevents further corrosion attack [98, 106]. Phosphate ester efficiency is closely related to its minimum effective concentration, which plays an important role in stabilising phosphate esters against Fe^{2+} catalysed hydrolysis [106].

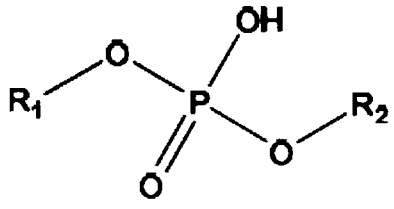

Figure 3-9: Generalised structure of phosphate esters [98]

3.5 Sour corrosion in carbon steel

Sour environments are characterised by the presence of both hydrogen sulphide and carbon dioxide in the system [68,107]. Hydrogen sulphide and carbon dioxide gas dissolve in the water turning the water acidic and corroding the steel surface [108, 109]. Sour corrosion is influenced by various operating parameters such as H_2S/CO_2 gas composition, temperature, pH and water chemistry [8, 110]. The reaction of H_2S and the steel may form an iron sulphide film on the steel surface and function as a barrier to protect the steel by reduce the corrosion rate [110]. Hydrogen sulphide tends to accelerate the corrosion rate in the initial stage until a protective film forms on the metal surface [1, 111, 112].

There are many types of iron sulphide film and, commonly, the protective iron sulphide film is composed of a mixture of iron sulphide (mackinawite) FeS_{1-x} and iron carbonate (siderite) $FeCO_3$ [51, 24, 113]. Iron sulphide films predominate in sour environments in which the sulphide concentration plays an important role in determining the film characteristics [41,111]. Iron carbonate is a secondary product in sour environments, and typically, it offers less protection compared with iron sulphide films [79]. Hydrogen sulphide is three times more soluble in water compared to

carbon dioxide but is a weaker acid in water compared to carbon dioxide [5, 24]. Sour corrosion just needs the H_2S/CO_2 ratio to exceed 1/5000 to form an iron sulphide film [5].

3.5.1 Electrochemistry of sour corrosion

Hydrogen sulphide will dissolve in water and take part in a cathodic reaction [51]. Hydrogen sulphide corrosion will form an iron sulphide film on the metal surface; the corrosion mechanism is described as follows: [1, 24, 51, 108, 111, 114, 115].

The anodic dissolution for the iron in aqueous solution is as follows:

Anodic reaction:

Iron oxidation

$$Fe_{(s)} \rightarrow Fe^{+2}{}_{(aq)} + 2e^{-} \qquad 3\text{-}10$$

The cathodic reaction is the reduction of hydrogen ions derived from H_2S to H_2 [1]

Cathodic reaction:

Hydrogen sulphide dissolution:

$$H_2S_{(g)} \leftrightarrow H_2S_{(aq)} \qquad 3\text{-}11$$

$$H_2S_{(aq)} \leftrightarrow H^{+}{}_{(aq)} + HS^{-}{}_{(aq)} \qquad 3\text{-}12$$

Bisulphide dissolution

$$HS^{-}{}_{(aq)} \leftrightarrow H^{+}{}_{(aq)} + S^{2-}{}_{(aq)} \qquad 3\text{-}13$$

Hydrogen sulphide reduction

$$2H_2S_{(aq)} + 2e^{-} \rightarrow H_{2(g)} + 2HS^{-}{}_{(aq)} \qquad 3\text{-}14$$

Bicarbonate reduction

$$2HS^{-}{}_{(aq)} + 2e^{-} \rightarrow H_{2(g)} + 2S^{-}{}_{(aq)} \qquad 3\text{-}15$$

Formation of the iron sulphide takes place
By precipitation

$$Fe^{+2}_{(aq)} + HS^{-}_{(aq)} \leftrightarrow FeS_{(s)} + H^{+}_{(aq)} \qquad 3\text{-}16$$

By direct solid state reaction:

$$Fe_{(s)} + H_2S \rightarrow FeS_{(s)} + H_{2(g)} \qquad 3\text{-}17$$

An iron sulphide film will form very quickly to cover the surface with a black film of sulphides [51, 108, 114, 115]. Hydrogen sulphide corrosion is divided in two stages [1, 111, 112]. In the first stage, the corrosion rate will accelerate; the process is primarily by the diffusion of ferrous iron through the iron sulphide until the plateau is reached [1, 114, 116]. Another pathway for iron sulphide formation is by the direct reaction from H_2S with fast oxidation of solid iron, which transforms directly into solid iron sulphide attached to the steel surface [24, 116]. The corrosion rate will start to decrease when the protective corrosion film is formed [114]. The metal loss due to diffusion controls the growth of the iron sulphide scale for 20 hours, after which the corrosion rate become constant controlled by the dissolution of scale into the aqueous environment [116].

3.5.2 Influence of operating conditions

The protective film in sour corrosion mainly depends on the factor of H_2S concentration, H_2S/CO_2 partial pressure, temperature, pH, chloride concentration and immersion time [4, 11, 107, 115, 117]. Supersaturation and temperature are important parameters that affect the film accumulation rate to define film morphology and film protectiveness [4, 118].

3.5.2.1 H_2S concentration

H_2S concentration plays an important role in determining the characteristics of the sulphide film and pitting ability on carbon steel [111, 117, 119]. A high concentration of hydrogen sulphide can slightly accelerate the corrosion rate depending on the protectiveness and characteristics of the iron sulphide scale [110].

However, at lower H_2S concentrations, the corrosion rate would decrease significantly [110]. CO_2 concentration does not have a significant effect on the corrosion rate under H_2S dominated conditions [110]. A concentration of 10 ppm of hydrogen sulphide in the solution will lead to a rapid and significant reduction of carbonate film rate [68, 118]. Hydrogen sulphide corrosion starts to accelerate the corrosion rate at H_2S concentration of 25ppm [68, 118].

3.5.2.2 Temperature

Temperature is not sensitive at lower H_2S concentrations; increasing the temperature will increase the corrosion rate for a period of time and then become constant [110]. At higher H_2S concentrations the temperature may change the type of FeS and the protectiveness of the film, which affects the corrosion rate [110, 120, 121]. Temperature influences the thermodynamic process related to the film compositional and morphology, which forms a more protective and stable iron sulphide film compared to the film at lower temperature [110, 120, 121]. Increasing the temperature also increases the solubility of FeS and decreases the solubility of $FeCO_3$ [122].

3.5.2.3 Solution composition

Solution composition factors are important parameters that have an effect on sour corrosion, such as pH, Fe^{2+} concentration, chloride concentration, organic acid and brine composition [110]. The overall corrosion rate is found to increase with a decrease in pH at lower H_2S concentrations. This is because the solution is undersaturated with respect to sulphide ions, which cause the FeS film to dissolve [1, 68, 111, 115, 117]. When the pH is kept constant, even in high H_2S concentrations, the solution may become supersaturated and form a stable iron sulphide film [110]. The Fe^{2+} concentration has a negligible effect on the H_2S corrosion, as the FeS scale is relatively small and easy to reach supersaturation level [110]. However, Fe^{2+} may affect the sour corrosion at lower H_2S concentrations [110]. The chloride concentration will affect the corrosion rate as a more permeable sulphide scale forms on the surface at higher chloride concentrations [12]. Higher chloride concentrations might also impair the iron sulphide film consistently and lead to pitting attack [110].

3.6 Sour corrosion films

In sour corrosion of mild steel, both iron sulphide and iron carbonate layers can form on the surface [123]. Iron sulphide films comprise mainly iron sulphide amorphous ferrous sulphide, mackinawite, cubic ferrous sulphide, smythite, greigite, pyrrhotite, trollite, kansite, marcasite and pyrite [1, 4, 110, 114-116]. The type of iron sulphide film that will form depends on the thermodynamic and kinetic process of the growth. The thermodynamics will determine the stability of the FeS species in a given environment and the kinetics will determine the growth rate of the film [109, 110]. The domains of stability of various iron sulphide species in the temperature and composition diagram are shown in Figure 3-10 [124].

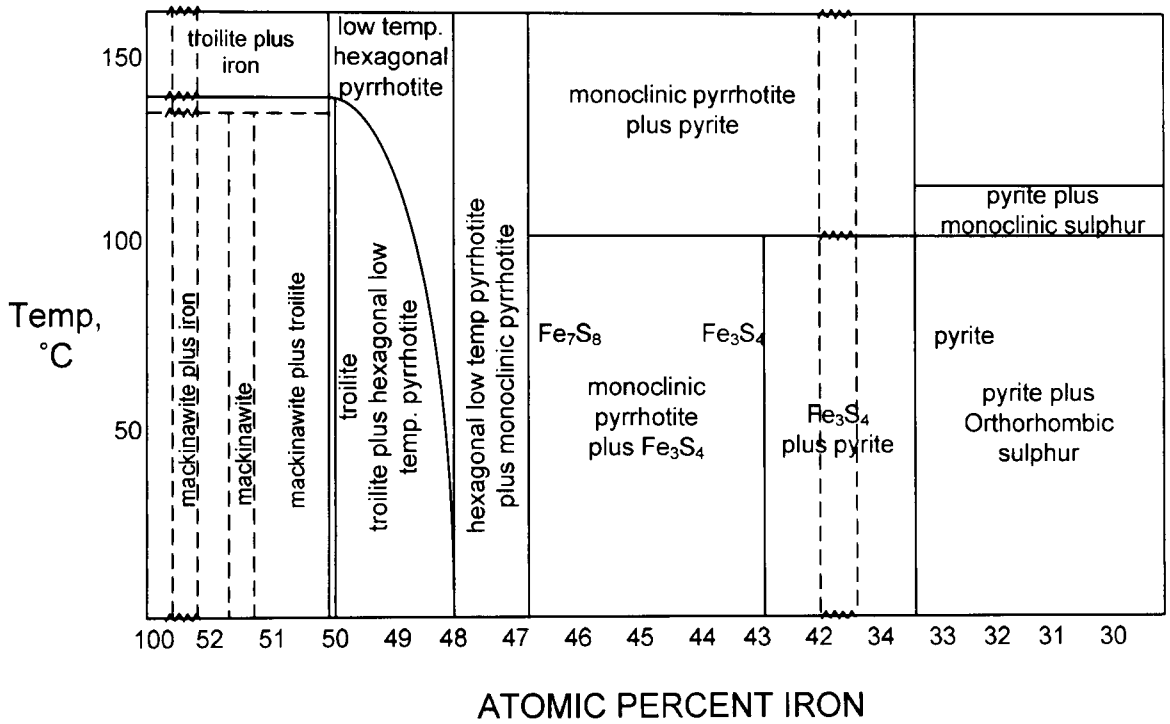

Figure 3-10: Temperature-composition diagram for the iron sulphide system [124]

A thin FeS film is often formed in a short duration of time and with an increased exposure time, a heavier film will form with more complicated layer structures and more than one type of FeS [110]. Figure 3-11 and Figure 3-12 shows the surface morphology with time [5].

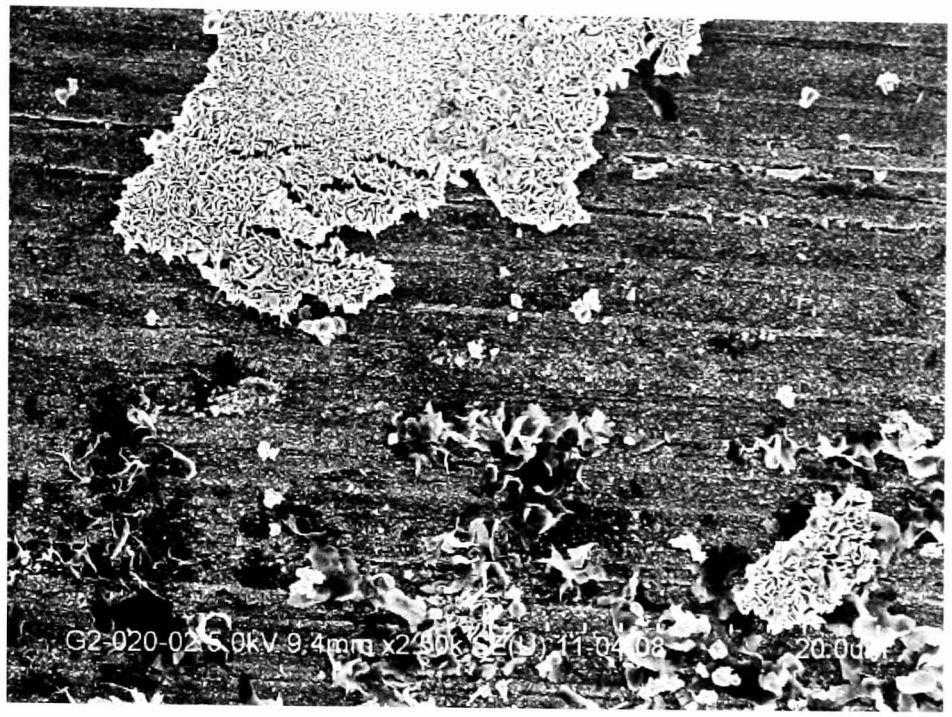

Figure 3-11: SEM image of FeS after 3 hours exposed time at 50% H_2S, 50% CO_2, 60°C, pH 5 [5]

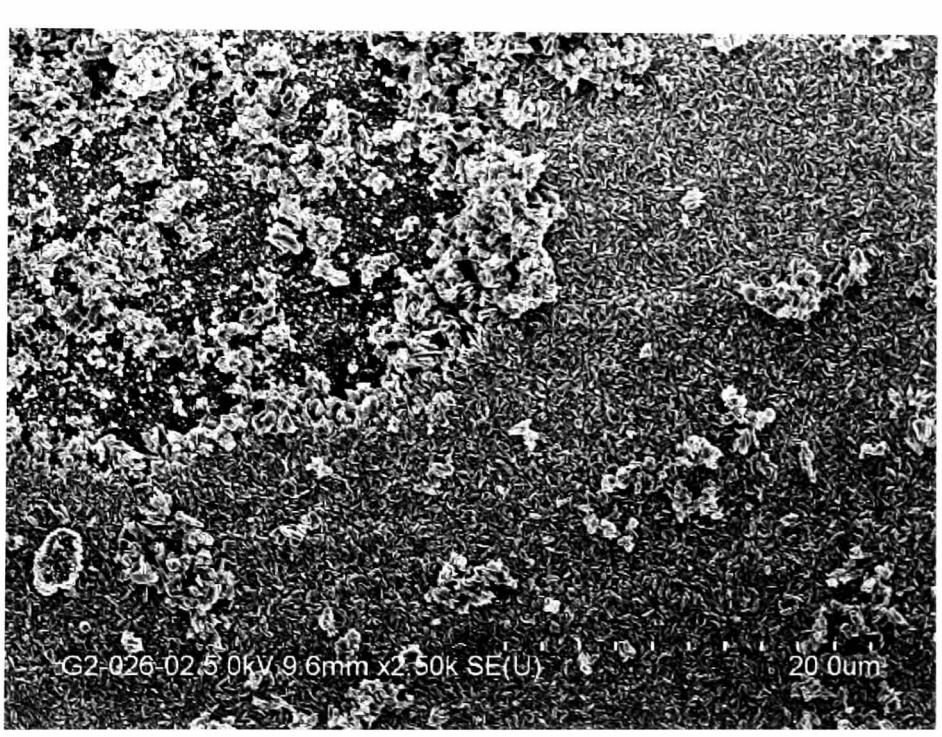

Figure 3-12: SEM image of FeS after 24 hours exposed time at 50% H_2S, 50% CO_2, 60°C, pH 5 [5]

Small amounts of H_2S lead to a rapid and significant reduction of CO_2 corrosion rate, which is associated with the formation of iron sulphide on the surface

[24]. There are three different regimes in the CO_2/H_2S systems that are classified based on the concentration of H_2S, as shown in Figure 3-13.

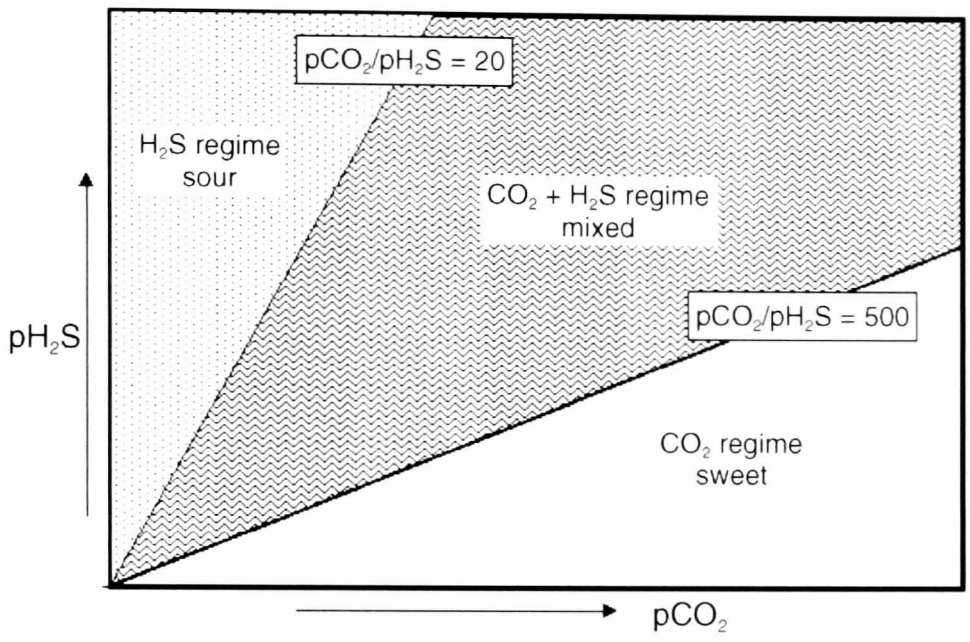

Figure 3-13: Corrosion regimes in CO2/H_2S corrosion [24]

Non-protective films in sulphide mainly comprise loose and brittle mackinawite coarse grains, which lead to film fracture and adherent mackinawite tends to support pit growth and localized attack [24, 114]. The formation of iron carbide in sulphide films also promotes the formation of non-protective films, which tends to accelerate the corrosion rate [54]. An iron sulphide film will form as a metastable species mackinawite and will transform due to salinity change to a more stable species trolite, pyrite and pyrrhotite [8, 12, 115]. The transformation may change the behaviour and protectiveness of the film [8, 114]. If the transformation is due to an increase in salinity, a heavier and more permeable sulphide film will form, which often leads to pitting under the scale [12]. The relationship between the type of corrosion product that forms as a function of temperature and H_2S concentration is shown in Figure 3-14 [24, 113]. The boundary of mackinawite region and pyrrhotite region is defined by the solubility of FeS in the bulk solution [113]. When the FeS is below the saturation limit in the bulk fluid and H_2S is greater than the level required then the mackinawite is the corrosion product [113]. When the FeS levels in the bulk fluid meet or exceed the saturation levels, the reaction kinetic finally allows pyrrhotite to become the corrosion product [113]. Iron sulphide films provide better conductivity

compared to iron carbonate films [8, 61, 124]. In the cathodic reaction for carbonate film, the process of transporting the reaction, protons and carbonic acids will penetrate under the film or at the defect to reach the metal surface [8]. However, for sulphide films, the cathodic process can occur on the film without being restricted by diffusion through the film [8]. Localised attack will start to take place if the local supply of H_2S is not sufficient to reform the sulphide film [8].

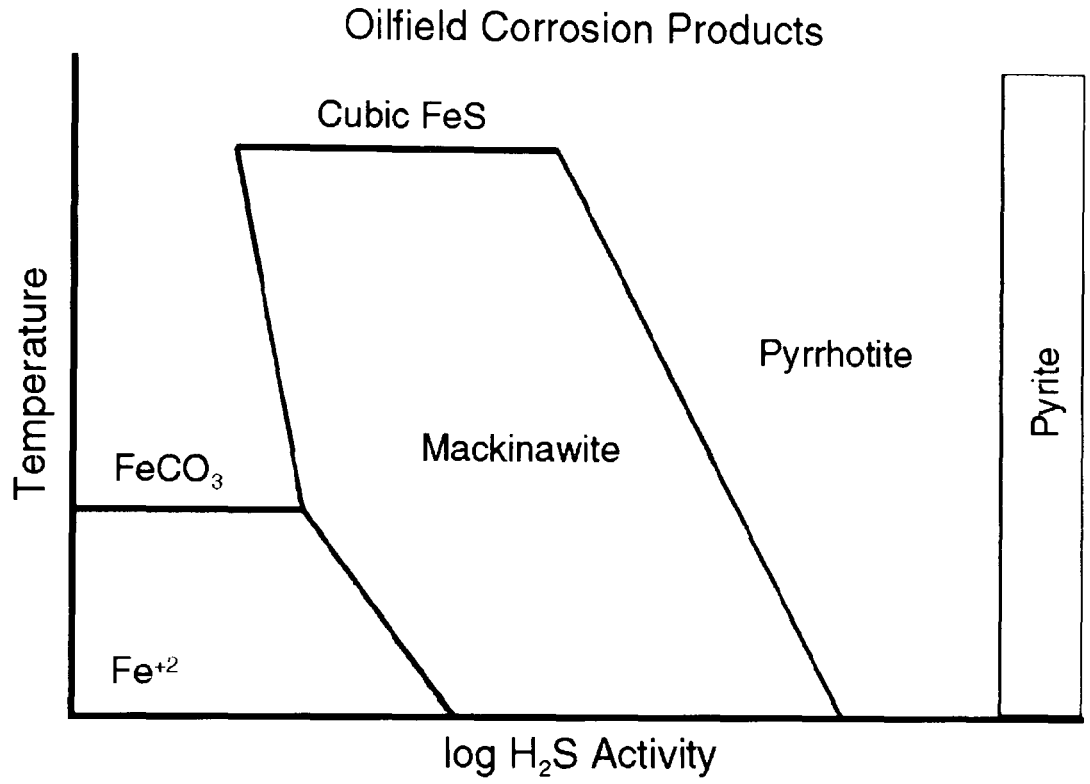

Figure 3-14: Corrosion product relationship [113]

3.6.1 Mackinawite

Mackinawite is a metastable form of FeS that forms in the presence of small amounts of H_2S [24]. Mackinawite is usually the dominant iron sulphur product and forms first then transforms into greigite or pyrrhotite and finally pyrite, as shown in Figure 3-15 [109, 120, 124]. The formation of mackinawite is very rapid and the composition contains between 50.9 to 51.6 atomic percent Fe [109]. Mackinawite is the predominant species at low H_2S concentrations and when the concentration increases, mackinawite might be substituted by pyrrhotite and then pyrite [125].

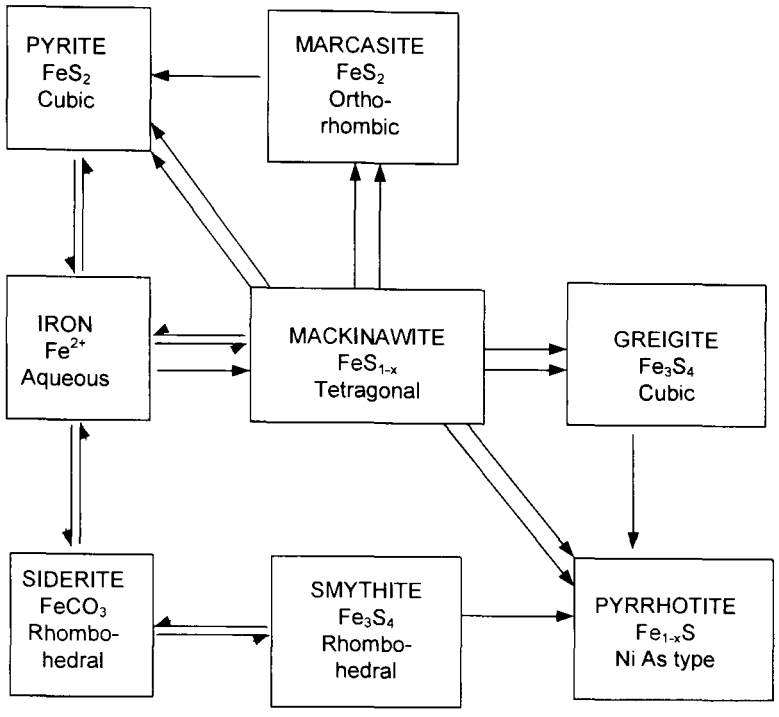

Figure 3-15: Summary of the major iron sulphur inter relationships in aqueous solution [124]

3.6.2 Pyrite

Pyrite formation from the mackinawite and greigite reaction with various sulphur species involves a complex multi step reaction mechanism to convert FeS to pyrite [109]. The rate of conversion is very slow in comparison to mackinawite formation and the kinetics of the formation reaction is shown in equation 3-18 [109]. Pyrite formation is associated with high H_2S partial pressure and believed to require elemental sulphur [24].

$$FeS + S \rightarrow FeS_2 \qquad 3\text{-}18$$

3.6.3 Pyrrhotite

Pyrrhotite is a non stoichiometric of FeS that forms hexagonal close packed (HCP) crystals [109]. Pyrrhotite is believed to be more thermodynamically stable than mackinawite because the pyrrhotite formation kinetic is much slower than mackinawite [24]. Pyrrhotite generally contained 46.5 to 48 per cent Fe in the study sample [109].

3.6.4 Amorphous FeS and cubic FeS

Amorphous iron sulphide is limited as it is unstable and either dissolves or transforms into mackinawite very quickly [109]. Cubic FeS seemed to form in the neutral pH range and was also found to gradually transform to mackinawite at room temperature [109]. Cubic FeS did not form in the presence of oxygen and chloride [109].

3.6.5 Smythite and greigite

Smythite deposits tend to form in hexagonal flakes much like pyrrhotite and is strongly ferromagnetic. It has a similar overall crystal structure to pyrrhotite along the axis but is stacked differently [109]. Greigite is a polymorph of smythite with a nominal composition of Fe_2S_4 [109]. Greigite is often an intermediary between mackinawite and pyrite and the oxidation of Fe^{2+} and Fe^{3+} may play a role in the transformation [109].

3.7 Sour pitting corrosion on carbon steel

The majority of corrosion failures that occur in sour oil and gas production, down hole tubing, pipelines and equipment constructed from carbon steel are attributed to localised corrosion [126]. The presence of sour gas invariably causes localised corrosion if the produced fluid is not treated properly and will quickly result in failure [126]. A sensible approach towards predicting and mitigating localised corrosion is through improving the understanding of the behaviour of iron sulphide, especially the interaction between protective films and pits [127]. The iron sulphide scale that forms on the steel surface can be very protective but localised corrosion attack may occur in the presence of high chloride levels, elemental sulphur or exposure to stagnant water [128]. The higher corrosion potential difference between sour scale and steel causes greater pitting tendency in sour corrosion compared to sweet corrosion [72]. The precipitated film forms on top of the existing mackinawite films, decreases the effect of flow, and increases the overall corrosion rate and probability of localised corrosion [114, 118]. Figure 3-16 shows the SEM image of pitting growth under the sour film [118].

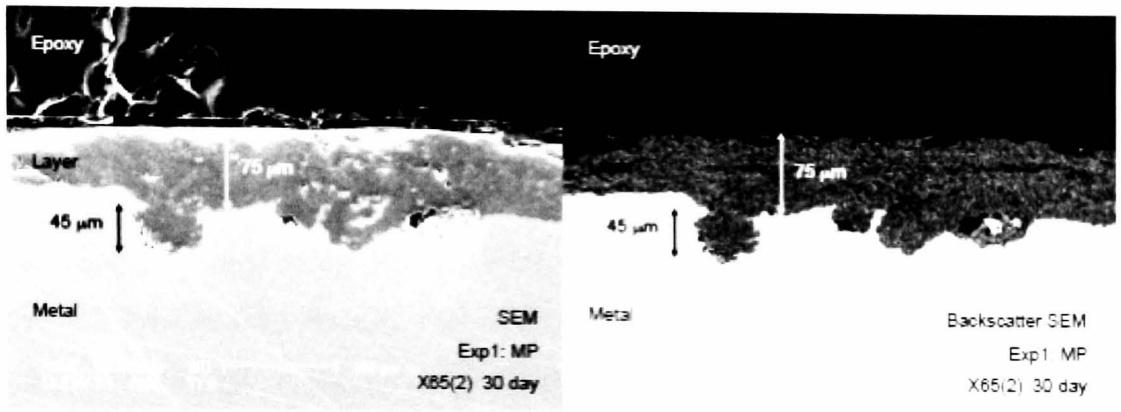

Figure 3-16: SEM cross-section image showing pit growth under film on X65 carbon steel at T=60°C, pH=6, P_{CO2}=0.77Mpa, H_2S at 25ppm, and V=1m/s for 30 days [118]

There are several methods to characterise pitting corrosion, such as pit initiation, pit propagation, repassivation, total number of pits, average pits and maximum pit depth [21, 129]. Sun et al. characterised pitting corrosion by pit initiation, pit propagation and repassivation [129]. Propagation of pits is a kinetic process and will normally lead to the failure of the facilities [129]. Stewart et al. characterised and ranked the maximum pit depth because it represents the worst case scenario that leads to failure, as shown in Figure 3-17 [21].

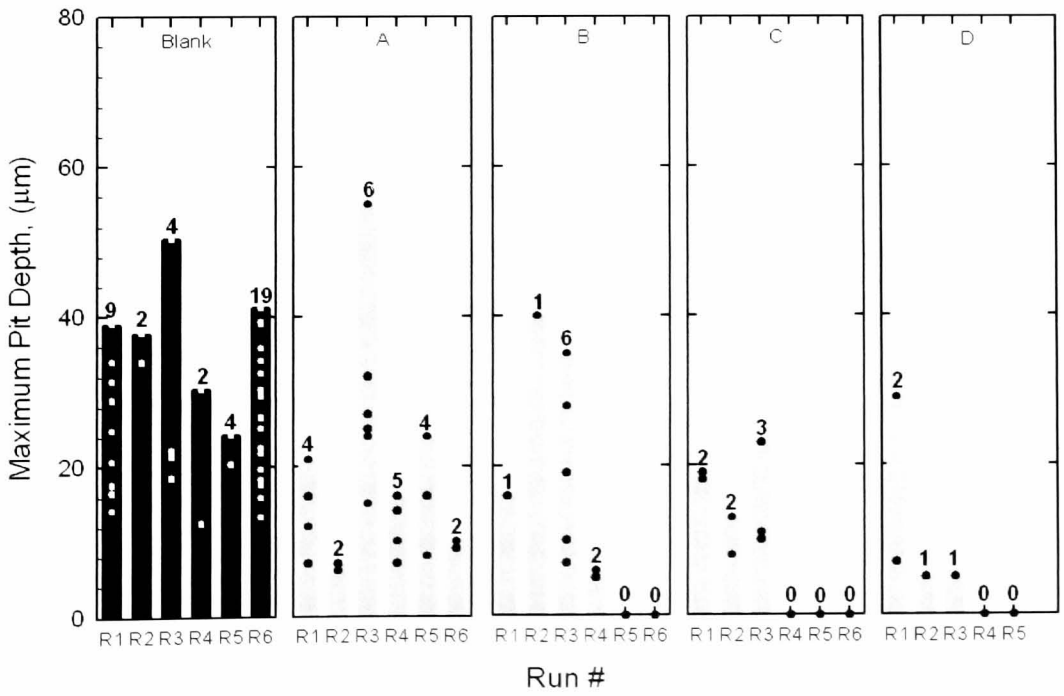

Figure 3-17: Pit depth measurements and pit counts for blank tests and inhibitors [21]

3.7.1 Sour pitting corrosion process

Iron sulphide films on the carbon steel surface can be very protective but depending on the various environmental factors, the different thermodynamics in some cases can be non-protective and results in localised corrosion [24, 128, 130]. The changing form of the iron sulphide layer can develop internal stress in the film and can lead to film fracture that causes the potential of localised attack [24, 128, 130]. The change in the electrochemical kinetics will also increase the corrosion potential over time and lead to a region where local breakdown of the protective film and pitting corrosion could occur [119, 124, 128, 131]. This will lead to the situation where the area at the film breakdown becomes small local anodes and the film area at the steel surface will work as efficient cathodes [114, 124]. The corrosion product films consist of iron sulphides, mostly mackinawite, and are more porous and apparently less protective [131, 132].

3.7.2 Sour pitting corrosion initiation

There are various ways how pits are initiated in a sour environment. Steel microstructure, such as manganese, sulphide inclusions plays an important role in the pitting initiation in X65 carbon steel due to sulphide inclusion and mixed manganese and iron sulphide films [124]. These promote pitting attack by acting as weak points in the metal surface and have been found to act as susceptible spots for the nucleation of pits [124]. Another way of pitting initiation is due to the Fe_3C phase that is left behind, the cathodic reaction is supported by the iron sulphide film and the anodic dissolution of ferritic iron will proceed beneath the films. This may result in undermining of the film and the Fe_3C phase with subsequent groove formation, which may eventually grow into pits that consume the ferrite grains surrounding the pearlite [130].

The other way of pitting initiation is if the metal surface is not fully covered with iron sulphide or if the film breaks down in certain locations [126]. This will create an anodic site on the metal surface and the iron sulphide area will act as cathodic sites [126]. Consequently, there will be a situation of a small anodes and a large cathode set up on the metal that will accelerate corrosion at the anodic sites that will cause pits to form [126]. Kvarekvnal found that pits in sour environments can be

of many different shapes and types under identical conditions [130]. Moloney et al. found that many smaller pits are initiated adjacent to each other and initiate near the larger pits [133].

3.7.3 Sour pitting corrosion propagation

Under some conditions a transient pitting mechanism can take place in which pits are initiated for a limited period of time [132]. Pit depth does not vary significantly with the exposure time, which indicates that the process of pit initiation, growth and passivation takes place within a rather limited space of time [132]. Pit growth is decelerated or maybe even stops after a while, probably due to the accumulation of corrosion products in the pits [132]. The incubation time between pit initiation and the maximum pit depth appears to be independent of the duration of exposure time [132]. The pit growth rate may decrease with time and then stop growing in some cases probably because of the deposits of solid corrosion products in the pits [132]. Kavarekval et al. shows a cross section image of 50μm pit accumulation of corrosion products as shown in Figure 3-18 [132].

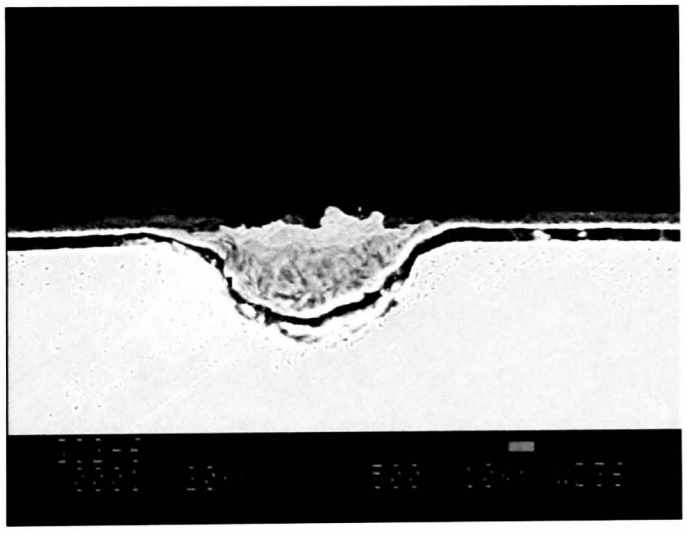

Figure 3-18: SEM picture of a pit filled with corrosion product [132].

Sun et al. indicated that the pit propagation rate under a sour environment is a nonlinear process with respect to time due to passivation and repassivation taking place to reduce the pit propagation rate [129]. In addition, Stewart et al. shows that pit depth increases over time, which means that longer tests will generate more severe localised corrosion and thus deeper pits [134]. Stewart et al. observed that larger pits

were severe enough to last for most of the 72 hours test duration [134]. Moloney et al. indicated that the speed of pitting rate is due to localised high Fe^{2+} concentration from pitting leading to saturation of salts, such as iron chloride ($FeCl_2$), iron sulphide (FeS), iron carbonate ($FeCO_3$) within the pit mouth [133]. These will impede the irons travelling to and from the active pit metal surface retarding the pit from propagating further and resulting in consequential pit death [133].

3.8 Sour corrosion inhibitors

Corrosion inhibitors are typically applied in oil and gas production to mitigate corrosion caused by the presence of sour gases [18, 123]. Most laboratory testing methods are only suitable to assess inhibitor performance in preventing general or uniform corrosion [126]. Additional corrosion monitoring techniques should be used to confirm that pitting corrosion is not taking place and optimise the inhibitor concentration accordingly [126]. The ability of the corrosion inhibitor to interact with those layers determines the effectiveness of the inhibitor and its ability to prevent pitting [135]. The performance of the inhibitor is determined not only by the absorption of the steel surface but by its ability to bind into a product layer providing protection and changing the morphology of future scale growth, as shown in Figure 3-19 and Figure 3-20 [135].

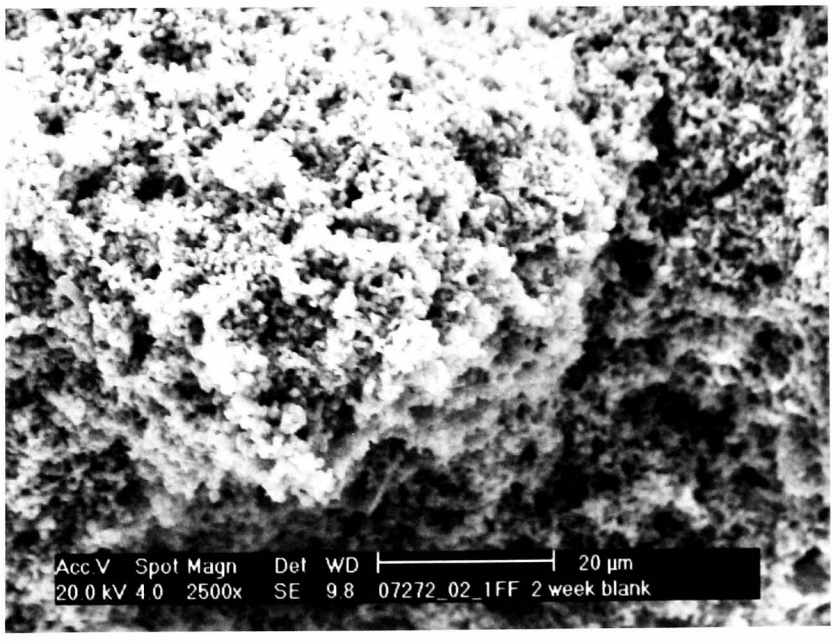

Figure 3-19: SEM image after 14 Days at 3% NaCl, pH 6, 689Kpa H_2S [135].

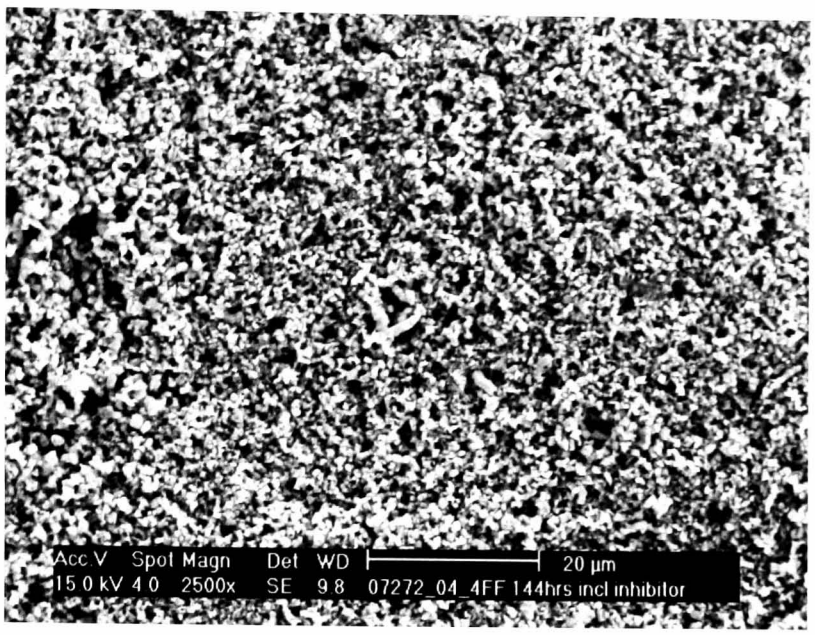

Figure 3-20: SEM image after 14 Days at 3% NaCl, pH 6, 689Kpa H_2S with inhibitor[135].

Moloney et al. showed that corrosion inhibitors that provide high general corrosion inhibition may not always offer localised corrosion protection [7, 27]. Furthermore, Jenkins determined that higher dose rates of inhibitor are required to prevent localised corrosion compared to the dose rate required to prevent general corrosion [27, 126]. Schmitt et al. showed that adding inhibitors at sufficient concentration on pre-corroded specimens may stop pitting corrosion [27].

The inhibition effect is related to the formation of a protective layer with ferrous sulphide grains on the electrode surface [115]. The metal surface is practically always covered with a protective film and the build up of adsorbed inhibitor results in a synergetic effect in the common protective activity [18]. Sastri et al. showed that the inhibitor layer was detected using XPS at the outer layer of the film to prevent the dissolution and recrystallisation of the lower iron sulphide layer [136]. The type of inhibitor is important so that the most appropriate chemical is selected to control the corrosion process [12]. There are many types of sour corrosion inhibitor; one of the most commonly used is a cationic inhibitor composed of cyclic aliphatic and aromatic amine complexes with non-ionic surfactants [12]

Stewart et al. evaluated sour inhibitors in terms of the maximum and average pit depth penetration and analysed the depth/size and distribution of the pits in conjunction with the electrochemical technique [134]. Moloney et al. described that some inhibitor tests that resulted in deeper pits than were observed on the blank test could be the adverse effect of the corrosion inhibitor interaction with various chemistries contained in the test environment, and which could result in nullification of the corrosion inhibitor or may be based on the competitive adsorption of the molecules within each product of the metal surface [7].

3.8.1 Type of sour corrosion inhibition

Inhibitors have often been used to control sour corrosion such as substituted imidazolines, alkyl pyridine quartenary amines, phosphate, nitrates and substitutes amines [116,136, 137]. Inhibitors may assist in generating a protective layer by forming a thin and effective barrier layer on the metal surface that will resist the chemical attack of liquids and gases [136]. This will also reduce the dissolution of scale into the aqueous environment and it may also hinder the diffusion control led growth of iron sulphide scale or prevent spilling of the scale surface [116, 136]. Schmitt et al. showed that inhibitors affect the morphology of iron sulphide by making the scale thin, smooth and adherent to the surface compared to without inhibitors in which it is thick, rough, and spongy with a poor adherence scale [138]. It was also found that the best performance inhibitors have the smallest scale thickness and provide good protectively [138]. Schmitt et al. found that amide derivatives with alky group inhibitors provide a good general corrosion and localised corrosion inhibitor [138]. Park et al. showed that corrosion inhibitor appears to change the crystal morphology [135].

Imidazoles have two types of nitrogen type inhibiting forms – pyridine and pyrrole. These are considered to influence the bonding of molecules with iron, as shown in Figure 3-21 [104]. Pyridine and substituted pyridine compounds have been used as inhibitors in a medium consisting of sodium chloride solution in sour environments [137]. Bhargava et al. showed that imidazole can react with metal if it is able to reach Fe through the channels formed in the oxide layer, which provides a greater surface coverage and protection [104].

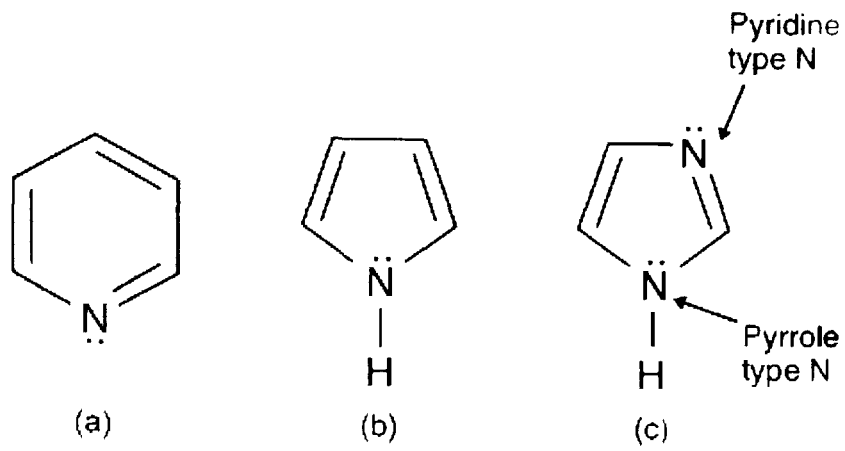

Figure 3-21: Molecular structure of a) pyridine, b) pyrrole, and c) imidazole

Amines and quaternary amines are popular inhibitors for use in sour gas applications [21]. Stewart et al. reported that amine based inhibitors exhibit good ability to inhibit pitting corrosion in a range of brine conditions and highly sour environments [21].

Field trials show that the amine based inhibitors slightly decrease the iron concentration and general corrosion rate as well as pitting corrosion in the system [21]. Wang et al. showed that many of the shallow pits observed after removing the black surface scale and the pitting were further prevented by the presence of the inhibitor [139]. A mixture of imidazoline and coco benzyl quaternary ammonium inhibitor could greatly reduce the general corrosion and significantly reduce the localised attack [139].

3.9 Environmentally friendly corrosion inhibitors

Corrosion inhibitors continue to play an important role in controlling internal corrosion and research efforts are necessary to develop corrosion inhibitor products that are more acceptable to the environment than the conventional types of inhibitor [138]. In recent years concern has increased concerning the environmental impact of the chemicals being used leaking into the environment and the toxic effect on the marine life [138]. Inorganic inhibitors were first developed by the use of inorganic salts or blends including chromates, nitrites, phosphates, borates, silicates, zinc salts and other cations [31, 40]. The use of anodic inhibitors such as nitrites and chromates

requires a high initial dose in order to achieve an effective passive layer on the metal surface; however, the concentration can be reduced in the presence of polyphosphates and zinc ions [31]. Zinc ions inhibit by the cathodic polarization mechanism and in combination with phosphates will lead to a protective film. The protective films caused by cathodic inhibitors are macroscopic and are mostly easily visible, whereas anodic inhibitors will generally form very thin, hardly detectable passive films. Although inorganic inhibitors provide reliable corrosion protection in aqueous solutions, the discharge or inorganic material has become increasingly unacceptable [30, 31, 40]. Organic inhibitors have been used to reduce the chemical impact on the environment and ensure chemical degradability under mild conditions and biodegradability. The most commonly used organic inhibitors are orthophonates, pyrophosphate, gluconates, phosphonates, polyacrylates, soluble oils and carboxylates [30, 40].

3.9.1 Corrosion inhibitor legislation

An improved understanding of corrosion inhibitors has led to a more environmentally acceptable chemistry that meets and exceeds the regulatory requirements. The legislative bodies have drawn up a set of guidelines on environmentally friendly or green inhibitors [39]. The regulations require chemicals for field applications to have specific properties regarding biodegradation, toxicity and bioaccumulation according to OSPAR guidelines (Convention for Protection of the Marine Environment of the North-East Atlantic) [39, 140].

The Norwegian authorities have divided offshore chemicals into four colour categories – black, red, yellow and green. The worst-case chemicals, categorised as black, are not permitted to be discharged unless in exceptional circumstances. Red category chemicals are to be phased out and banned. Yellow category chemicals are permitted and green chemicals are those listed in the PLONOR. The yellow category requirements include the following [39]:

- Biodegradation > 20%
- Log Pow < 3
- Toxicity > 10mg/l

For Norway, test data are required on biodegradation, bioaccumulation and toxicity according to OSPAR guidelines.

The UK legislation accepts extended marine biodegradation data beyond 28 days and also fresh water biodegradation data. Once the ecotoxicological data have been generated, the results are then entered into the pre-scheme. Typically, if the biodegradation of a chemical is more the 20% in 28 days then it is then judged according to the following three criteria [39]:

- Biodegradation < 70% (OECD 301A, 301E) or < 60% (OECD 301B, 301C, 301F, 306)
- Bioaccumulation log Pow > = 3 or BCF > 100 (considering molecular weight)
- Toxicity LC50 or EC50 < 10mg/l

If it then meets two out of three criteria, it is placed on the substitution list and is flagged for substitution [39].

3.10 Artificial pitting experiments

The artificial pit experiment setup was developed for inhibitor development testing to address the ability of the inhibitor to affect localised corrosion that is already propagated at a known rate [50, 69, 141]. There are various types of artificial pit techniques that have been used to accelerate the pitting process – pencil artificial pit, artificial pit, mechanical punched, drilled, electrochemical and chemical [69].

Turnbull et al. used the pencil artificial pit technique to generate the same pits repetitively in a controlled manner in both sweet and sour environments [69, 142-144]. The anode is formed by mounting a steel rod of small diameter in epoxy and pre-corroding it to a specific depth and coupled via a zero resistance ammeter (ZRA) as shown in Figure 3-22 [69]. This technique is flexible since the amount of pre-corrosion and pit depth can quite easily be altered and it is able to evaluate inhibitor performance [69, 143, 144].

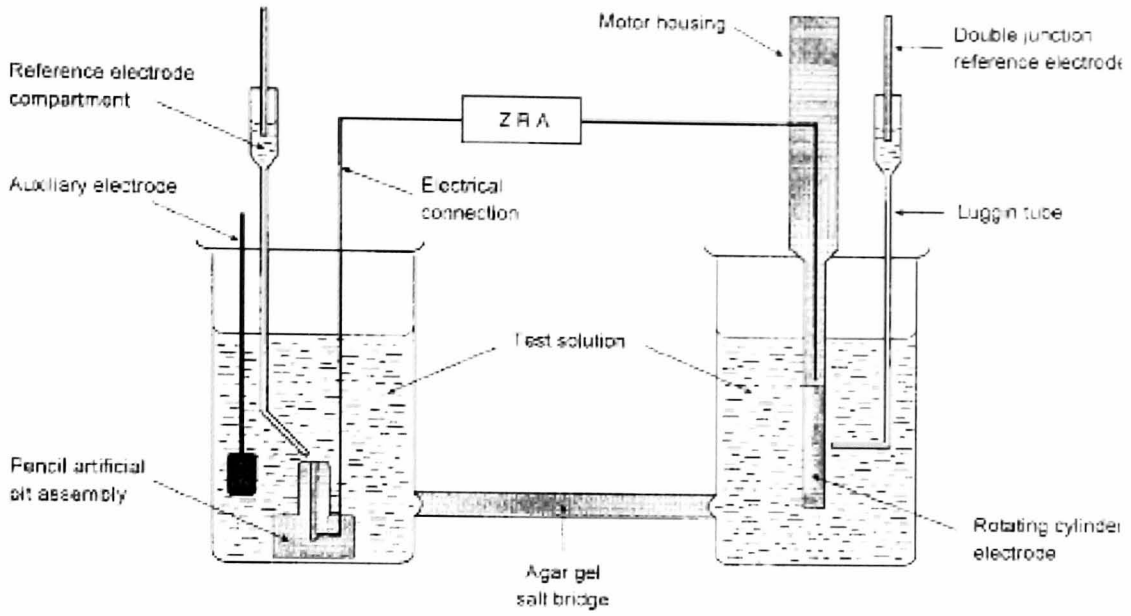

Figure 3-22: Schematic of two-compartment cell for pencil artificial pit experiment [69].

Marsh et al. designed an artificial pit-bar test consisting of zero resistance ammetry (ZRA) measuring the current between an artificial pit electrode connected to a counter of the same material but of much larger area [141]. The wire electrodes were recessed by anodic polarisation in an acid solution to achieve the required pit depth [141]. The inhibitor performance was tested in sweet and sour environments with respect to inhibition of general corrosion and localised corrosion [141].

Han et al. coupled a bare steel surface that acted as an anode and $FeCO_3$ layer covered steel that acted as a cathode in a conductive CO_2 solution. Nesic et al. used the mechanical and chemical film damaged technique to study film breakdown and pitting [26, 42, 43]. The mechanical film damage technique used hydrodynamic force to partially remove the film, whereas the chemical film damage technique used dissolution removal by mass transfer control to partially remove selective film that exposed an area of open pores on the film, as shown in Figure 3-23 [42, 43]. The difference between these techniques is in the kinetics of the process; it appears that the film dissolution produces a better effect compared to mechanical film removal [26].

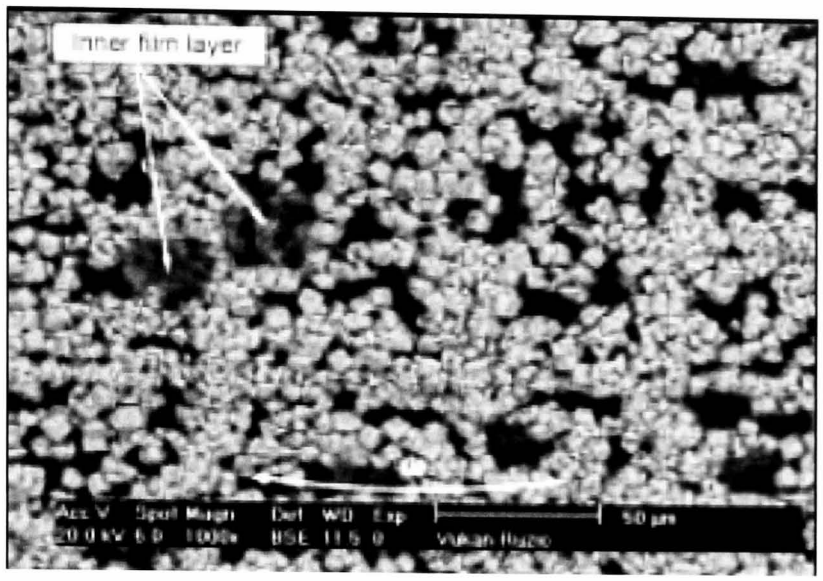

Figure 3-23: Typical surface topography of $FeCO_3$ film at the end of dissolution process at 10000rpm velocity, pH 5.8 [43].

3.11 *In-situ* pitting experiments

Direct observation of the characteristics of pitting formation requires tools with the appropriate resolution and that are suitable for *in-situ* study. The technique should be able to observe the initiation and growth of pits and assess the inhibitor activity towards pitting on carbon steel surfaces in sweet and sour conditions. Of the many techniques that have been used, one of the most appropriate is by Davenport using *in-situ* synchrotron X-ray diffraction. This technique can obtain the information on crystallite size, which influences the transport properties of the film and the roughness of the underlying metal [67]. *In-situ* X-ray absorption spectroscopy and electrochemical impedance spectroscopy can also be used to obtain quantitative data during alloy passivation [74, 76].

The *in-situ* imaging technique using optical video and camera in conjunction with electrochemical measurement was used to monitor crystallisation of calcium carbonate and pitting on stainless steel [78, 145]. This technique can map and monitor the pits and crystal growth in real time up to 1μm size [145, 146]. Schmitt et al. used video microscopic control with a window autoclave to study the parameters of the pitting initiation process under sweet conditions within the observation time of 120 minutes [146]. These techniques indicate that the inhibitor could inhibit pitting initiation [146]. Nyborg improved the *in-situ* visualization technique to observe

localised corrosion, developed previously by Joosten et al., to observe mesa attack growth overtime [47, 86]. This technique has shown that mesa attack in carbon steel was initiated from several small pits, which grow together in a large mesa attack [47].

There are also techniques that detect the temperature difference during the pitting process, such as thermal AFM and cyclic thermometry [147, 148]. Thermal AFM works on the principle of a temperature difference between the localised area to map the thermal image and cyclic thermometry using a linear thermal program to measure the critical pitting temperature [147, 148].

Other *in-situ* techniques can be combined with *ex-situ* surface analysis techniques to study pitting, such as the *in-situ* scanning reference electrode and *in-situ* scanning vibrating electrode technique [84, 88, 93, 149-151]. These techniques were used to map the pitting potential regions and are capable of determining the surface dimensions of the pits [84, 88, 149-151]. *In-situ* pitting depth readings can be obtained using ultrasound sensors as practiced to monitor pitting depth in service pipelines [152].

3.12 Surface analysis

The nature of sweet and sour films has been extensively studied using advanced surface sensitive techniques such as scanning electron microscopy (SEM), electron dispersive X-ray (EDX), Energy-dispersive spectroscopy (EDS), X-ray photoelectron Spectroscopy (XPS), Atomic Emission Spectroscopy (AES), X-ray diffraction (XRD) and Secondary ion mass spectrometry (SIMS) [2, 48, 77, 153-155]. EDX analysis has shown that the distribution of elements through the sweet film cross section is not homogeneous. The layer near the surface is enriched in carbon and depleted in iron, however, the layer near the material interface is rich in iron [48]. The differences in the XPS binding energy between surface and subsurface regions was attributed to the variation of the chemical environments [2, 156, 157]. The difference in binding energy for C 1s, O 1s and Fe 2p were found between surface and subsurface spectra [2]. Applying 30 seconds of argon etching to the surface can remove carbon and oxygen contamination on the surface [152]. The analysis shows that the sweet film layers are inhomogeneous and comprise a mixture of iron and

complex iron carbonates [2]. Sastri et al. have successfully used XPS to analyse the inhibitor film and iron sulphide layer under sour conditions as shown in Figure 3-24 [136].

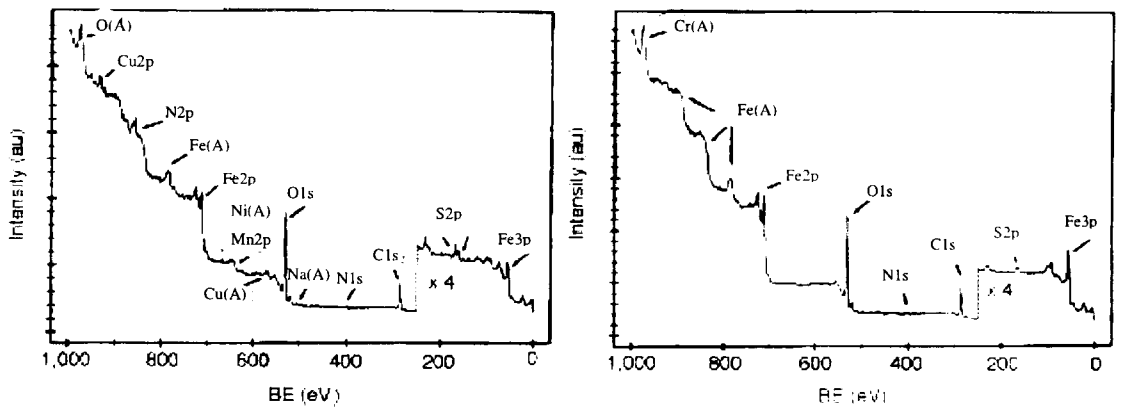

Figure 3-24: XPS survey spectra recorded from steel coupons exposed for 96 hours to deaerated aqueous solution of 5% NaCl CH_3COOH saturated with H_2S a) No inhibitor, b) with inhibitor added [136].

Fourier transform infrared spectroscopy (FTIR) is another surface analysis technique that is able to obtain information at the molecular level regarding the metal electrolyte interface [156, 158]. Durnie et al. has used FTIR to identify inhibitors that are tenaciously adsorbed to the steel [159]. It also provides useful information to study the mechanism of the inhibitor and evaluates newly developed inhibitors and its surfactants, such as fatty amido-amines, imidazolines, quaternary amines, phosphorous and other derivatives [158, 160, 161]. Legrand et al. has characterised iron carbonate on carbon steel surface and attributed the peaks at 1420, 1345, 1068 and 860 cm^{-1} [102, 163-165]. Using this technique, other sweet corrosion products could be characterised to indicate the corrosion deposit on the surface [165-168]. Various species of iron sulphide have been characterised using FTIR. Romero et al. characterised iron sulphide peak at 1400, 2700 and 2900cm^{-1} [169,-171]. Caldeira et al. and Chernyshova studied the morphology of pyrite and attributed the pyrite peak at 1430 and 1530 cm^{-1} [172, 173]. Baird et al. have studied the mackinawite morphology and structure using FTIR and identified the mackinawite peak at 310, 435, 674, 1626 and 3384 cm^{-1} [156].

3.13 Literature review summary

The majority of sweet and sour film surface analysis studies in the literature have been conducted in environments having a bulk solution pH of greater than pH 5 and temperatures greater then 60°C. Most of these experiments were conducted in the temperature range of 70°C to 80°C, however, many pipeline operating conditions can be significantly lower than this.

A mixture of iron carbide and iron carbonate leads to a semi-protective film that provides little protection to the material. Mixed iron carbide/iron carbonate films are the most common type found on carbon steel under sweet conditions. The films may change their characteristics to be more protective depending on the build-up of iron carbonate film over time. The structure of these mixed films also influences their susceptibility to film breakdown and pit initiation and propagates below the porous corrosion film by local cell mechanisms.

H_2S concentration plays an important role in determining characteristics of the sulphide film and pitting ability on carbon steel under sour conditions. Hydrogen sulphide starts accelerating the corrosion rate at H_2S concentrations of 25ppm where localised corrosion was observed.

The pitting corrosion process can be divided into a sequence of three steps – initiation by breakdown of passive film; initiation of metastable pit growth and stable growth of pits. The chloride ion content is an important factor because it weakens the protective film and leads to film breakdown and pitting initiation.

The *in-situ* imaging technique using optical video and camera in conjunction with electrochemical measurement is a robust technique that can map and monitor the pits and crystal growth in real time up to 1μm size. This technique combines with *ex-situ* surface analysis and can be used to study the mechanisms of the action of commercial inhibitors to improve the inhibitor performance on pitting problems in sweet and sour conditions.

The literature has demonstrated a great deal of research about sweet and sour corrosion and the interaction of various inhibitors. However, most of the research concentrates on general corrosion and there are still a number of unknowns about the corrosion reactions that leads to pitting and the interactions between inhibitors and pitting. In this thesis, the pitting process will be studied including film formation, film breakdown, pitting process and its inhibition in sweet and sour conditions.

Chapter 4 *In-situ* visualisation rig and sour rig design, building and commissioning and setup

4.0 *In-situ* visualisation rig and sour rig design and setup

This chapter is divided into two different test designs and setups. The first section explains the *in-situ* visualisation design, while the second section explains the sour rig design and procedure for running the rig. The *in-situ* visualisation rig and sour rig were developed as part of this study project.

4.1 Sweet *in-situ* pitting rig

In-situ visualisation using an optical microscope with *in-situ* electrochemistry will be used to study the behaviour of film growth, localised film breakdown, pitting growth and assessment of localised corrosion inhibitor. The *in-situ* visualisation rig for sweet and sour experiments was designed, built and commissioned as part of this project study. The imaging method will monitor the interaction on the sample surface in real time in conjunction with electrochemical data. The special features of the cell are the ability to control the temperature up to 80°C, indent an artificial pit and simulate sweet and sour conditions. Figure 4-1 shows the specimens used and Figure 4-2 shows the sweet *in-situ* pitting rig.

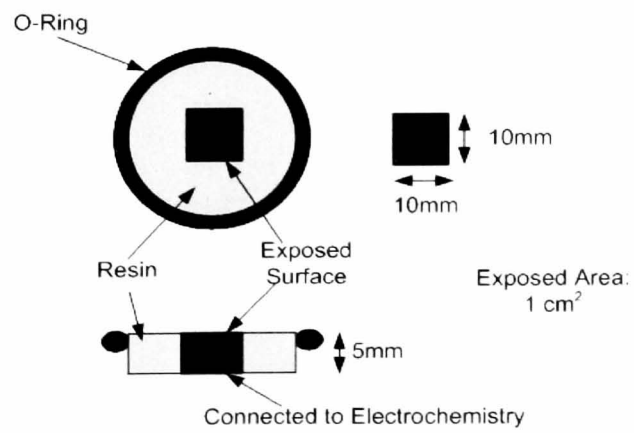

Figure 4-1: Specimens for *in-situ* rig

The rig assembly was composed of an electrochemical cell, specimen vessel and camera set-up. The camera assembly contained an adjustable lens to change zoom on the object, lighting system, camera and image monitor, as shown in Figure 4-3.

The magnification power can monitor the pits initiated on the working electrode as soon as their size reached 1μm and followed the growth up to 300μm. By using image analysis software, the image obtained over a period of time can be converted into a short video. Figure 4-4 shows the artificial pitting image using different magnifications.

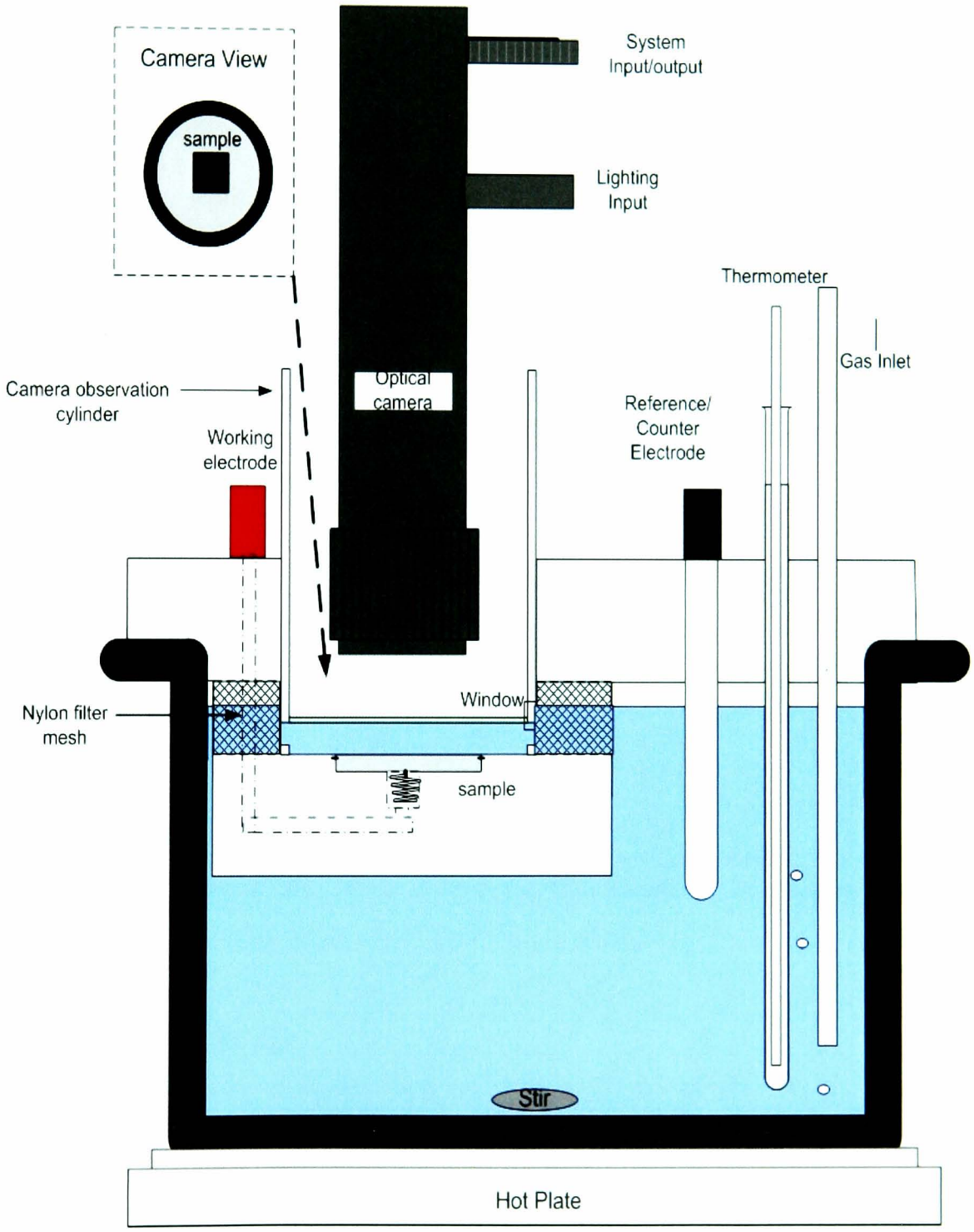

Figure 4-2: *In-situ* sweet pitting rig setup

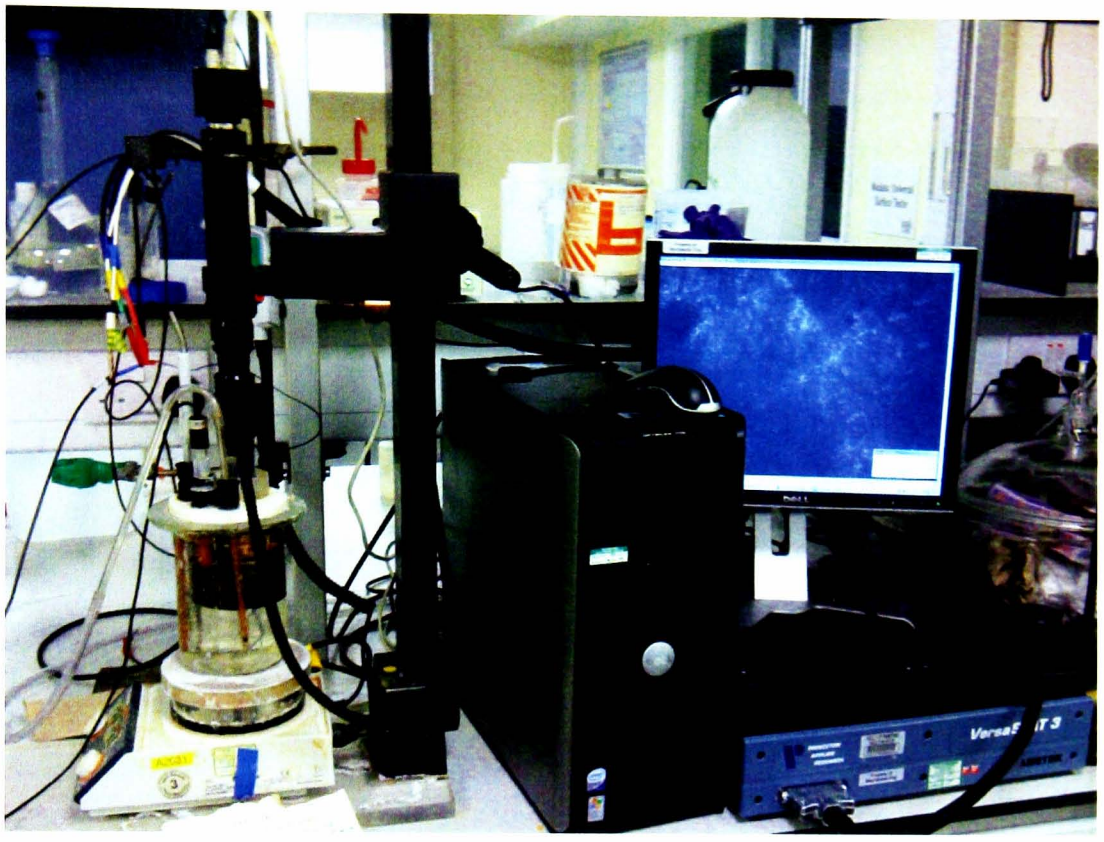

Figure 4-3: *In-situ* pitting rig system

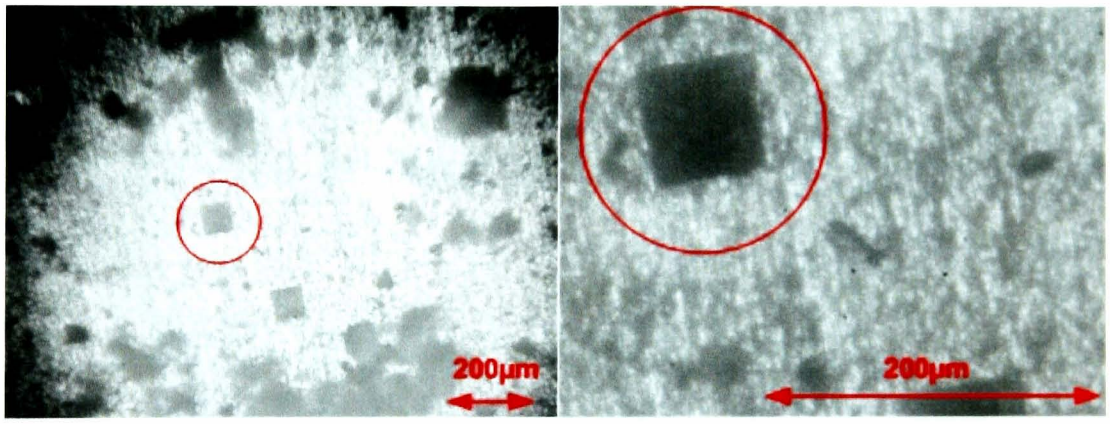

Figure 4-4: Artificial pitting image using different magnifications

4.2 Sour experiment rig

The sour rig was designed, built and commissioned as part of this study project. The sour experiment simulated the sour environment in an oilfield pipeline where the saturated hydrogen sulphide and carbon dioxide were present in the solution. The experiment was performed in an enclosed glass cell on X65 carbon steel to understand the electrochemical behaviour of the material in the sour solution. The

design parameters of the sour cell, as shown in Figure 4-5, were similar to the sweet cell but the emphasis on safety was prioritised due to the risk from hydrogen sulphide gas. Figure 4-6 shows the sour rig. The sour rig contains two experiment cells, which can perform a single or duplicate experiment at one time. The sour rig can also operate with or without *in-situ* visualisation equipment.

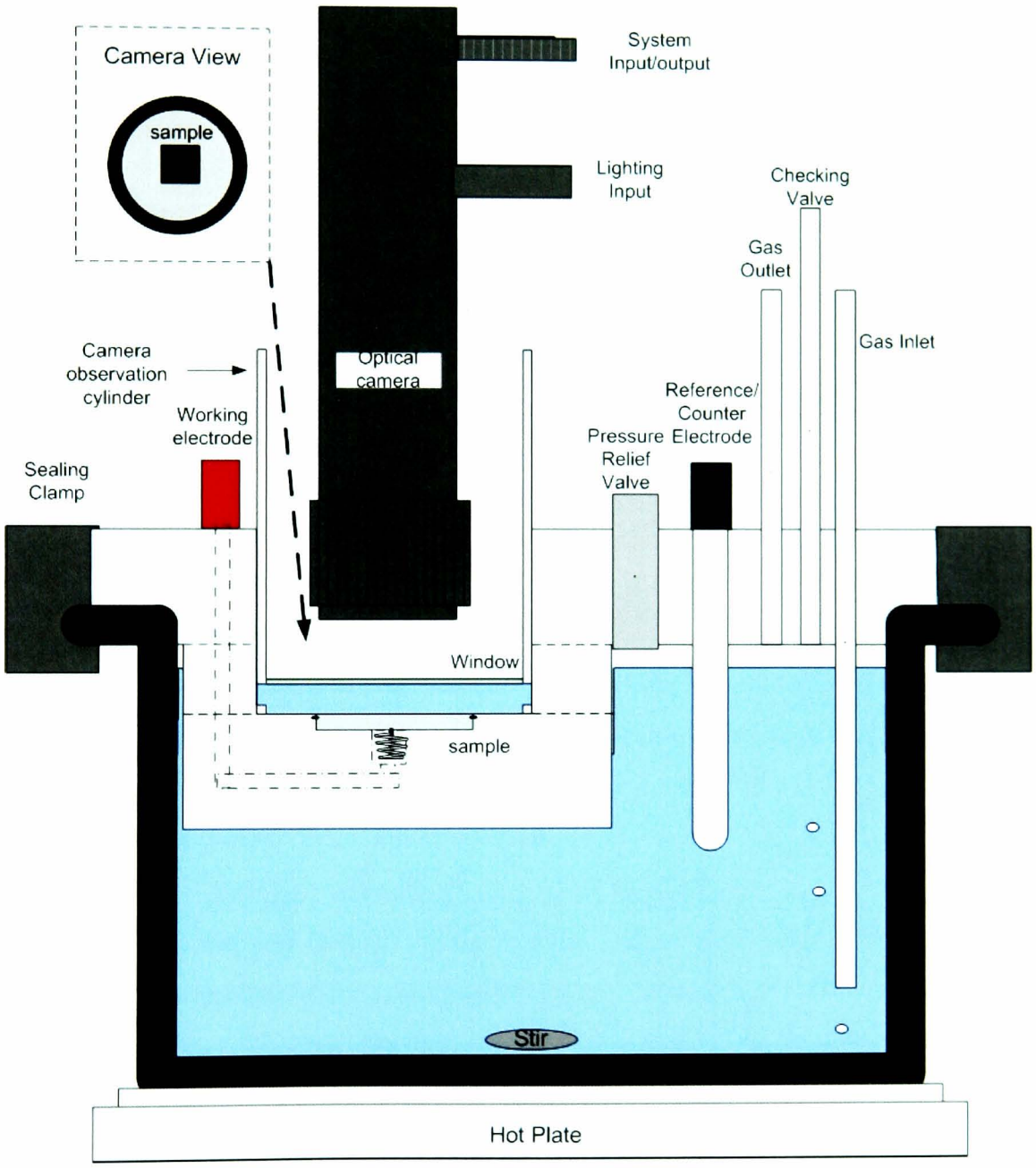

Figure 4-5: *In-situ* sour rig test setup

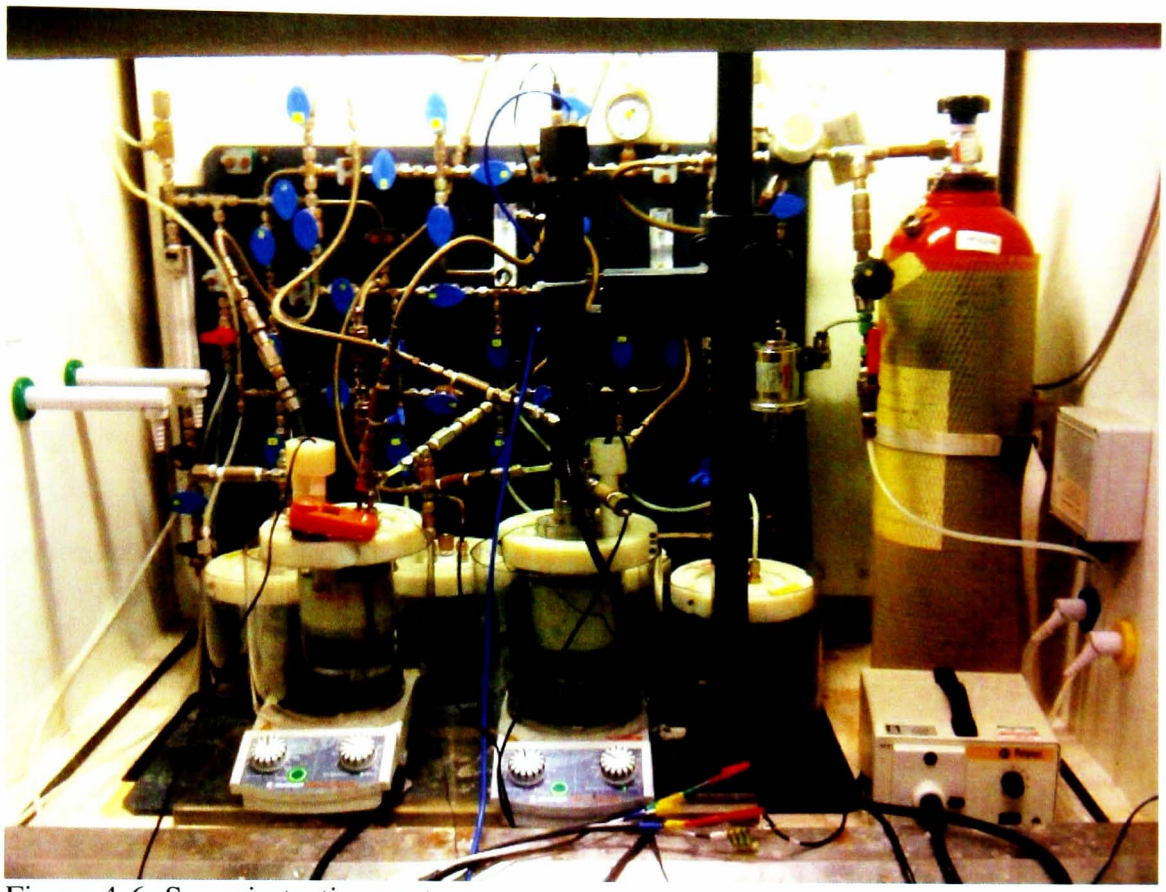

Figure 4-6: Sour rig testing system

4.2.1 Hydrogen sulphide safety

The sour gas system isolated the gas in the system to avoid any escape of the gas due to the danger of the hydrogen sulphide [174, 175, 176]. Hydrogen sulphide is a flammable, colourless gas that is toxic at extremely low concentrations. It smells like rotten eggs at concentrations of less then 10ppm and quickly causes a loss of sense of smell when the concentration increases [174, 175, 176]. The sour gas experiment was placed inside the fume cupboard to extract any leak of the hydrogen sulphide gas. A hydrogen sulphide detector was placed inside and outside the fume cupboard to detect any leakage of the gas. Any hydrogen sulphide leakage above 5ppm would make the safety system automatically shut down the hydrogen sulphide gas supply [174, 175, 176]. The risk assessment and safety procedure was followed every time before starting any sour experiment.

4.2.2 Sour experiment system.

The sour experiment system setup is shown in Figure 4-7. The sour system uses a mixture of 10% hydrogen sulphide (H_2S) and 90% carbon dioxide (CO_2) as a sour gas, and nitrogen (N_2) gas as a flushing gas. A special two-step regulator is used

to handle H_2S with N_2 as the line flushing gas. The experiment vessel contains 800ml of test solution with X65 carbon steel submerged inside it. All the glass vessels used in the sour rig system include a 0.1 bar blow off valve to avoid the glass exploding due to overpressure. The excess outlet gas flows from the experiment vessel to the air bottle before entering the H_2S scrubbing system to trap any solution passing through the outlet line. The excess sour gas passes through two sodium hydroxide (NaOH) traps to pull the H_2S gas into the NaOH solution and then oxidises the sulphide to sulphate. The outlet from the NaOH trap passes through potassium permanganate ($KMnO_4$) to oxidise the remaining H_2S before releasing the excess gas to the fume cupboard extractor [117, 176].

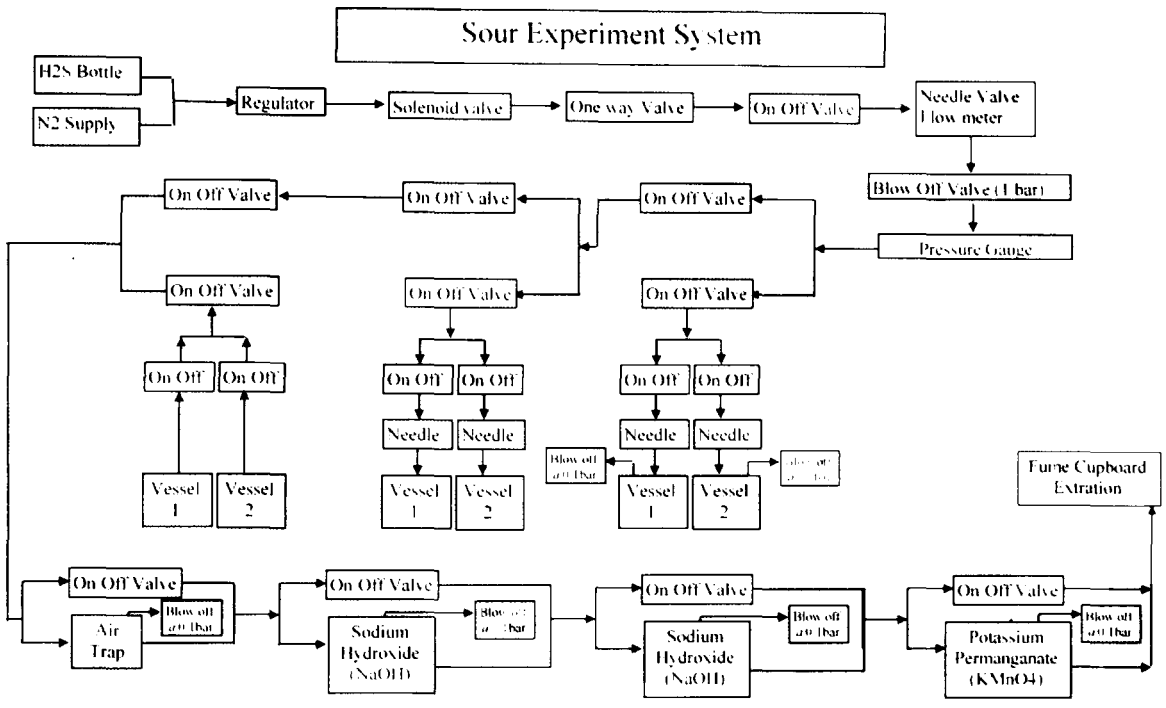

Figure 4-7: Sour experiment system diagram

4.2.3 Operation and emergency procedure of the rigs

The operating and emergency procedure for the sour rig should be understood and followed by any sour rig operator before running the sour experiment. The full H_2S system safety protocol was developed as part of the project and details are shown in Appendix A.

4.2.4 Experiment setup procedure

1) Check that all parts of the equipment are safe and ready to use.
2) Test the pipeline (not experiment vessel) at 0.8 bar with N_2 and hold the pressure for 5 minute to check the connection.
3) Increase the test pressure to 1 bar to check the blow off valve is operating.
4) Finish the 1 bar N_2 pressure test and release the pressure.
5) Fill the vessel with test solution.
6) Set and activate the temperature control to the experiment temperature.
7) Mount the specimen on the specimen holder.
8) Insert the test electrodes into the vessel and test the electrode assembly.
9) Check the O-ring position.
10) Seal the test vessel.
11) Start the N_2 flow test. Test the system with N_2 for 15 minutes. (Both inlet and outlet valves must be open to allow gas to flow through the vessel and scrubber units.
12) Observe any gas and solution leaking.
13) Observe the pressure indicator to make sure there is no trapped pressure.
14) Finish the N_2 flow test.
15) Switch on the H_2S mixed gas and continue purging for the required time. The person in charge of the experiment must be in the laboratory all the time when H_2S is in use.
16) Start the electrochemistry test.
17) H_2S gas can only be purged during core hours starting from 0800 until 1700.
18) Following the completion of the gas purging process, close the H_2S gas valve.
19) Purge the N_2 in the gas line for 10 minutes to clear the gas line from remaining H_2S gas for 10 minutes.
20) Purge the N_2 in the gas line at a slow rate for the experiment that running overnight to clear any free H_2S from the test vessel.

4.2.5 Completion of the experiment procedure

1) Switch off the heater and stirrer unit.
2) Allow the vessel to cool to below $50^{o}C$.

3) Purge the vessel with N_2 and the outlet gas should be routed to the scrubber unit for at least 120 minutes.
4) Slightly open the vent valve on top of the vessel lid.
5) Carefully check the presence of any residual H_2S in the vessel using an alarm. If any appreciative amount of H_2S, more then 5ppm is present, close the valve and restart purging with nitrogen.
6) Loosen the lid clip.
7) Lift the lid carefully out of the vessel.
8) Remove the specimen from the mounting assembly.
9) Clean the specimen following the experiment cleaning procedure.
10) Empty the vessel. Dispose of the solution into a designated container. (The solution in the container should be treated by the addition of a H_2S scavenger and mixed with water to remove any H_2S in the solution prior to final disposal).

4.2.6 Helium pressure test procedure

The helium pressure test procedure has been designed to ensure the rig is safe to use and needs to be undertaken if any modification or change to the sour rig component has been implemented. The full helium pressure test protocol was developed as part of the project and details are shown in Appendix B.

4.2.7 Cleaning the scrubber procedure

Cleaning the scrubber procedure must be undertaken if the quantity of precipitation in the NaOH scrubber is reaching the limit or the scrubber needs changing every 6 months. The full scrubber cleaning protocol was developed as part of the project and details are shown in Appendix C.

Chapter 5 Experimental setup

5.0 Experimental section

This chapter is divided into three different test setups. The first test setup explains the laboratory samples and field samples received from Baker Hughes for investigation of the surface film. The second test setup explains the procedure for the sweet and sour experiments on natural pits, and the third test setup describes the sweet and sour experiments on artificial pits.

5.1 Material used for study

The material used in these studies comprises X65 carbon steel. The specimens for sweet experiment studies were embedded in a non-conducting resin. The average chemical composition of the material is given in Table 5-1. The specimen was isolated with an O-ring and connected with wire for electrochemistry measurement.

C	Mn	Si	P	S	Cr	Mo	Ni	Cu	Sn
0.12	1.27	0.18	0.008	0.002	0.11	0.17	0.07	0.12	0.008
Al	**B**	**Nb**	**Ti**	**V**					
0.022	0.0005	0.054	0.001	0.057					

Table 5-1: Chemical analysis in % of carbon steel X65

5.2 Sample preparation procedure

Sample preparation for testing varied depending on the experiment, however, in general, the process was divided into cutting, mounting, polishing and cleaning. The materials were mounted using an automatic mounting press machine (Buehler Simpliment 1000) in bakelite edge retaining mounting compound. The grinding and polishing of the samples were carried out on a polishing machine (Buehler Beta Grinder Polisher). The grinding and polishing were done using various grades of silicon carbide paper (Buehler SiC paper) depending on the experiment. The polished surfaces were cleaned with distilled water, rinsed with acetone and dried with compressed air.

5.3 Corrosion testing setup

Electrochemical corrosion testing was used to investigate the corrosion behaviour of the material using the Princeton Applied Research Versastati3. Electrochemical tests included linear polarisation scans and potentiostatic tests using a conventional three-electrode cell for the electrochemical test setup. The setup comprised a high temperature saturated Ag/AgCl electrode as the reference electrode and a platinum rod as the counter electrode and the sample as the working electrode.

In the linear polarisation test the experiments were performed at various exposure times depending on the experiment. The polarisation measurements started at 20mV more negative than the open circuit potential value and the measurements ended at 20mV more positive than the open circuit potential value. The scan rate used for measurements was 15mV/min (0.25mV/sec). The potentiostatic test scans the potential to 100mV in a positive direction from the open circuit potential and holds the potential constant for 20 hours to activate and propagate the artificial pit. The resulting current was recorded with time to observe the current behaviour.

5.4 *In-situ* camera setup

The *in-situ* visualisation assembly contained a camera system (Navitar), a 10X long working distance objective (Mitutoyo), a lighting system and image monitoring system, as described in the previous chapter. The camera recorded the surface image every 20 seconds during the experiment. Thus, by using an image analysis system, the film and pit growth could be analysed.

5.5 Experiment procedure for surface film investigation for sweet and sour conditions.

This section describes the experimental procedure on sweet and sour specimens for corrosion film characterisation; the results are presented in Chapter 6. The sweet experiments were performed in a 350rpm stirred solution with 1 bar total pressure of carbon dioxide gas with the temperature controlled at 50°C. The exposure time varied from 0.5 hours to 72 hours in different experiments. Initially, 2 litres of distilled water and 1 wt% sodium chloride (NaCl) were filled in the solution bottle and it was purged with CO_2 gas for 4 hours to remove any dissolved oxygen. To begin

an experiment, 850ml solution was transferred to a test vessel and was purged with CO_2 for another 1 hour and the temperature was increased to 50°C, resulting in the solution having dissolved oxygen at 30ppb and pH 4 saturation. The specimen with a final exposed area of 2.094 cm^2 and final grinding with 320 grit SiC paper was prepared according to the sample preparation procedure. After that, the specimen was submerged in the solution and the reference and counter electrode were added to the system, as shown in Figure 5-1.

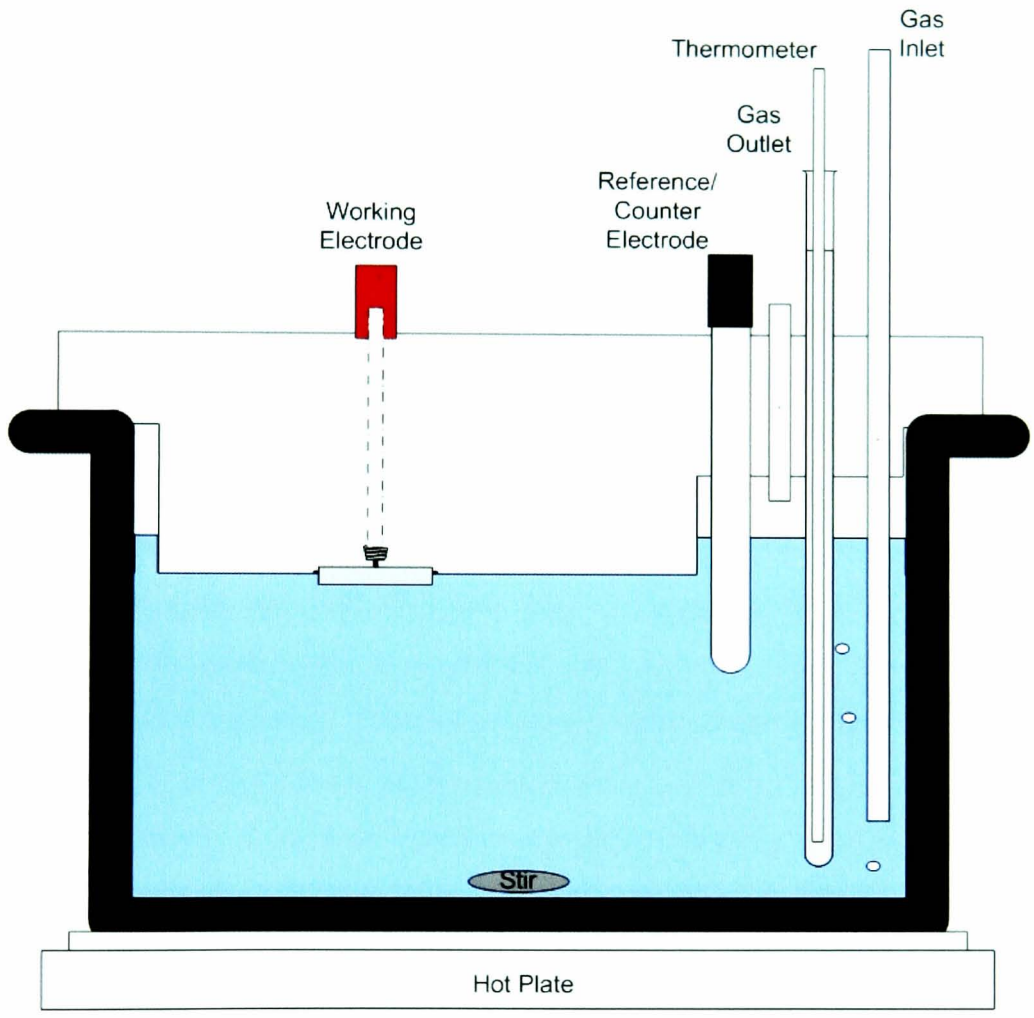

Figure 5-1: Experimental setup for sweet tests.

Then, the system was connected with the electrochemical testing instrument. During the test, the vessel was sealed with continuously bubbling CO_2 and stirred at 350rpm using a 2.5cm magnetic stirrer to equally mix the CO_2 gas with the solution and simulate a low flow velocity. The experiments were performed at various exposure times, as shown in Table 5-2 and all of the experiments were repeated twice.

Specimen	Time (h)
1	0
2	0.5
3	1
4	2.5
5	4
6	8
7	24
8	72

Table 5-2: Corrosion immersion time for sweet tests at 50°C with 1% NaCl

The sour corrosion specimens were generated by Baker Hughes using X65 carbon steel in a solution made by mixing oilfield brine and hydrocarbon for the purpose of surface analysis study. The corrosion tests for the sour specimens were performed at Baker Hughes and then the specimens were sent to the University of Leeds for the purpose of studying the sour film characteristic. This was in the early stages of the project to allow for a sour rig to be set up in our laboratory. The specimens for the sour corrosion tests were first pre-corroded for 2.5 hours in sweet conditions then transferred to an autoclave for sour gas experiments in a field brine and 1% field condensate. These experiments were conducted for 70 hours at various temperatures to observe the differences of iron sulphide species on the surface film. The temperatures of the sour corrosion specimens were as shown in Table 5-3. At the and of the experiments, the specimens were rinsed with distilled water, dried with compressed air and kept in a vacuum container

Specimen	Corrosion descriptions
S09	Sweet pre-corrosion for 2.5 h and sour condition at 90°C for 70 h
S10	Sweet pre-corrosion for 2.5 h and sour condition at 15°C for 70 h
S11	Sweet pre-corrosion for 2.5 h and sour condition at 15°C for 2 h followed by 90°C for 70 h

Table 5-3: Sour experiment specimens-all specimens pre-corroded in sweet environment first

5.6 Experiment procedure for natural pitting test for sweet and sour conditions.

This section describes the experimental procedure for sweet and sour specimens for natural pitting experiments; the results of which are presented in Chapter 7. The sweet experiments were performed in a solution stirred at 250rpm and the temperature was controlled at 80°C, as shown in Figure 4.2 Chapter 4. Initially, 5 litres of distilled water and 10% sodium chloride (NaCl) were filled in a solution bottle and purged with CO_2 gas for 24 hours to remove dissolved oxygen. To begin an experiment, 800ml solution was transferred to a test vessel and purged with CO_2 for another 1 hour and the temperature was increased to 80°C. The specimen was prepared according to sample preparation procedure with a final exposed area of 1 cm^2 and final grinding with 1200 grit SiC paper. After that the specimen was immersed in the solution and the reference and counter electrodes were added to the system. Then, the system was connected to the electrochemical testing instrument. On the first set of tests, the blank tests were performed at various time durations, as shown in Table 5-4 and were performed in triplicate to explore whether repeatable pitting corrosion behaviour could be obtained. Then, in the second set of tests, two different inhibitors – phosphate ester and imadazoline – were introduced at different concentrations after 120 hours pre-corrosion and the pitting depths recorded after 150 hours. The concentrations of both of the inhibitors that were tested are shown in Table 5-5. During the test, the vessel was sealed with continuously bubbling CO_2 and stirred at 250rpm using a 2.5cm magnetic stirrer to equally mix the CO_2 gas within the solution.

Specimen	Time (h)
1	2
2	24
3	70
4	96
5	120
6	150

Table 5-4: Natural pits blank test specimens at CO_2, 80°C, 10% NaCl, pH 5.65, 1000ppm Fe^{2+}.

Specimen	Conditions
1	10ppm phosphate ester
2	25ppm phosphate ester
3	50ppm phosphate ester
4	75ppm phosphate ester
5	100ppm phosphate ester
6	200ppm phosphate ester
7	300ppm phosphate ester
8	10ppm imidazoline
9	25ppm imidazoline
10	50ppm imidazoline
11	75ppm imidazoline
12	100ppm imidazoline
13	200ppm imidazoline
14	300ppm imidazoline

Table 5-5: Natural pit inhibitors test specimens at 150 hours, CO_2, 80°C, 10% NaCl, pH 5.65, 1000ppm Fe^{2+}.

In order to achieve the desired conditions and obtain a protective film, several steps were taken during the first 4 hours of the test. After 2 hours, the pH was adjusted to 5.65 by adding a sodium bicarbonate ($NaHCO_3$) solution to reduce the corrosion rate and initiate the pitting condition. After 4 hours, 1000ppm of iron chloride ($FeCl_2$) was added to achieve a high concentration Fe^{2+} to generate a protective iron carbonate film ($FeCO_3$). For the inhibitor test, after 120 hours various concentrations of inhibitor were added to the solution to study the effect on pitting propagation.

The sour experiments were performed on the sour rig, as shown in Figure 4-5 in Chapter 4. The tests were conducted at various temperatures, as shown in Table 5-6, to observe the pitting behaviour under sour conditions. All the sour tests were performed in 10% NaCl at 80°C. At the end of the experiments, the specimens were rinsed with distilled water, dried with compressed air and kept in a vacuum container before surface analysis. In order to achieve the desired conditions at the beginning of

the test, pH was adjusted to 5.65 by adding a sodium bicarbonate ($NaHCO_3$) solution and 1000ppm of iron chloride ($FeCl_2$) was added to achieve a high concentration of Fe^{2+} .

Specimen	Corrosion descriptions
1	10% NaCl, pH 5.65, 1000ppm Fe^{2+} for 4 h
2	10% NaCl for 4 h
3	10% NaCl, pH 5.65 for 4 h
4	10% NaCl, pH 5.65 for 96 h

Table 5-6: Natural pit test specimens at 10% H_2S, 90% CO_2, 80°C, 10% NaCl

5.7 Experimental procedure for artificial pitting test for sweet and sour conditions.

This section describes the experimental procedure for sweet and sour specimens for artificial pit experiments; the results of which are presented in Chapter 8 and Chapter 9. The solution and specimens were prepared the same as in the previous section 5.6 at 80°C and 10% sodium chloride (NaCl). Artificial pits were used in these studies to evaluate the effectiveness of the inhibitor. For all specimens two artificial pits were generated by a microhardness indenter to make each pit 9µm deep as shown in Figure 5-2. The specimens were finally rinsed with acetone and dried with compressed air before being placed in the specimen holder on the lid, as shown in Figure 4-2 in Chapter 4. All possible care was taken to prevent surface contamination of the sample.

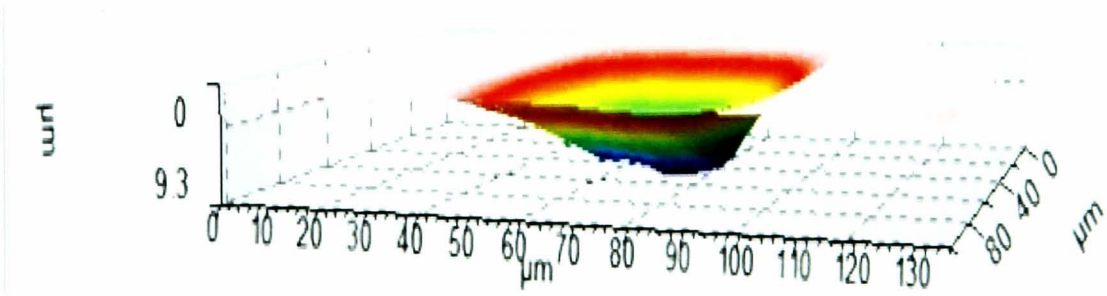

Figure 5-2: Artificial pit depth of X65 carbon steel before the test.

In order to achieve the desired conditions and obtain a protective film, several steps were taken during the first 4 hours of the test. After 1.5 hours, pH was adjusted to 5.65 by adding a sodium bicarbonate ($NaHCO_3$) solution to reduce the corrosion rate and initiate the pitting condition. After 3 hours, 1000ppm of iron chloride ($FeCl_2$) was added to achieve a high concentration Fe^{2+} to generate a protective iron carbonate film ($FeCO_3$). After 3.5 hours various concentrations of phosphate ester and imidazoline were added to the solution to study the effect on artificial pitting, as shown in Table 5-7.

Specimen	Conditions
1	Blank
2	25ppm phosphate ester
3	50ppm phosphate ester
5	100ppm phosphate ester
6	200ppm phosphate ester
9	25ppm imidazoline
10	50ppm imidazoline
12	100ppm imidazoline
13	200ppm imidazoline

Table 5-7: Artificial pits inhibitor test specimens at 150 hours, CO_2, 80°C, 10% NaCl, pH 5.65, 1000ppm Fe^{2+}.

Corrosion testing was performed using DC Linear Polarisation Resistance (LPR) after every step to monitor the corrosion rate and after 4 hours the specimen was immersed in the solution and achieved the desired condition; potentiostatic tests were carried out. These experiments were conducted for 24 hours and at the end of the experiment, the specimens were rinsed with distilled water, dried with compressed air and kept in a vacuum container before the surface analysis.

The sour experiments were performed on the *in-situ* sour rig, as shown in Figure 4-5 in Chapter 4. The solution, specimens and artificial pits were prepared the same way as for in the sweet experiment setup at 80°C and 10% sodium chloride (NaCl). Various concentrations of nonoxynol-6 phosphate and poly alkyl pyridine

inhibitors, as shown in Table 5-8, were added in the test vessel at the beginning of the test to study the behaviour of the inhibitors.

Specimen	Conditions
1	Blank
2	25ppm nonoxynol-6 phosphate
5	100ppm nonoxynol-6 phosphate
6	200ppm nonoxynol-6 phosphate
9	25ppm poly alkyl pyridines
12	100ppm poly alkyl pyridines
13	200ppm poly alkyl pyridines

Table 5-8: Artificial pit inhibitor test specimens at 24 hours, at 10% H_2S, 90% CO_2, 80°C, 10% NaCl

5.8 Post test analysis

Various surface analysis techniques were used in this study to measure the pit depth, investigate the corrosion film and understand the inhibitor interaction. The pit depth measurement was carried out using white light interferometry, profilometry and optical microscopy. The topographical detail measurement was carried out using secondary electron microscopy, focused iron beam and atomic force microscopy. The chemical characterisation was carried out using the energy dispersive X-ray technique, X-ray photoelectron spectroscopy and fourier transform infrared spectroscopy.

5.8.1 Talysurf5 profilometry

A talysurf5 contact surface profilometer (Taylor and Hobson) was used in this study to measure the surface profile of pre-test and post test specimens and to measure the pitting depth. The profilometer uses a software tool, Talymap Gold, which gives 3D and 2D data after mapping the surface and provides significant data to identify pit depth.

5.8.2 White light interferometer

A white light interferometer (Veeco WYKO) has high magnification and high resolution non-contact surface profilometry. The pit depth, which has a very rough surface, was carried out using this surface analysis technique. This technique is capable of measuring the objective in the magnification range from 2X-50X.

5.8.3 Optical microscopy

A Nikon optical microscope was used for viewing the corrosion surface and pit depth surface. The microscope was capable of measuring surfaces with magnification between 10X to 50X magnification. The microscope uses a software tool to view surface images for additional image processing.

5.8.4 Secondary Electron Microscopy and Energy Dispersive X-ray Analysis (SEM-EDX)

SEM-EDX (Phillips XL 30 instrument) is a surface analysis technique to characterise the surface morphology and chemical characteristics of the surface film under vacuum conditions. An SEM scans the surface of the specimen with an electron beam to study the shape and form of structure on the surface. This technique is extremely useful for studying and characterising the morphology of surface corrosion film or cross-section corrosion film. For this study, all specimens were scanned using input voltage 20KeV. EDX techniques were able to analyse the constituent elements present on the surface. The chemical elements analysed in this study were carbon (C), iron (Fe), oxygen (O) and sulphur (S).

5.8.5 Atomic Force Microscopy (AFM)

AFM instrument (Veeco) was used to investigate topographical structures and provide a high resolution and high magnification topographical measurement in ambient conditions. There are three common modes used in the AFM techniques – contact mode, non-contact mode and tapping mode. For this study, the AFM contact mode was used in which a constant force was maintained between the probe and specimen surface and probe raster scans on the surface to obtain topographical details of the corrosion film [71].

5.8.6 Focused Ion Beam (FIB)

FIB (Nova 200 NanoLab) with a high-resolution field emission gun scanning electron microscope (FEGSEM) was used to investigate the cross-sectional surface detail at the very early stages corrosion film formation. A platinum layer was coated on the top of the area of interest to protect the surface from any damage from irradiated high energy Ga ion during the cross-section ion bombarding process. For this study, the specimens after 0.5 hours corrosion were examined to measure the thickness of the corrosion film.

5.8.7 X-ray Photoelectron Spectroscopy (XPS)

XPS analysis provides information on the elements present and their chemical species on the surface film [177-181]. The specimens were cleaned using acetone to remove contaminations before doing XPS analysis [182]. The specimens were then mounted on the sample holder and placed in an XPS chamber to proceed with analysis. The calibration of XPS spectra was carried out on the area of interest to achieve maximum intensity of XPS signal [183]. The carbon peak was selected to calibrate XPS spectra and achieve maximum intensity. Then, the survey scan spectra was acquired for each sample. Figure 5-3 shows the survey scan for the bank specimen.

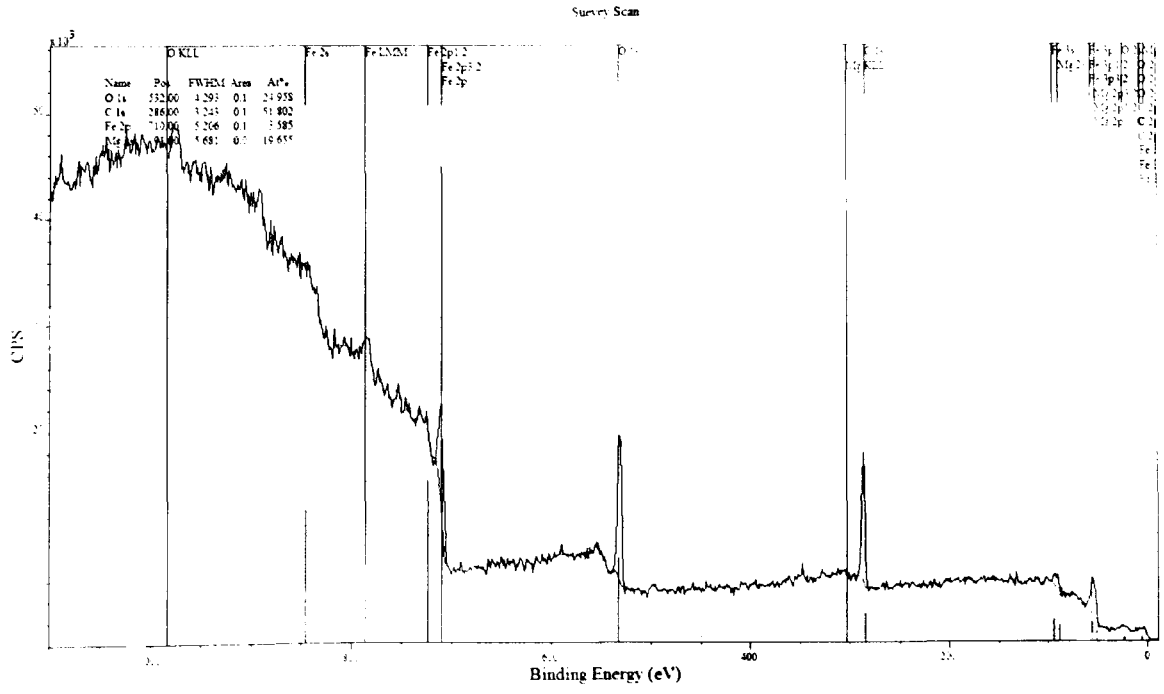

Figure 5-3: XPS survey scan for X65 carbon steel surface before the test.

The survey scan provides the information concerning the elements that are present in the area of interest. Following acquisition of the survey scan spectra, the acquisition of individual elemental scan was carried out for the elements observed on the surface and the elements expected on the surface. Argon ion bombardment of the surface was carried out to enable depth profiling of the specimen and provide the distribution of elements as a function of depth into the sample [77]. An area of 500 μm x 500 μm in corrosion film was analysed using a monochromatised A1 K[α] source in the XPS. The spatial mode was chosen to acquire the spectra and argon etching was performed using an ion gun set at beam energy 3 keV and 1μA set at 0 second and after 60 seconds. CasaXPS software was used to fit the curves on the acquired individual elemental peaks and the quantitative analyses of the peaks were performed using peak area sensitivity factors [184, 185]. The area of individual elemental peak was selected and curve fitting was performed keeping the area and full with half maximum consistent for that peak. Doublet peaks for Fe $2p_{3/2}$ were also fitted. The form of peaks used in all fitting procedures was Gaussian-Lorenzian [77]. Shirley background subtraction was used for all quantification to remove the data to symmetric shape to represent quantification results [2, 48, 185]. The relative sensitivity factor used in the software is 1 to compare the peak intensities.

5.8.8 Fourier Transform InfraRed (FTIR)

FTIR measurements were carried out with Perkin Elmer model spotlight 400. FTIR is a technique used to obtain an infrared spectrum [186-189]. FTIR has been used in this study to identify inhibitors that are tenaciously adsorbed to steel surface and corrosion film. A point mode operation and reflectance sampling mode were used in this study. IR reflectance spectra in the region 600 to 4000 cm^{-1} were collected. A background reflectance of a gold electrode was performed as a reference before measurements were made on all test specimens. The average of ten scans was recorded for each specimen spectra. Spectrum software was used to analyse the FTIR data obtained. The individual data line was further processed by data tune up and a smoothing process to reduce the data noise.

5.9 Inhibitors

Four different single inhibitor components from Baker Hughes were designed to inhibit localised corrosion in this study [190]. Phosphate ester and imidazoline were used in the sweet condition test and nonoxoxnol-6 phosphate and poly alkyl pyridines were used in the sour condition test.

5.9.1 Phosphate ester inhibitor

Alcohol ethoxylate phosphate, or the generic name used in this study – phosphate ester – is a 5 mole ethoxylated iso-tridecanol. This is made by trimerisation of n-butene and then hydroformylation (oxo synthesis) of the olefin with carbon monoxide and hydrogen to produce an isomeric mixture of primary isotridecyl alcohols with a branched alkyl chain [190]. Then this mixture was reacted with P_2O_5 to give a nominal structure, as shown in Figure 5-4 [190], and subsequently diluted in 10% methanol for use in the sweet condition test.

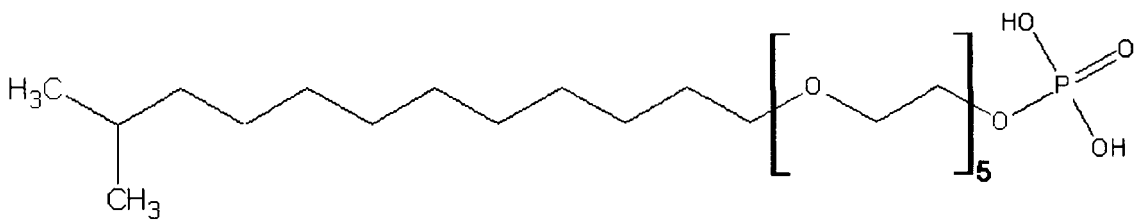

Figure 5-4: Nominal structure of phosphate ester inhibitor [190]

5.9.2 Imidazoline inhibitor

Diethylenetriamine alkly imidazoline, or the generic name used in this study – imidazoline – is the reaction product of tall oil fatty acid with diethylenetriamine (1:1), which gives a nominal structure, as shown in Figure 5-5 [190]. Then this mixture was diluted in 10% isopropanol with 2% acetic acid for use in the sweet condition test.

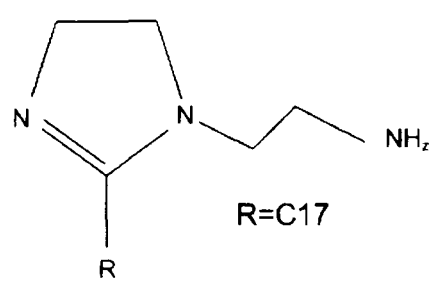

Figure 5-5: Nominal structure of imidazoline inhibitor [190]

5.9.3 Nonoxoynol-6 phosphate inhibitor

Nonoxoynol-6 phosphate inhibitor is a 6 ethoxylated p-nonylphenol, which is reacted with P_2O_5 to give a nominal structure, as shown in Figure 5-6 [190], and then diluted in 10% methanol for use in the sour condition test.

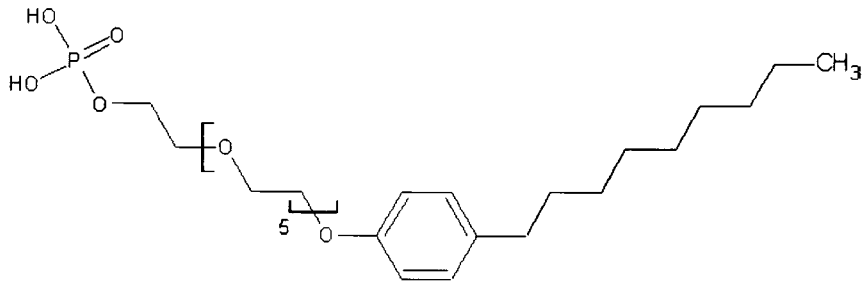

Figure 5-6: Nominal structure of nonoxoynol-6 phosphate inhibitor [190]

5.9.4 Poly alkyl pyridine inhibitor

Poly alkyl pyridine inhibitors are a waste stream that contain many alkyl pyridine components, some of which are shown in Figure 5-7 [190]. Each of the pyridine components could quaternise the benzyl chloride, as shown in Figure 5-8 [190]. Then this mixture was diluted in 10% methanol for use in the sour condition test.

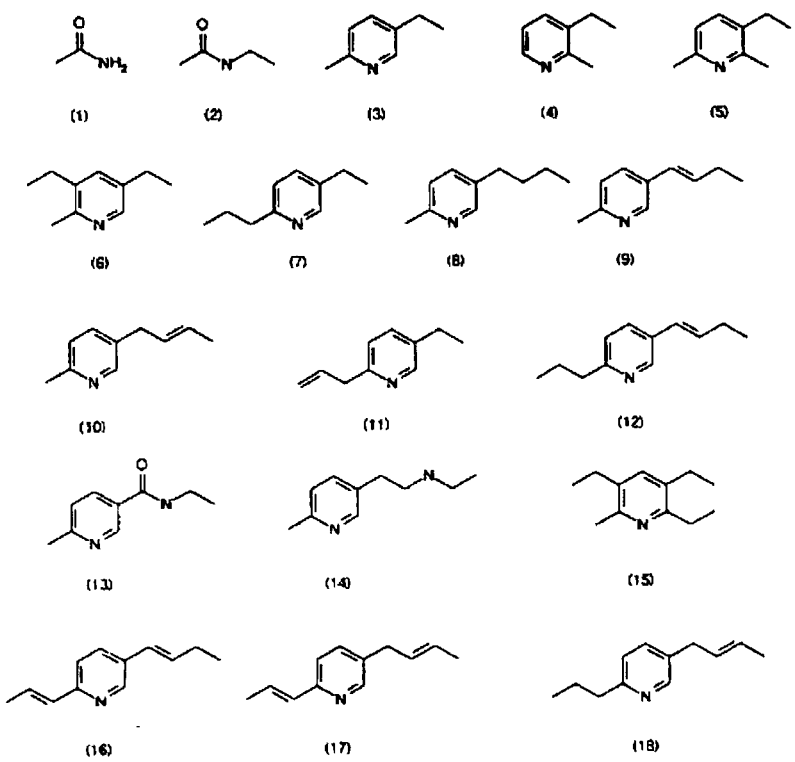

Figure 5-7: Nominal structure of poly alkyl pyridines inhibitor [190]

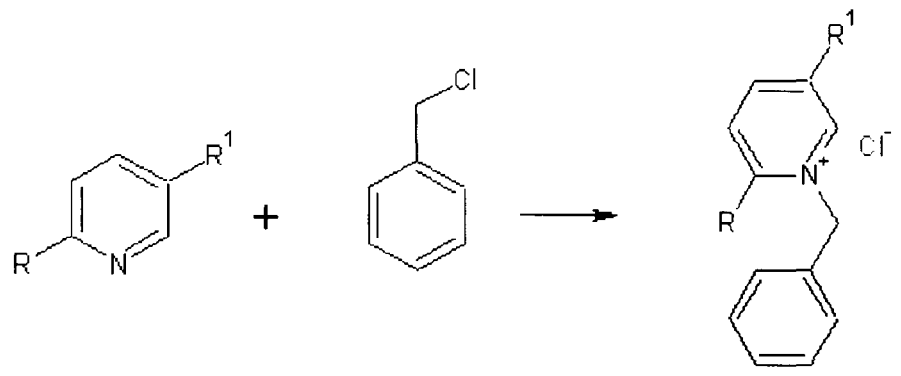

Figure 5-8: Nominal structure of pyridine components quaternise the benzyl chloride [190]

Chapter 6 Characterisation of the surface film formed from sweet and sour corrosion

In this chapter the results of surface analysis in sweet and sour environments are presented. Surface analysis was performed using Scanning Electron Microscopy (SEM), Energy Dispersive X-Ray (EDX), X-Ray Photoelectron Spectroscopy (XPS), Atomic Force Microscope (AFM) and Focus Ion Beam (FIB-SEM) to investigate the compositional and morphological difference of corrosion product films grown on X65 carbon steel in the early stages of sweet and in sour conditions. This Chapter is divided in two stages: the first stage studies the growth of sweet films under different exposure times. The second stage is to understand the corrosion films under sour conditions after 2.5 hours sweet corrosion. The objective of this chapter is to understand the corrosion films morphology and corrosion species in sweet and sour conditions and understand the film breakdown phenomena.

6.1 Corrosion current measurement

6.1.1 Sweet experiments

The sweet experiments were performed in 850ml, 1% sodium chloride at 1 bar total pressure of carbon dioxide gas with the temperature controlled at 50°C. The exposure time varied from 0.5 to 72 hours in different experiments. Electrochemical corrosion measurements using DC linear polarisation resistance were carried out to monitor the corrosion rate during sweet film formation. The corrosion rates recorded ranged between 3 mm/yr and 4 mm/yr. Figure 6-1 shows the corrosion rates for tests from 0.5 to 8 hours immersion. It shows that the corrosion rate started in the range between 2.6 mm/yr and 2.8 mm/yr in the first 26 minutes and then increased to the range between 3 mm/yr and 4 mm/yr, and was maintained at this rate until the end of the 8-hour test. This shows that the film formation process takes about 52 minutes to reach steady state conditions at this temperature and in this solution. Figure 6-2 shows the corrosion rate for longer time tests at 24 hours and 72 hours. The corrosion rates for the longer duration tests show similar behaviour in the first 52 minutes. The corrosion rates range between 3 mm/y and 4 mm/yr, and stays at this rate until the end of the 72-hours test.

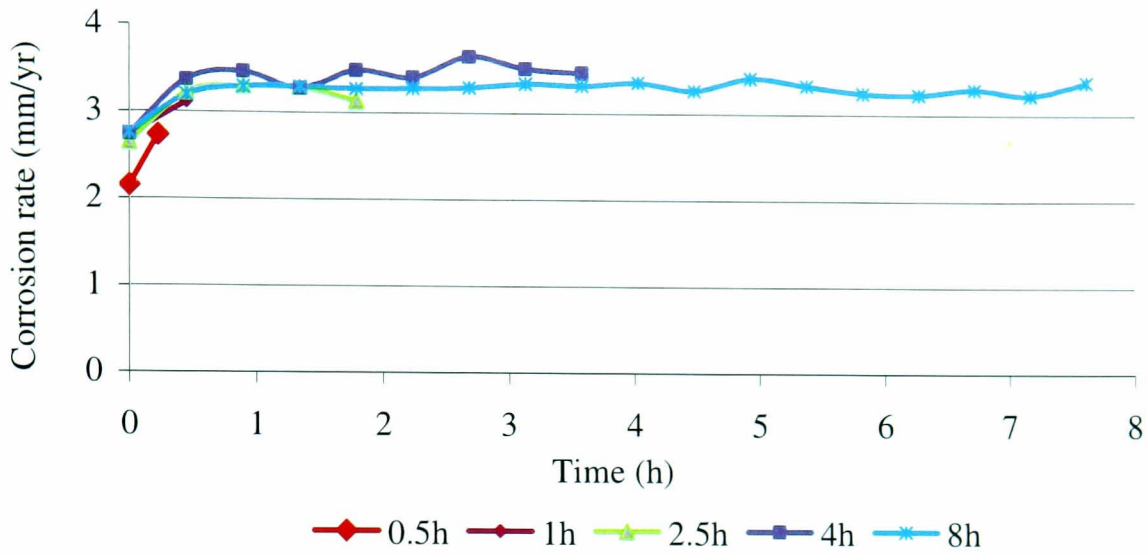

Figure 6-1: Corrosion rate versus time for short tests on X65 carbon in CO_2-saturated 1% NaCl brine at 50°C and 1 bar total pressure.

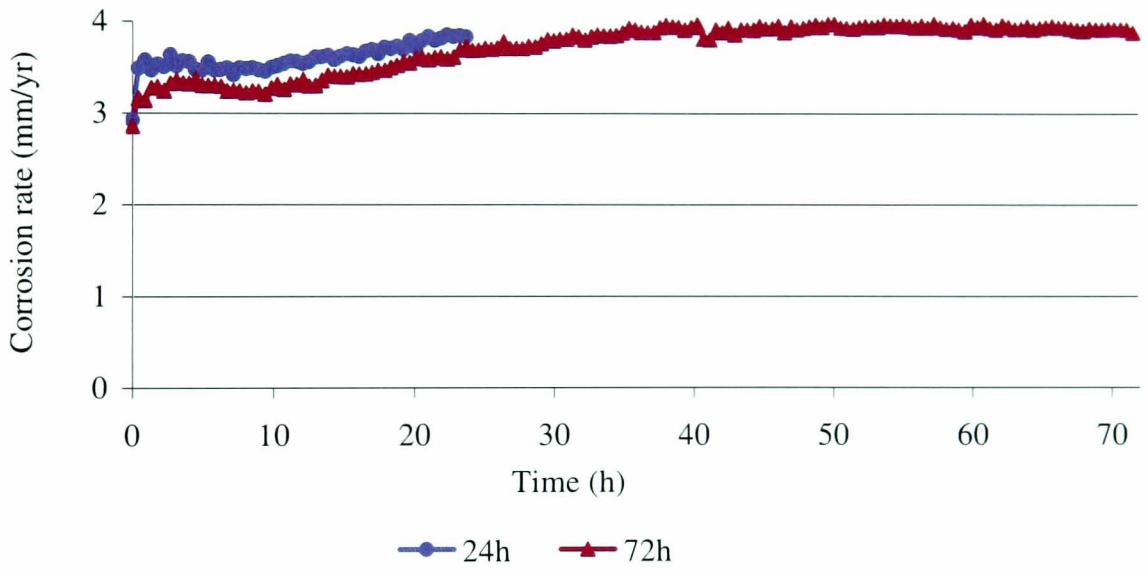

Figure 6-2: Corrosion rate versus time for long tests on X65 carbon in CO_2-saturated 1% NaCl brine at 50°C and 1 bar total pressure

This result is in agreement with Crolet et al. who obtained 3.3 mm/yr corrosion rate at pH 4, 22°C and saturated CO_2 [191]. The corrosion rate measurements show that the film formation under this condition is non-protective. This is supported by Schmitt et al., which shows that the typical films formed at 50°C with saturated CO_2 typically contains flaws and inhomogeneties [62].

6.1.2 Sour experiments

The sour specimens were prepared by the researcher at Baker Hughes [190] for the purpose of the surface analysis for this project. This was in the early stages of the project while the H_2S rig in our laboratory was being set up. The specimens were prepared in 1% NaCl for 2.5 hours in sweet conditions and then transferred to an autoclave for sour conditions in Shell pearl HTDS brine and 1% field condensate for 70 hours at 15°C, 90°C and mixed temperatures starting at 15°C and increasing to 90°C after the specimen was immersed. Figure 6-3 shows the corrosion rates for specimens under sour conditions after 2.5 hours pre-corrosion in a sweet environment.

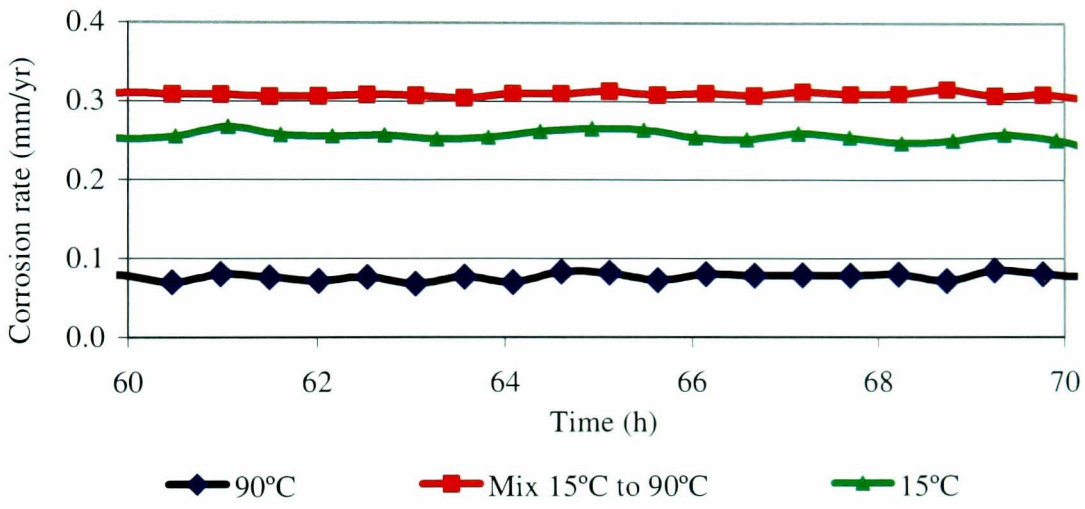

Figure 6-3: Corrosion rate versus time at 3.3 bar H_2S and 5.0 bar CO_2 at various temperatures [190]

The specimen at 90°C has the lowest corrosion rate at 0.08 mm/yr after the first hour and the specimen at 15°C has a slightly higher corrosion rate at 0.25 mm/yr. Both specimens maintained their corrosion rate until the end of the test and both show that the film that forms under this sour condition is a semi-protective type [4, 5, 111]. The specimen at 90°C has a greater protective film due to the higher temperature and its effect on the characteristics and morphology of the film [5]. It is interesting to note that the corrosion rate of the specimens with mixed temperatures was substantially higher than the specimens at 90°C and 15°C which was at 0.3 mm/yr.

6.2 SEM analysis

6.2.1 Sweet experiments

The morphology of the pre-corrosion surface is shown from Figure 6-4 to Figure 6-11. It can be seen that the corrosion deposits grow with time, which is in agreement with electrochemical measurements conducted during the corrosion test. Figure 6-4 shows the specimen surface before the test. The corrosion film starts growing on the surface after 0.5 hours by eradicating the polishing mark on the surface, as shown in Figure 6-5. It can be seen that the surface darkens due to the film building up on the surface after 1 hour, as shown in Figure 6-6. After 2.5 hours the corrosion layer formed on the metal surface is compact and quite homogeneous, however, the film is getting thicker, as shown in Figure 6-7.

After 4 hours corrosion, the corrosion films starts to create a porous morphology with the Fe_3C network frame structure observed on the surface, as shown in Figure 6-8. The corrosion product build-up follows the preferential carbide network, which can be seen until 8 hours, as shown in Figure 6-9. The film build up process continues and gets thicker after 24 hours and 72 hours, as shown in Figure 6-10 and Figure 6-11. It can be seen that the morphology of the film at 24 hours and 72 hours is porous and non-uniform; some of the unfilled regions between the surfaces could be influenced by the carbide layer on the surface, as observed by Lopez et al. [1].

A cross-section analysis was carried out to measure the thickness of the film. The specimens were mounted in another non-conducting resin and the cross-sectional surface was polished with silicon carbide paper (320, 500, 800 and 1200 grit), and finally polished to a 1μm diamond finish. These were cleaned with acetone and distilled water and finally dried. The cross-sectional analyses were performed for samples 0.5 hours, 2.5 hours and 24 hours. Cross-sectional analysis observed an average thickness of 3μm on the 0.5 hours corrosion, as shown in Figure 6-12 and 4μm on the 2.5 hours corrosion, as shown in Figure 6-13.

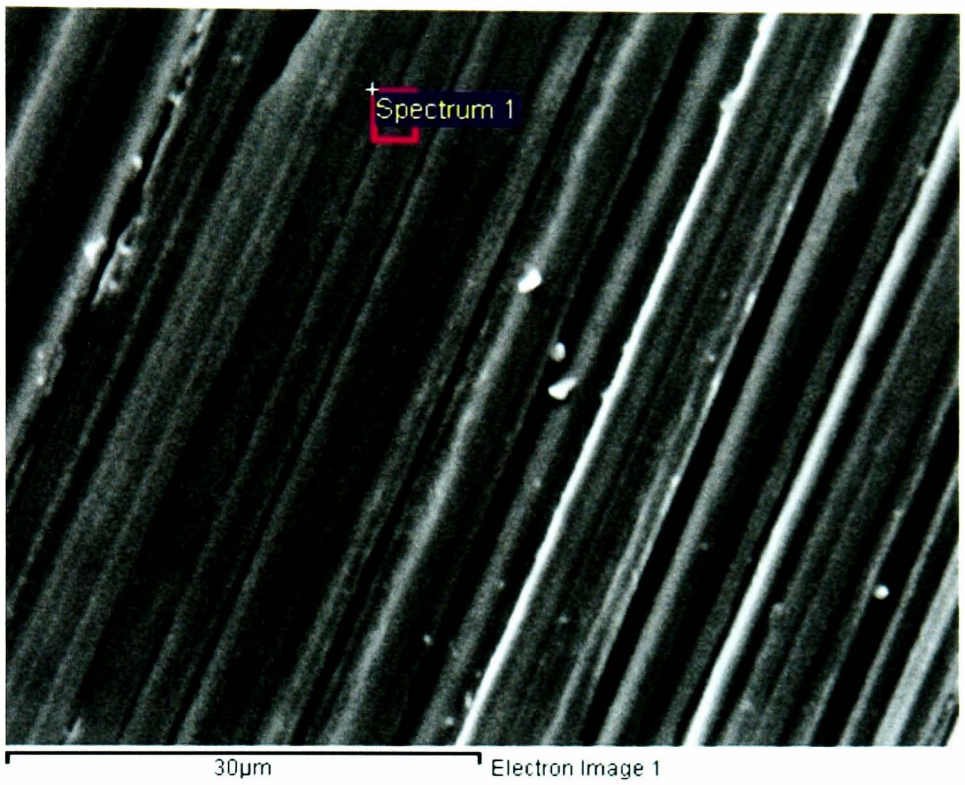

Figure 6-4: SEM image of the specimens before the experiments

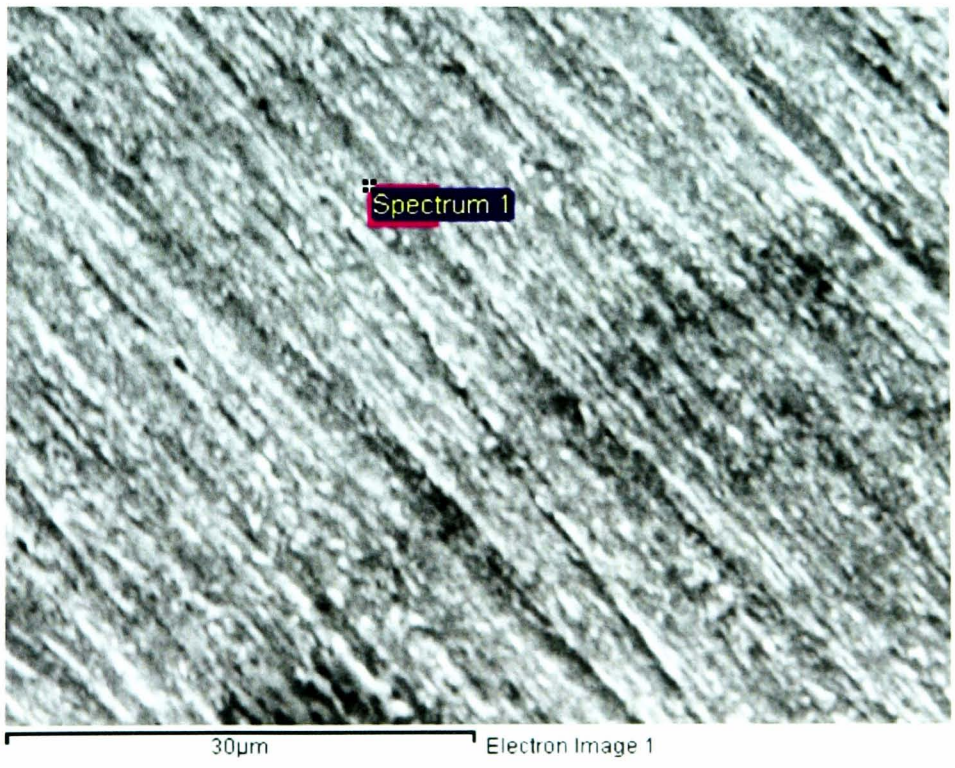

Figure 6-5: SEM image of the sweet pre-corrosion specimens at 50°C after 0.5 hours

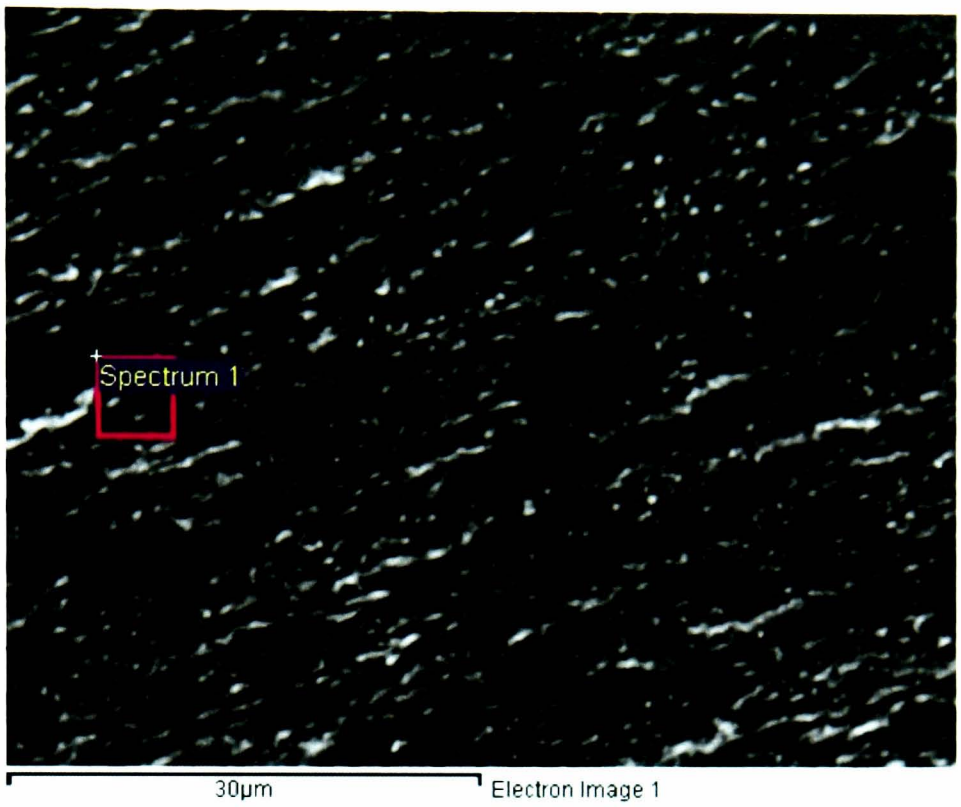

Figure 6-6: SEM image of the sweet pre-corrosion specimens at 50°C after 1 hour

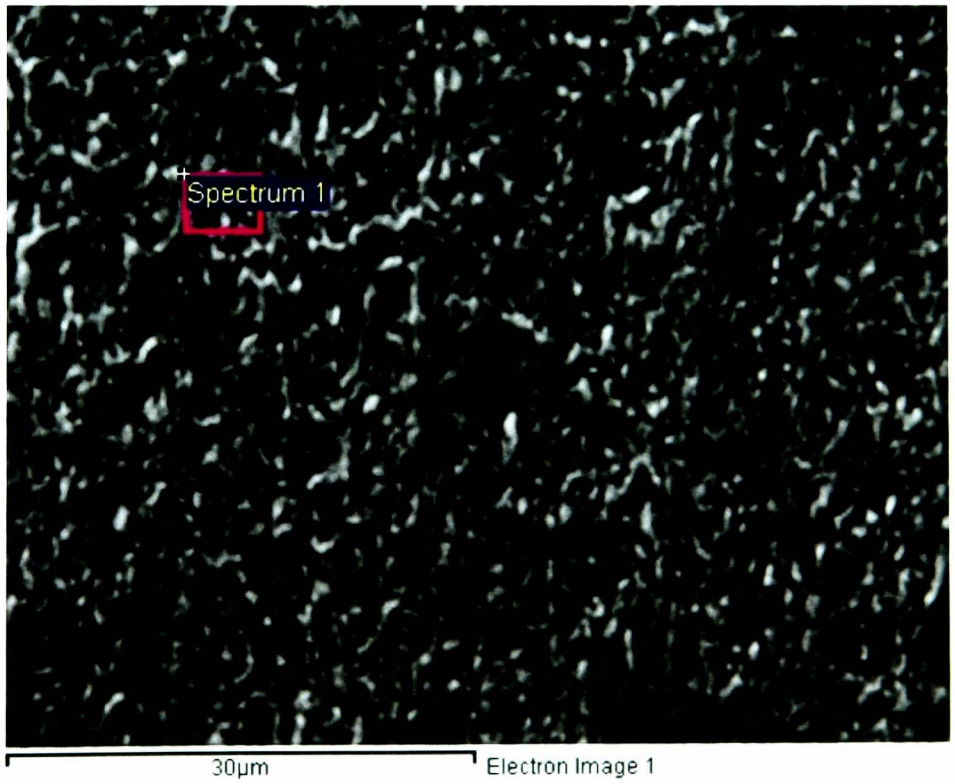

Figure 6-7: SEM image of the sweet pre-corrosion specimens at 50°C after 2.5 hours

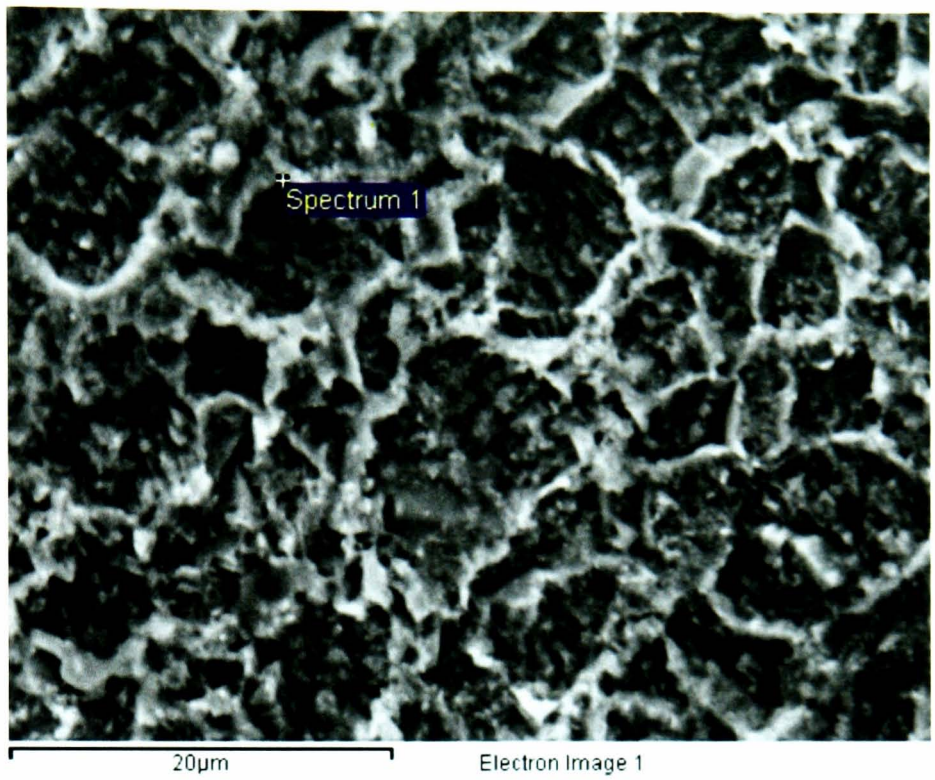

Figure 6-8: SEM image of the sweet pre-corrosion specimens at 50°C after 4 hours

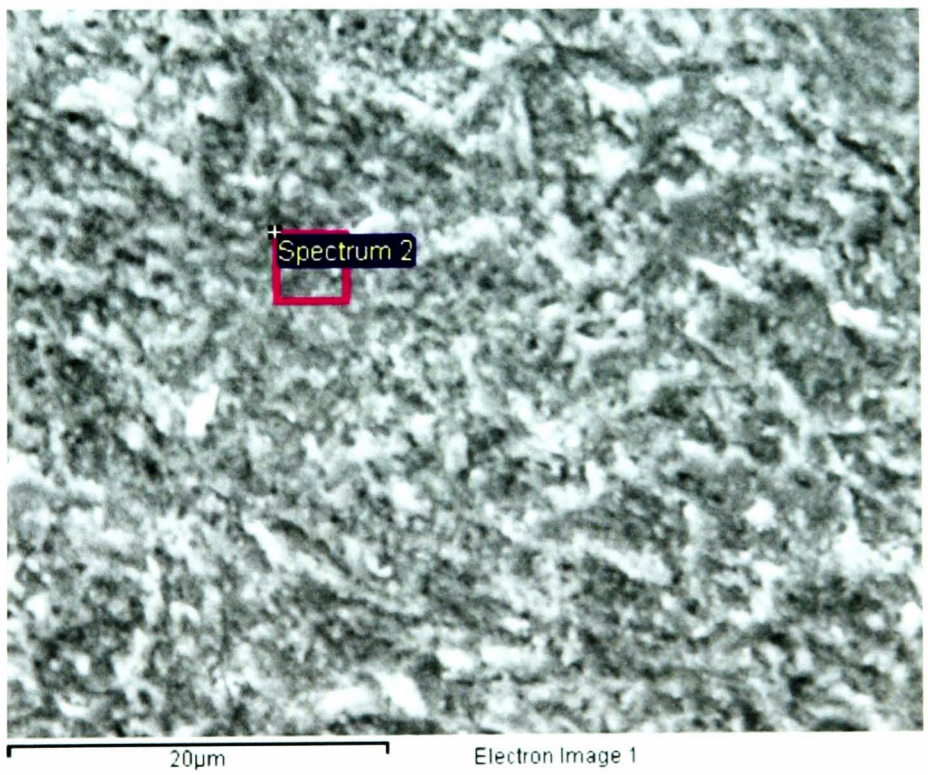

Figure 6-9: SEM image of the sweet pre-corrosion specimens at 50°C after 8 hours

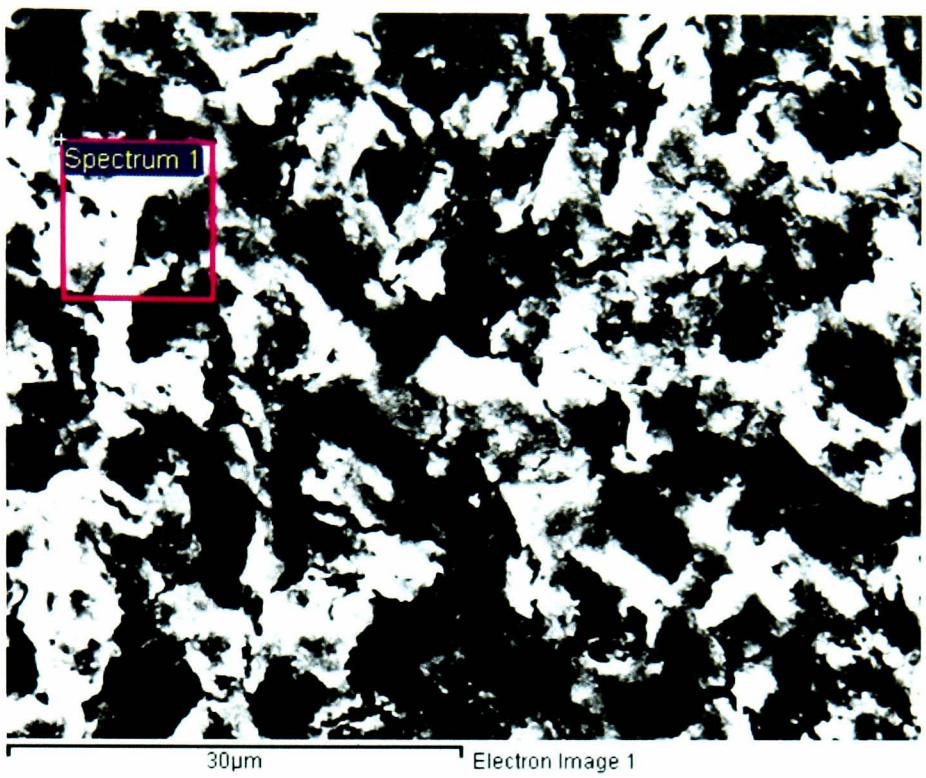

Figure 6-10: SEM image of the sweet pre-corrosion specimens at 50°C after 24 hours

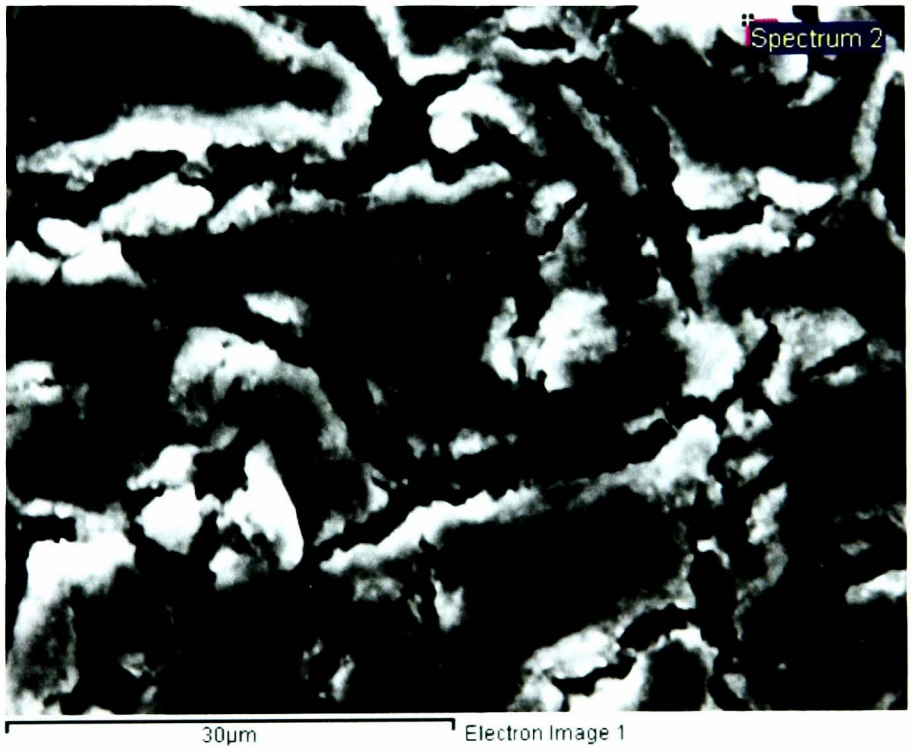

Figure 6-11: SEM image of the sweet pre-corrosion specimens at 50°C after 72 hours

The external part of the corrosion film seems to be denser and more compact but has poor contact and bonding to the metal surface. The film thickness grew thicker, to 23μm after 24 hours, as shown in Figure 6-14.

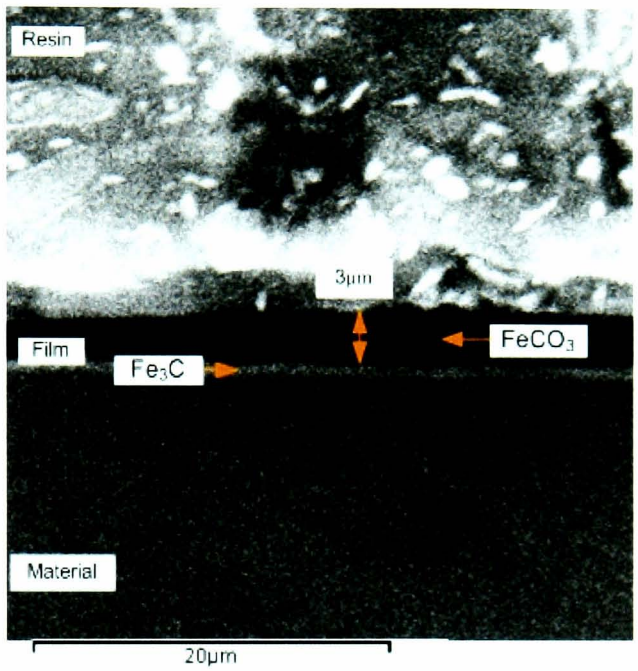

Figure 6-12: SEM image of the cross-section of sweet pre-corrosion at 50°C after 0.5 hours

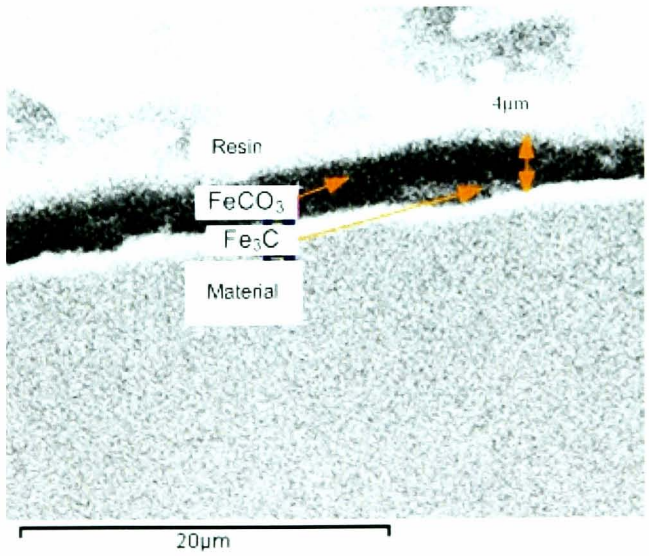

Figure 6-13: SEM image of the cross-section of sweet pre-corrosion at 50°C after 2.5 hours

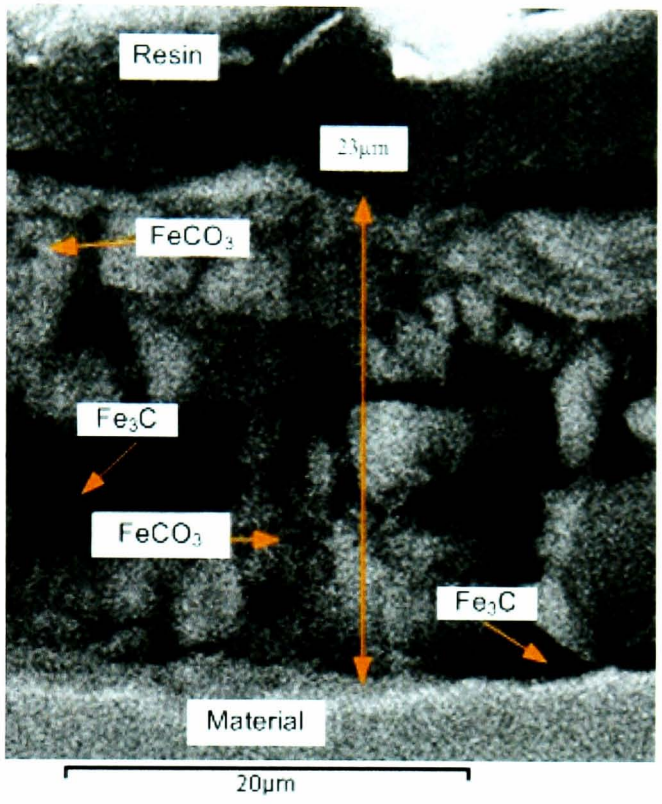

Figure 6-14: SEM image of the cross-section of sweet pre-corrosion at 50°C after 24 hours

The morphology after 24 hours shows that the external part of the films seems to be porous and non-homogeneous with the internal part appearing to be more dense and compact [1]. This shows that compact and denser deposits grow in the first instance followed by the growth of a porous layer in the film, which made the film non-uniform. This caused the result to be in agreement with the low corrosion rate at 2.6 mm/yr to 2.8 mm/yr in the first hour when the film is controlled by compact and dense deposits, which could be iron carbonate. Then, the corrosion rate increases to the range between 3 mm/yr to 4 mm/yr when the porous layer is present in the film, which could be a mix of iron carbonate and iron carbide and caused the film to be of the not protective type [5].

6.2.2 Sour experiments

In sour conditions, the microstructure pattern that is observed on the specimen is different at high and low temperatures. The sour corrosion deposits at high temperature are composed of two different layers, as shown in Figure 6-15. The first

layer deposit grows uniformly all over the material interface and the second layer grows in scattered domains on the first layer, as observed by Svenningsen et al. [127]. The films in low temperature sour corrosion look different because the pre-corrosion film can still be seen as the base film and a new corrosion layer grows sporadically on top of this base film, as shown in Figure 6-16.

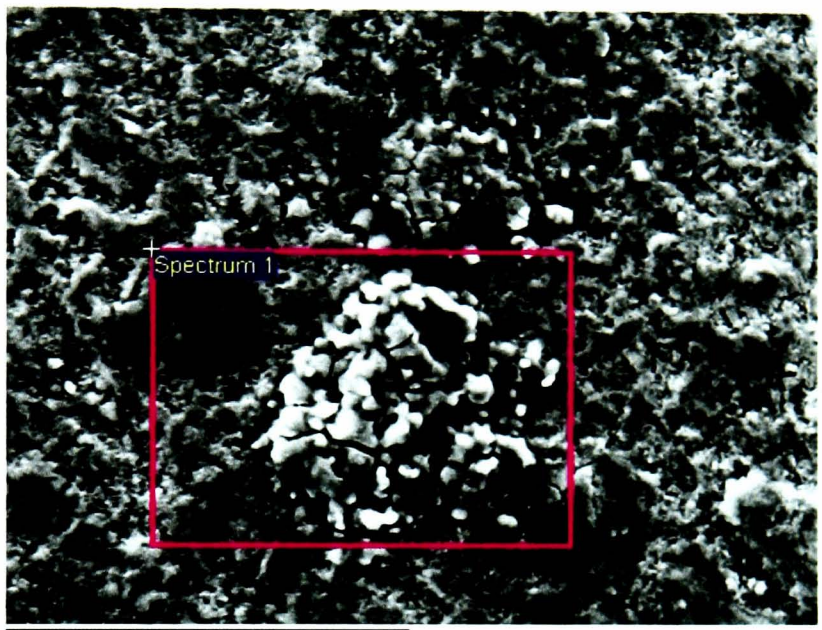

Figure 6-15: SEM image of the sour corrosion specimens at 90°C for 70 hours

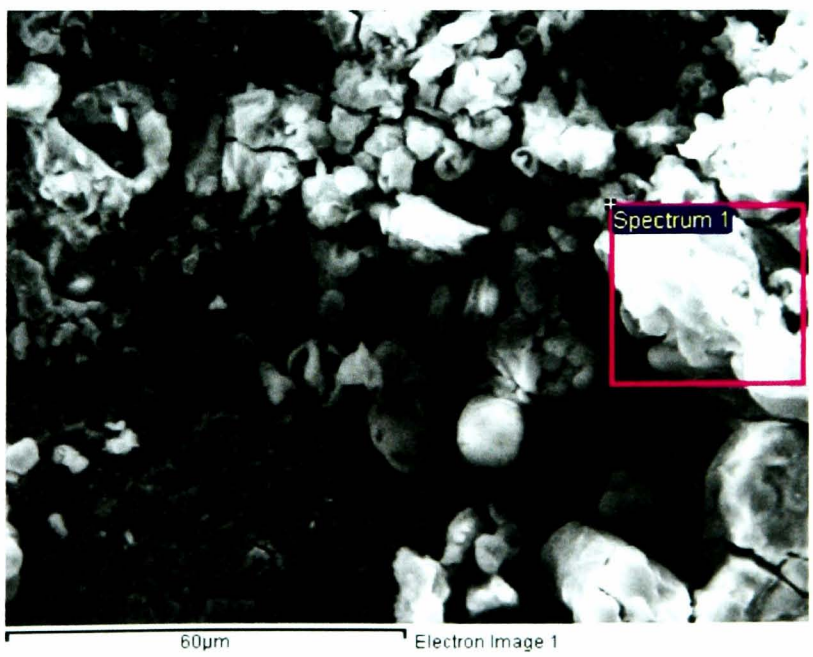

Figure 6-16: SEM image of the sour corrosion specimens at 15°C after 70 hours

It seems that the morphology of the resulting film for mixed temperature specimens is dominated by the nature of the low temperature pattern, as shown in Figure 6-17. The specimen is charging, which could be due to it being non-conductive. It is interesting to note that the sour corrosion film provides good protectiveness in a constant high or low temperature environment. This is in agreement with Sun et al. who observed a weak temperature dependence on the protectiveness, but suggested that the protectiveness is dependent on longer exposure time [4].

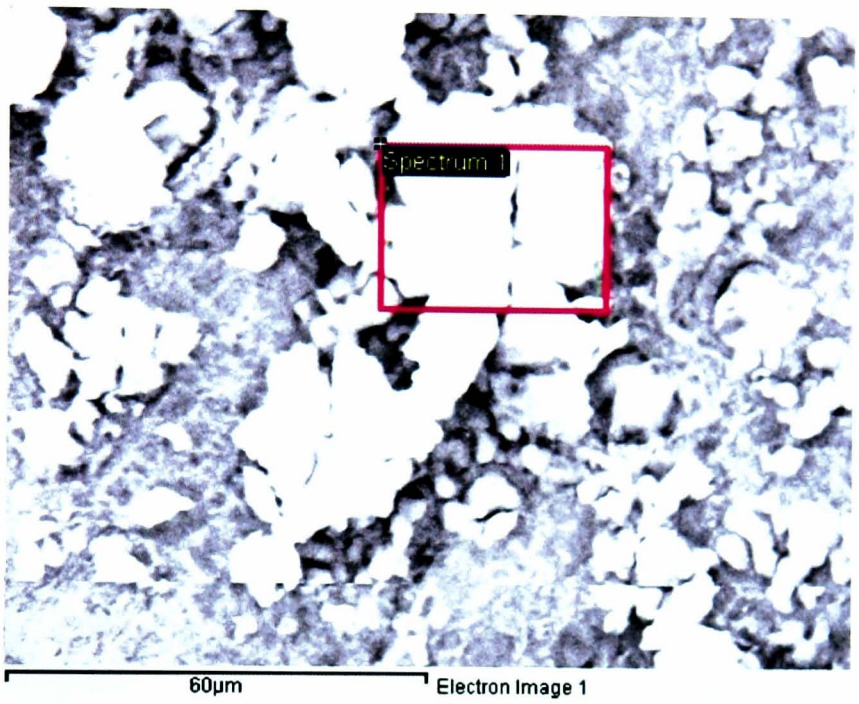

Figure 6-17: SEM image of the sour corrosion specimens at 15°C for 1st hour and increased to 90°C after 70 hours

6.3 FIB/SEM analysis

The Focused Ion Beam and SEM cross-sectional technique were performed for the sample exposed for 0.5 hours to observe the film thickness. Figure 6-18a and Figure 6-18b show the platinum layer that was placed onto the surface to protect the top surface during the process of helium etching the cross-section. It can be seen that the average film thickness of 1.3µm was observed on the 0.5 hours specimen, as shown in Figure 6-18c.

The morphology is shown to be denser and more compact at the film interface and some porous structure is more visible at the base of the film adjacent to the

substrate. The porous structure in the film shows the corrosion initiation stage with small spots generated at the internal part of the film, which could be due to the formation of Fe_3C as a result of the anodic reactions, as shown by the FIB-SEM topography image after 0.5 hours corrosion in Figure 6-19. The observation of 0.5 hours corrosion film specimens from the SEM cross-sectional method is not very clear due to the small film thickness. At higher magnification the FIB technique reveals that the corrosion film has a lower thickness and that the film has a good contact and bonding to the metal surface.

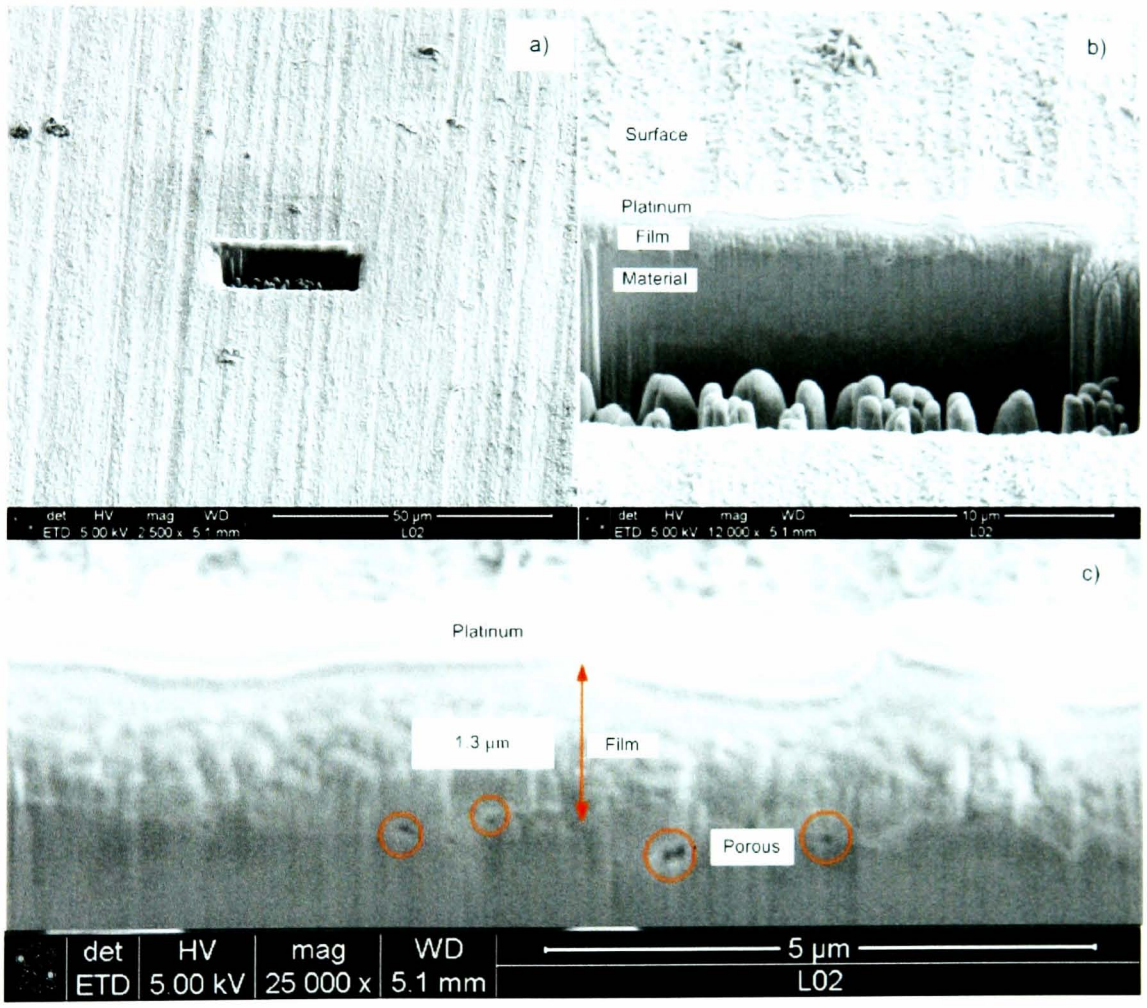

Figure 6-18: FIB/SEM image of the cross-section for sweet pre-corrosion at 50°C after 0.5 hours

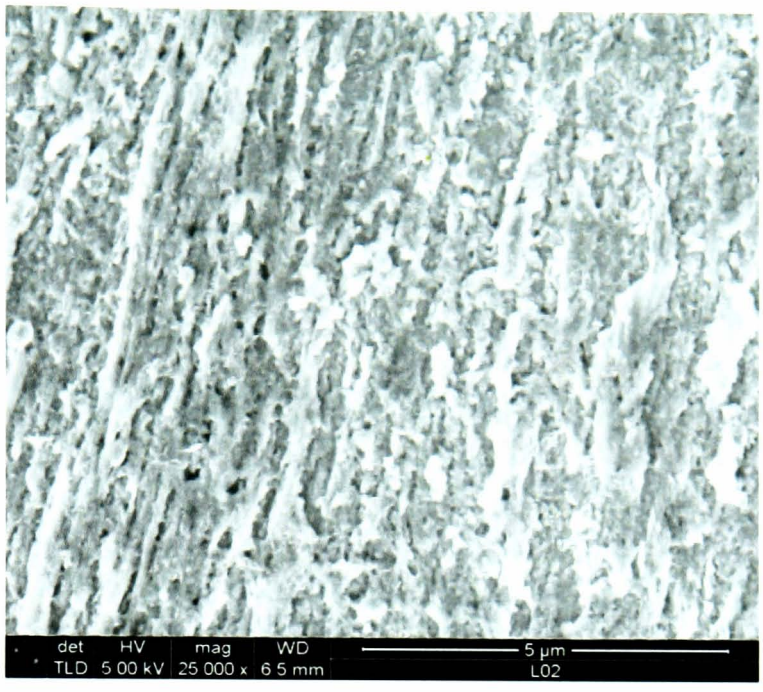

Figure 6-19: FIB-SEM image of undissolved Fe_3C after 0.5 hours for X65 carbon steel in CO_2 saturated 1% NaCl brine at 50°C and 1 bar total pressure

6.4 AFM analysis

The morphology of early stage sweet corrosion films was also observed by a contact AFM method. Surface morphologies of uncorroded and corroded specimens are compared to study the thickness and roughness of the film. The image in Figure 6-20 indicates that the corrosion deposits are increasing with time. The thickness of the 0.5 hour film is estimated to be 1.37µm, which is in agreement with the thickness obtained by FIB/SEM. The roughness and thickness of the film increased with the exposure time, as shown in Table 6-1. The thickness of the film also increases when the corrosion rate increases, as shown in Figure 6-21.

The difference between the peak to valley height is increasing showing that the film growth due to the increase of corrosion rate generates a non-uniform film on the surface. The difference between the uncorroded and 0.5 hours specimen is very small, which could be because the film seems to be denser, and more compact and smooth in the early stages. This could be supported by the lower corrosion rate observed at 0.5 hours during the corrosion initiation stage. The film roughness starts increasing after 1 hour at 84.4nm to 138.3nm after 4 hours due to the deposit growth on the film. This makes the surface fluctuation increase indicating non-homogeneous

film growth on the external part of that film which makes the film continue unprotected.

Time (hour)	**0**	**0.5**	**1**	**2.5**	**4**
Thickness, t (μm)	0.7	1.4	1.5	1.8	2.1
Average roughness, Ra (nm)	78.9	68.8	84.4	112.8	138.3
Max. Peak to valley height, Rt (nm)	418.3	487.2	622.7	667.8	993.5

Table 6-1: AFM analysis for sweet pre-corrosion specimens.

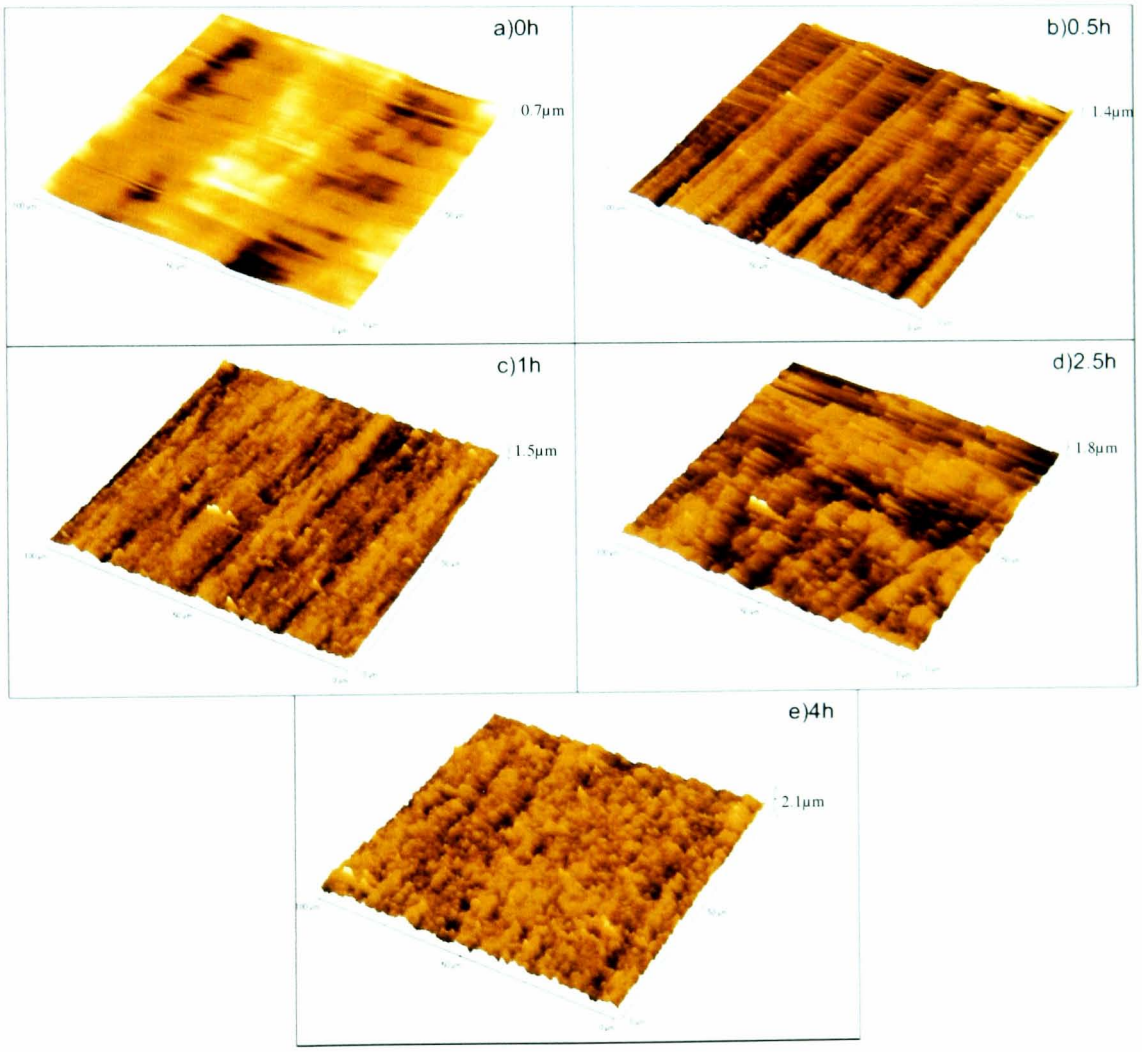

Figure 6-20: AFM images of the sweet pre-corrosion surface after difference exposure times at 50°C. a) 0 hour; b) 0.5 hours; c) 1 hour; d) 2.5 hours; e) 4 hours

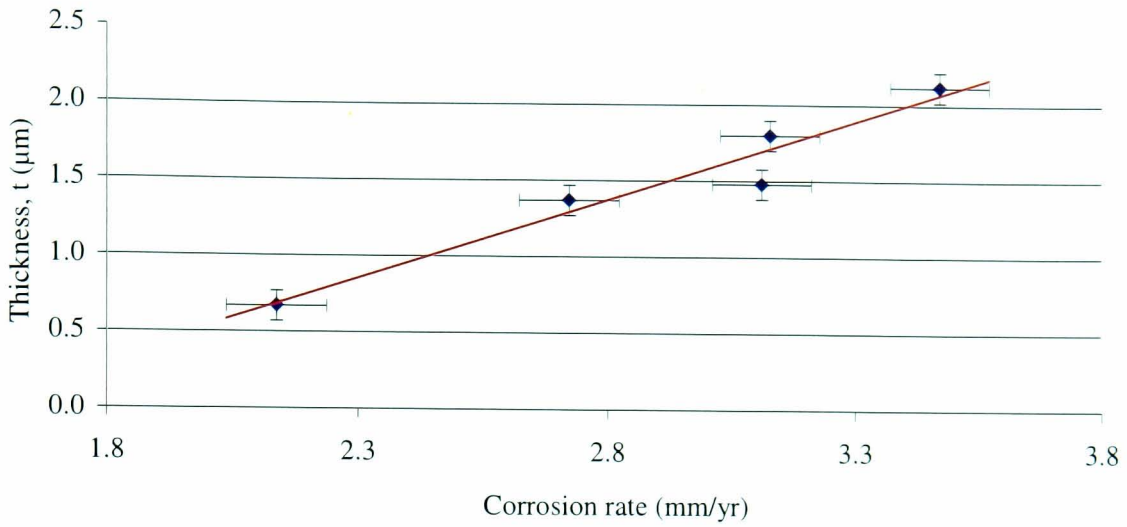

Figure 6-21: Film thickness versus corrosion rate versus time for X65 carbon in CO_2 saturated 1% NaCl brine at 50°C and 1 bar total pressure

6.5 EDX analysis

The nature of the surface film can be defined more accurately by observing the relative compositions of elements carbon, oxygen and iron performed by EDX. Table 6-2 shows the composition of the elements in the pre-corrosion layers.

Time (hour)	**0**	**0.5**	**1**	**2.5**	**4**	**8**	**24**	**72**
C wt %	1.8	2.5	2.4	4.2	5.2	6.4	8.2	9.2
O wt%	0	0	3.6	5.3	5.2	5.9	14.5	18.8
Fe wt%	98.2	97.5	94.0	90.5	86.5	87.8	77.3	72.0

Table 6-2: Relative element composition of sweet pre-corrosion layers

It was found that the percentage of carbon and oxygen in the corroded layers is higher than for the uncorroded specimens, as expected [48]. The reduction of iron and increment of oxygen and carbon is time dependent because the highest percentage of iron was found in the 0.5 hours specimen, which has the lowest immersion time and the lowest iron was found in the 72 hours specimen, which has the longest immersion time. The increasing of C and O and decreasing of Fe is suggested as the result of iron carbonate film growth [42]. Figure 6-22 shows that the film thickness increases as a result of the iron content decreasing with time. This reaction turns to a linear relation after 1 hours exposure, as shown in Figure 6-23. After 24 hours, Figure 6-24 shows that the morphology of the film reveals two distinct phases consisting of

flat dark grey regions, which are porous film with scattered whitish flakes type film around the surface. EDX data shows that the percentage ratio of Fe:C:O for the whitish flakes area is 60:9:26, which indicates a $FeCO_3$ film and the porous film area shows that the percentage ratio of Fe:C:O is 88:5:4, which indicates a Fe_3C film. This is in agreement with Ruzic et al. who in their studies prove that the EDX content of the whitish flakes type film is identified as a pure $FeCO_3$ type film [42].

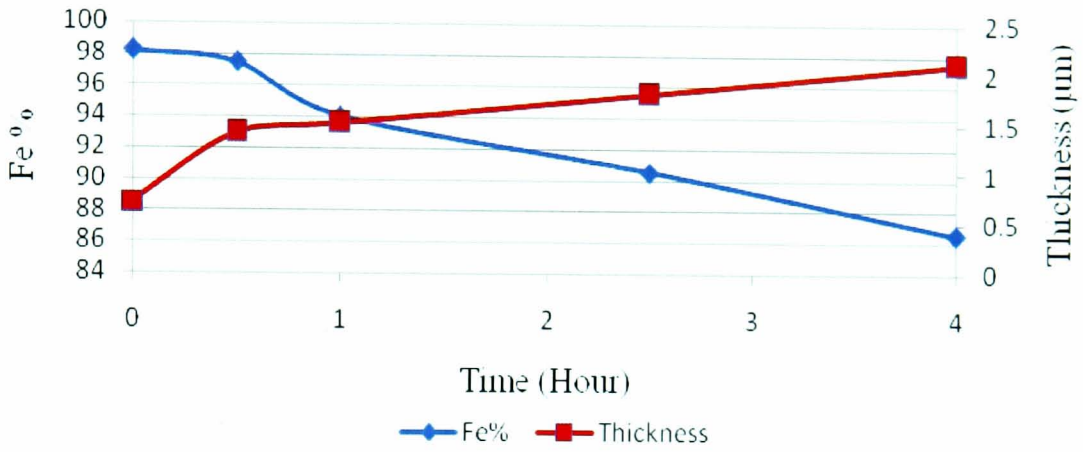

Figure 6-22: Film thickness and Fe% content versus time for X65 carbon steel in CO_2 saturated 1% NaCl brine at 50°C and 1 bar total pressure

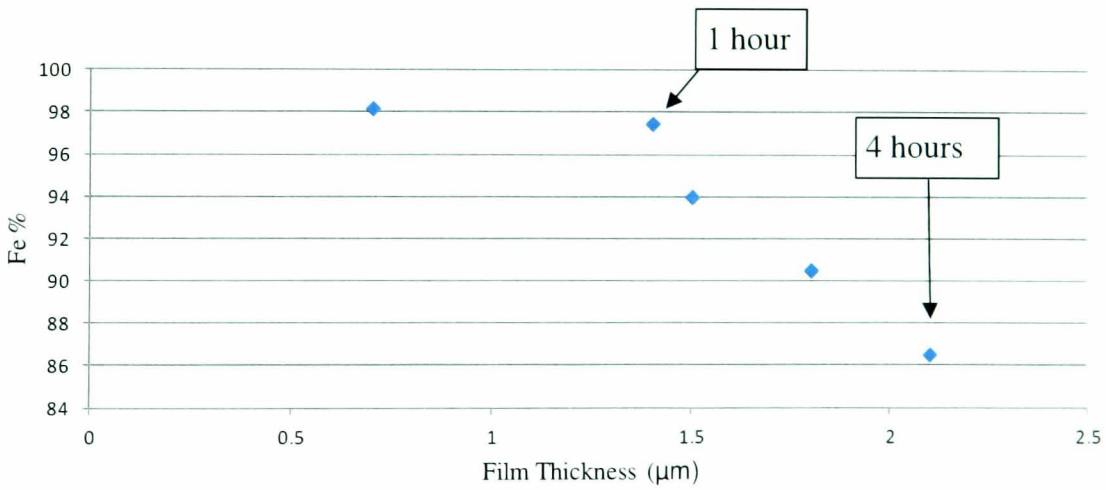

Figure 6-23: Film thickness versus Fe% content for X65 carbon steel in CO_2 saturated 1% NaCl brine at 50°C and 1 bar total pressure

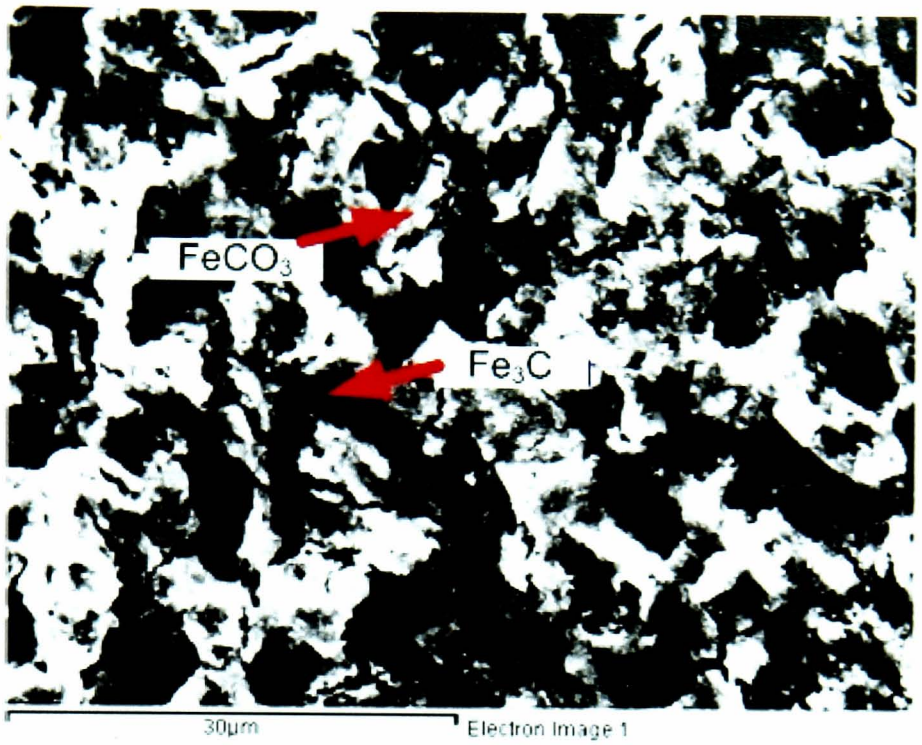

Figure 6-24: SEM image after 24 hours for X65 carbon steel in CO_2 saturated 1% NaCl brine at 50°C and 1 bar total pressure

Table 6-3 shows the relative composition of elements in sour corrosion layer. It shows that the carbon and sulphur were enriched in the specimen at 90°C and 15°C providing good corrosion protection. The oxygen percentage is the same for all specimens. It is interesting to note that the carbon to oxygen ratio is higher in the 0.5 hours sweet specimen and the sour specimen at 90°C and 15°C, which have a similarity in the low corrosion rate.

Temp.	**90°C**	**15°C**	**15°C to 90°C**
C wt%	8.6	7.1	4.7
O wt%	25.4	27.5	26.3
S wt%	12.7	7.1	0.9
Fe wt%	53.3	58.3	68.1

Table 6-3: Relative composition of elements in sour corrosion layers

6.6 XPS analysis

Surface films on selected corroded specimens are analysed using X-ray Photoelectron Spectroscopy (XPS). Survey spectra were recorded for all specimens and high-resolution scans were conducted over the following regions of interest; C 1s and Fe 2p. Sputtering of the sample surface was performed with an argon ion gun and were measured after 0 and 60 seconds of Ar^+ sputtering. Casa XPS software was used to fit the curves on XPS peaks and the XPS handbook was used to find the chemical species at the respective binding energies [177-180].

6.6.1 Evolution of C 1s peaks

XPS analyses on carbon spectra for 0 hour specimens (as-polished surface), 2.5-hour sweet specimens and sour specimens are shown in Table 6-4 to identify the presence of cementite and carbonate on the films.

C 1s Peak	Element	0 h polished surface		2.5 h sweet at 50°C		70 h sour at 90°C	
		BE(eV)	Wt%	BE(eV)	Wt%	BE(eV)	Wt%
I	Graphitic/ Hydrocarbonate	285.72	100	285.62	66	285.47	72.6
II	Fe_3C	-	-	281.78	4.5	282.29	3.6
III	$FeCO_3$	-	-	287.8	17.2	288.68	13.6
IV	$FeCO_3$	-	-	289.81	12.3	291.38	10.3

Table 6-4: Curve fitting analysis for C 1s spectrum.

Figure 6-25 shows the C 1s spectra curve fitting for the as-polished surface, which revealed a carbon peak at 285.72eV that represents the carbon atom in graphitic or hydrocarbonate absorbed in the surface layer [2, 48, 152]. For specimens after 2.5 hours sweet corrosion, Figure 6-26 shows the curve fitting for C 1s spectra at 285.62eV, which represents the same carbon in graphitic or hydrocarbonate absorbed peak as-polished surface [2, 48, 152]. A new peak is also revealed at binding energies of 287.80eV and 289.81eV corresponding to pure iron carbonate and at binding energies of 281.81eV corresponding to cementite [2, 48, 152].

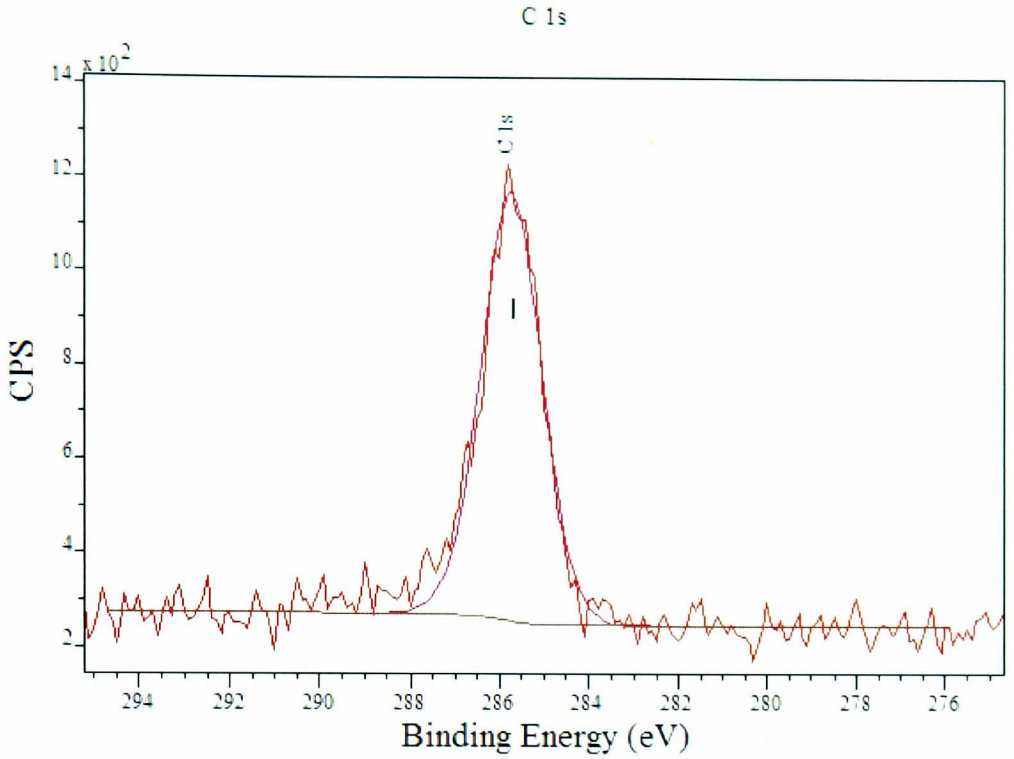

Figure 6-25: Surface scan of C 1s spectrum and curve fitting for 0 hour

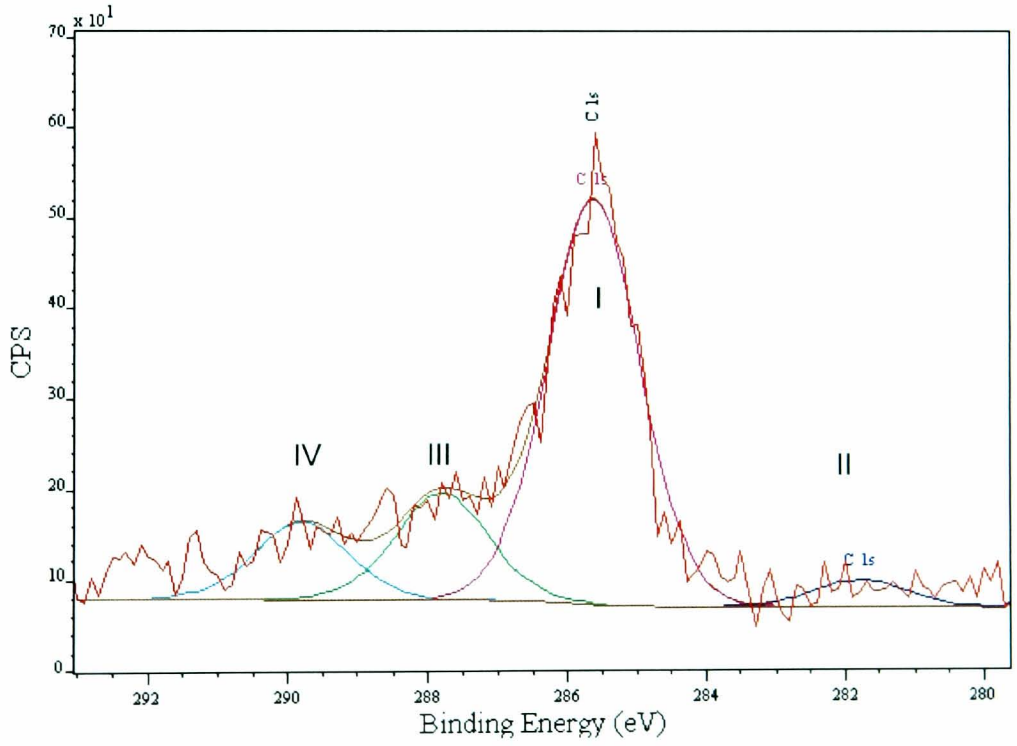

Figure 6-26: Surface scan of C 1s spectrum and curve fitting for 2.5 hour sweet pre-corrosion at 50°C.

The surface weight concentration analysis shows that a mixed type of film was formed on the surface with iron carbonate as the main species at 29.5% compared to cementite at 4.5%. A longer etching time is needed to obtain a stronger iron carbide peak because iron carbonate mostly grows on the film surface. These results are in agreement with the SEM images, which show the film morphology of the mixed iron carbonate/iron carbide.

The sour specimen Figure 6-27 reveals the peaks at binding energies of 288.68eV and 291.38eV, corresponding to pure iron carbonate, and the peaks at binding energies of 282.29eV, corresponding to cementite [2, 48, 152]. This reveals that a mixed type of film was formed on the surface with iron carbonate as the main species at 23.9% compared to cementite at 3.6%. The surface weight concentration of iron carbonate species is lower compared to the 2.5-hour sweet corrosion specimens. This conforms to the presence of iron carbonate and iron carbide film in this sour specimen. The presence of iron sulphide film will be investigated by observing the iron Fe $2p_{3/2}$ spectra.

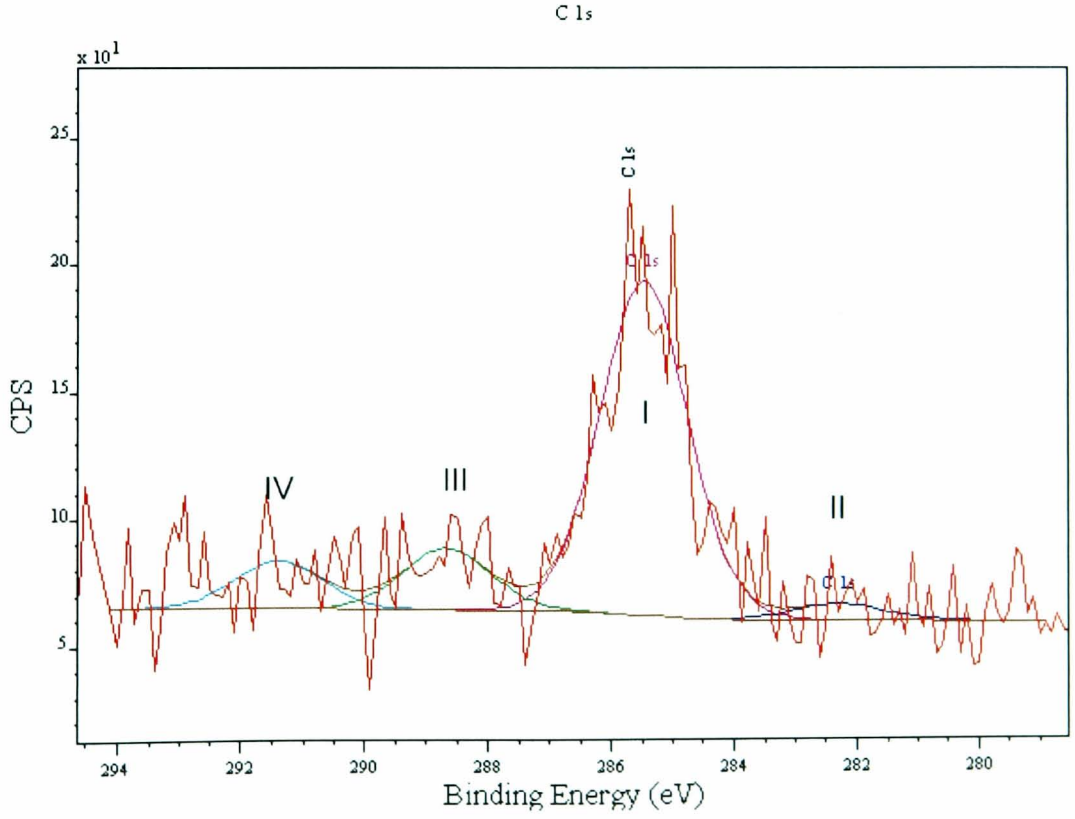

Figure 6-27: Surface scan of C 1s spectrum and curve fitting for the sour corrosion after 70 hours at 90°C

6.6.2 Evolution of Fe $2p_{3/2}$ peaks

XPS analyses on Fe $2p_{3/2}$ peak for 0-hour specimens (as-polished surface), 2.5-hour sweet specimens, sour specimens at 90°C and sour specimen at 15°C are shown in Table 6.5 to identify the presence of Fe, Fe^{2+} and Fe^{3+} on the surface and subsurface. The Fe $2p_{3/2}$ peak shows the doublet for the 0-hour (as-polished surface) specimens before and after 60 seconds etching, as shown in Figure 6-28. It shows that a clear Fe peak can be obtained after 60 seconds etching, estimated to be about 5nm below the film, which removes iron oxide on the surface probably due to air contamination during sample preparation [48, 77, 192]. It has been observed by Sakai et al. that the etching rate of polystyrene by the gun was determined to be 5nm/min [192]. The curve fitting for the as-polished surface after 60 seconds etching is shown in Figure 6-29. The peak at 707.39 represents a combination of iron as iron metal and cementite on the surface [177, 181]. It has been reported by Li et al. that the binding energies of Fe $2p_{3/2}$ for cementite and iron are at 707.3eV and 707.0eV, respectively [181]. The binding energy of cementite is 0.3eV higher then iron, which is very small to be properly identified. The presence of oxidised species at 709.80eV and 711.98eV in the film could be attributed to a mixture contribution from the presence of Fe^{2+} and Fe^{3+} in the form of FeO and Fe_2O_3 due to the contamination by surface reaction with the atmosphere during the sample preparation [1, 2 112, 181].

Fe $2p_{3/2}$	**Element**	**0 h polished surface**		**2.5 h sweet at 50°C**		**70 h sour at 90°C**		**70 h sour at 15°C**	
Peak		**BE(eV)**	**Wt%**	**BE(eV)**	**Wt%**	**BE(eV)**	**Wt%**	**BE(eV)**	**Wt%**
I	**Fe/ Fe_3C**	707.39	55.9	-	-	-	-	-	-
I	**Fe/ FeS**	-	-	-	-	707.58	25.6	-	-
II	**FeO-Fe_2O_3**	709.80	27.2	710.39	84.9	710.09	42.7	710.40	53.3
III	**Fe_2O_3**	711.98	16.9	-	-	-	-	-	-
IV	**FeS**	-	-	-	-	712.47	22.6	712.47	8.8
V	**$FeCO_3$**	-	-	714.83	15.1	715.48	9.1	714.23	19.9
VI	**Fe_2O_3**	-	-	-	-	-	-	717.81	18

Table 6-5: Curve fitting analysis for Fe $2p_{3/2}$ spectrum at 60s

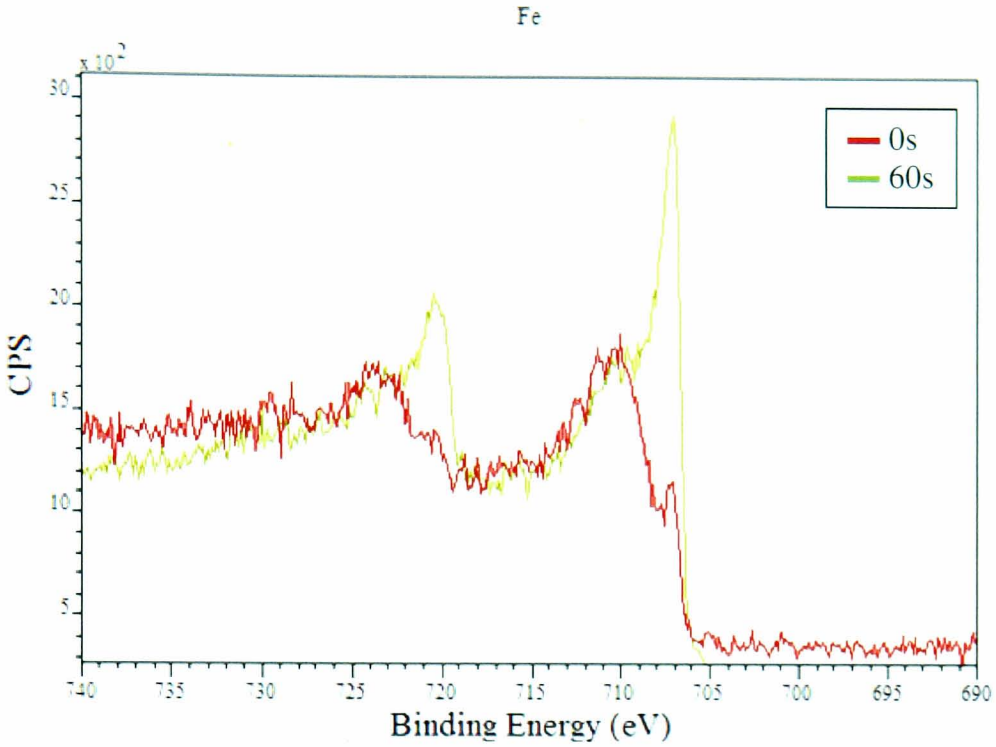

Figure 6-28: Sputtering of Fe $2p_{3/2}$ spectrum for 0-hour (as polished surface) specimen at 0s and after 60s etching.

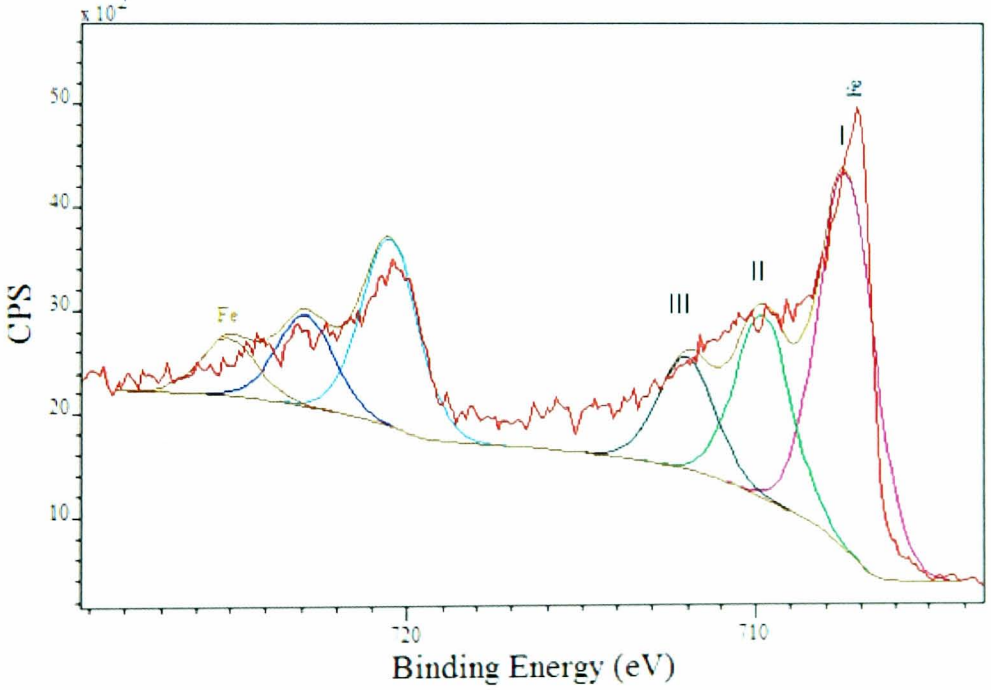

Figure 6-29: Surface scan of Fe $2p_{3/2}$ spectrum and curve fitting for 0-hour (as-polished sample) after 60s etching.

Figure 6-30 shows the 2.5-hour sweet specimen spectra, the peak at 714.3eV represents iron carbonate and the peak at 710.39eV in the binding energy covered by FeO and Fe_2O_3 [48, 112]. It has been reported by Lopez et al. that the decomposition process that iron carbonate may undergo at temperatures below 100°C will finally lead to FeO and Fe_2O_3 [48]. Figure 6-31 and Figure 6-32 show the Fe $2p_{3/2}$ spectrum for the sour specimen at 90°C and the sour specimen at 15°C. The binding energy at 707.58eV for 90°C sour specimens indicates the presence of FeS_2, which is pyrite [171, 177]. It has been reported by Neal et al. that pyrite was observed at binding energy 707.5eV [171]. It is interesting to reveal that the pyrite peak is only present in the 90°C sour specimens and absent in the 15°C sour specimen. Smith's review indicates that pyrite formation is influenced by high H_2S activity and the presence of elemental sulphur, as shown in Figure 3.10 in Chapter 3 [109, 113]. This shows that the higher temperature influences the solubility and rate of kinetic reaction, which increases the H_2S activity that leads to the formation of pyrite at 90°C [20, 109, 110, 113, 122].

The binding energy at 712.47eV on both specimens also indicates the presence of FeS on the surface [177]. The area under the curve fitting indicates that sulphide species is likely to grow at high temperature with a surface weight concentration of 48.2% compared to 8.8% at low temperature. This is supported by Kvarekval et al., who show that iron sulphide is more likely to form at higher temperatures compared to iron carbonate [122]. This is because the solubility of FeS increases when temperature increases [110, 122]. A peak at 715.48eV for 90°C sour specimen and at 714.23eV for 15°C sour specimens shows the presence of iron carbonate. The higher percentage of oxidised species observed in the low temperature sour sample could be due to the dominant iron carbonate [48, 112]. The reaction of Fe ions and excess H_2S subsequently results in ferrous sulphide production and effect the oxidation, this will affect the quantitative analysis on the curve fitting, however literature report that ion bombardment can cause various physical and chemical change on the surface and underlying layers such as compositional mixing and crystalline structure [48, 171].

Figure 6-33 summarise the XPS results and shows that after 2.5 hour sweet corrosion, the corrosion films were iron carbide and iron carbonate. Then, after 70 hours sour test, the sour corrosion product growth on top of sweet corrosion product.

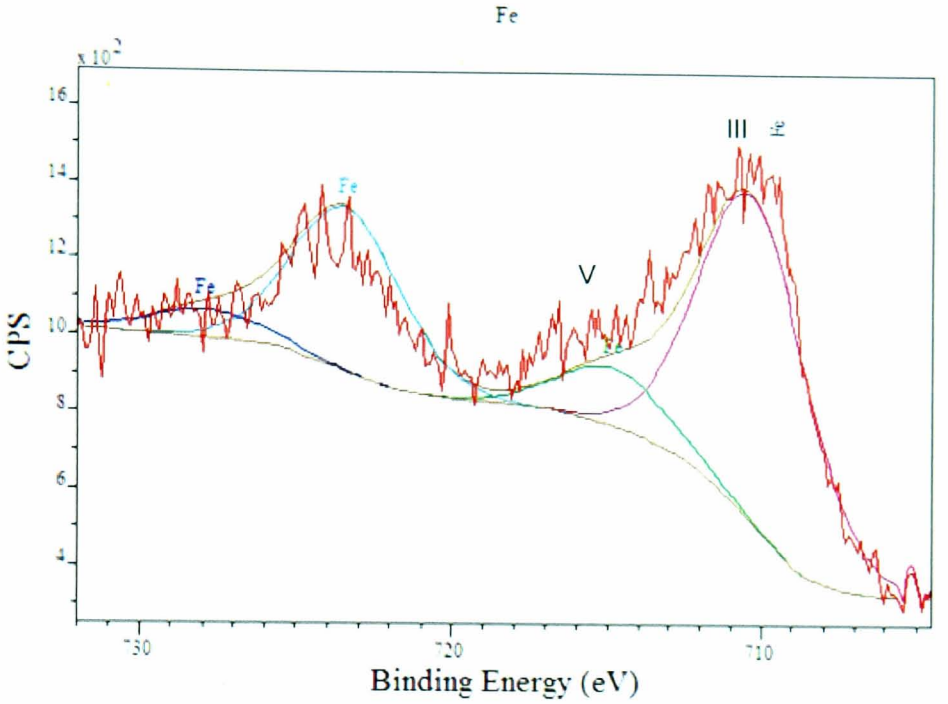

Figure 6-30: Surface scan of Fe $2p_{3/2}$ spectrum and curve fitting for 2.5-hour sweet pre-corrosion at 50°C after 60s etching.

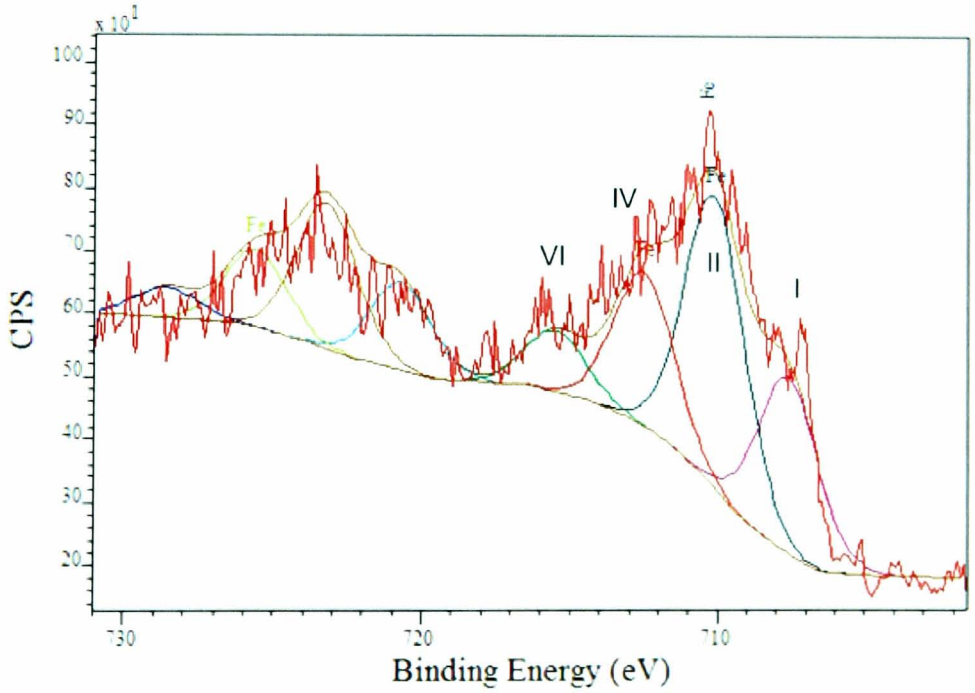

Figure 6-31: Surface scan of Fe $2p_{3/2}$ spectrum and curve fitting for the sour corrosion after 70 hours at 90°C after 60s etching.

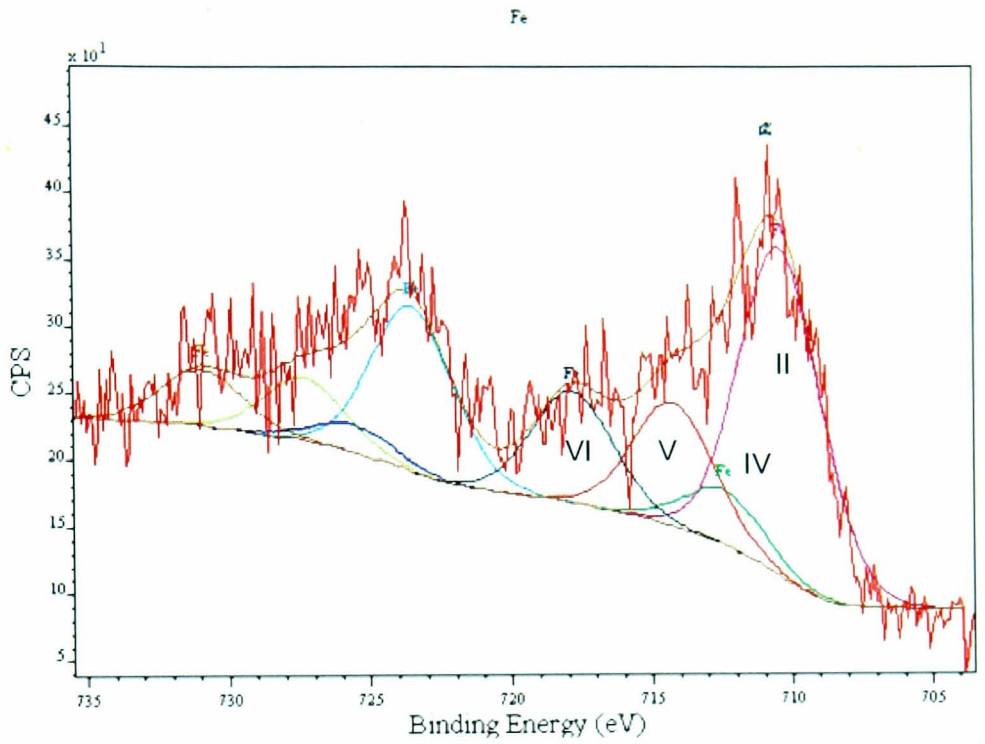

Figure 6-32: Surface scan of Fe $2p_{3/2}$ spectrum and curve fitting for the sour corrosion after 70 hours at 15°C after 60s etching.

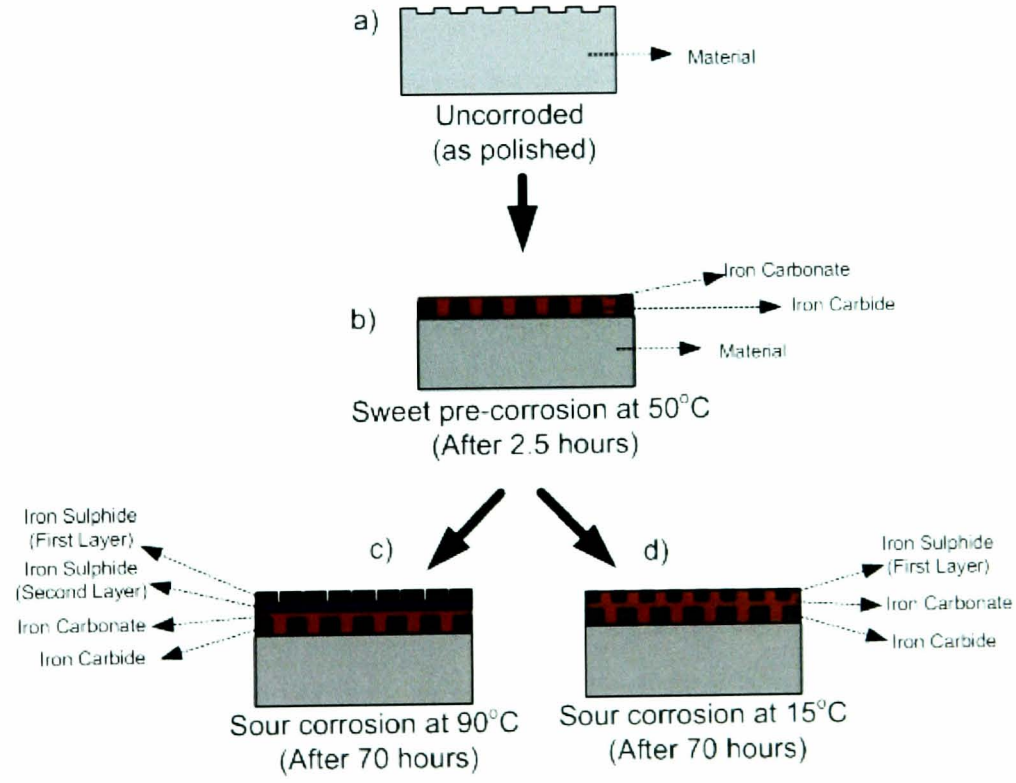

Figure 6-33: Summary of XPS results; a) Uncorroded; b) Sweet at 50°C after 2.5 hours, c) Sour at 90°C after 70 hours, d) Sour at 15°C after 70 hours

The specimen at 90°C sour contains two layers of iron sulphide, however for specimens at 15°C only one layer of iron sulphide is detected. The presence of dominant iron sulphide species at 90°C sour specimens explains the difference of 0.17 mm/yr corrosion rate observed between the high and low temperature sour environments. This is supported by Pugh et al., who showed that the corrosion rate decreased with increasing temperature and claimed that a more protective FeS film formed at high temperatures compared to lower temperatures [120].

6.7 Summary

This chapter revealed surface film characterisation for sweet pre-corrosion specimens from 0.5 hours to 72 hours and sour specimens at different temperatures using various surface analysis techniques. The studies reveal that the morphology of sweet films is denser and more compact on the external part of the film and some porous structures at the bottom of the film. Chemical analysis observed the presence of mixed iron carbonate and iron carbide film under the test conditions, which means the films are semi-protective. Under sour conditions, these studies reveal that iron sulphide is the predominant product for 90°C specimens, which provides better protection compared to 15°C specimens. The studies also show that both iron carbonate and iron carbide are present in sour specimens.

Chapter 7: Investigation of pitting corrosion in sweet and sour conditions

In this Chapter the main objective is to understand pitting and pitting inhibition. The corrosion films in sweet and sour conditions were evaluated previously in Chapter 6. This chapter studies the findings from the previous chapter as a reference to understand the film breakdown phenomena, which lead to pitting growth. This chapter presents and discusses the natural pitting growth on X65 carbon steel surface in sweet and sour conditions and the effect of inhibition in sweet conditions. This chapter is divided into two stages; in the first stage, pitting growth experiments have been performed at various times to understand the pitting depth behaviour with respect to time. The second stage experiments use the first stage results as a reference to evaluate the performance of phosphate ester and imidazoline inhibitors towards pitting propagation. The corrosion rate was monitored by electrochemical methods and profilometry analyses were used to determine the pit depth.

7.1 Pitting growth

7.1.1 Corrosion current measurement for sweet experiments

The sweet experiments were performed in 850ml, 10% sodium chloride at 1 bar total pressure of carbon dioxide gas with the temperature controlled at 80°C. The exposure time varied from 6 to 150 hours in different experiments. Electrochemical corrosion measurements using DC linear polarisation were carried out to monitor the corrosion rate during the 150 hour experiments. The film formation procedure was developed, which was inspired primarily by the previously published protective scale formation procedure by Han et al [55]. This film formation procedure, as described below, was developed with reference to the film characterisation findings from Chapter 6 to create a semi protective film that could lead to film breakdown. The change in conditions was introduced in 2 hour steps to allow different film properties to grow on the surface in different layers to promote the film breakdown and have pitting. The corrosion rates after 2 hours immersed in the solution ranged between 2.75 mm/yr and 3.25 mm/yr. After 2 hours, the pH of the solution was initially around pH 3.9, and then the pH was adjusted to 5.65 by adding sodium bicarbonate ($NaHCO_3$). This decreased the corrosion rate significantly to within the range of 1.75

mm/yr to 2.25 mm/yr, as shown in Figure 7-1. During this period more compact iron carbonate film formed on top of the mixed iron carbonate and iron carbide film, as shown in Figure 7-2.

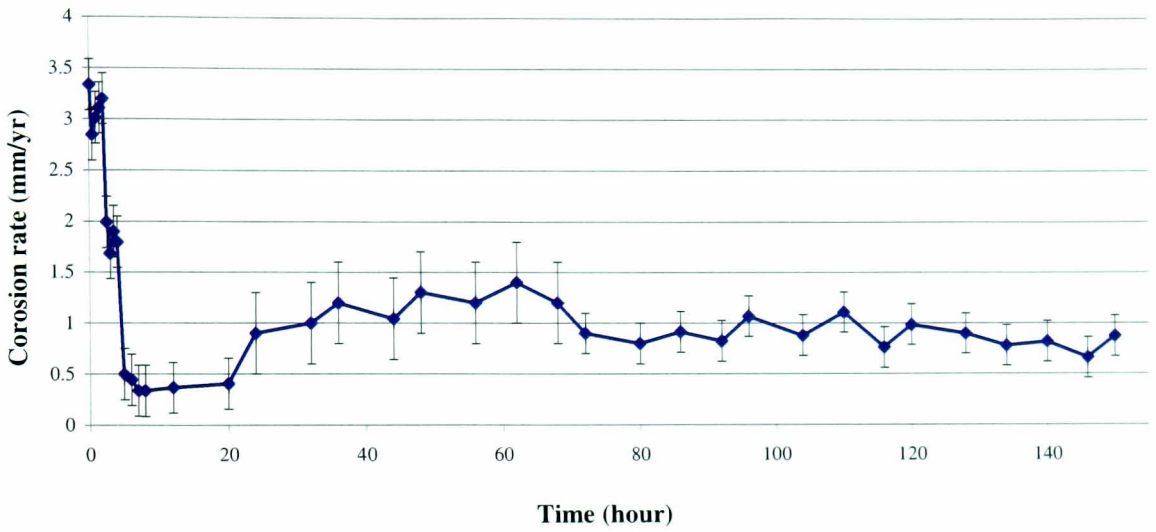

Figure 7-1: Corrosion rate versus time for the X65 carbon steel in CO_2 saturated, 10% NaCl brine at 80°C, pH 5.65 and 1000ppm Fe^{2+}

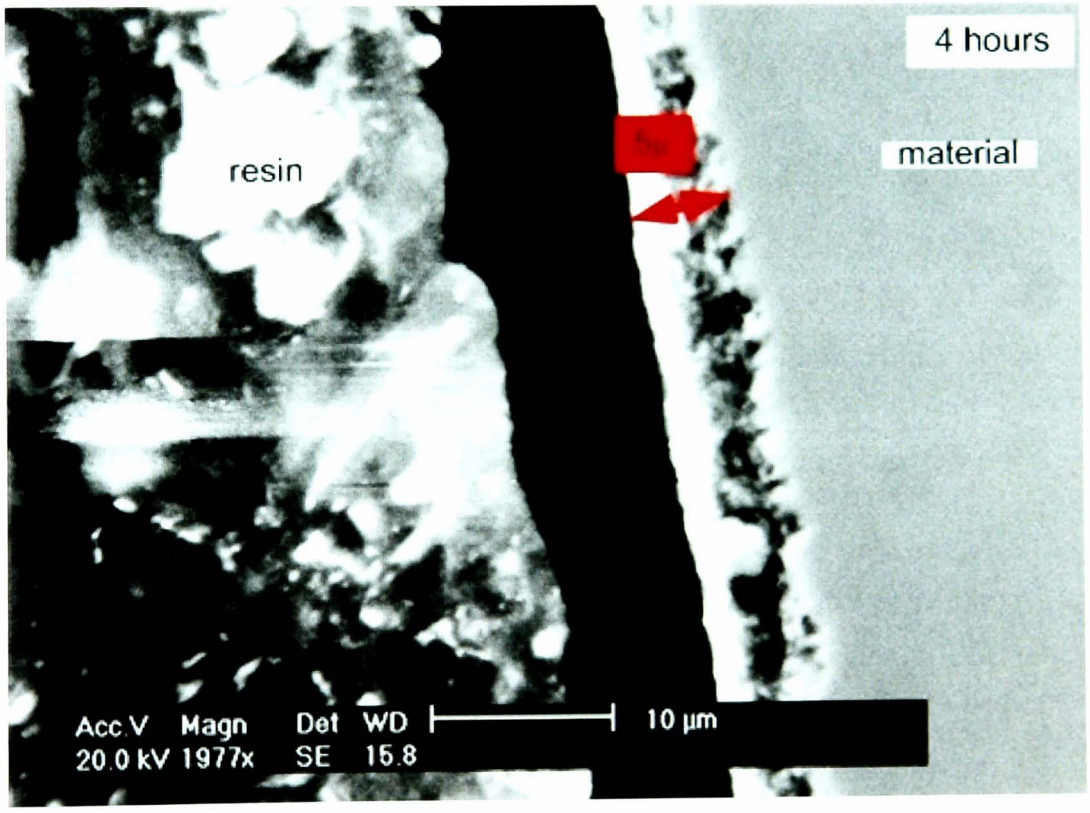

Figure 7-2: SEM cross-section image of X65 carbon steel in CO_2 saturated 10% NaCl, pH 5.65 at 80°C after 4 hours

After 4 hours, 1000ppm of iron chloride ($FeCl_2$) was added, which decreased the corrosion rate to a range of 0.75 mm/yr, and this remained fairly constant for up to 20 hours. The corrosion rate started to increase after 24 hours to around 1.25 mm/yr until 72 hours and then the corrosion rate dropped to 0.75 mm/yr until the end of the experiment at 150 hours. The corrosion rate obtained is supported by Han et al. who observed that the corrosion rate at 0.3 supersaturation of $FeCO_3$ 80°C and pH 5.6 was 0.75 mm/yr during the chemical scale removal process [55]. It is interesting to observe the pit growth from an *in-situ* camera observation in Figure 7-3. The camera displays the real time image and recorded the image every 20 seconds.

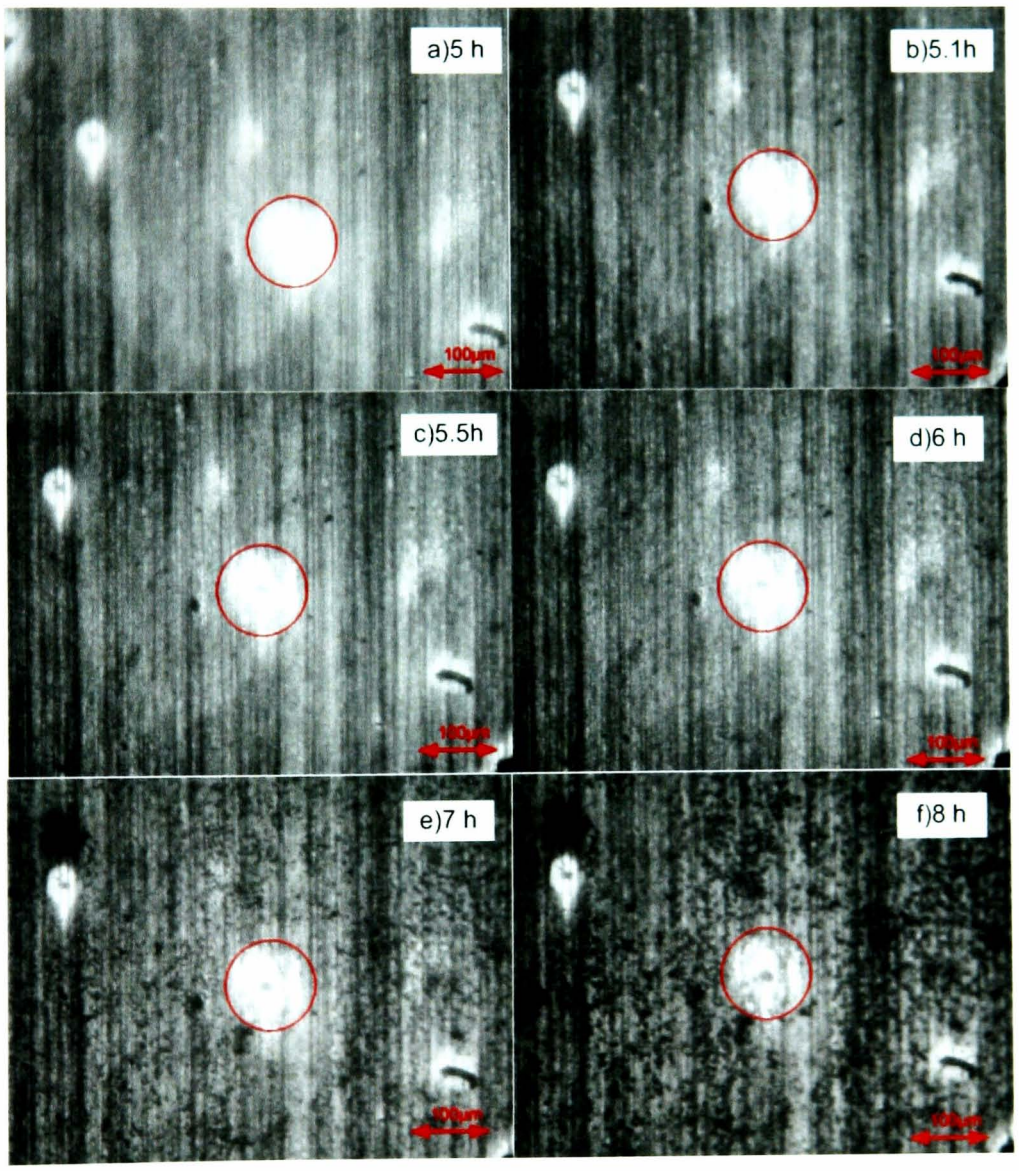

Figure 7-3: *In-situ* camera observation on pit initiation on X65 carbon steel in CO_2 saturated 10% NaCl, pH 5.65, 1000ppm Fe^{2+}, at 80°C from 5 hours to 8 hours

The initiation of pits was observed after 5 hours at uncorroded spots and propagated to 30μm in pit mouth diameter until 8 hours. The pit diameter grows actively in the first 3 hours after initiation and then the pit diameter propagation rate slows down and stops at 10 hours, as shown in Figure 7-4.

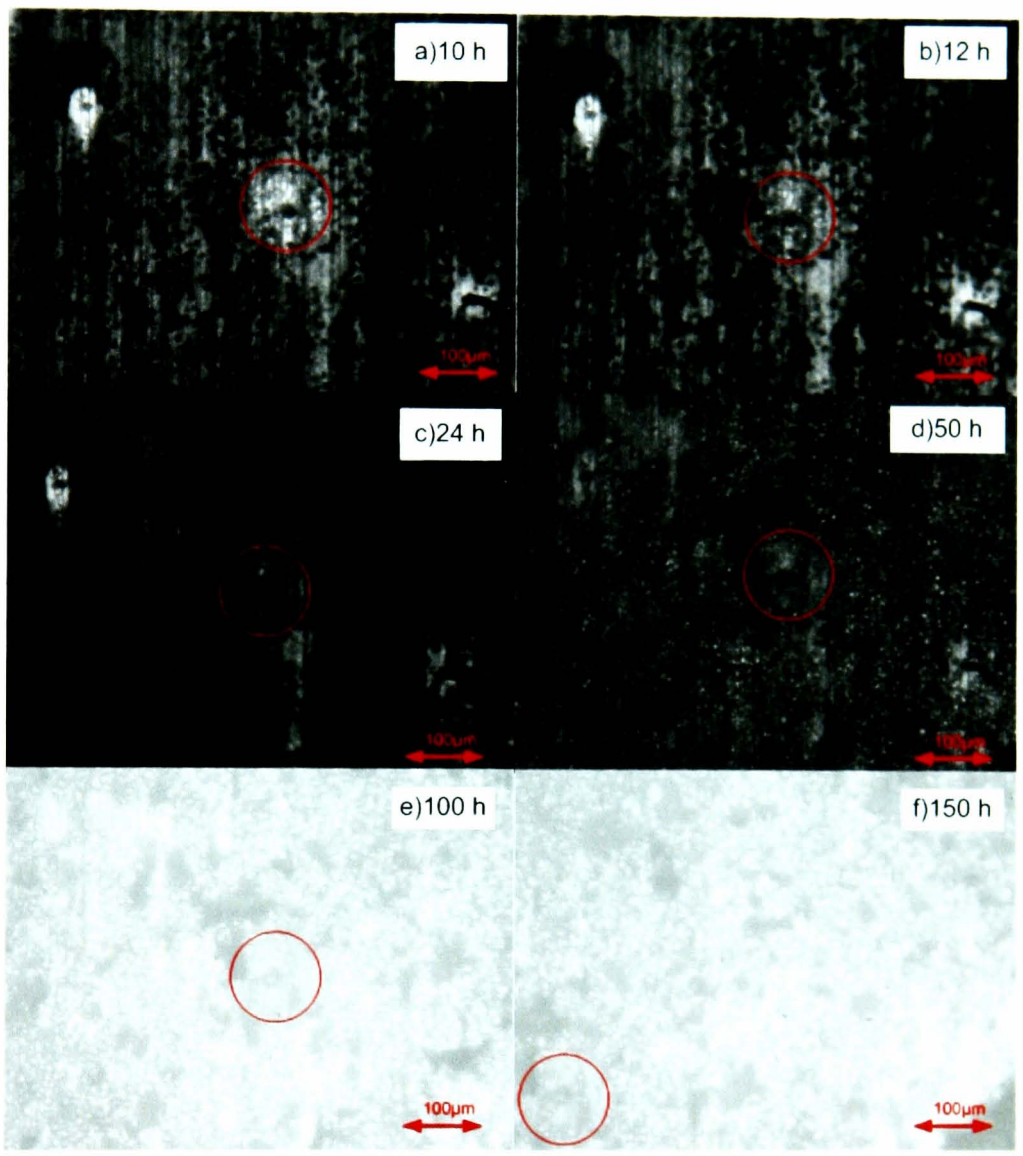

Figure 7-4: *In-situ* camera observation on film formations at the pit site on X65 carbon steel in CO_2 saturated 10% NaCl, pH 5.65, 1000ppm Fe^{2+}, at 80°C from 10 hours to 150 hours

The uncorroded spots represented by the white regions around the pits could indicate a lower pH area or a chloride cap. The *in-situ* image also shows that the uncorroded spots around the pit site remained during the pitting initiation process; however, the film formation started taking place at the uncorroded site after the pitting

growth process slowed down after 7 hours. The active film growth continues until 50 hours and then the film growth does not show much difference until 150 hours. Figure 7-5 shows the SEM image of iron carbonate film on the surface after 150 hours and some surface damage appears in which the film leaves a footprint of iron carbonate crystals. Figure 7-6 shows the cross-sectional image of the iron carbonate film, which filled the iron carbide network left behind after 150 hours. Gulbrandsen et al. showed that long time exposure at 50°C, pH 5 in CO_2 conditions may result in a thicker cementite film growth on the surface and lead to higher average corrosion rate and localised attack [192]. This shows that the pits propagate beneath the porous corrosion film and coalesce into a larger pit and the remaining corrosion film on top will fill the pit completely or be removed stepwise by flow [62, 55]. The build up and change of kinetics of the iron carbonate film with time causes the variation of corrosion rate during the experiments.

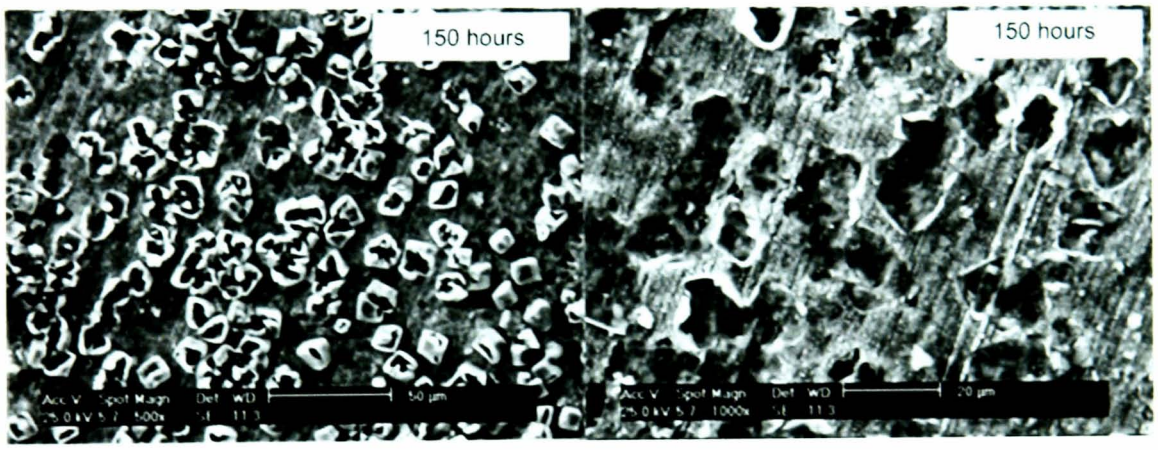

Figure 7-5: SEM surface image on X65 carbon steel in CO_2 saturated 10% NaCl, pH 5.65, 1000ppm Fe^{2+}, at 80°C after 150 hours

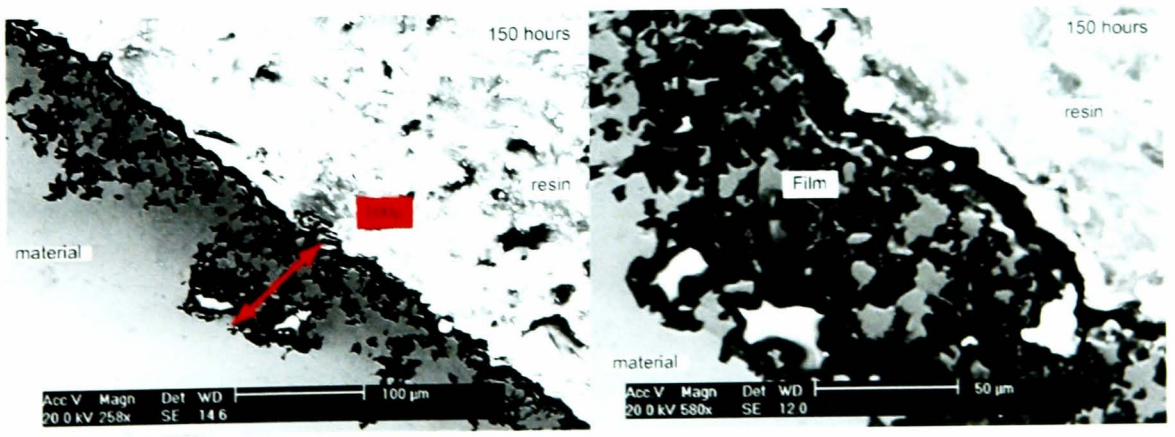

Figure 7-6: SEM cross-section on X65 carbon steel in CO_2 saturated 10% NaCl, pH 5.65, 1000ppm Fe^{2+}, at 80°C after 150 hours

7.1.2 Corrosion current measurement for sour experiments

Sour experiments were performed in 10% NaCl for 4 hours at 80°C at various conditions to explore the optimum condition to obtain deep pits against a relatively low corrosion rate. The first specimen, which was immersed in 10% NaCl and natural pH at around 4 showed a consistent corrosion rate of 0.8 mm/yr for the duration of the 4-hour experiment. The second specimen, which was immersed with the addition of sodium bicarbonate ($NaHCO_3$) to adjust the pH to 5.65, showed that the corrosion rate decreased significantly to 0.4 mm/yr. However, the third specimen with an adjusted pH of 5.65 and 1000ppm Fe^{2+} showed contrasting behaviour with an increased corrosion rate of 16 mm/yr, as shown in Figure 7-7.

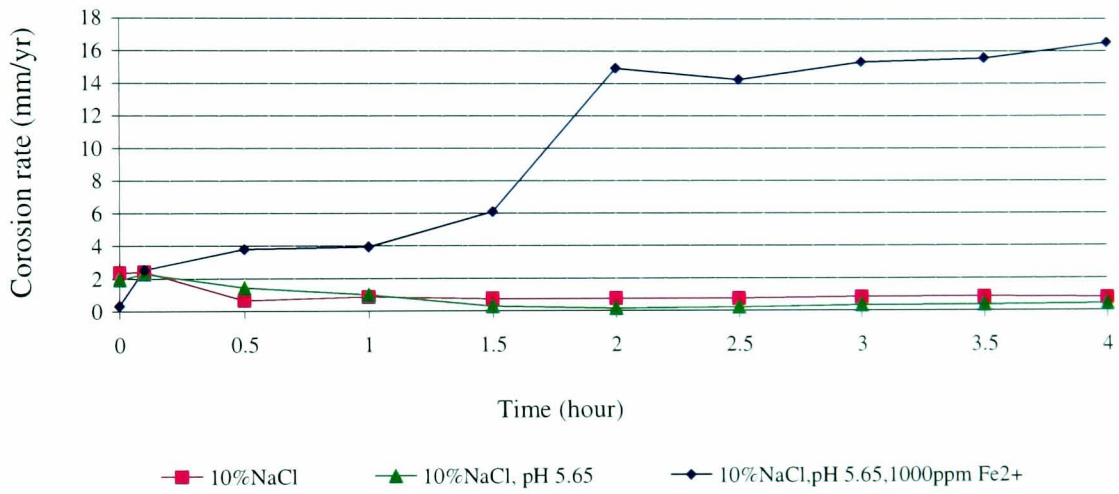

Figure 7-7: Corrosion rate versus time for the X65 carbon steel in 10% H_2S, 90% CO_2 saturated, 10% NaCl brine at 80°C

Therefore, based on the earlier test results, an extended test was carried out at 10% NaCl with pH 5.65 for 96 hours to study the behaviour of pitting propagation in sour conditions. In the first 10 minutes of the test, the corrosion rate was around 0.7 mm/yr. The corrosion rate decreases to 0.15 mm/yr after 4 hours as the protective iron sulphide film is built up, as shown in Figure 7-8.

After 24 hours of immersion the corrosion rate starts to increase to 0.4 mm/yr and fluctuates between the range 0.3 mm/yr to 0.4 mm/yr until the end of the experiment at 96 hours. The corrosion rate obtained is supported by Svenningsen et al., who observed that the corrosion rate at 60°C, pH 5 with a mixture of 50% H_2S and 50% CO_2 was 0.3 mm/yr during 72 hours exposure [127]. After the 96 hours test, the

SEM image shows that an iron sulphide film formed on the surface, as shown in Figure 7-9. The film layer consists of two irregular layers of crystals in which the top layer was poorly adherent to the surface and formed pit clusters [4, 130].

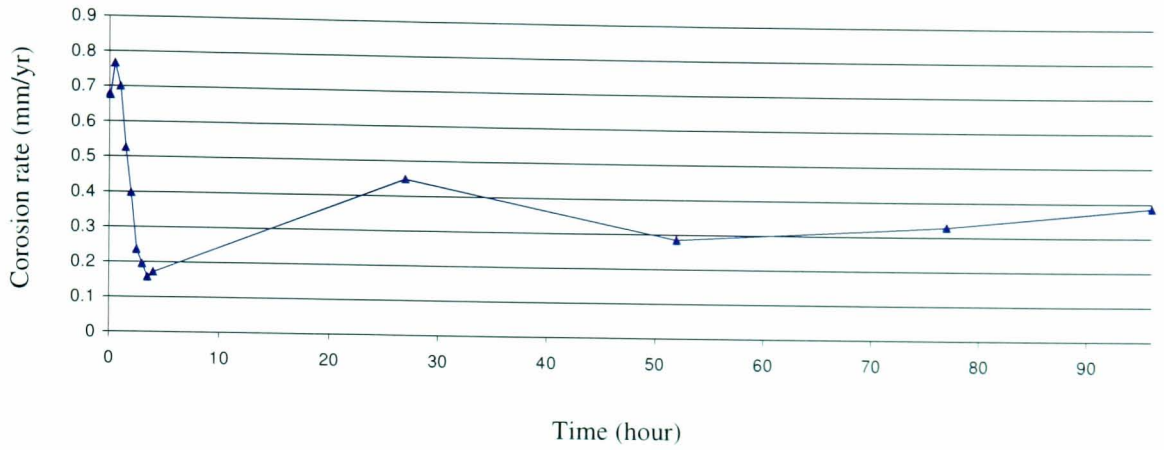

Figure 7-8: Corrosion rate versus time for the X65 carbon steel in 10% H_2S, 90% CO_2 saturated, 10% NaCl brine at 80°C, pH 5.65

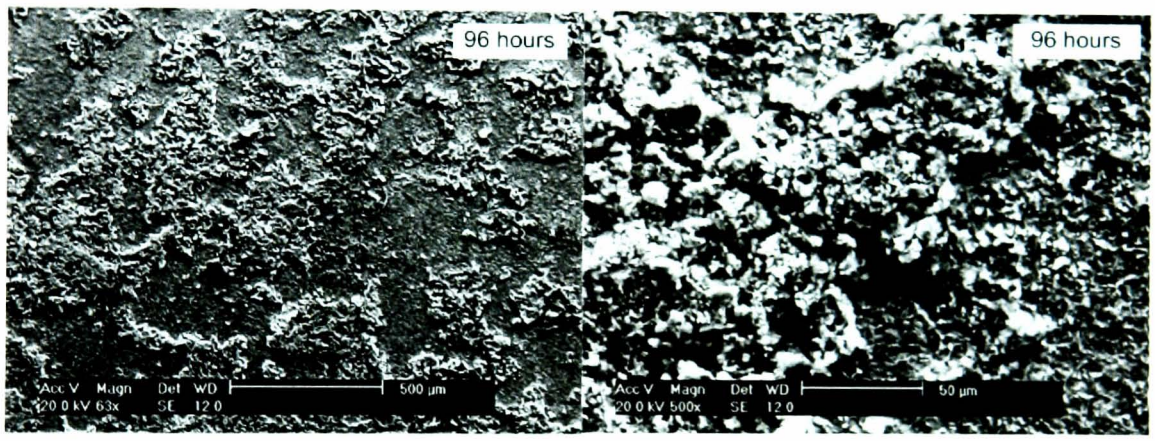

Figure 7-9: SEM image on X65 carbon steel in 10% H_2S, 90% CO_2 in 10% at 80°C in sour after 96 hours

7.1.3 Pit Depth analysis for sweet experiments

The analyses were conducted using contact surface profilometry Talysurf-120 and non-contact white light interferometer WYCONT3300S. Pit growth varies in number and size on the surface but the maximum pit depth is the main parameter that leads to failure. Figure 7-10 shown the pits obtained after 150 hours exposure time. A 2Dimage as shown in Figure 7-10b showing that the deepest pits obtained are around 73µm. The pit growth is scattered all over the surface as shown in Figure 7-10 (a-f).

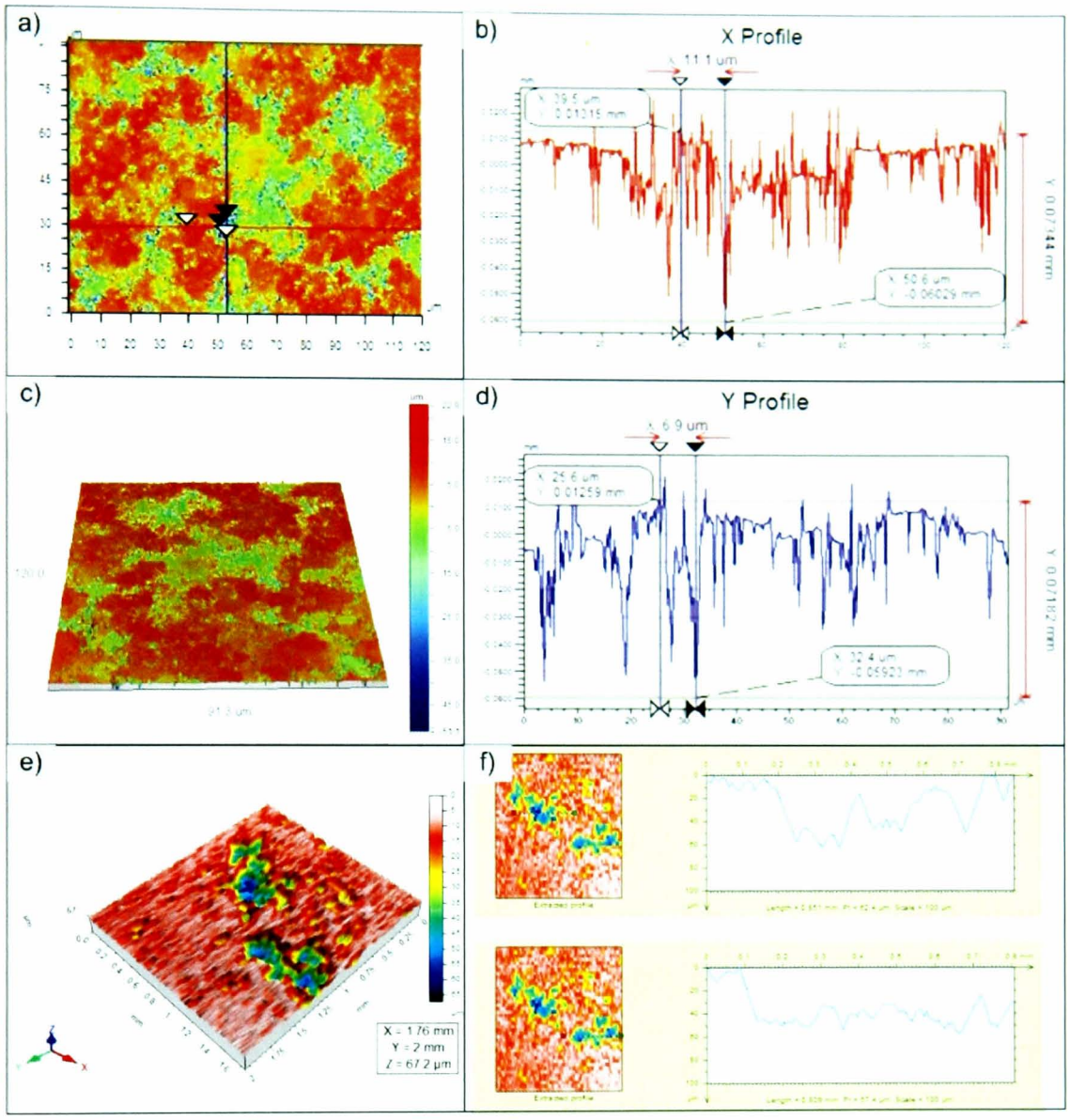

Figure 7-10: Profilometry analysis for 150 hours specimens of X65 carbon in CO_2 saturated 10% NaCl brine at 80°C, pH 5.65, 1000ppm Fe^{2+} and 1 bar CO_2; a) 2D view of pits surface, b) Cross-section for x-profile from 2D view, c) 3D View of pits surface, d) Cross-section for y-profile from 2D view, e) 3D view of pits surface, f) Cross-section from 3D view pits

The depth varies from micro pits, starting at 1µm to the deepest pit at around 73µm. In this study, the entire surface of the sample was analysed with the threshold set according to the value of the third deepest pit on the surface to determine the three deepest pit depths on the surface. These three maximum pits obtained on the surface were evaluated to measure the extent of pitting corrosion, because the deepest pit is

the main parameter that can cause failure. Figure 7-11 shows the maximum pit depth and average of three maximum pit depths obtained on the surface at different times. Tests were conducted for durations of 6, 24, 70, 96, 120 and 150 hours in separate experiments to obtain the pit depth, which is necessary for inhibitor evaluation.

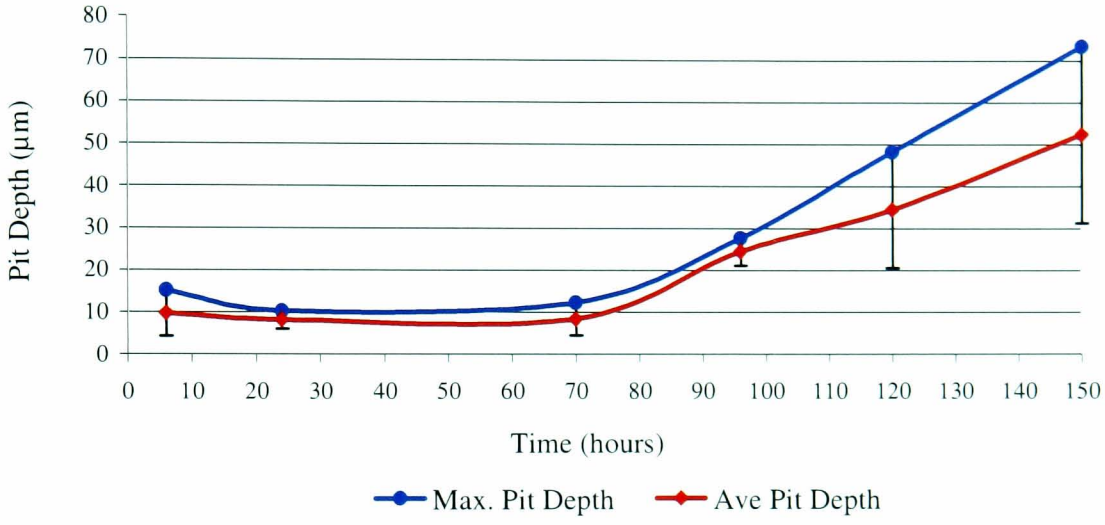

Figure 7-11: Maximum pit depth and average of 3 maximum pit depth of X65 carbon in CO_2 saturated 10% NaCl brine at 80°C, pH 5.65, 1000ppm Fe^{2+} and 1 bar total pressure at different times

The results show that the pit depth increases over time, which means that the longer tests generate more severe localised corrosion and, thus, deeper pits as expected. Pitting depths obtained for the 6 hours test are around 15µm. However, the pitting depth obtained for 24 and 70 hours was around 12µm. No increase in the depth over time is shown for the 24 hours and 70 hours specimens. However, the tests at 96, 120 and 150 hours show a significant increase in pitting depth over time with a linear propagation rate.

The results show that the pitting propagation was non-linear in the first 72 hours due to the film build-up process overtime, as indicated by the fluctuation in the corrosion rate from 20 hours to 70 hours in Figure 7-1. After 72 hours, a stable film form is shown by the consistent corrosion rate, which enhances the propagation process.

7.1.4 Pit depth analysis of sour experiments

The pitting that was generated from all 4-hour tests did not show a significant final pit depth to enable any difference between the conditions to be determined. Figure 7-12 shows that the average pits generated are around 6µm to 8µm depth for all 4-hour tests and for the extended test to 96 hours, the pit depth obtained is around 30µm depth. Figure 7-13b and Figure 7-13d shows that the profilometry analysis for the pits obtained from the 4-hours test to have a depth of 8.9µm and after 96 hours was 31.4 µm. Figure 7-13a shows that the pit grows as a single pit on the surface but the surrounding area is not effected by pitting corrosion. After 96 hours, Figure 7-13e shows that single pits are merged together to form bigger pits with greater depth. This also shows that the pit depth increases over time and generates more severe localized corrosion and deeper pits.

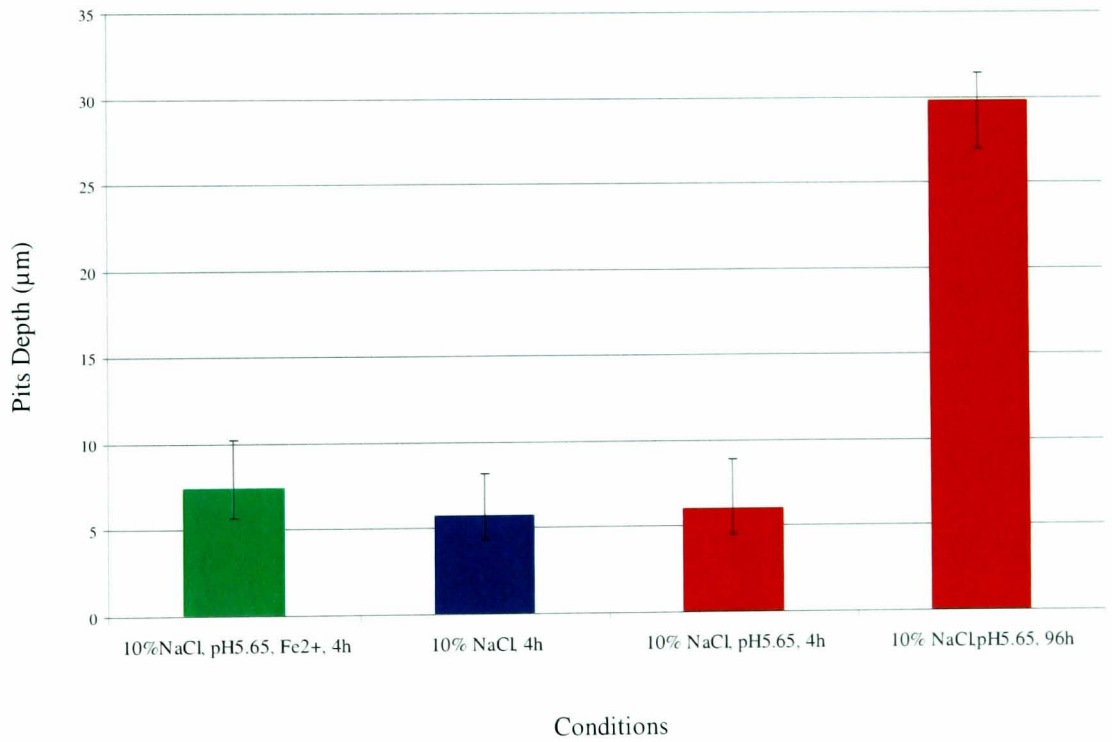

Figure 7-12: Pit Depth of X65 carbon in 10% H_2S, 90% CO_2 saturated, 10% NaCl brine at 80°C

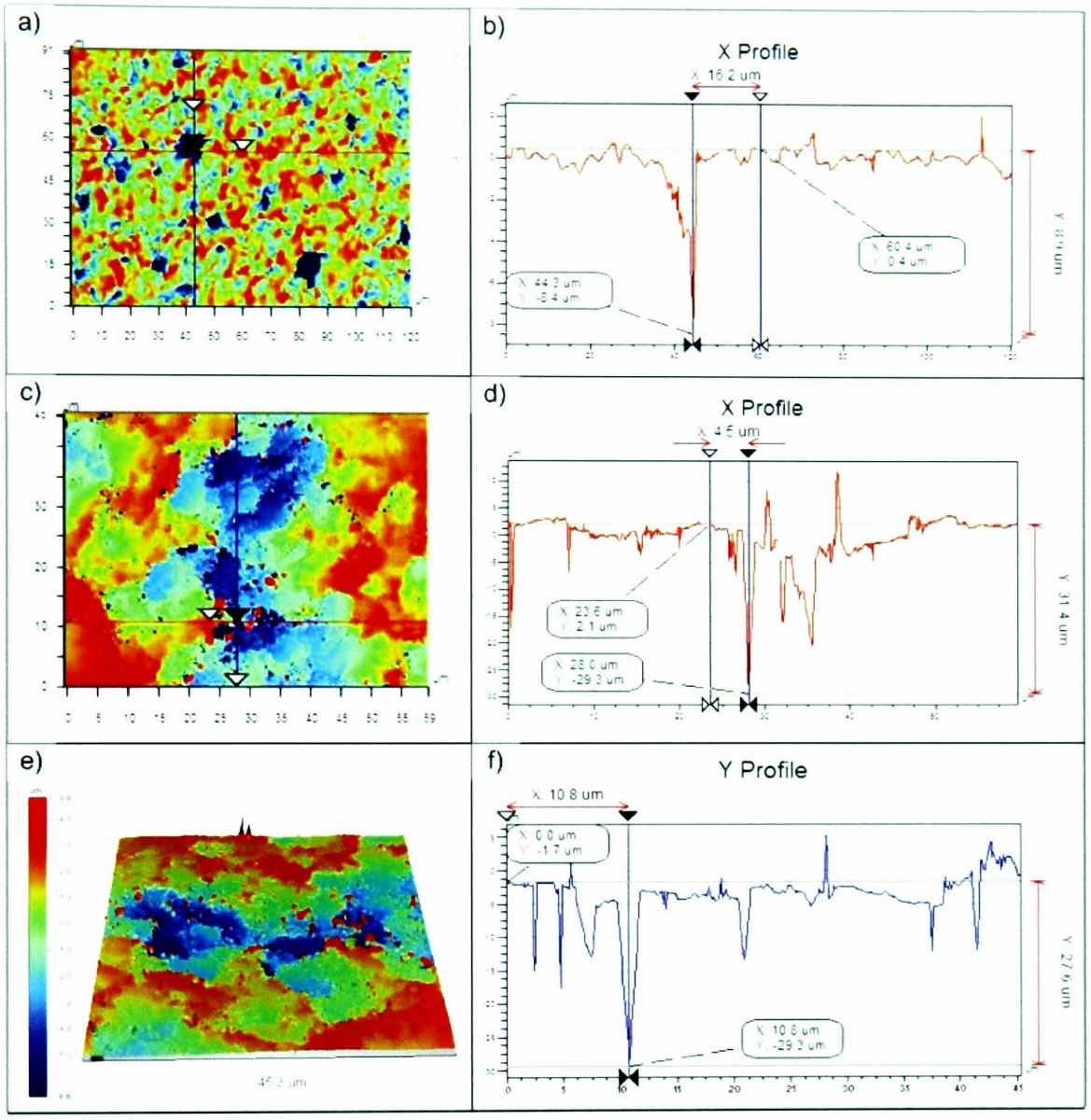

Figure 7-13: Profilometer analysis of X65 carbon steel in 10% H_2S, 90% CO_2 saturated, 10% NaCl brine at 80°C, pH 5.65; a) 2D view of pits surface after 4 hours, b) Cross-section from 2D view pits after 4 hours, c) 2D view of pits surface after 96 hours, d) Cross-section for x-profile from 2D view, e) 3D view of pits surface after 96 hours, f) Cross-section for y-profile from 2D view

7.2 Inhibition of pitting in sweet experiment

7.2.1 Corrosion current measurement for phosphate ester inhibitor

Corrosion rates were monitored during the experiment to observe the change after different concentrations of phosphate ester were added into the test vessel after 120 hours pre-corrosion. The effectiveness of the inhibitor was evaluated towards overall corrosion protection in which the main goal is preventing the pitting propagation, and, at the same time, to control the general corrosion. Figure 7-14 shows the corrosion rate observed during the test.

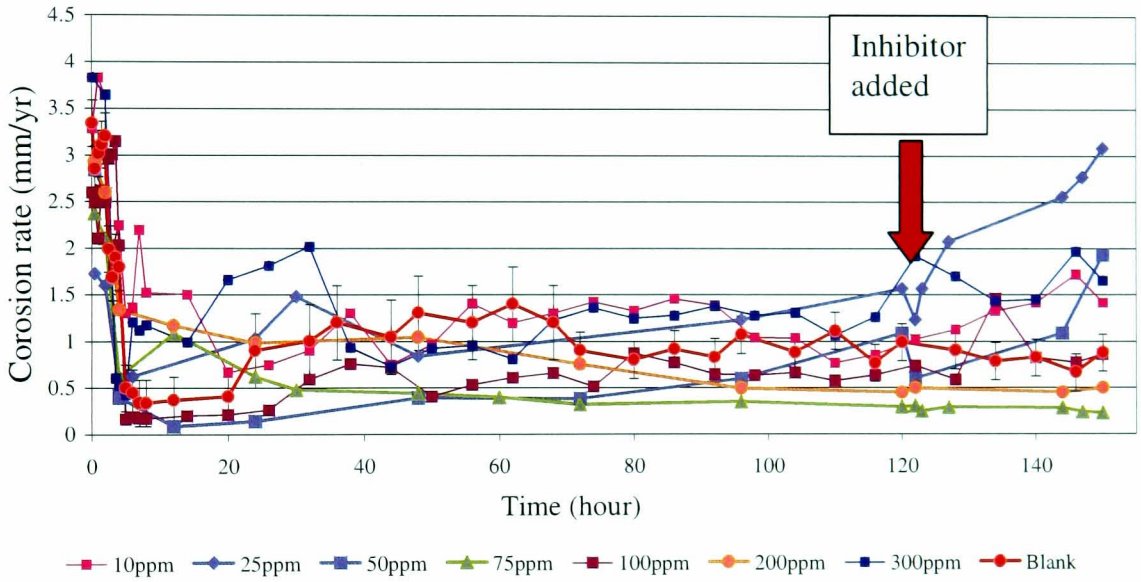

Figure 7-14: Corrosion rate versus time for the X65 carbon steel in CO_2 saturated, 10% NaCl brine at 80°C, pH 5.65 and 1000ppm Fe^{2+} with different concentrations of phosphate ester

The corrosion rate at 120 hours pre-corrosion was observed and varies in the range between 0.3 mm/yr and 1.3 mm/yr. The corrosion rate variation could not be avoided with such a long pre-corrosion time due to the formation of a cementite layer on the surface mixed with iron carbonate film to offer a semi-protective film in this test condition [91, 192]. Wong et al. also observed that the corrosion rate varies between 0.25 mm/yr and 1 mm/yr after 15 hours corrosion at 10000ppm Cl^-, pH 6.5, 80°C with saturated CO_2 [99]. This is supported by Han et al. who showed that at pH 5.65, the solubility of iron carbonate is at the saturation line and suggested that localised corrosion is more likely to propagate [50]. Han et al. also showed that at

10% NaCl, the solubility of $FeCO_3$ increases, which makes it more difficult to form a fully protective $FeCO_3$ film and increases localised attack [50]. The corrosion rate effect for every inhibitor concentration was compared individually before the inhibitor was added and after the inhibitor was added at 120 hours. Figure 7-15 shows the expanded version of the corrosion rate with time from 110 hours to 150 hours.

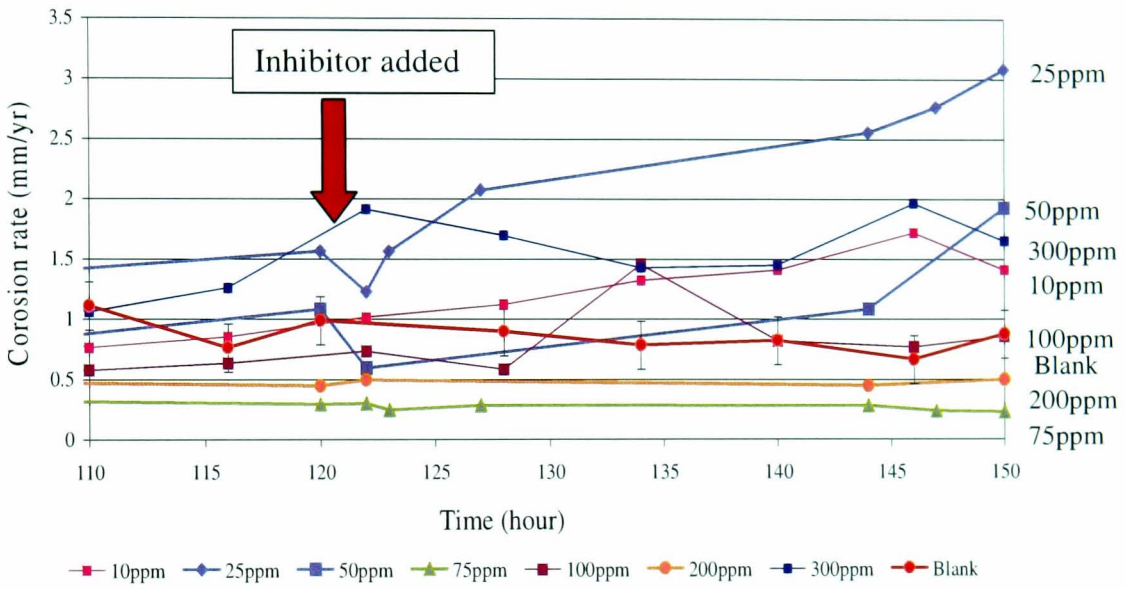

Figure 7-15: Expanded version of corrosion rate versus time for the X65 carbon steel in CO_2 saturated, 10% NaCl brine at 80°C, pH 5.65 and 1000ppm Fe^{2+} with different concentrations of phosphate ester

The corrosion rate measured for 10ppm, 25ppm and 50ppm inhibitors shows a 50% increase in the corrosion rate after the inhibitor was added. The general corrosion rate almost doubles at lower concentrations. The corrosion rate, which was monitored for 75ppm, 100ppm, 200ppm and 300ppm inhibitor, did not show any significant change in the corrosion rate after the inhibitor was added. This result is supported by Foss et al., who showed that there was no further effect on the corrosion rate when the phosphate ester inhibitor was added after 280 hours pre-corrosion at 60°C, 0.8bar CO_2 [91]. However, Wong et al. showed that phosphate ester reduces the corrosion rate significantly when added at the beginning of the test [98]. This is supported by Gulbrandsen et al., who showed that a long pre-corrosion time at 50°C, pH 5 in CO_2 conditions may impair inhibitor performance due to the presence of a layer of cementite on the surface, which makes the surface unstable due to the large cathodic surface [192]. This shows that at the above minimum effective concentration of

inhibitor, the phosphate ester does not show a significant effect on the corrosion rate due to the pre-corrosion film that had already built up in the first 120 hours. The pre-corrosion films have a strong influence in controlling the corrosion rate and kinetically hinder the corrosion force [192]. The pre-corrosion conditions simulate the situation to inhibit a pipeline that is already in service, in which the surface might be covered with iron carbonate precipitates, uncorodded iron carbide and many different types of scale [192].

7.2.2 Corrosion current measurement for imidazoline inhibitors

Imidazoline inhibitors were also evaluated using the same procedure as the phosphate ester inhibitor for which the main goal is to prevent the pitting propagation and at the same time to control the general corrosion. The performance of imidazoline inhibitors is better in terms of controlling the corrosion rate, mainly at higher concentrations, as shown in Figure 7-16. Figure 7-17 shows the expanded version of the corrosion rate with times from 110 hours to 150 hours. The corrosion rate measured for the 10ppm inhibitor initially shows a 25% increase after the inhibitor was added to the test vessels, however, it improved the performance with time towards the end of the test. There were no significant changes in the monitored corrosion rates for 25ppm, 50ppm, 75ppm and 100ppm inhibitors.

After the concentration of the inhibitor was increased to 200ppm and 300ppm, a 50% decrease in the corrosion rate was observed. These results are supported by Foss et al., who showed a decrease in the corrosion rate when imidazoline inhibitor was added after 290 hours pre-corrosion at 60°C, 0.8bar CO_2 [91]. Wong et al. also showed that imidazoline reduces the corrosion rate significantly when added at the beginning of the test [98]. This shows that at above the minimum concentrations of imidazoline, the inhibitor will influence the existing corrosion film on the surface to reduce the corrosion rate. Chokshi et al. observed that imidazoline inhibitors could decrease the concentration of Fe^{2+} at the pre-corrosion surface and hamper the growth of $FeCO_3$ to slow down the anodic as well as the cathodic reactions [65].

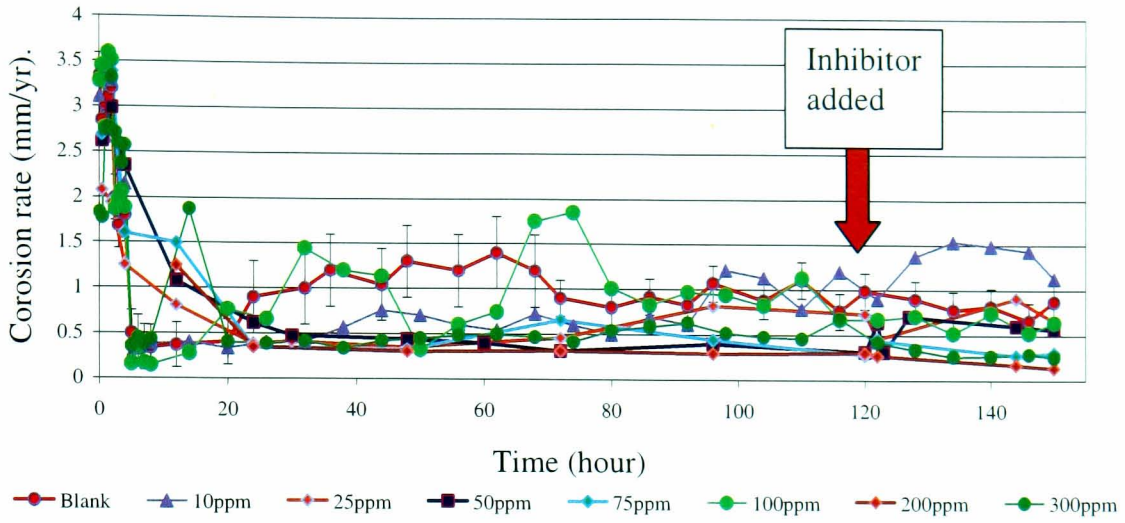

Figure 7-16: Corrosion rate versus time for the X65 carbon steel in CO_2 saturated, 10% NaCl brine at 80°C, pH 5.65 and 1000ppm Fe^{2+} with different concentrations of imidazoline

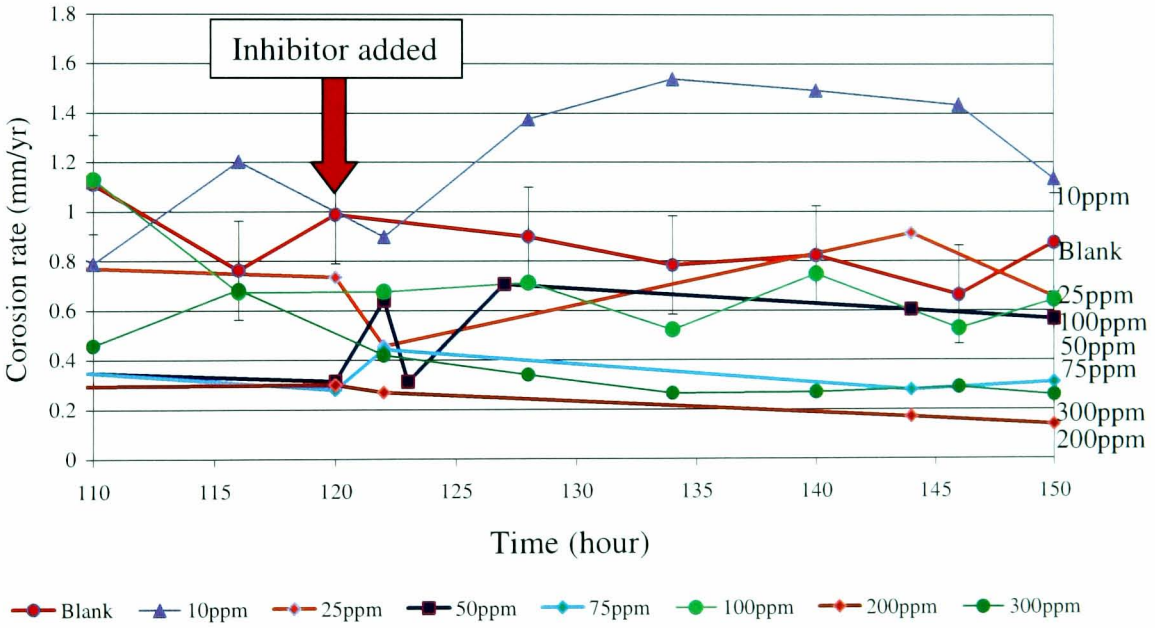

Figure 7-17: Expanded version of corrosion rate versus time for the X65 carbon steel in CO_2 saturated, 10% NaCl brine at 80°C, pH 5.65 and 1000ppm Fe^{2+} with different concentrations of imidazoline

7.2.3 Pit depth analysis for phosphate ester inhibitor

For the blank test, the results show that, on average, the pit depth ranged between 20µm and 48µm after 120 hours and between 40µm and 73µm after 150 hours. Phosphate ester was introduced at various concentrations to the experiment at 120 hours to control pitting propagation between 120 hours and 150 hours. Figure 7-18 shows that phosphate ester can control the pit propagation if a sufficient concentration is applied.

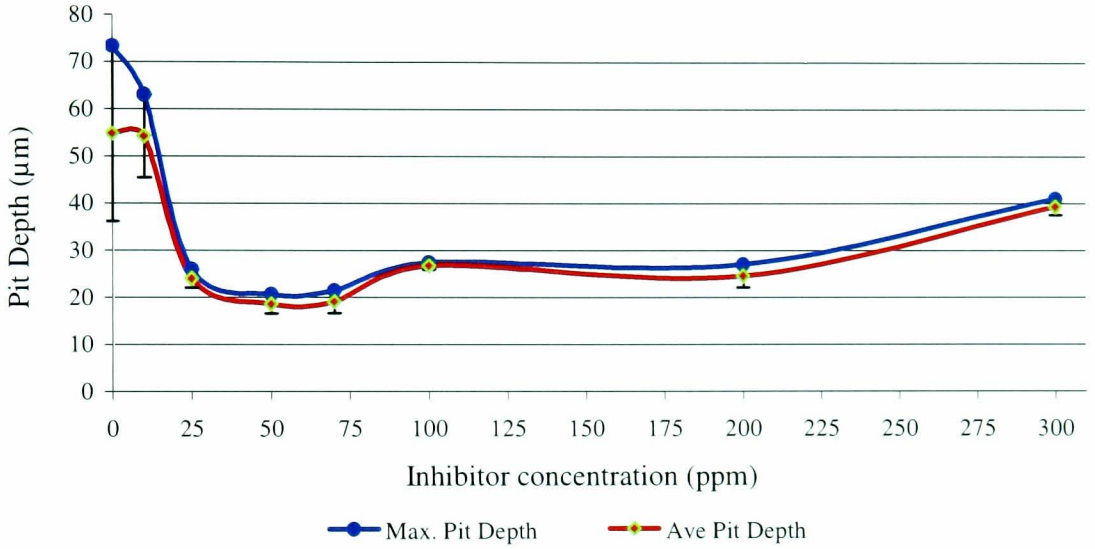

Figure 7-18: Maximum pit depth and average of 3 maximum pit depth of X65 carbon in CO_2 saturated 10% NaCl brine at 80°C, pH 5.65, 1000ppm Fe^{2+} with different concentrations of phosphate ester

Phosphate ester performs at effective performance at concentrations between 25ppm to 200ppm with the final pit depth obtained between 17 µm and 27 µm. Figure 7-19 (a-d) shows that the pit depth profile at 100ppm phosphate ester with the pit depth obtained around 27µm. At 300ppm, the phosphate ester inhibitor has little effect on slowing down the pit propagation, in which the final pit depth obtained was between 37 µm and 41 µm; the decrease in the inhibition efficiency is postulated to be due to the higher inhibitor concentration beyond the critical concentration value of the inhibitor. However, with a low concentration of 10ppm phosphate ester, the pitting propagation was not decreased, obtaining a final pit depth of around 46µm to 63µm, as shown in Figure 7-19.

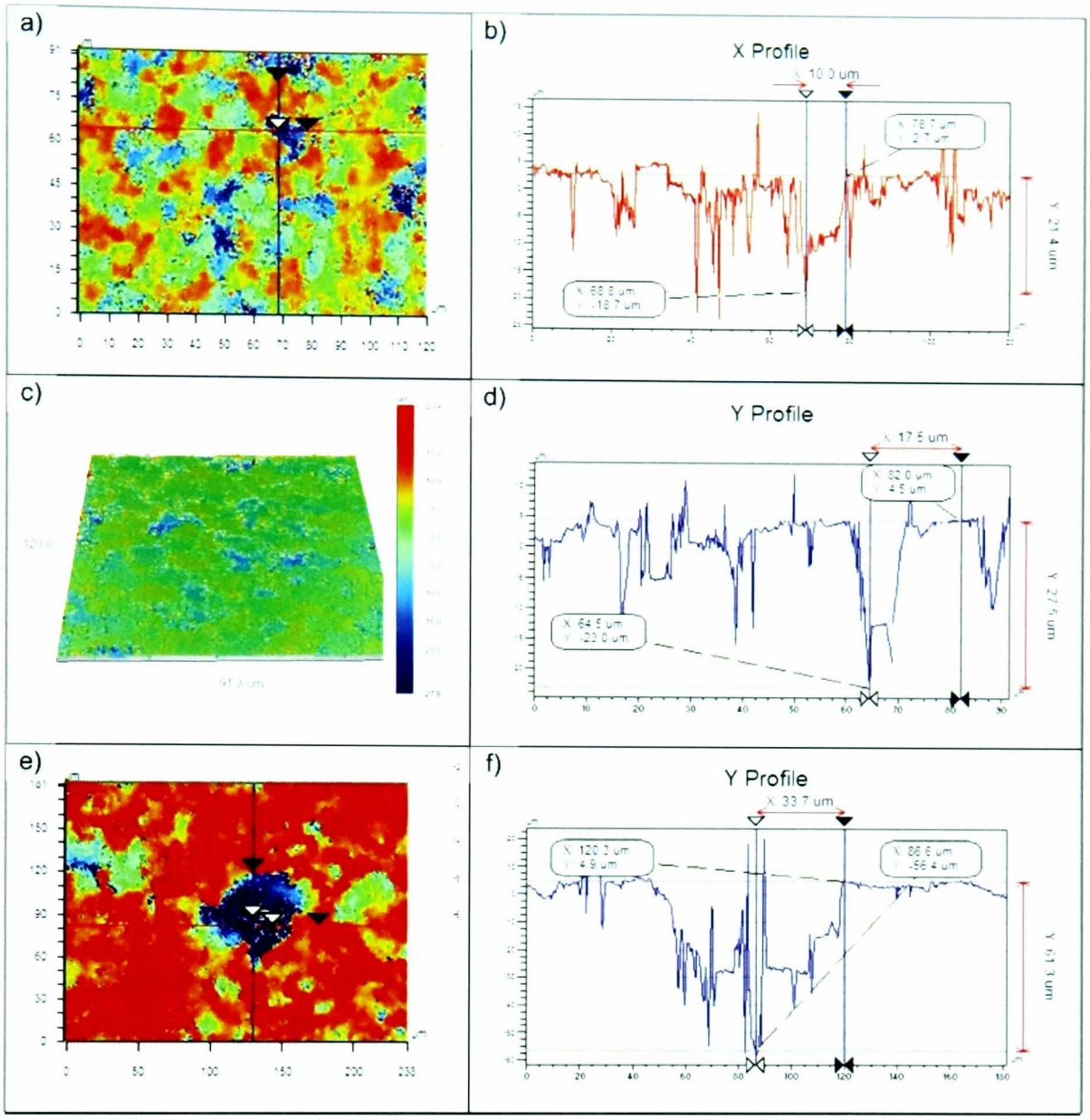

Figure 7-19: Profilometer analysis of X65 carbon steel in CO_2 saturated 10% NaCl brine at 80°C, pH 5.65, 1000ppm Fe^{2+} with different concentrations of phosphate ester; a) 2D view of pits surface at 100ppm, b) Cross-section from 2D view pits at 100ppm, c) 3D view of pits surface at 100ppm, d) Cross-section for x-profile from 2D view at 100ppm, e) 2D view of pits surface at 10ppm, f) Cross-section for y-profile from 2D view at 10ppm

The lack of any significant difference from the blank test is postulated to be due to the insufficient effect of the inhibitor, which reduced the inhibitor performance. It is interesting to compare the correlation between the corrosion rate effect and the final pit depth obtained, as at 10ppm phosphate ester both the corrosion rate and pit depth result show a decrease in performance.

7.2.4 Pit depth analysis for imidazoline inhibitors

Imidazoline slows down the pitting propagation at almost all concentrations between 10ppm and 300ppm, as shown in Figure 7-20.

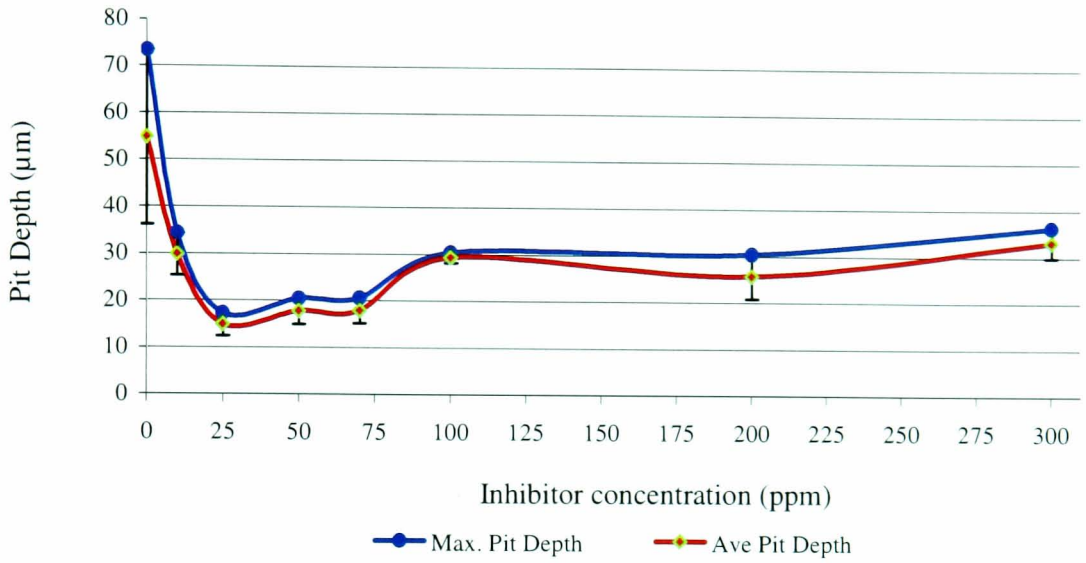

Figure 7-20: Maximum pit depth and average of 3 maximum pit depth of X65 carbon in CO_2 saturated 10% NaCl brine at 80°C, pH 5.65, 1000ppm Fe^{2+} with different concentrations of imidazoline

Imidazoline performs at effective concentration between 25ppm and 300ppm where the maximum pit depth obtained was between 17.3 µm and 20.5 µm. Figure 7-21(a-d) shows that at 100ppm the pit depth obtain was 30.4µm and the 2D and 3D image shows that the pit distribution on the surface were in the form of single pits with less general corrosion attacked. Imidazoline has little effect on slowing down the pit propagation at 10ppm where the maximum pit depth obtained was 34.4 µm, which was postulated to be due to the insufficient effect of the inhibitor, which reduced the inhibitor performance. Imidazoline also has little effect on slowing down the pit propagation at 300ppm where the maximum pit depth obtained was 36.4 µm, as shown in Figure 7-21f, which was postulated to be due to the higher inhibitor concentration beyond the inhibitor concentration critical value.

Imidazoline shows a good performance in almost all concentrations tested towards general corrosion and pitting. It is interesting to compare the mechanism of

action between imidazoline and phosphate ester towards corrosion rate and pit depth in discussion chapter.

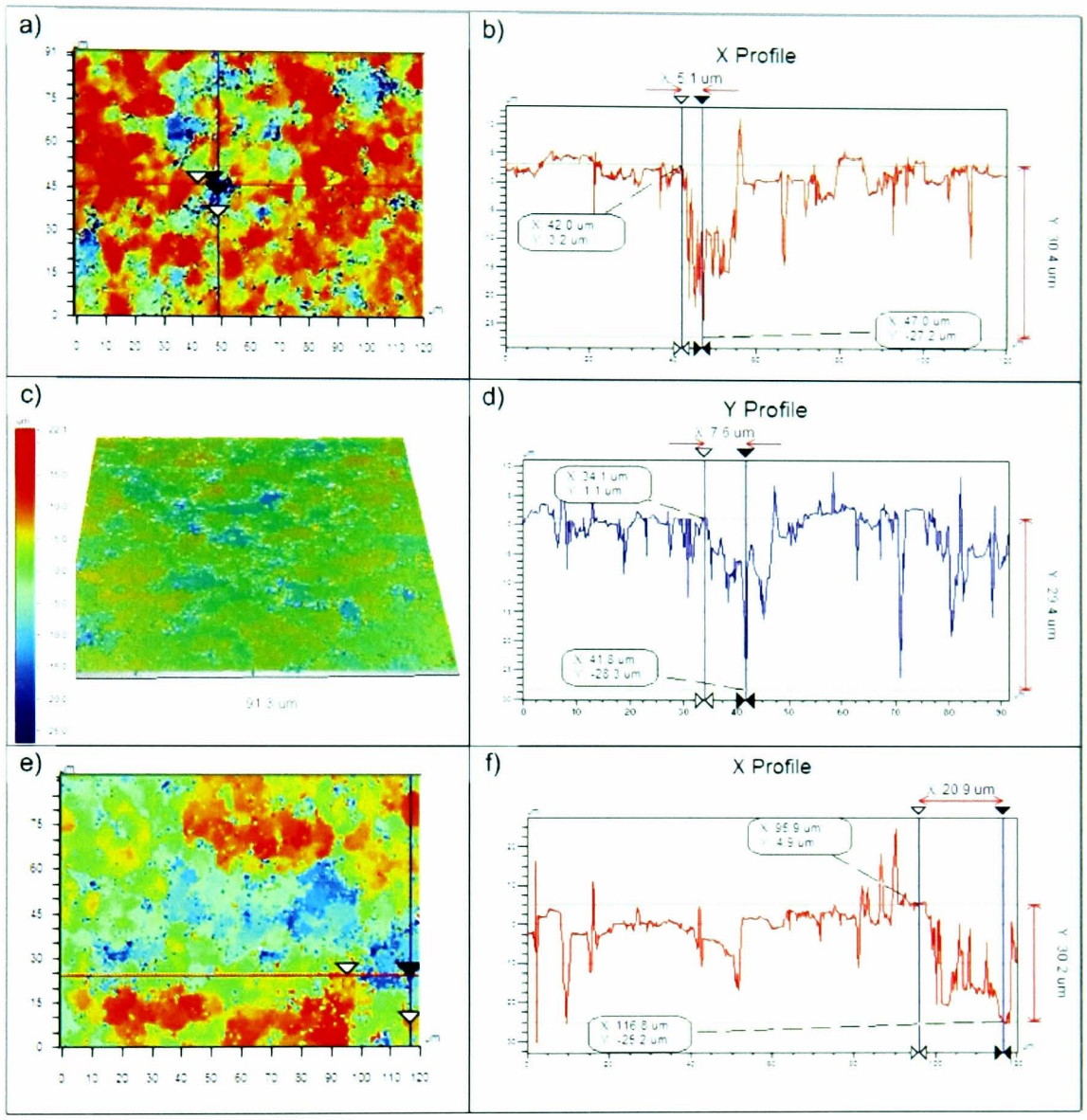

Figure 7-21: Profilometer analysis of X65 carbon steel in CO_2 saturated 10% NaCl brine at 80°C, pH 5.65, 1000ppm Fe^{2+} with different concentrations of imidazoline; a) 2D view of pits surface at 100ppm, b) Cross-section from 2D view pits at 100ppm, c) 3D view of pits surface at 100ppm, d) Cross-section for x-profile from 2D view at 100ppm, e) 2D view of pits surface at 300ppm, f) Cross-section for x-profile from 2D view at 300ppm

7.3 Summary

This chapter revealed the pitting growth process from 6 hours to 150 hours. The study reveals that the pit does not show a consistent pit depth increase over time until 70 hours of immersing time. However, tests at 96, 120 and 150 hours show a linear increase of pitting depth over time. Both phosphate ester and imidazoline inhibitors showed excellent performance to stop pit propagation if optimum concentrations are applied. However, imidazoline shows a better performance in reducing the general corrosion rate compared to phosphate ester.

Chapter 8: Evaluation of inhibitor performance using artificial pit technique under sweet conditions

In the previous chapter, results from the characterisation of the corrosion film under sweet and sour conditions, natural pitting growth and inhibition effects on natural pitting were presented. In order to accelerate the inhibition test method and further understand the pitting interaction between the inhibitors and corrosion films, an *in-situ* monitoring technique was developed and artificial pits were introduced to the studies. This chapter uses the pitting inhibition test procedure from Chapter 7 as a reference and develops an accelerated inhibition test procedure with *in-situ* monitoring technique and artificial pits in sweet conditions. The artificial pit growth on X65 carbon steel surfaces in sweet conditions was assessed using an *in-situ* monitoring technique. Phosphate ester and imidazoline inhibitors were used. The inhibitors were evaluated in terms of artificial pit propagation and using DC linear polarisation resistance (LPR) test methodologies. Assessment of the pits by FTIR analysis was used to characterise the chemical constituents of the surface and profilometer analysis was used to determine the pit depths.

8.1 Corrosion current measurement

Electrochemical corrosion measurements using DC linear polarisation resistance tests were carried out to monitor the corrosion rate after every step until a protective film was obtained in the first 3.5 hours. The corrosion rates after 1 hour immersed in the solution were 2.5 mm/yr. After 1.5 hours, the pH was adjusted to 5.65 by adding sodium bicarbonate ($NaHCO_3$), which decreased the corrosion rate significantly to 1.75, as shown in Figure 8-1. After 3 hours, 1000ppm of iron chloride ($FeCl_2$) was added, which dropped the corrosion rate to 1.25 mm/yr. After 4 hours, electrochemical corrosion measurements using a potentiostatic test were carried out. The potentiostatic test procedure was developed, which was primarily inspired and previously published by Neville et al., involving scanning stainless steel to 100mV more positive then SCE and holding it constant for a period of time to observe the localised effects [58]. During the test development stage, the constant electrode potential applied was varied to obtain pits of the required depth. A constant electrode potential at 100mV more positive than the free corrosion potential was chosen in this test to activate the artificial pit on the surface to a desired pit depth.

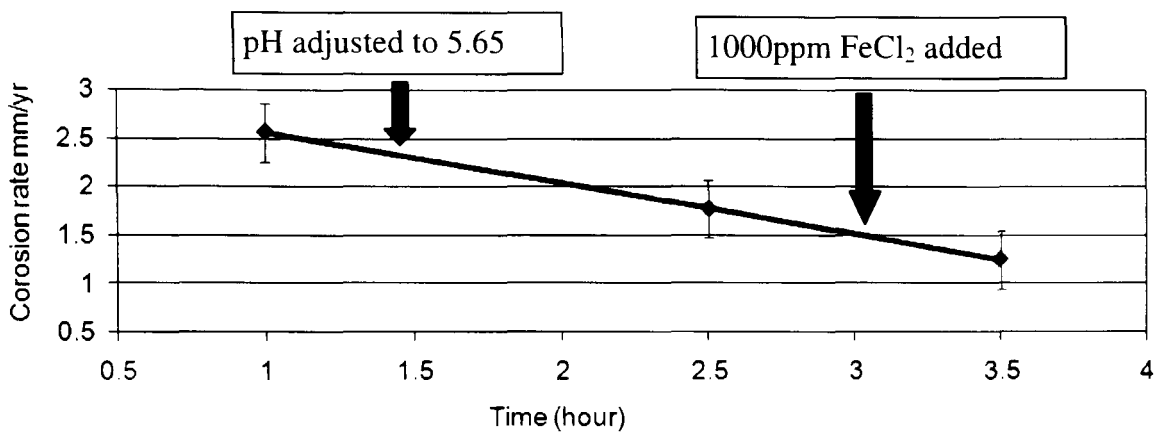

Figure 8-1: Corrosion rate versus time for the first 3.5 hours for the step change process on X65 carbon steel in CO_2 saturated, 10% NaCl brine at 80°C, pH 5.65 and 1000ppm Fe^{2+}

Figure 8-2 presents the potentiostatic results for three experiments without inhibitor. It shows that, initially, the current decreased in the first 100s and is maintained in the range between 4mA to 7mA for the next 35000s (9.5 hours) for all 3 runs. After that, Run 2 shows that the current keeps constant until the end of the 24-hour test but Run 1 shows that the current increased to 8mA and finished at 7mA. However, Run 3 shows that the current decreased to 2mA and finished at 3mA. The results showed significant current variation between the 3 runs after 9.5 hours, which could be due to the long time exposure, and indicated the formation of a layer of cementite on the surface mixed with a film of iron carbonate and the growth and propagation of pits on the surface [91, 192, 193].

The current represents the general dissolution behaviour of the surface, which is influenced by the film breakdown process of the corrosion film. Mok et al. observed that potential fluctuation in a long-term test indicates the pit propagation process characteristic [193]. Iimura et al. also observed that the change in current could be attributed to the change of surface condition of the pit and/or the change of property of the formed corrosion products covering the pit [194]. This is also supported by Cheng et al. who observed that the current fluctuation was caused by the pit growth kinetics, which are associated with a new deposited cover over the mouth of the pit [195]. Depending on the test conditions, the deposit present on the pit could contain flaws or defects from ionic current passed between the pit anolyte and the bulk solution [195]. Referring to Figure 7.1 the corrosion rate observed in this condition is around 0.75 mm/yr with the formation of a layer of cementite on the

surface mixed with iron carbonate film to offer a semi-protective film. The current behaviour in this test shows a similar fluctuation characteristic with the linear polarization behaviour for the 150 hours blank test in Chapter 7 and shows a good correlation in simulating the test conditions in a shorter time.

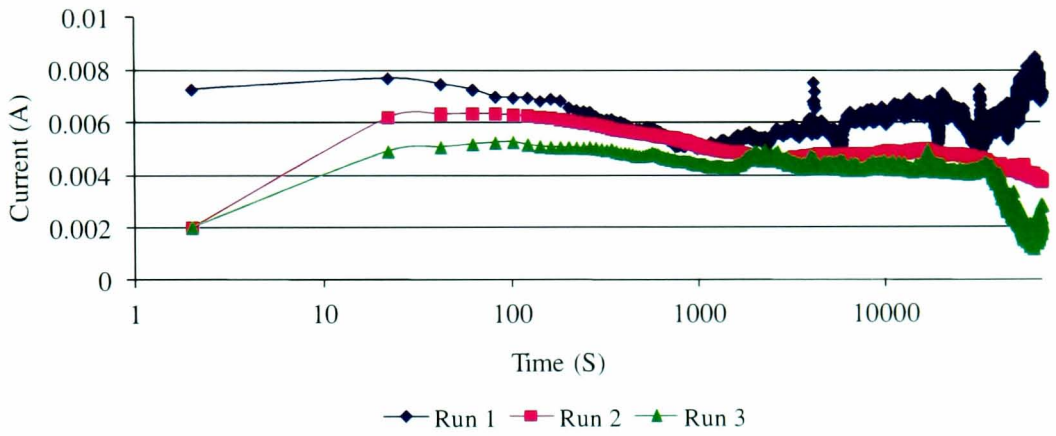

Figure 8-2: Potentiostatic polarisation curve at 4 hours to 24 hours on X65 carbon steel in CO_2 saturated 10% NaCl brine at 80°C, pH 5.65 and 1000ppm Fe^{2+} without inhibitor

8.1.1 Effect of phosphate ester

The performance of phosphate ester inhibitor was studied by adding different concentrations after 3.5 hours. Figure 8-3 presents the results of the potentiostatic tests with different concentrations of phosphate ester. The presence of inhibitors does not significantly decrease the current but causes current oscillations postulated to be due to the reaction of the inhibitor on the surface. It shows that the lowest concentration of inhibitor results in higher currents up to 8mA. However when the inhibitor concentration increases, it does not show much effect on the overall trend compared to the tests without inhibitor.

Figure 8-4 presents the final current effects on inhibitor concentrations. It shows that the final current at 25ppm inhibitors is higher than the test without inhibitor, however, when the inhibitor concentration increases to 50ppm, the final current is lower than the test without inhibitor. It is interesting to observe that at 100ppm and 200ppm, there is no significant change in the final current. Alink et al. observed that phosphate ester type inhibitors form fairly insoluble Fe^{2+} complexes and

are closely related to minimum effective concentration [106]. This shows that phosphate ester inhibitor does not affect the current after it reaches the minimum effect concentration, which under the conditions studied is 100ppm.

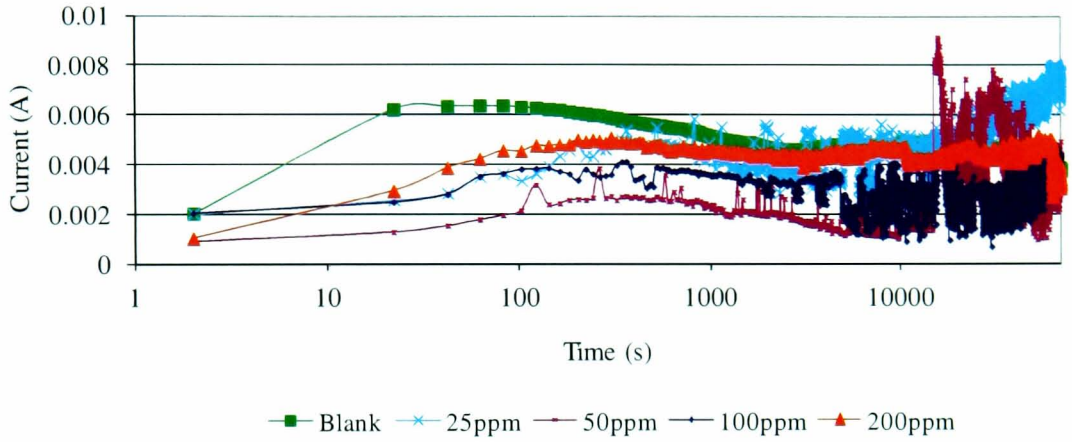

Figure 8-3: Potentiostatic polarisation curve for 24-hour test on X65 carbon steel in CO_2 saturated 10% NaCl brine at 80°C, pH 5.65, 1000ppm Fe^{2+} and 1 bar total pressure with different concentrations of phosphate ester

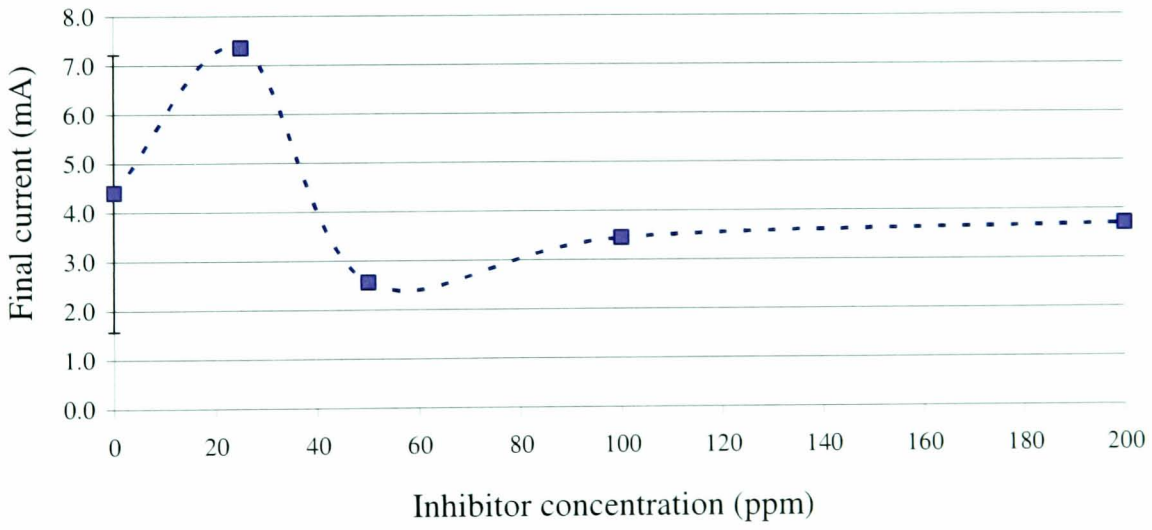

Figure 8-4: Final potentiostatic current after 24-hour test on X65 carbon steel in CO_2 saturated 10% NaCl brine at 80°C, pH 5.65, 1000ppm Fe^{2+} and 1 bar total pressure with different concentrations of phosphate ester

8.1.2 Effect of imidazoline

The performance of the imidazoline inhibitor was also studied. Figure 8-5 presents results of the potentiostatic tests when different concentrations of imidazoline were added to the solution after 3.5 hours. The presence of inhibitors significantly decreases the current. It shows that at 25ppm the current was 3mA; as the inhibitor concentration increased to 200ppm it reduced the current down to less then 0.1mA. Figure 8-6 presents the final current effects on inhibitor concentrations.

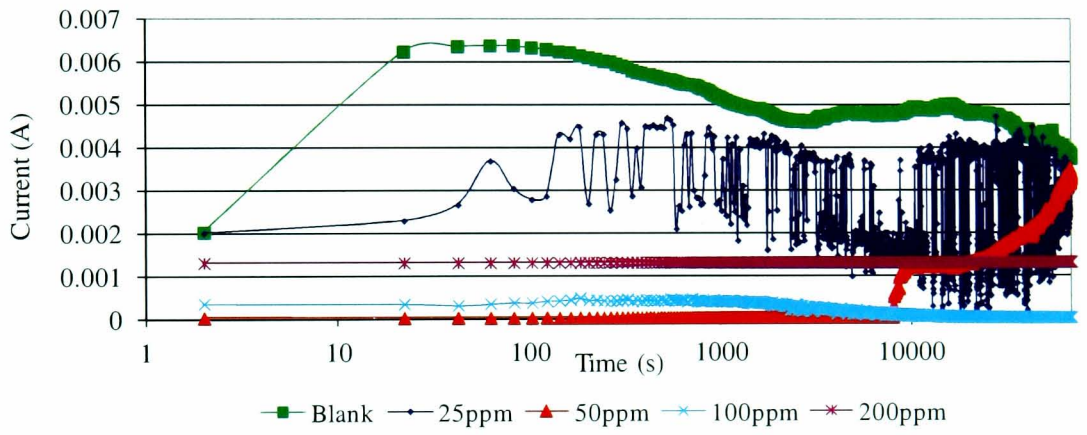

Figure 8-5: Potentiostatic polarisation curve for 24-hour test on X65 carbon steel in CO_2 saturated 10% NaCl brine at 80°C, pH 5.65, 1000ppm Fe^{2+} and 1 bar total pressure with different concentrations of imidazoline

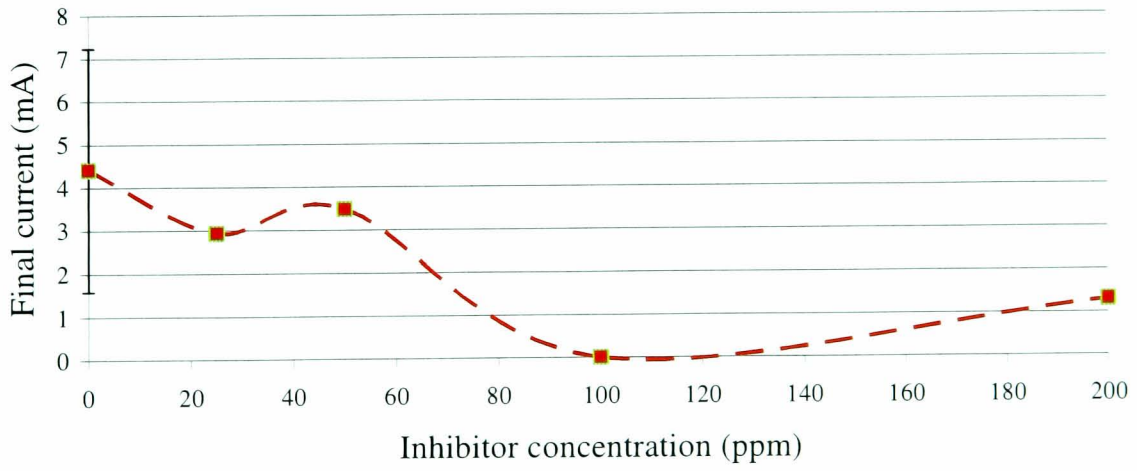

Figure 8-6: Final potentiostatic current after 24-hour test on X65 carbon steel in CO_2 saturated 10% NaCl brine at 80°C, pH 5.65, 1000ppm Fe^{2+} and 1 bar total pressure with different concentrations of imidazoline

It shows that the final current for all concentrations is lower than the test without inhibitor. This shows that imidazoline provides better protection to reduce the current, which might be because the inhibitor protects the overall surface by providing a barrier film [104].

8.2 *In-situ* camera monitoring techniques.

Surface images were recorded using a LABVIEW program. The program displays the real time image and records the image every 20 seconds. Figure 8-7 shows an early stage image after the specimen was immersed into the solution. It clearly shows that the film formation took place over the initial grinding lines on the metal surface. This indicates that a vast amount of corrosion occurred on the surface eradicating these marks on the surface in the first 20 minutes of the process. After that the surface darkens due to the uniform formation of a film building up on the surface. Areas of the surface continued to darken and the thicker film affects the ability to focus the camera.

Figure 8-8 shows an image after increasing the light supply and refocusing the surface. It shows that the film grows on the film and covers most of the surface with some uncorroded areas still existing after 1 hour. After 1.5 hours, the pH was adjusted to 5.65 by adding sodium bicarbonate ($NaHCO_3$) and the film continued to generate uniformly to cover the overall surface, which caused a reduction in the corrosion rate. After 3 hours, 1000ppm of iron chloride ($FeCl_2$) was added to achieve a high concentration of Fe^{2+}, which generated a small black deposit on the surface. After 3.5 hours, the dissolved iron chloride formed a protective iron carbonate film on top of the previous film and the film became richer and significantly decreased the corrosion rate up to 24 hours. No significant growth in pit diameter was observed during the test due to the geometry of the artificial pits, which have a large diameter pit mouth compared to depth. It is likely that the corrosion product constitutes the edge of the pit mouth covering the cementite layer left behind and the pit propagated beneath the original corrosion film on top of the edge of the pit mouth [47, 194, 195]. This is supported by Iimura et al., who observed that pits were covered with corrosion product and the pH within the pit dropped to 3.3 from 8.9 [194]. Nyborg shows that based on video observation, the mesa corrosion attack grew beneath the original

corrosion film on top of the specimen's surface leaving only a thin lid of original corrosion film behind [47].

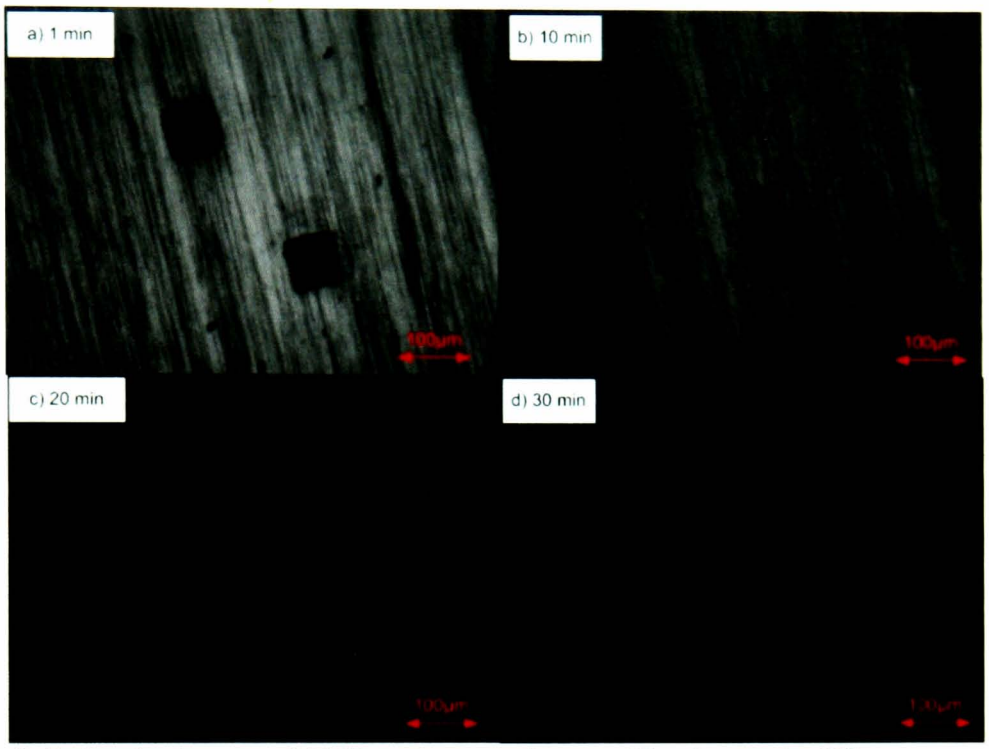

Figure 8-7: *In-situ* image of X65 carbon steel up to 30 minutes in CO_2 saturated 10% NaCl brine at 80°C without inhibitor; a) 1 min, b) 10 min, c) 20 min, d) 30 min.

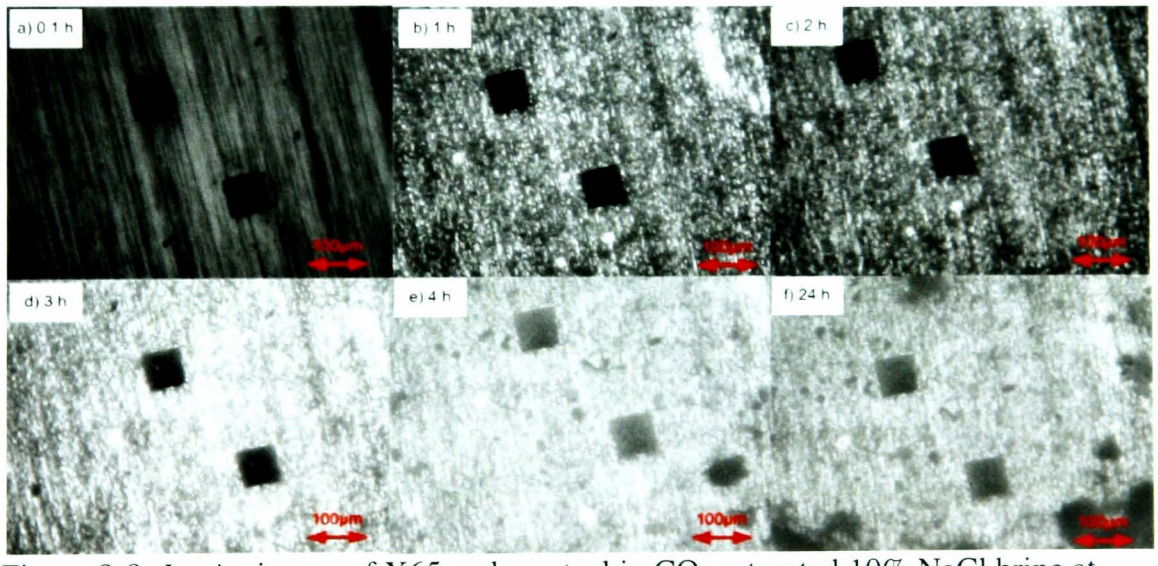

Figure 8-8: *In-situ* image of X65 carbon steel in CO_2 saturated 10% NaCl brine at 80°C, pH 5.65, 1000ppm Fe^{2+} and 1 bar total pressure without inhibitor; a) 0.1 h, b) 1 h, c) 2 h, d) 3 h, e) 4 h, f) 5 h.

8.2.1 Effect of phosphate ester

The *in-situ* camera was able to monitor the film growth and the physical interaction of the inhibitor with the film at the pit site. Figure 8-9 shows the effect of phosphate ester when it is present at different concentrations on the surface. At lower inhibitor concentrations, it is seen that it promotes the formation of black deposits on the surface. After 24 hours, the specimen with 25ppm inhibitor was fully covered by the black deposit, which creates a favourable condition for the pitting process. However, after the inhibitor concentrations were increased to 50ppm, the formation of the black deposit was reduced by a significant amount. At 100ppm of inhibitor, the black deposit was seen to be at a minimum level compared to the other specimens.

The black deposit is postulated to be a product from the reaction of the phosphate ester and iron ions if the stochiometric ratio of the reaction is not at the effective concentration. Alik et al. observed that at a stochiometric ratio of Fe^{2+} to phosphate ester, the product will provide effective protection [106]. The phosphate ester inhibitor has a limited solubility in brine and this affects the stabilising phosphate ester to complexes iron ion in the solution [106]. At 200ppm, it seems that the black deposit starts to reform on the surface due to exceeding the optimum value that is needed to protect the pit.

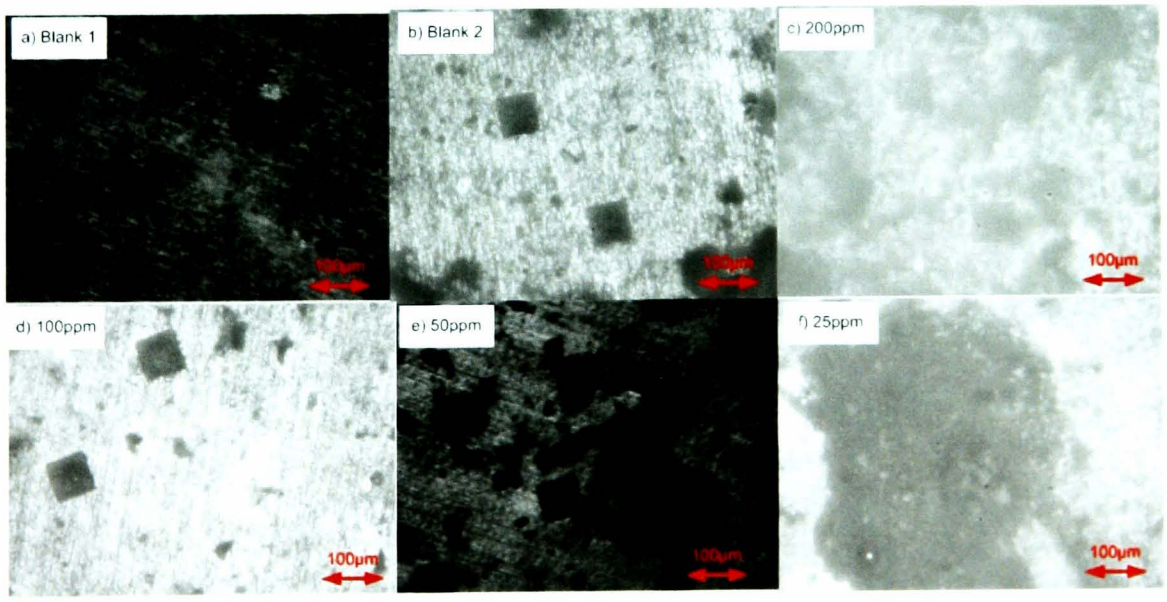

Figure 8-9: *In-situ* image of X65 carbon steel in CO_2 saturated 10% NaCl brine at 80°C, pH 5.65, 1000ppm Fe^{2+} and 1 bar total pressure with phosphate ester; a) Blank 1, b) Blank 2, c) 200ppm, d) 100ppm, e) 50ppm, f) 25ppm.

8.2.2 Effect of imidazoline

Figure 8-10 shows the effect of imidazoline when it is present at different concentrations on the surface. The interaction between the imidazoline and iron ion creates a thicker film spread across the surface. At lower 200ppm inhibitor concentrations, it is seen that it promotes the formation of a black deposit on the surface and enhances the favourable pitting condition. However, after the inhibitor concentrations were decreased to 100ppm, 50ppm and 25ppm, the formation of the black deposit is significantly reduced. At 100ppm of inhibitor, the black deposit is seen to be at the minimum level compared to other specimens. Imidazoline has a good solubility in brine resulting in the formation of an adsorbed surfactant monolayer or bilayer on the surface of the metal [98,104]. The black deposit is postulated to be a mixture product between the inhibitor film and the corrosion product film.

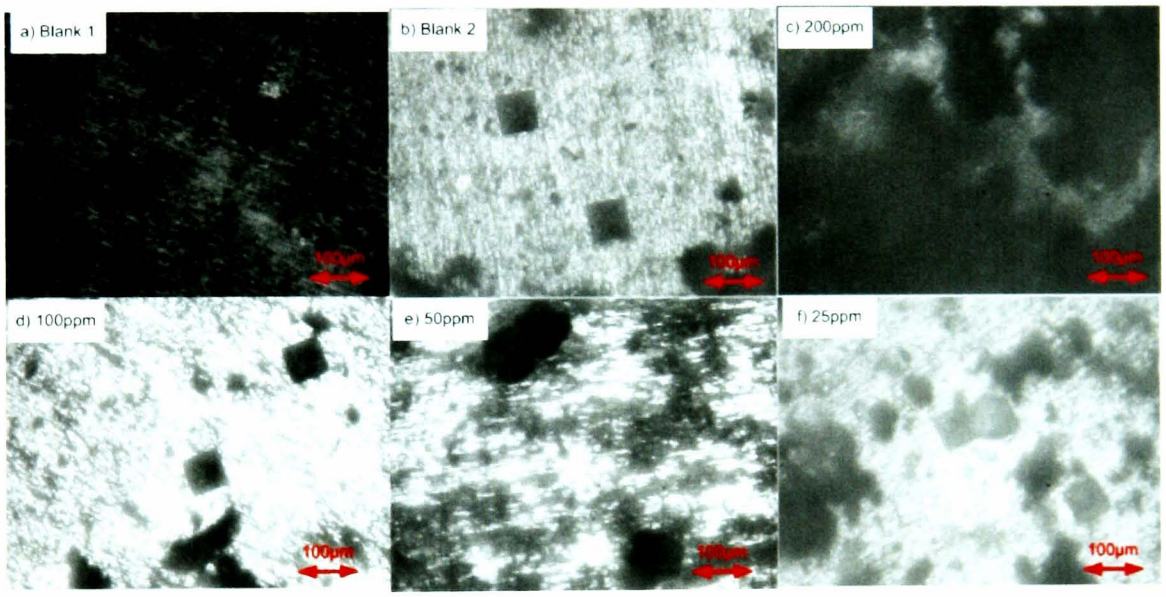

Figure 8-10: *In-situ* image of X65 carbon steel in CO_2 saturated 10% NaCl brine at 80°C, pH 5.65, 1000ppm Fe^{2+} and 1 bar total pressure with imidazoline; a) Blank 1, b) Blank 2, c) 200ppm, d) 100ppm, e) 50ppm, f) 25ppm.

8.3 Pit depth analysis

The analyses were conducted using contact surface profilometry Talysurf-120 and non-contact white light interferometer WYCO NT3300S. The artificial pits generated by a microhardness indenter to make the pit 9µm deep. The blank test was carried out to assess the severity of the test condition and to enable evaluation of the performance of the inhibitor. Figure 8-11 shows the comparison in pit depth results

between the artificial pit (AP) and natural pit (NP) on the surface of all three runs of the blank test.

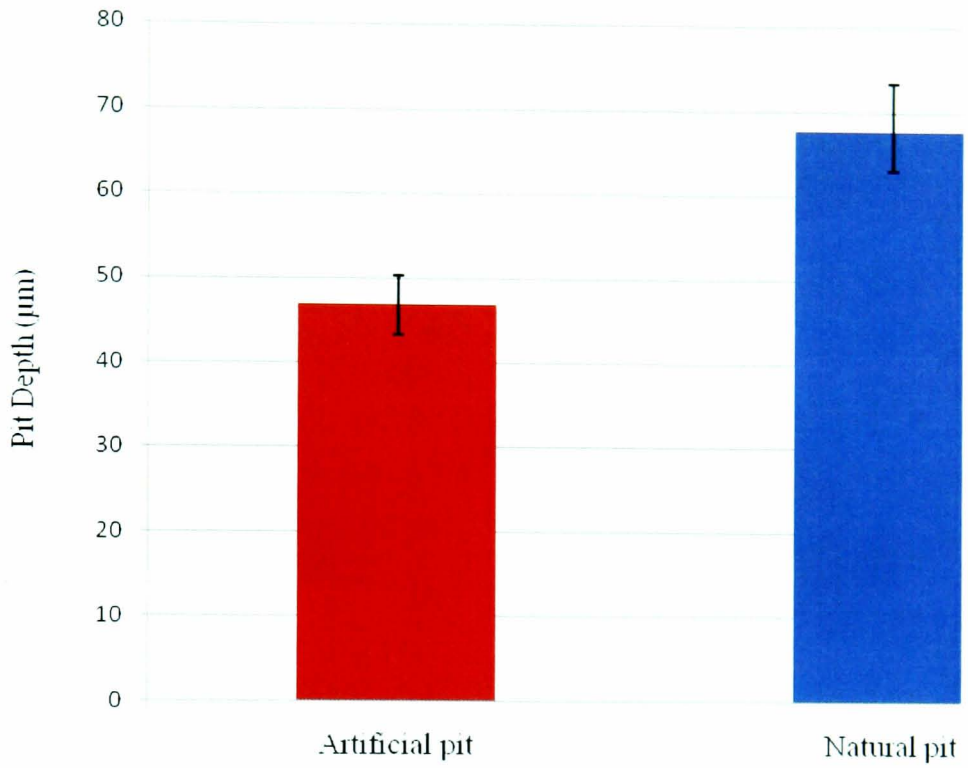

Figure 8-11: Average of maximum pit depth of X65 carbon steel in CO_2 saturated 10% NaCl brine at 80°C, pH 5.65, 1000ppm Fe^{2+} and 1 bar total pressure without inhibitor

After the blank test was conducted for 24 hours the pit growth scattered all over the surface, as shown in Figure 8-12 (a-f); the depth varied from micro pits to the deepest pit at 103µm. The artificial pits on the surface propagated to around 48.9µm to 53.1µm deep, as shown in the 3D profilometer image in Figure 8-12c and Figure 8-12f. The artificial pit propagated both laterally and in the depth direction. It is very interesting to compare the artificial pit image in Figure 8-12c and Figure 8-12f, and the *in-situ* image of artificial pits in Figure 8.8f, which proves that the pit propagated laterally but beneath the original corrosion film on top of the edge of the pit mouth. This is supported by Nyborg, who showed that the video observation revealed that the original corrosion film covering the mesa attack beneath the film could be broken off by the mechanical forces caused by turbulent flow [47].

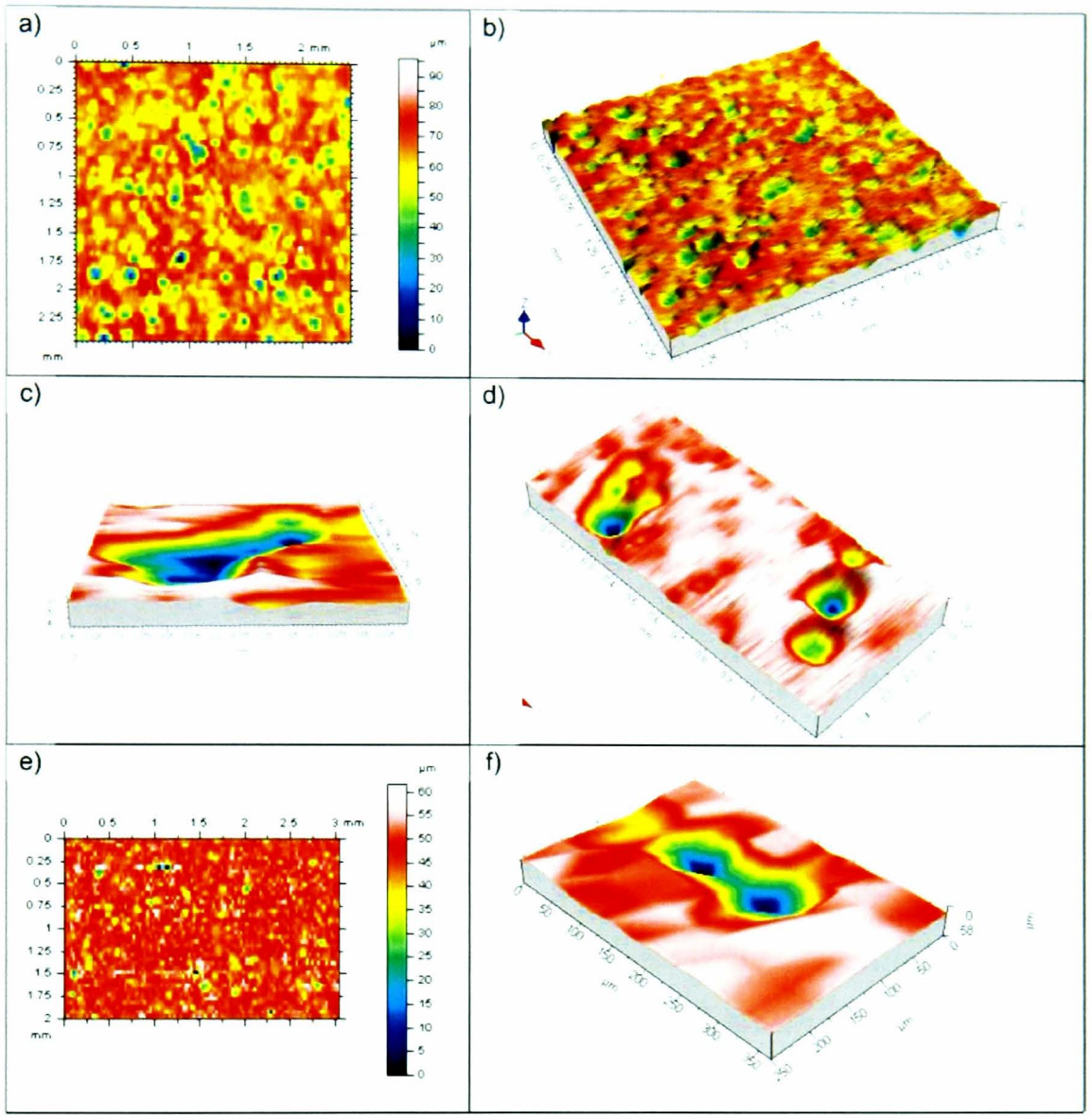

Figure 8-12: Artificial Pit Depth of X65 carbon steel in CO_2 saturated 10% NaCl brine at 80°C, pH 5.65, 1000ppm Fe^{2+} and 1 bar total pressure after test without inhibitors; a) 2D view of pits surface, b) 3D view of pits surface, c) 3D View of artificial pits surface, d) 3D view of natural pits surface, e) 2D view of pits surface, f) 3D view of artificial pits surface.

While the potential applied also initiated and propagated other natural pitting on the surrounding surface. The natural pits on the surface propagated to around an average depth of 70µm, however, in some blank specimens the natural pit propagated to 103µm as shows in Figure 8-12d. The nature of the pitting process caused the natural pit depth to vary tremendously.

8.3.1 Effect of phosphate ester

Phosphate ester was introduced to the experiment, which can control the pitting propagation if the required concentration is applied. Figure 8-13 shows the comparison in pit depth results for the artificial and natural pits on the surface with different concentrations of phosphate ester. At 200ppm of phosphate ester it slowed the pitting propagation process down to 23.5μm, as shown in Figure 8-14(a-d).

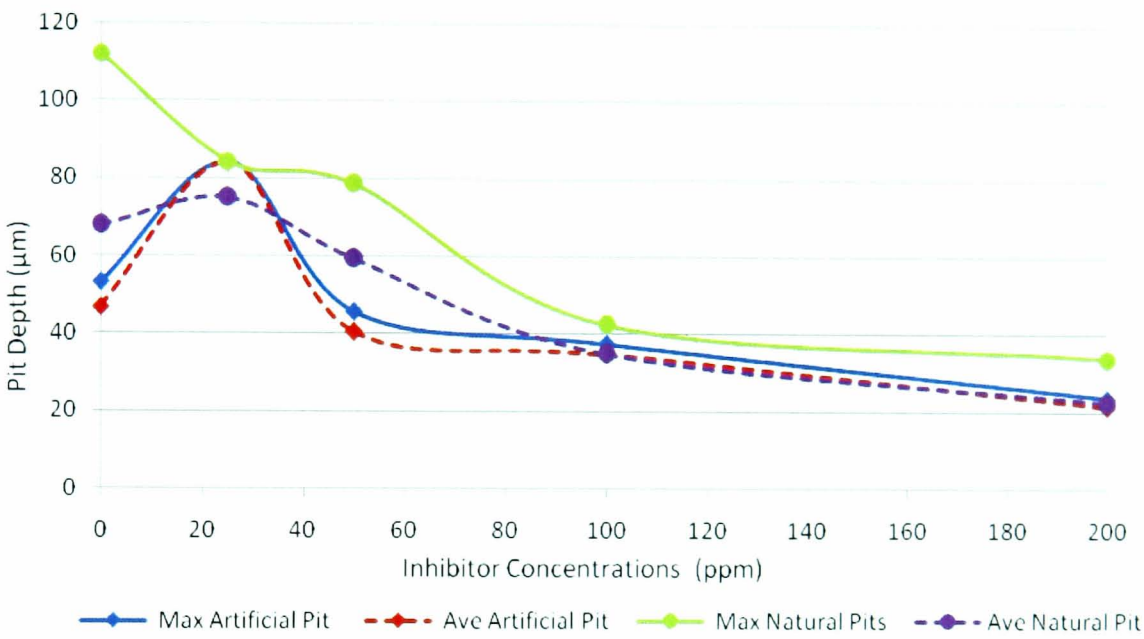

Figure 8-13: Pit Depth of X65 carbon steel in CO_2 saturated 10% NaCl brine at 80°C, pH 5.65, 1000ppm Fe^{2+} and 1 bar total pressure with phosphate ester.

However, with 25ppm of phosphate ester, the artificial pit propagated to 83.7μm, which is significantly higher than the blank test as shown in Figure 8-14f. This is postulated to be because of the reduced adsorption of the inhibitor molecules within the pit sides resulting in the reduction of inhibitor performance and consequential increase in the propagation activities [7, 133].

Consequently, after the phosphate ester concentration increased to 50ppm and 100ppm, the artificial pit depths were reduced to 45.6 μm and 37.4 μm. It is interesting to compare the pit depth of the artificial pit and natural pit on the surface, as they are in good agreement in terms of the reaction towards the action of the inhibitor.

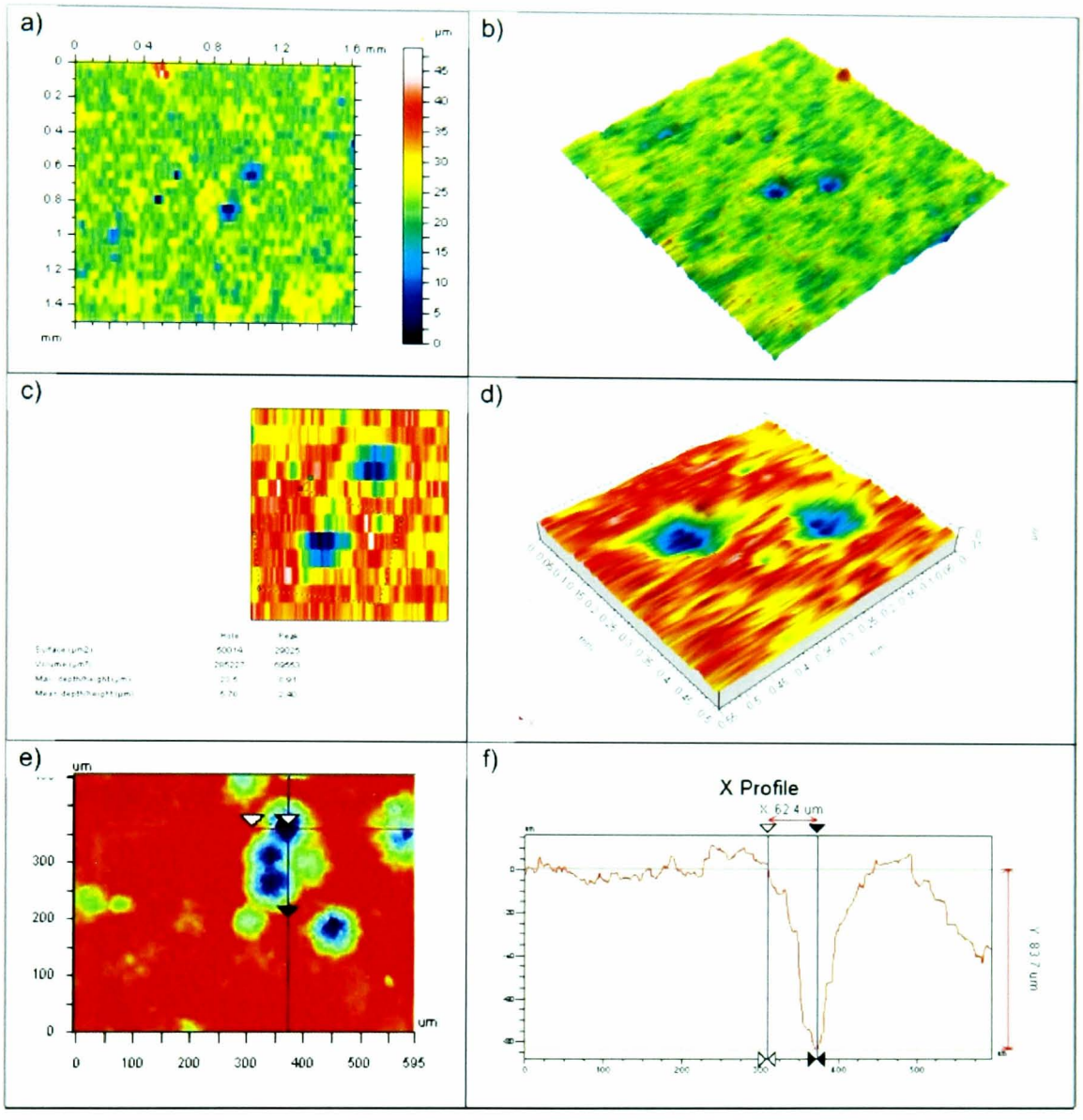

Figure 8-14: Profilometer image of artificial pit on X65 carbon steel in CO_2 saturated 10% NaCl brine at 80°C, pH 5.65, 1000ppm Fe^{2+} and 1 bar total pressure with phosphate ester inhibitors; a) 2D view of pits surface at 200ppm, b) 3D view of pits surface at 200ppm, c) 2D view of artificial pits surface at 200ppm, d) 2D view of artificial pits surface at 200ppm, e) 2D view of pits surface at 25ppm, f) 2D cross-section of artificial pits at 25ppm.

8.3.2 Effect of imidazoline

Imidazoline slows down the pitting propagation at lower concentrations and the inhibitor performance will decrease if an overdose of inhibitor is applied. Figure 8-15 shows the comparison in pit depth results for the artificial and natural pits on the surface with different concentrations of imidazoline. The pit depth slows down to 23.8μm with 25ppm of imidazoline and as the inhibitor increased to 50ppm, the performance increased by decreasing the pit depth to 21.1μm. Imidazoline performed at the optimum level at 100ppm by completely controlling the pitting attack with a pit depth recorded at 11.5μm, as shown in Figure 8-16(a-d). However, with 200ppm imidazoline, the artificial pit propagated to 68.7μm as shown in Figure 8-16f, which is significantly higher that the blank test. It is postulated that this is due to an overdose effect. The interaction was due to the excessive inhibitor molecules enhancing the chemistry within the pit site resulting in the reduction of inhibitor performance and consequential increase in the propagation activities [7, 133]. The artificial and natural pits on the surface show that the pit depth trend is similar. These similar trends indicate that the pitting activities and the reaction with the inhibitor are comparable between the artificial pits and natural pits.

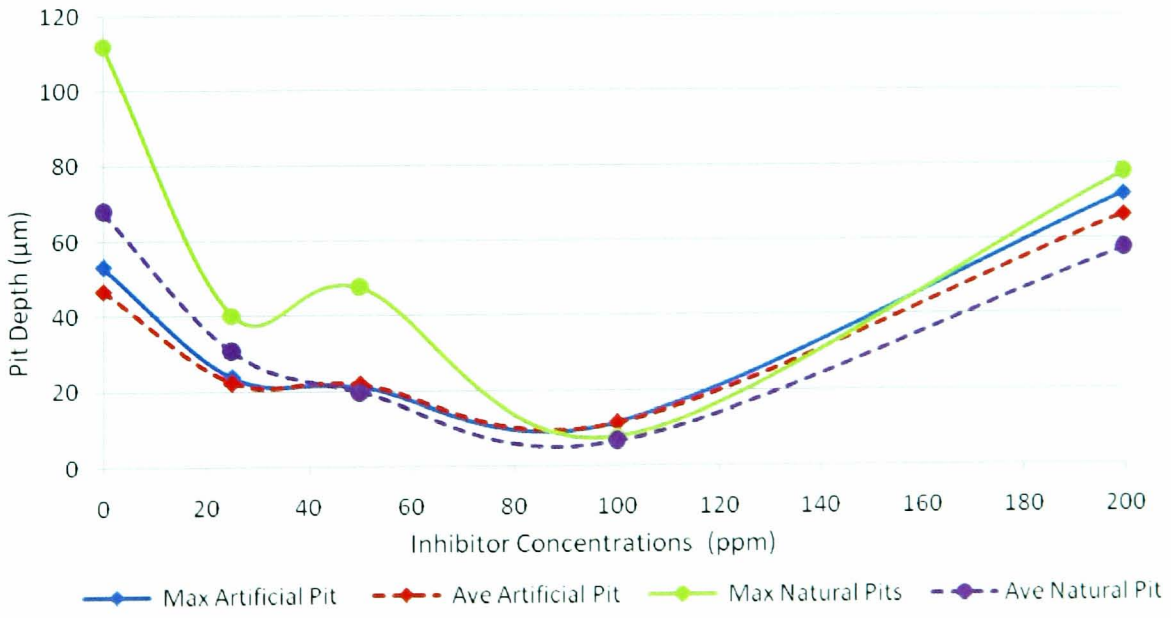

Figure 8-15: Artificial Pit Depth of X65 carbon steel in CO_2 saturated 10% NaCl brine at 80°C, pH 5.65, 1000ppm Fe^{2+} and 1 bar total pressure with imidazoline.

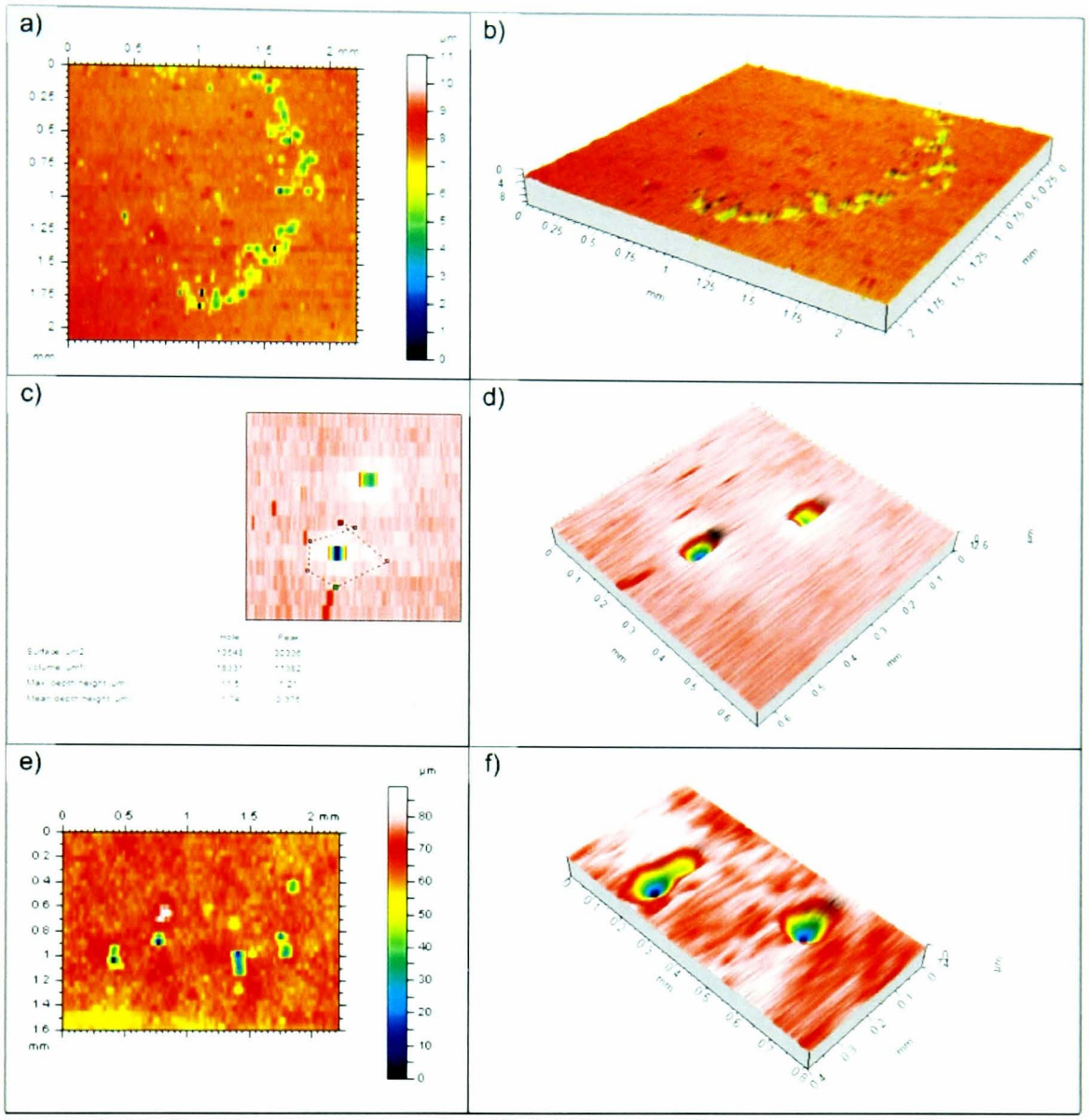

Figure 8-16: Profilometer image of artificial Pit on X65 carbon steel in CO_2 saturated 10% NaCl brine at 80°C, pH 5.65, 1000ppm Fe^{2+} and 1 bar total pressure with imidazoline inhibitor; a) 2D view of pits surface at 100ppm, b) 3D view of pits surface at 100ppm, c) 2D view of artificial pits surface at 100ppm, d) 3D view of artificial pits surface at 100ppm, e) 2D view of pits surface at 200ppm, f) 3D cross-section of artificial pits at 200ppm.

The natural pits propagate severely to 76µm on the surface with 200ppm imidazoline, the natural pit delayed propagation down to 7.8µm with 100ppm imidazoline.

8.4 Fourier transform infrared (FTIR) spectroscopy

IR reflectance spectra in the region 600 to 4000 cm^{-1} were collected with Perkin Elmer model spotlight 400. The objective of the test is to understand the mechanisms of the inhibitor interaction with the surface in the pit region and outside the pitting region. A background reflectance of a gold electrode was performed as a reference before measurements were made on all test specimens. A complete summary of the spectra assignments is shown in Table 8-1.

Wavenumber (cm^{-1})	**Peak assignment**	**References**
Corrosion products		
1638.4	(R-S-)$_2$C=O stretching of $FeCO_3$	[162, 164, 167, 184]
874.62	(R-S-)$_2$C=O stretching of $FeCO_3$	167
Inhibitor A		
Component 1		
2956.91	O-CH_3 ester group from methanol/CH_3 alkanes	[159, 161, 182]
2928.27	O-CH_3 ester group from methanol/CH_2 alkanes	[159, 161, 182]
2874.20	O-CH_3 ester group from methanol/CH_3 alkanes	[159, 161, 182]
Component 2		
1145.86	(CH_3-O)$_3$P trimethylphosphite CH_3 group / alkyl ethers	[182, 183]
1120.00	(CH_3)$_2$P(O)$_2$Na dialkylphosphinate salts	[183]
Inhibitor B		
Components 1		
3350	Aromatic amide (bonded NH)	[159, 182, 184]
Component 2		
3030	CH=CH alkenes / acid amino	[159, 182]
2855	CH_2 alkanes	[159, 182]
Component 3		
1675	Amide and imide/nitrites	[159, 182]
1423	Fatty acid amine/CH_2/phenols	[159, 182]

Table 8-1: FTIR spectra assignments for sweet condition

Figure 8-17 shows the spectrum obtained from the blank test after the test and after the film was removed by Clarke's solution. It can been seen that there were two peaks on the film and on the artificial pit, which were identified at 1638.4 cm^{-1} and 874.62 cm^{-1} and are attributed to $(R\text{-}S\text{-})_2C{=}O$ stretching, which corresponds to iron Carbonate [164,183]. These peaks were present on the film after the test but were absent after being remove by Clarke's solution.

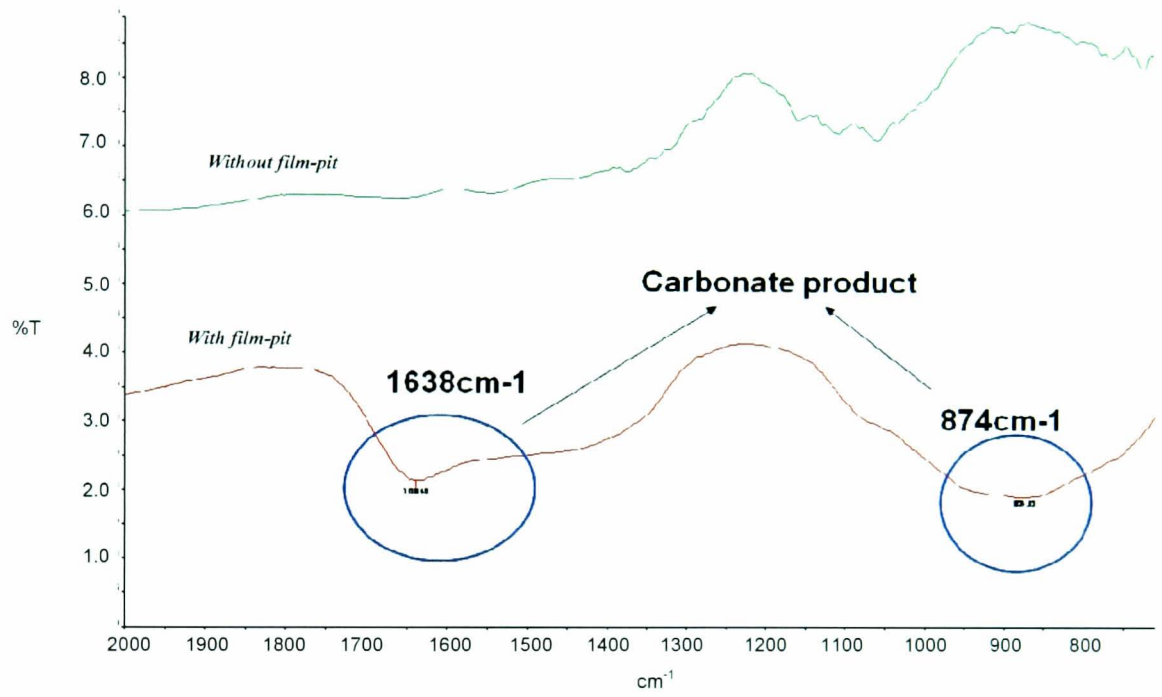

Figure 8-17: FTIR analysis of X65 carbon steel in CO_2 saturated 10% NaCl brine at 80°C, pH 5.65, 1000ppm Fe^{2+} and 1 bar total pressure after blank test

8.4.1 Effect of phosphate ester

Figure 8-18 shows the spectrum of the neat phosphate ester and the spectrum obtained from the specimen diluted phosphate ester at 100ppm concentration in distilled water. It can be seen that there were two distinctively strong peaks on the neat phosphate ester spectrum. Those peaks were at around 2956.91 cm^{-1} to 2874.20 cm^{-1}, which corresponds to $O\text{-}CH_3$ from the ester and CH_3 from the methanol, at around 1145.86 cm^{-1} to 1120.00 cm^{-1}, which corresponds to $(CH_3\text{-}O)_3$ Ptrimethyl phosphate CH_3 group and $(CH_3)_2P(O)_2Na$ dialkylphosphinate salts [161, 183]. The spectra for 25ppm, 50ppm, 100ppm and 200ppm specimens were taken on the surrounding film and on the artificial pits and the summary results are shown in Table 8-2.

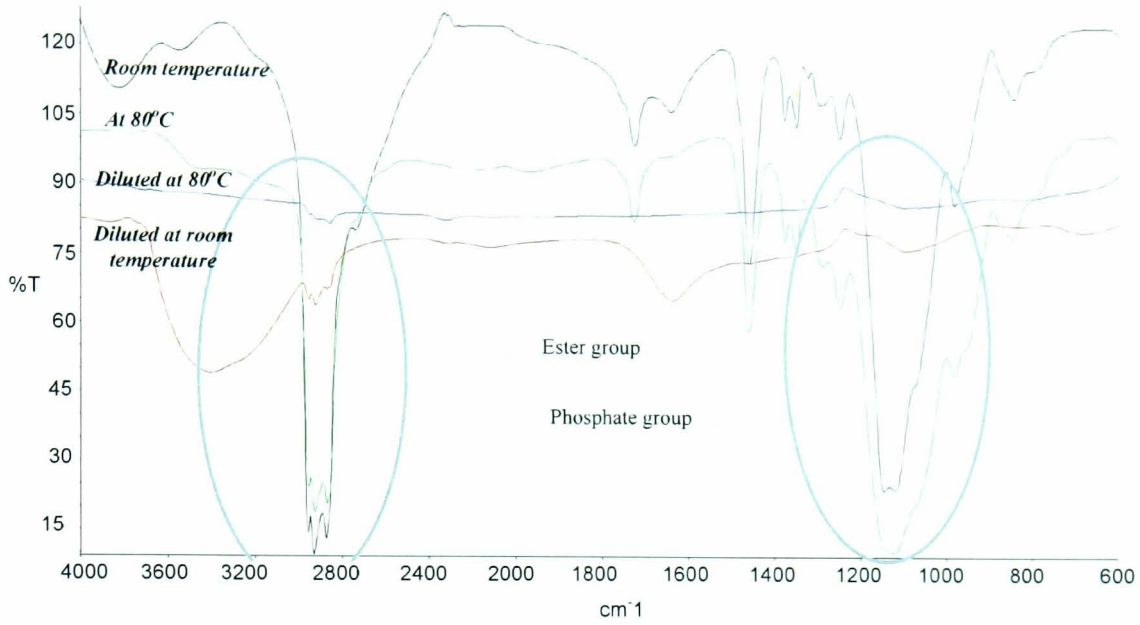

Figure 8-18: FTIR analysis of phosphate ester inhibitor in different conditions.

Condition	Component 1		Component 2	
	Pit	Film	Pit	Film
25 ppm	No	No	No	No
50 ppm	No	No	No	No
100 ppm	Yes	No	Yes	No
200 ppm	Yes	No	Yes	No

Table 8-2: Summary FTIR results for phosphate ester inhibitor at different concentrations after the test.

It can be seen that there were several phosphate ester matching peaks on the artificial pit site but phosphate ester was absent on the surrounding film area, as shown in Figure 8-19 and Figure 8-20. There were fairly strong peaks at around 2956.91 cm^{-1} to 2874.20 cm^{-1}, which corresponds to the ester group and also a weak peak at around 1145.86 cm^{-1} to 1120.00 cm^{-1}, which corresponds to the phosphate group [182, 183].

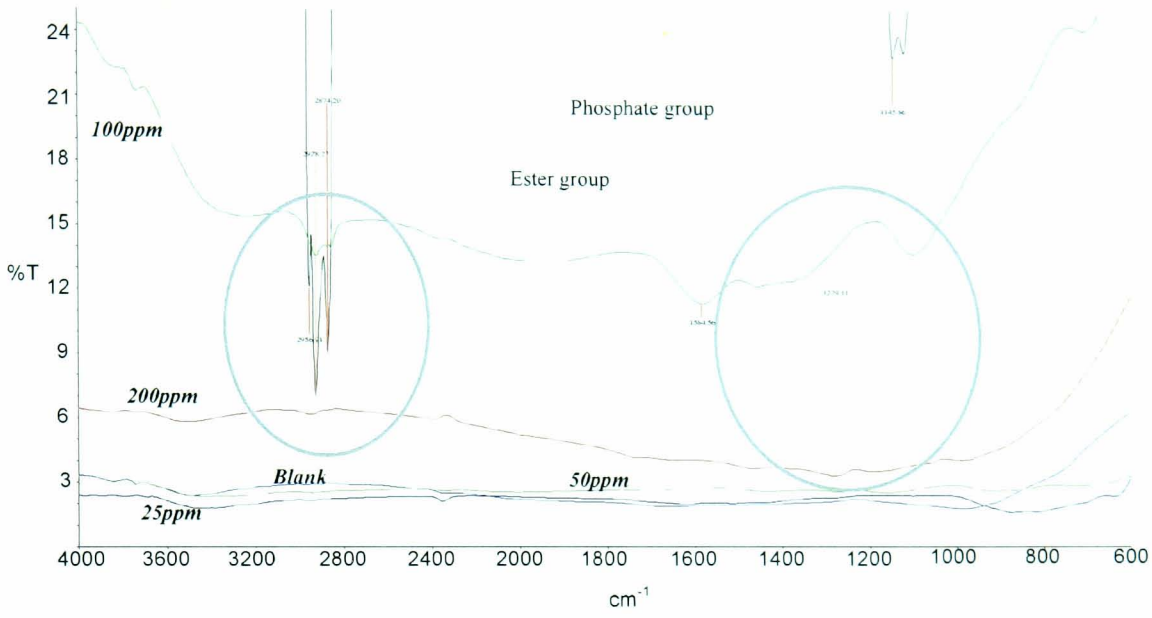

Figure 8-19: FTIR analysis on the pit site area of X65 carbon steel in CO_2 saturated 10% NaCl brine at 80°C, pH 5.65, 1000ppm Fe^{2+} and 1 bar total pressure with phosphate ester in different concentrations.

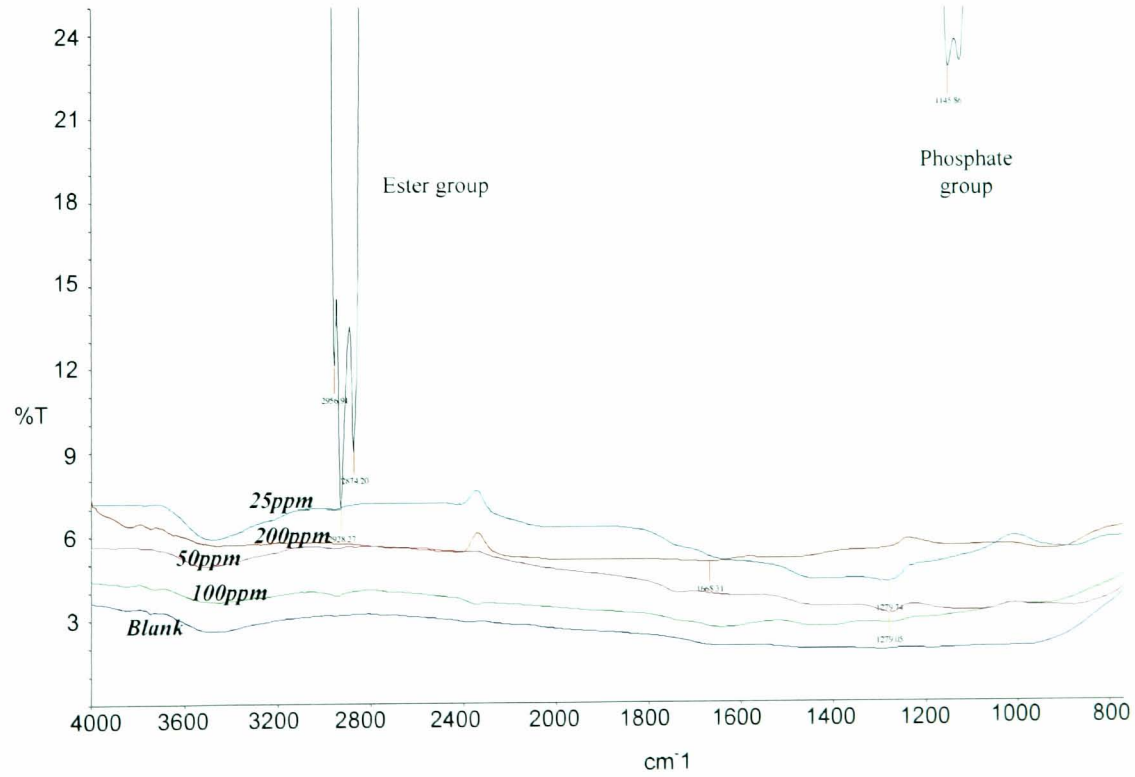

Figure 8-20: FTIR analysis on the film area of X65 carbon steel in CO_2 saturated 10% NaCl brine at 80°C, pH 5.65, 1000ppm Fe^{2+} and 1 bar total pressure with phosphate ester in different concentrations.

This shows that the inhibitor was attracted towards the pits rather than to the surrounding film area. However, at lower phosphate ester concentrations of 50ppm and 25ppm, phosphate ester was absent on the pits site and the surrounding area. Phosphate esters were absent due to the low concentration effect cause and did not inhibit at the pit site area.

8.4.2 Effect of imidazoline

Figure 8-21 shows the spectrum of the neat imidazoline and the spectrum obtained from 100ppm imidazoline diluted in distilled water.

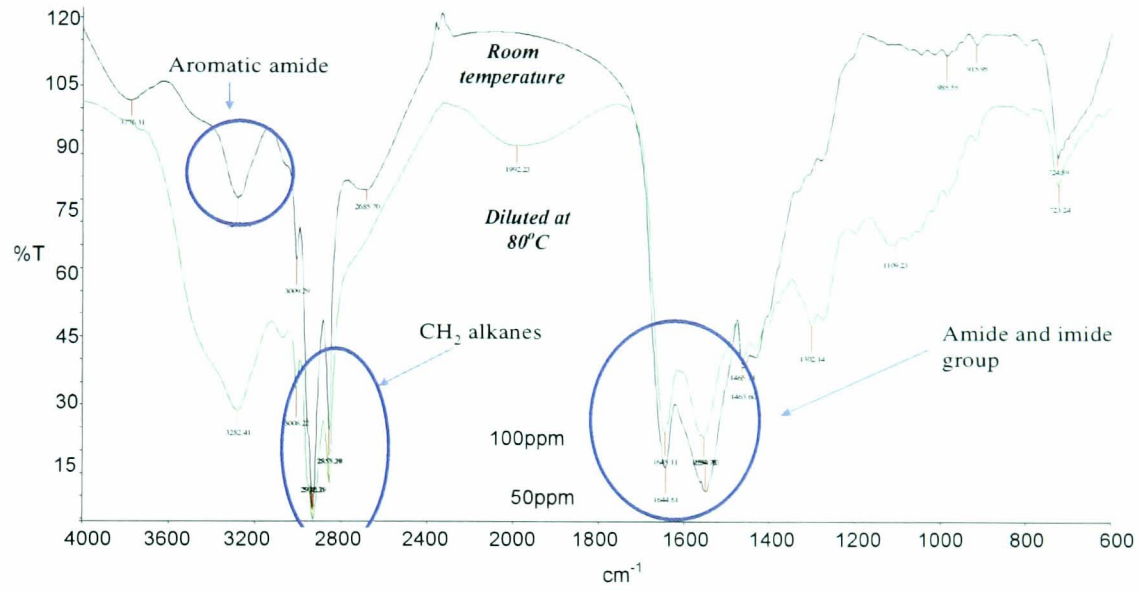

Figure 8-21: FTIR analysis of imidazoline inhibitor in difference conditions.

It can be seen that there were three distinctively strong peaks on the neat imidazoline spectrum. There were fairly strong peaks at around 3285 cm^{-1} to 3350 cm^{-1}, which corresponds to Aromatic amide, 2855 cm^{-1} to 3030 cm^{-1}, which corresponds to fatty acid amide and also a peak at around 1423 cm^{-1} to 1675 cm^{-1}, which corresponds to the amide and imide group [159, 182, 184]. The spectra for 25ppm, 50ppm, 100ppm and 200ppm specimens were taken on the surrounding film and on the artificial pits and the summary results are shown in Table 8-3. During the scan on 100ppm and 50ppm specimens, these three major components of imidazoline peaks were detected on the pit sides and the surrounding film, as shown in Figure 8-22 and Figure 8-23. However, none of the peaks was found in the 200ppm and 25ppm specimens due to the concentration effect. It is interesting that the inhibitor was found

both on the pit sites and the surrounding film, which indicates that the imidazoline will form an adsorbed surfactant monolayer or bilayer on the surface of the metal to protect the surface from corrosion.

Condition	**Component 1**		**Component 2**		**Component** 3	
	Pit	Film	Pit	Film	Pit	Film
25 ppm	No	No	No	No	No	No
50 ppm	Yes	Yes	Yes	Yes	Yes	No
100 ppm	Yes	Yes	Yes	Yes	Yes	Yes
200 ppm	No	No	No	No	No	No

Table 8-3: Summary FTIR results for imidazoline inhibitor in different concentrations after the test.

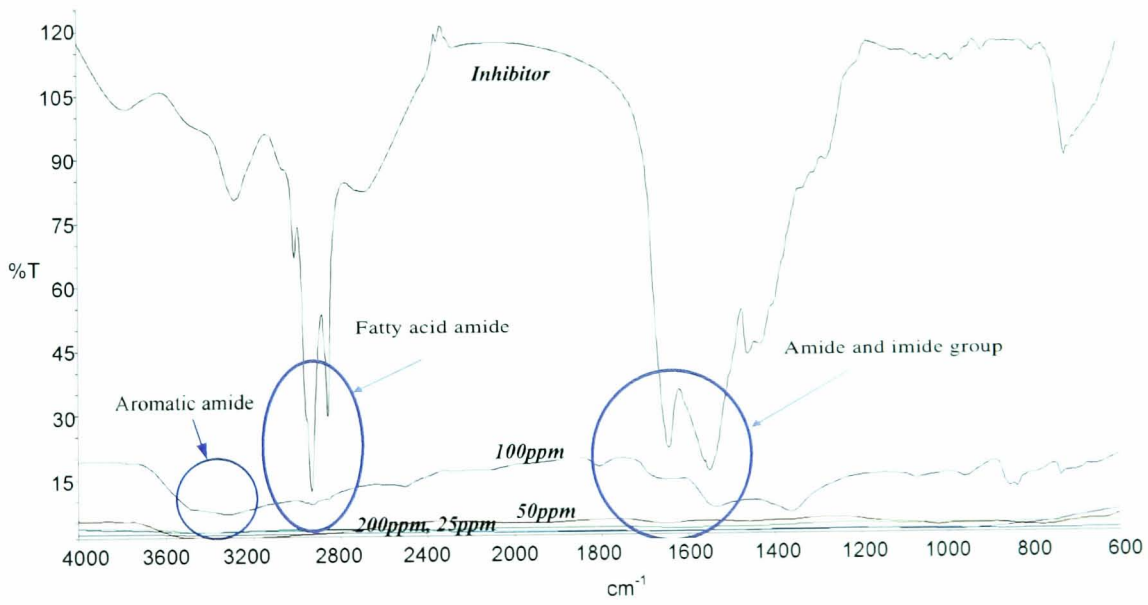

Figure 8-22: FTIR analysis on the pit site area of X65 carbon steel in CO_2 saturated 10% NaCl brine at 80°C, pH 5.65, 1000ppm Fe^{2+} and 1 bar total pressure with imidazoline in different concentrations

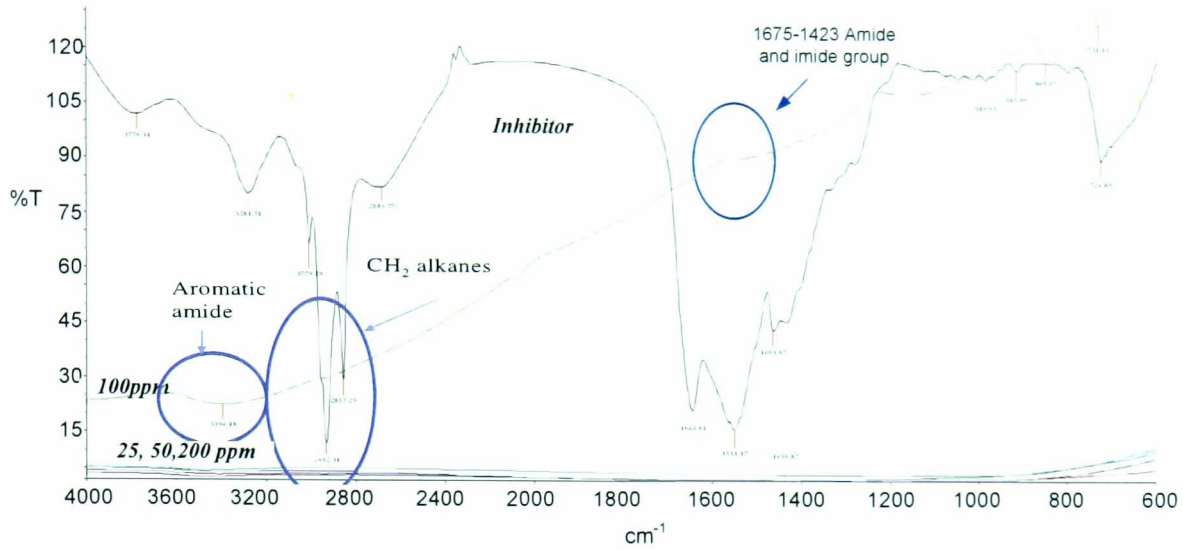

Figure 8-23: FTIR analysis on the film area of X65 carbon steel in CO_2 saturated 10% NaCl brine at 80°C, pH 5.65, 1000ppm Fe^{2+} and 1 bar total pressure with phosphate ester in different concentrations

8.5 Summary

This chapter shows that the potentiostatic approach on artificial pits allows the artificial pit to propagate to around 48.9µm to 53.1µm depth. Both phosphate ester and imidazoline inhibitors showed excellent performance to stop pit propagation if optimum concentrations are applied. The *in-situ* camera observed that pit propagation is due to a black deposit forming on the surface and covering the artificial pits, which results in a favourable condition for pits to grow. The FTIR analysis indicated that the phosphate ester inhibitor inhibits pits by absorbing the inhibitor at the pit site and the imidazoline inhibitor inhibits the pits by absorbing the film.

Chapter 9: Evaluation of inhibitor performance using artificial pit technique under sour conditions

In the previous chapter, the performance of inhibitors was evaluated under sweet conditions. This chapter uses the same techniques developed for testing in sweet conditions and adapt the technique for the sour conditions. The artificial pit growth on X65 carbon steel surfaces in sour conditions was assessed using the *in-situ* monitoring technique. Nonoxynol-6 phosphate and poly alkyl pyridines single components from corrosion inhibitors were used. Inhibitors were evaluated in terms of artificial pit propagation using electrochemical methods, which was supported by post-test analysis. Assessment of the pit chemistry by FTIR analysis was used to characterize the surface and profilometry analysis was used to determine the pit depth.

9.1 Corrosion current measurement

Electrochemical corrosion measurements using DC linear polarisation resistance measurements were carried out to monitor the corrosion rate during the formation of the iron sulphide film in the first 2.5 hours. The corrosion rate after 0.5 hours purging with the sour gas in the solution was typically 1.5 mm/yr. The corrosion rate dropped after 1.5 hours to 1.25 mm/yr, which is indicative of the formation of an iron sulphide film on the surface. After 2.5 hours, the corrosion rate dropped to 1.0 mm/yr, as shown in Figure 9-1, which indicates that the formation of iron sulphide provides a protective film on the surface.

After 3 hours, electrochemical corrosion measurements using a potentiostatic test were carried out to apply a constant electrode potential at 100mV more positive than the free corrosion potential to activate the artificial pit on the surface to a desired pit depth. Figure 9-2 presents the potentiostatic results for two experiments without inhibitor. It shows that in the first blank specimen the current initially dropped from 3.5mA to 0.75mA for the first 45000s (12.5 hours) followed by a sharp rise to 2mA until 57600s (16 hours) and was then held constant until the end of the test. The second blank specimen started with a very sharp rise of current to 3.5mA and then a decrease to 2.5mA at 1000s (0.25 hours), and, slowly, a further decrease to 2mA at the end of the test.

Both specimens reached the higher current at 3.5mA, and have a long slow current interval and achieve 2mA current at the end of the test. The current variation could not be avoided with such a long exposure time, which involved film formation and changes of the kinetics of the iron sulphide film with time. The current represents the general dissolution behaviour of the surface, which is influenced by the film breakdown process of the iron sulphide film.

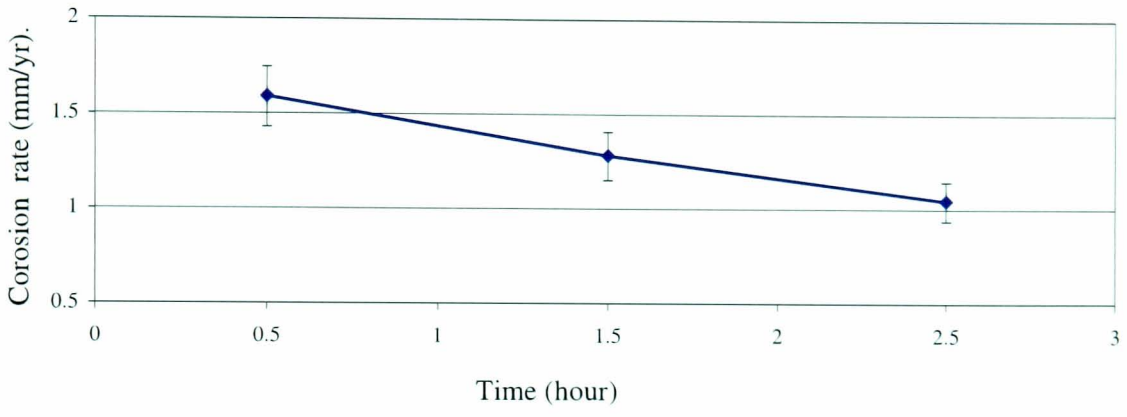

Figure 9-1: Corrosion rate versus time for the first 2.5 hour on X65 carbon steel in 10% NaCl brine at 80°C and 10% H_2S, 90% CO_2

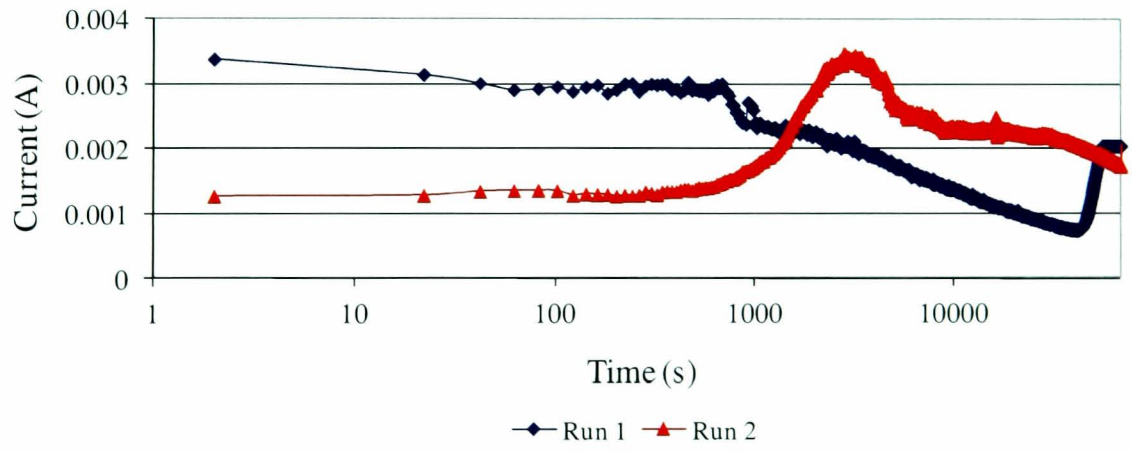

Figure 9-2: Potentiostatic polarisation curve at 4 hour to 24 hour on X65 carbon steel in 10% NaCl brine at 80°C and 10% H_2S, 90% CO_2.

9.1.1 Effect of nonoxynol-6 phosphate

The performance of nonoxynol-6 phosphate inhibitor has been studied by adding different concentrations at the start of the experiments. Electrochemical corrosion measurements using DC linear polarisation resistance were carried out to monitor the corrosion rate with nonoxynol-6 phosphate inhibitor in the first 2.5 hours. There was a significant reduction in the corrosion rate in the presence of nonoxynol-6 phosphate inhibitor. The corrosion rate dropped to 0.5 mm/yr at 25ppm after 2.5 hours; it provided 50% corrosion protection to the surface. Increasing the inhibitor concentration results in a further decrease in the corrosion rate. At 100ppm and 200ppm of the inhibitor, the corrosion rates after 2.5 hours were 0.35 mm/yr and 0.25 mm/yr, which provided 65% and 75% corrosion protection on the surface, as shown in Figure 9-3. These results show that the presence of the inhibitor appeared to provide a protective film on the surface to reduce the corrosion rate.

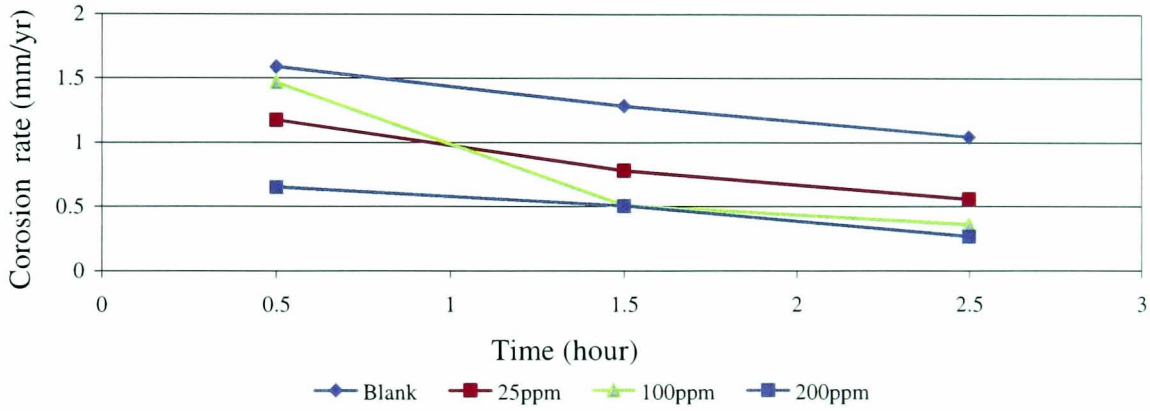

Figure 9-3: Corrosion rate versus time for the first 2.5 hours on X65 carbon steel in 10% NaCl brine at 80°C and 10% H_2S, 90% CO_2 with nonoxynol-6 phosphate

After 3 hours, electrochemical corrosion measurements using a potentiostatic test were carried out to apply a constant electrode potential at 100mV more positive than the free corrosion potential to activate the artificial pit on the surface. Figure 9-4 presents the potentiostatic results for experiments with nonoxynol-6 phosphate inhibitor. It shows that at 25ppm and 100ppm the current is reduced to 1mA and 0.1mA and the current maintained a steady value throughout the experiment. However, at 200ppm the current had an initial rise to 4mA at 18000s (5 hours) followed by a slow decrease to 3mA and a slow increase again to 4mA at 50400s (14

hours). After that, the current had a sharp rise to 9mA at 57600s (16 hours) and maintained a steady value before dropping to 8.5mA at the end of the test. The increase in the current from the start at 1mA and finish at 8mA indicates that the surface was changing towards an unprotective film over time.

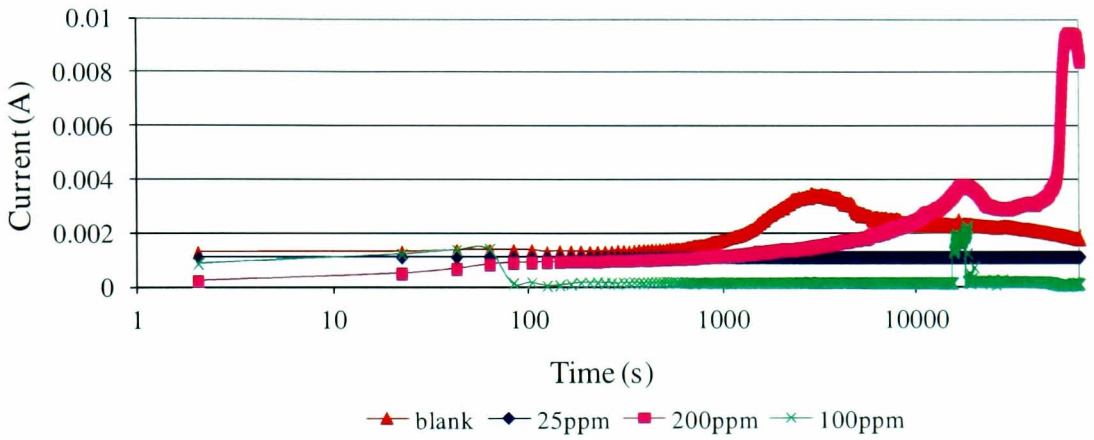

Figure 9-4: Potentiostatic polarisation curves for 24 hour tests on X65 carbon steel in 10% NaCl brine at 80°C and 10% H_2S, 90% CO_2 with nonoxynol-6 phosphate

Figure 9-5 presents the final current effects on inhibitor concentrations. It shows that the final current at 25ppm and 100ppm inhibitors are lower than the test without inhibitor, however, when the inhibitor concentration increases to 200ppm, the final current is higher than the test without inhibitor.

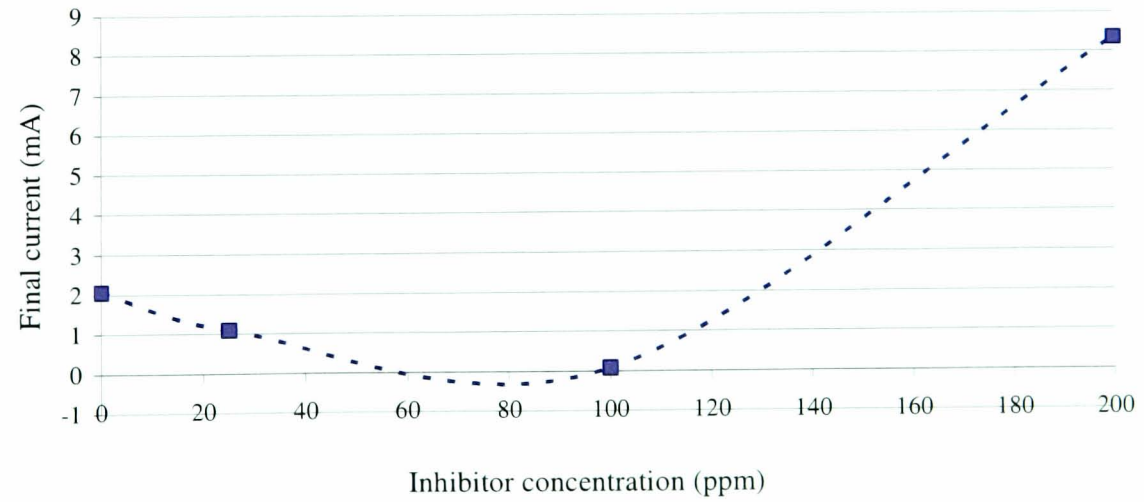

Figure 9-5: Final potentiostatic current after 24-hour test on X65 carbon steel in 10% NaCl brine at 80°C and 10% H_2S, 90% CO_2 with nonoxynol-6 phosphate

This shows that nonoxynol-6 phosphate inhibitor lowers the current if the effective concentration is applied; however, overdose of the inhibitor could increase the current.

9.1.2 Effect of poly alkyl pyridines

The performance of poly alkyl pyridine inhibitor was studied by adding different concentrations at the start of the experiments. Electrochemical corrosion measurements using DC linear polarisation resistance measurements were carried out to monitor the corrosion rate during the formation of an iron sulphide film with poly alkyl pyridine inhibitor in the first 2.5 hours. There were massive reductions in the corrosion rates in the presence of poly alkyl pyridine inhibitor. The corrosion rate dropped to 0.5 mm/yr at 25ppm after 2.5 hours and provided 50% corrosion protection to the surface. An increase in the inhibitor concentration resulted in a dramatic decrease in the corrosion rate. With 100ppm and 200ppm of the inhibitor, the corrosion rate after 2.5 hours was 0.05 mm/yr, which provided 95% corrosion protection on the surface, as shown in Figure 9-6. These results show that the presence of the inhibitor appeared to provide a protective film on the surface, which greatly reduced the corrosion rate.

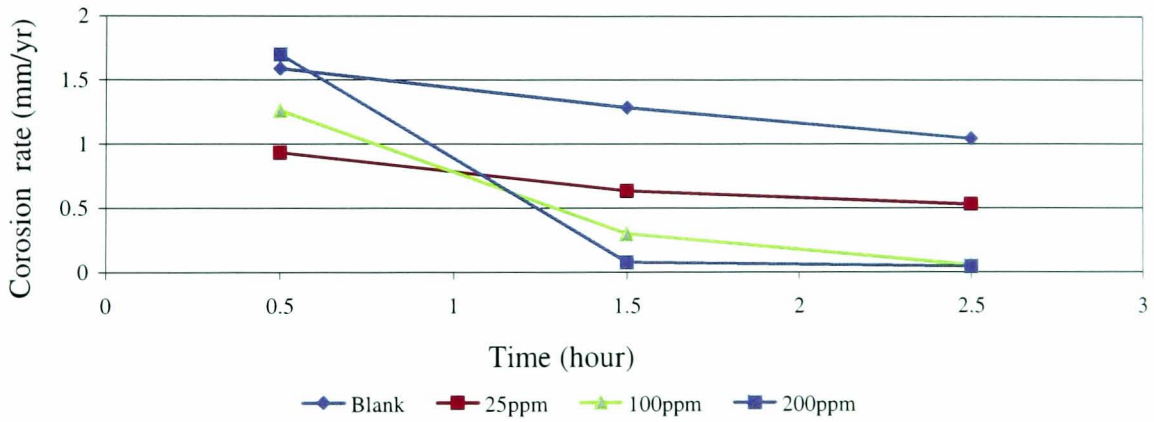

Figure 9-6: Corrosion rate versus time for the first 2.5 hours on X65 carbon steel in 10% NaCl brine at 80°C and 10% H_2S, 90% CO_2 with poly alkyl pyridines

After 3 hours, electrochemical corrosion measurements using a potentiostatic test were carried out to apply a constant electrode potential at 100mV more positive than the free corrosion potential to activate the artificial pit on the surface. Figure 9-7 presents the potentiostatic results for experiments with Nonoxynol-6 phosphate

inhibitor. It shows that at 100ppm and 200ppm there was a massive reduction in the current to 0.1mA and the current maintained a steady value throughout the experiment. This current is very low indicating the presence of a protective film on the surface, which is supported by a lower corrosion rate before the current was applied. However, at 25ppm the currents increased to a much higher value, to 8.5mA, and were held constant throughout the experiment. Figure 9-8 presents the final current effects on inhibitor concentrations.

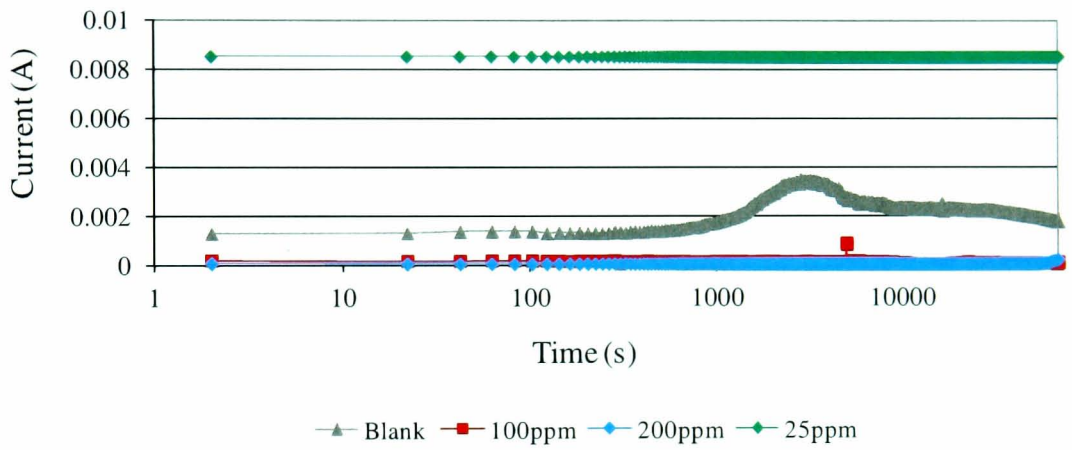

Figure 9-7: Potentiostatic polarisation curves for 24-hour test on X65 carbon steel in 10% NaCl brine at 80°C and 10% H_2S, 90% CO_2 with poly alkyl pyridine

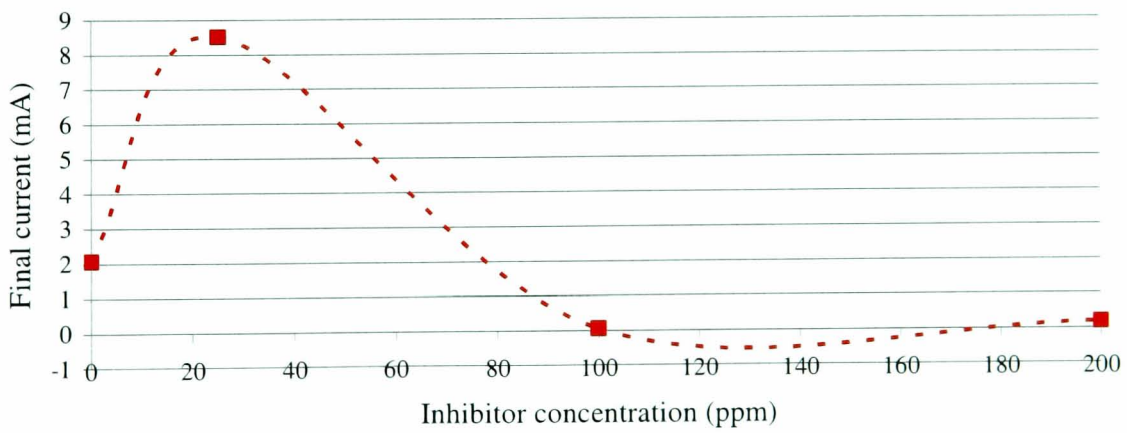

Figure 9-8: Final potentiostatic current after 24-hour test on X65 carbon steel in 10%NaCl brine at 80°C and 10% H_2S, 90% CO_2 with poly alkyl pyridine

It shows that the final current at 25ppm inhibitor is higher than the test without inhibitor, however, when the inhibitor concentration increased to 100ppm and 200ppm, the final current was lower than the test without inhibitor. This shows that poly alkyl pyridine inhibitor reduces the current after it reaches the minimum effect concentration, which under the conditions in the study is 100ppm.

9.2 *In-situ* camera monitoring techniques.

Figure 9-9 shows an early stage image after the specimen was immersed into the solution. It clearly reveals that the formation of iron sulphide film took place over the surface within 1 hour after purging the sour gas. The iron sulphide film build up started in the first 5 minutes, as shown by a darkening of the surface. The surface continued to darken and eradicated the grinding lines, and after 30 minutes little of the original surface could be seen. After the film covered most of the surface, the film started getting thicker and took place over the artificial pit, as shown at 60 minutes. The surface and the solution continued to darken and affect the ability of the camera to continue monitoring the surface activity.

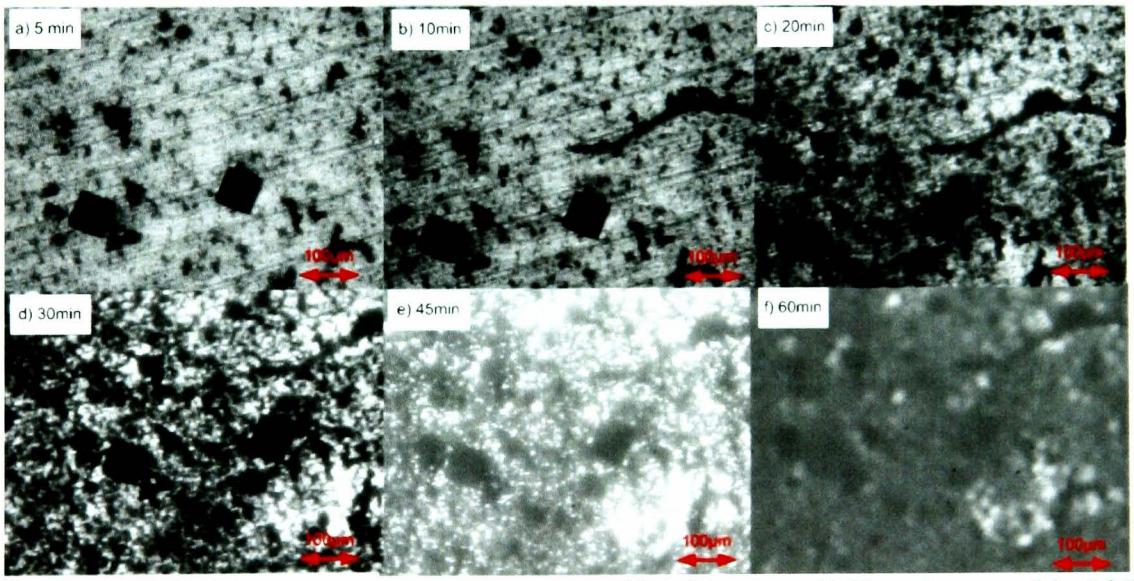

Figure 9-9: *In-situ* image of X65 carbon up to 60 minutes on X65 carbon steel in 10% NaCl brine at 80°C and 10% H_2S, 90% CO_2; a) 5min, b)10min, c) 20min, d) 30min, e) 45min, f) 60min

9.2.1 Effect of nonoxynol-6 phosphate

Figure 9-10 shows the effect of nonoxynol-6 phosphate inhibitor when it is present at 100ppm and 200ppm concentrations in the solution. Nonoxynol-6 phosphate inhibitor in solution changes the solution to a milky colour when it is present at high concentration. At 100ppm, the inhibitor delays the formation of the iron sulphide film. The surface can be observed until 4 hours. The formation of iron sulphide is much less at 4 hours compared to the specimen without inhibitor. After 4 hours, the solution started to darken and affected the ability of the camera to continue to monitor the surface activity. The camera was unable to monitor the activity on the surface when 200ppm of nonoxynol-6 phosphate inhibitor was added due to it changing the solution to a milky colour, as stated.

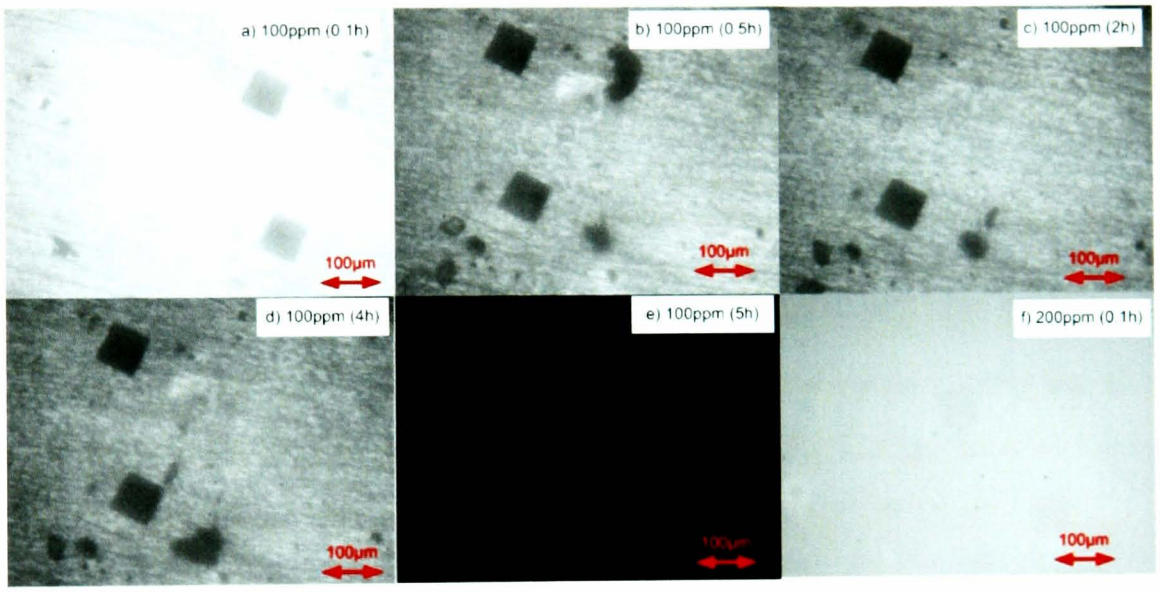

Figure 9-10: *In-situ* image of X65 carbon steel in 10% NaCl brine at 80°C and 10% H_2S, 90% CO_2 with nonoxynol-6 phosphate; a) 100ppm at 0.1 h, b) 100ppm at 0.5 h, c) 100ppm at 2 h, d) 100ppm at 4 h, e) 100ppm at 5 h, f) 200ppm at 0.1 h

9.2.2 Effect of poly alkyl pyridine

Figure 9-11 shows the effect of poly alkyl pyridine inhibitor when it is present in 100ppm and 200ppm concentrations on the surface. At higher concentrations, the inhibitor stops the formation of iron sulphide films on the surface and does not turn the solution to a blackish colour. At 100ppm, the inhibitor delays the formation of iron sulphide film up to 30 minutes, however, after that the formation of the iron sulphide film forms very quickly and takes place over the surface. After the

concentration was increased to 200ppm, the formation of the iron sulphide film is seen to stop and it also stops turning the solution blackish. The camera was able to observe the artificial pit activity until the end of the experiment at 24 hours. The surface grinding lines and some uncorroded areas still exist and can be observed after 24 hours. A very thin corrosion product layer is seen to exist across most of the surface. There was no significant growth in pit diameter during the test due to the geometry of the artificial pits, which have a large diameter compared to the depth.

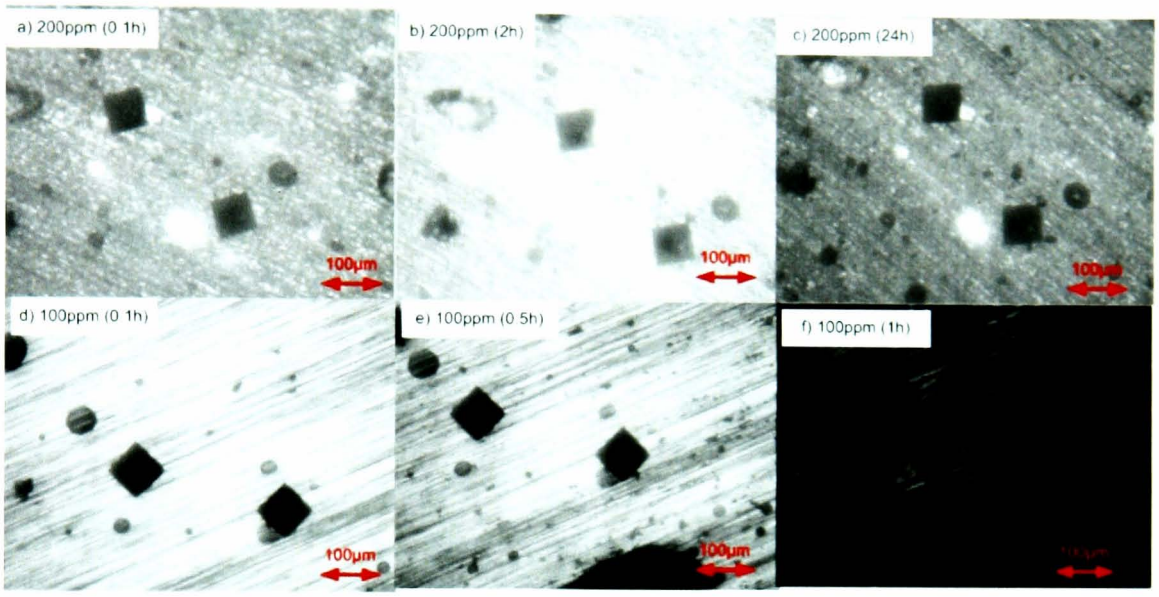

Figure 9-11: *In-situ* image of X65 carbon steel in 10% NaCl brine at 80°C and 10% H_2S, 90% CO_2 with poly alkyl pyridine; a) 200ppm at 0.1 h, b) 200ppm at 2 h, c) 200ppm at 24 h, d) 100ppm at 0.1 h, e) 100ppm at 0.5 h, f) 100ppm at 1 h

9.3 Pit depth analysis

The blank test was carried out to assess the severity of the test condition and to enable evaluation of the performance of the inhibitor. The specimens were analysed by measuring the artificial pits on the specimens surface as well as the three deepest natural pits with the purpose of trying to detect the most significant pits that create failure. The profilometer analysis shows that after 24 hours of blank test the average artificial pits propagate from 9µm to around 31.6µm, however, in some blank samples the maximum artificial pit depth obtained is 34.9µm, as shown in Figure 9-12(a-f).

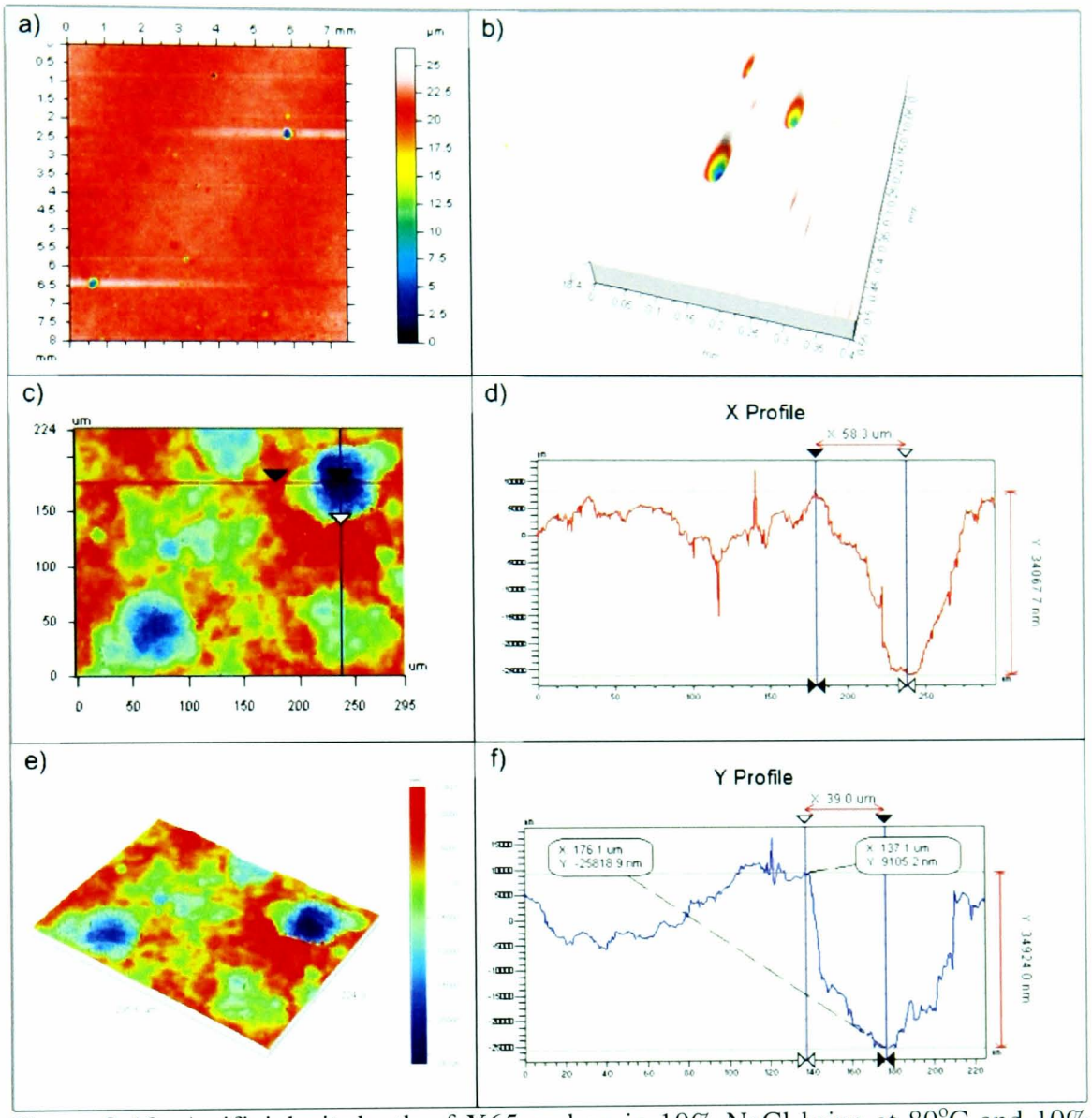

Figure 9-12: Artificial pit depth of X65 carbon in 10% NaCl brine at 80°C and 10% H_2S, 90% CO_2 after the blank test; a) 2D view of pits surface, b) 3D view of artificial pits surface, c) 2D View of artificial pits surface, d) Cross-section view x-profile of artificial pits surface, e) 3D view of artificial pits surface, f) Cross-section view y-profile of artificial pits surface.

The potential applied to the surface also initiates and propagates other natural pits on the surrounding surface. The three deepest natural pits detected on the surface were within the range of 22.2µm to 49.3µm and the average natural pit detected on the surface was 34.3µm.

9.3.1 Effect of nonoxynol-6 phosphate

Nonoxynol-6 phosphate slows down the pitting propagation at 25ppm and 100ppm, however, the inhibitor performance decreases after 200ppm of inhibitor is applied. Figure 9-13 shows the comparison in pit depth results for the artificial and natural pits on the surface with different concentrations of nonoxynol-6 phosphate.

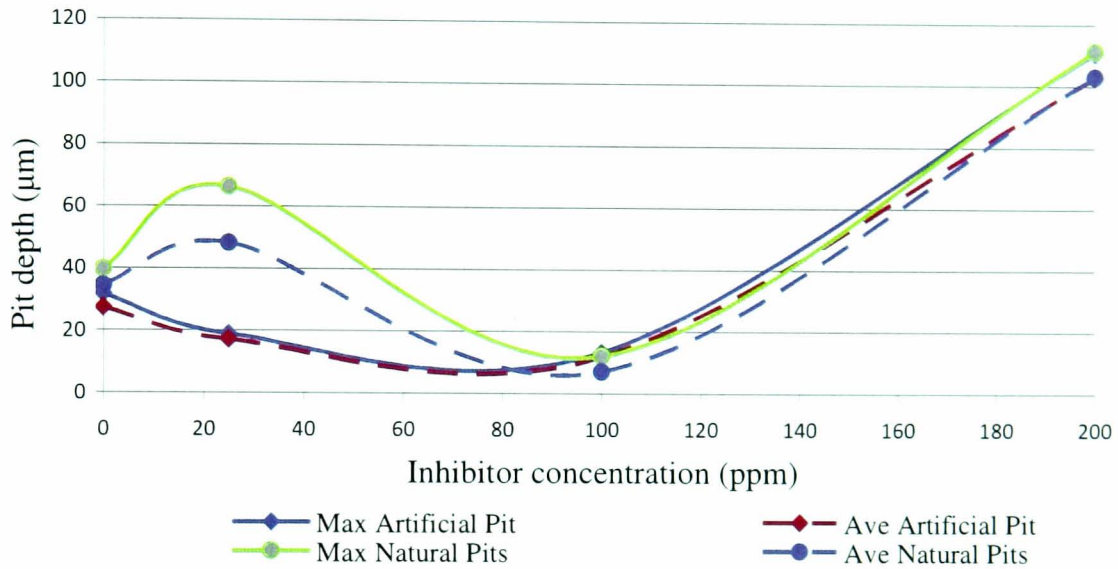

Figure 9-13: Pit depth analysis of X65 carbon steel in 10% NaCl brine at 80°C and 10% H_2S, 90% CO_2 with different concentrations of nonoxynol-6 phosphate

At 25ppm of nonoxynol-6 phosphate the artificial pit depth is slowed to 18.8µm and as the inhibitor increased to 100ppm, the performance performed at optimum level by completely controlling the pitting attack with a pit depth recorded of 13.2µm, as shown in the 3D image in Figure 9-14(a-d).

However, at 200ppm of nonoxynol-6 phosphate inhibitor the artificial pit propagated to 113µm, which is significantly higher than the blank test and is attributed to an overdose effect as shown in Figure 9-14f.

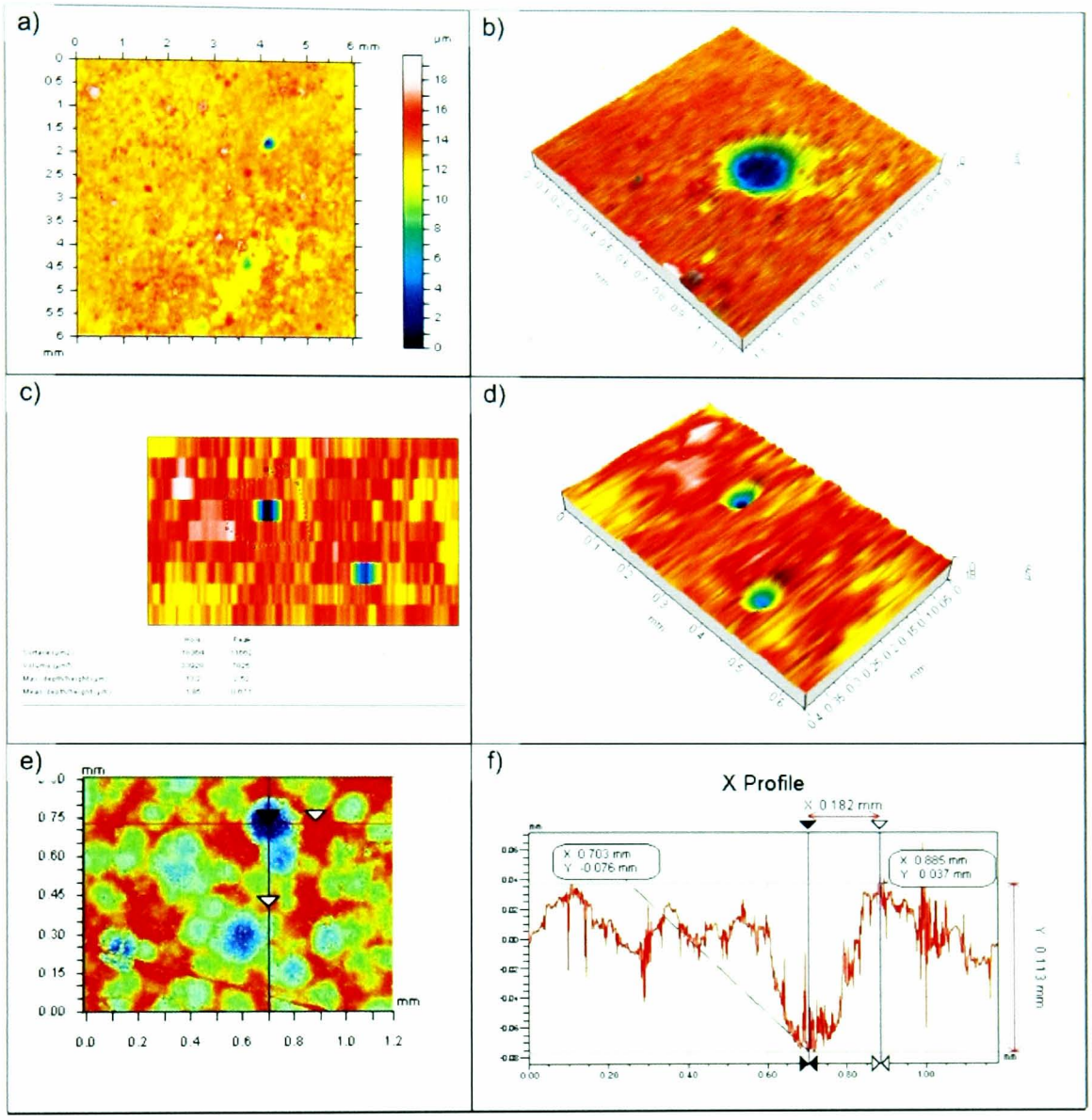

Figure 9-14: 3D image of profilometer analysis of artificial pit on X65 carbon steel in 10% NaCl brine at 80°C and 10% H_2S, 90% CO_2 with nonoxynol-6 phosphate; a) 2D view of pits surface at 100ppm, b) 3D view of natural pits surface at 100ppm, c) 2D view of artificial pits surface at 100ppm, d) 3D view of artificial pits surface at 100ppm, e) 2D view of artificial pits surface at 200ppm, f) 2D cross-section of artificial pits at 200ppm.

The interaction was due to the excessive inhibitor molecules enhancing the chemistry within the pit site, which resulted in the reduction of inhibitor performance and consequent increase in the propagation activities. The natural pit on the surface shows that the pit depth for 25ppm is 66.1 µm, which is significantly higher than the blank specimens and has an opposite effect compared to the artificial pits on the

surface. The performance of the inhibitor at 25ppm is attributed to the underdose effect and in the transition region towards inhibiting the surface. The trend for natural pits for 100ppm and 200ppm show a similar effect to the natural pits where the natural pits detected were 12µm at 100ppm and 117µm at 200ppm.

9.3.2 Effect of poly alkyl pyridines

The introduction of poly alkyl pyridines into the experiment can control the pitting propagation if the required amount of concentration is applied. Figure 9-15 shows the comparison in pit depth results for the artificial and natural pits on the surface with different concentrations of poly alkyl pyridines.

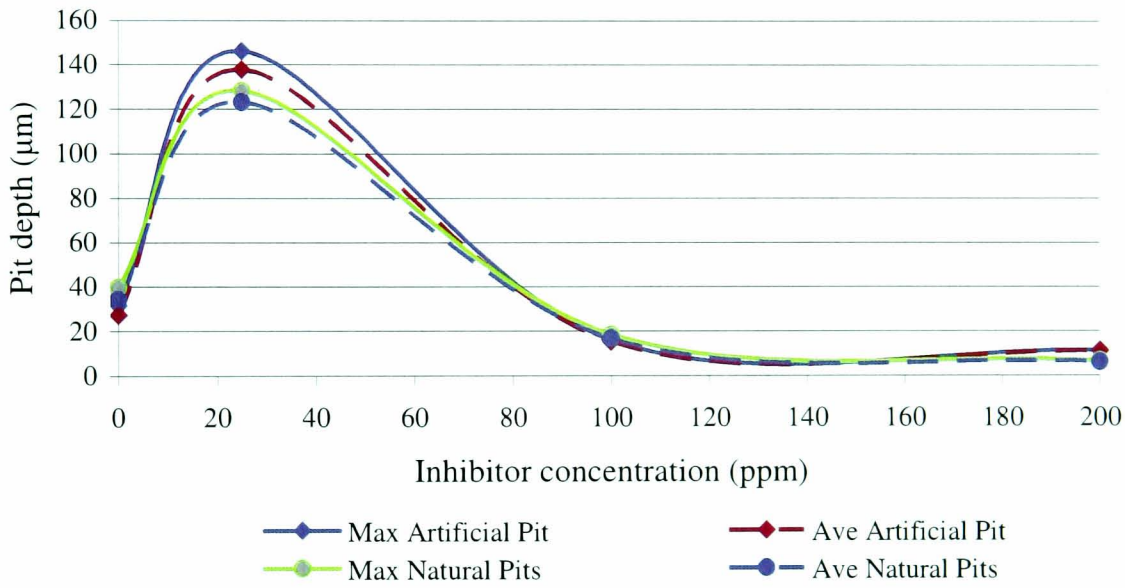

Figure 9-15: Pit depth analysis of X65 carbon steel in 10% NaCl brine at 80°C and 10% H_2S, 90% CO_2 with different concentrations of poly alkyl pyridines.

At 200ppm of poly alkyl pyridines it can slow down the artificial pit propagation process to 11.2µm, as shown in the 3D image in Figure 9-16(a-d). However, with 25ppm poly alkyl pyridines, the artificial pits propagate to 146µm, which is significantly higher than the blank test as shown in Figure 9-16f. This is attributed to be caused by the lower adsorption of the inhibitor molecules within the pit sides resulting in the reduction of inhibitor performance and consequential increase in the propagation activities [7, 133].

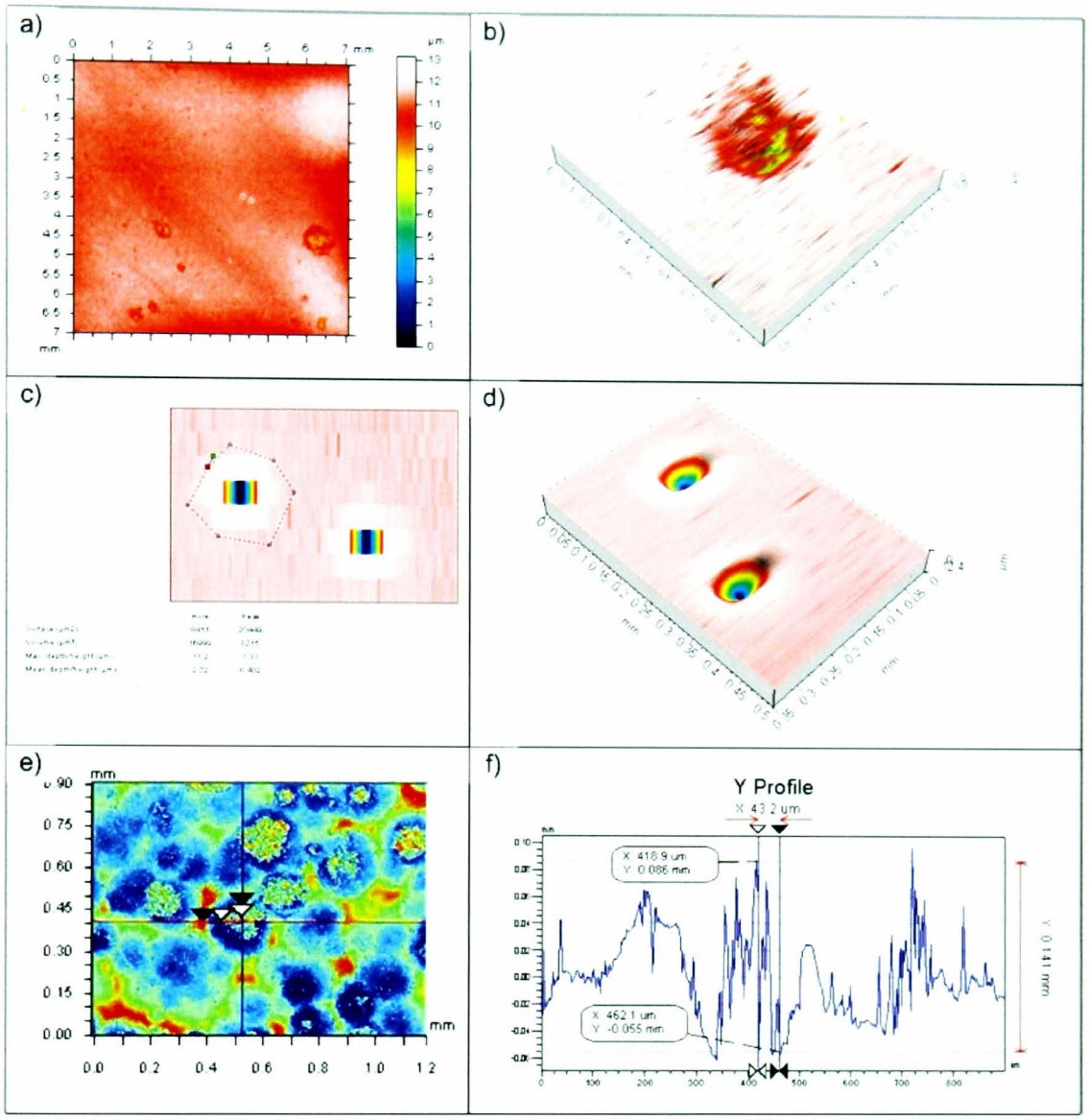

Figure 9-16: 3D image of profilometer analysis of artificial pit on X65 carbon steel in 10% NaCl brine at 80°C and 10% H_2S, 90% CO_2 with poly alkyl pyridines; a) 2D view of pits surface at 200ppm, b) 3D view of natural pits surface at 200ppm, c) 2D view of artificial pits surface at 200ppm, d) 3D view of artificial pits surface at 200ppm, e) 2D view of artificial pits surface at 25ppm, f) 2D cross-section of artificial pits at 25ppm.

Consequently, when the poly alkyl pyridines concentration increased to 100ppm the artificial pit depth reduced to 16 µm. It is interesting to compare the pit depths of the artificial pit and natural pit on the surface, which are in good agreement in terms of the reaction towards the inhibitor. The natural pits detected at 200ppm were 6.48 µm, which shows that the poly alkyl pyridines fully control the localised activity on the surface. These similar trends indicate that the pitting activities and the

reaction with poly alkyl pyridines are comparable between the artificial pits and natural pits.

9.4 Fourier Transform InfraRed (FTIR) Spectroscopy

IR reflectance spectra in the region 600 to 4000 cm^{-1} were collected on the surface after the test. A complete summary of the spectra assignments is shown in Table 9-1.

Wavenumber (cm^{-1})	Peak assignment	References
Corrosion product		
3432	H-O stretching refer to	[159]
3370	H-O stretching respectively refer to mackinawite	[159]
3250	Precipitation of Fe(II) as $FeCO_3$	[166]
2900	FeS	[169]
2343	CO_2 asymmetric stretching	[164, 168]
2198	CO_2 asymmetric stretching	[164, 168]
1621	H-O stretching refer to mackinawite	[156, 173]
1364	FeOOH with adsorbed of carbonate	[162]
1000-1245	Polythionates assigned to pyrite	[172]
665	Fe-O and Fe-OH to mackinawite	[156]
Inhibitor C		
3000-3500	C-H stretching refers to aromatic amine or phenol	[159, 182, 183, 184]
2959	O-CH_3 from ester group	[159, 161, 182, 183, 184]
1725	C=O stretching of fatty acid amine	[182, 183, 184]
1377-1610	CH_3 and CH_2 scissor	[182, 183, 184]
1111-1377	$(CH_3\text{-}O)_3$ ptrimethlyphosphateand $(CH3)_2P(O)_2$ nadialkylphosphinate salts	[182, 183, 184]
Inhibitor D		
2800-3500	C-H stretching refers to aromatic amine or phenol	[159, 161, 182, 183, 184]
2242	Nitrile substituted amine salts, alkynes, deuterated aliphatic	[182. 183, 184]
1377-1472	Carboxylate salt of CH_3 and CH_2	[161]
662-1028	C-N assignment to ketone, amude and aromatic aldehyde	[182, 183, 184]

Table 9-1: FTIR spectra assignments for sour condition

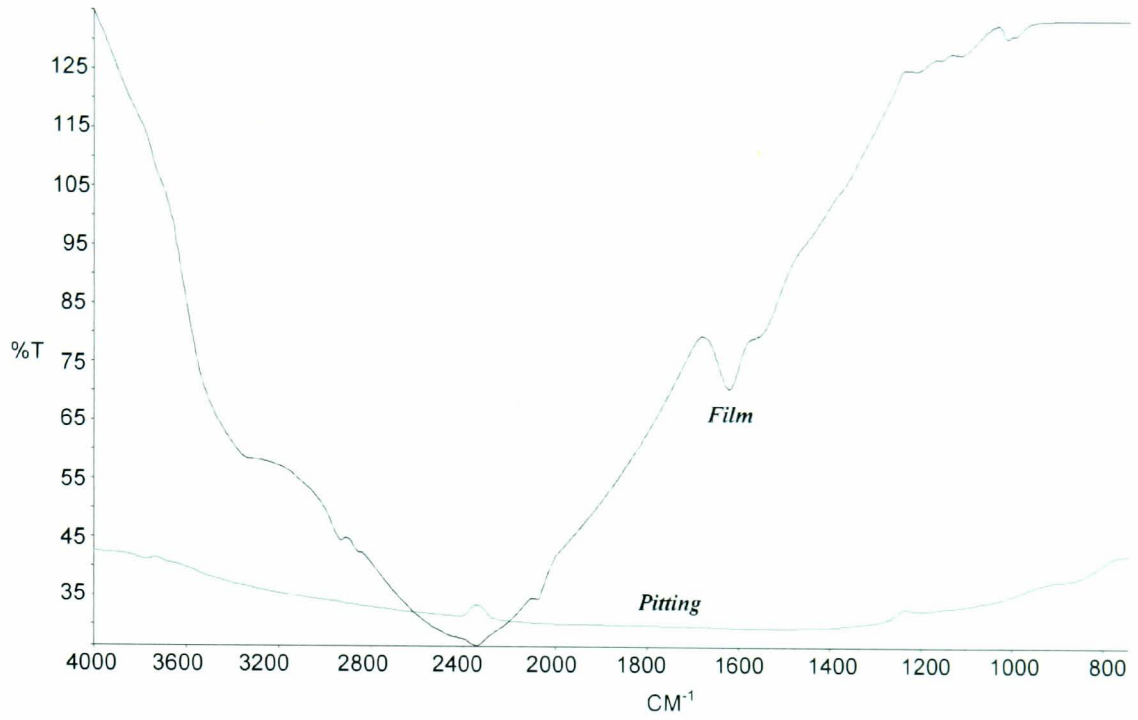

Figure 9-17: FTIR analysis on X65 carbon steel in 10% NaCl brine at 80°C and 10% H_2S, 90% CO_2.

9.4.1 Effect of nonoxynol-6 phosphate

Figure 9-18 shows the spectrum of the neat nonoxynol-6 phosphate and the spectrum obtained from 100ppm nonoxynol-6 phosphate diluted in distilled water at 80°C. It can be seen that both spectra possess several matching peaks, however, the spectra after being diluted is weaker and some peaks are absent. A distinctively large peak is identified at around 3498 cm^{-1}, which corresponds to the C-H stretching band that is usually present between 3000-3500 cm^{-1}, which is assigned to aromatic amine or phenol functional group [161, 159, 161, 183, 184, 185]. Another large peak is identified at 2959 cm^{-1}, which represents the O-CH_3 ester group from the methanol [159, 161]. A peak at 1725 cm^{-1} represents the C=O stretching band of carbonyl peak, which is indicative of the carboxylic acid functionality of fatty acid amine [159, 161]. The appearance of a peak around 1377-1610 cm^{-1} is due to inorganic carboxylate salt, which is probably due to CH_3 and CH_2 scissor [182]. The broad peaks around 1111 – 1377 cm^{-1} correspond to the $(CH_3\text{-}O)_3$ ptrimethyl phosphate CH_3 group and $(CH_3)_2P(O)_2$ nadialkylphosphinate salts [183, 184]. Some of the peaks cannot be conclusively assigned to a particular functional group as the inhibitor active component is just a 10% mixture in methanol.

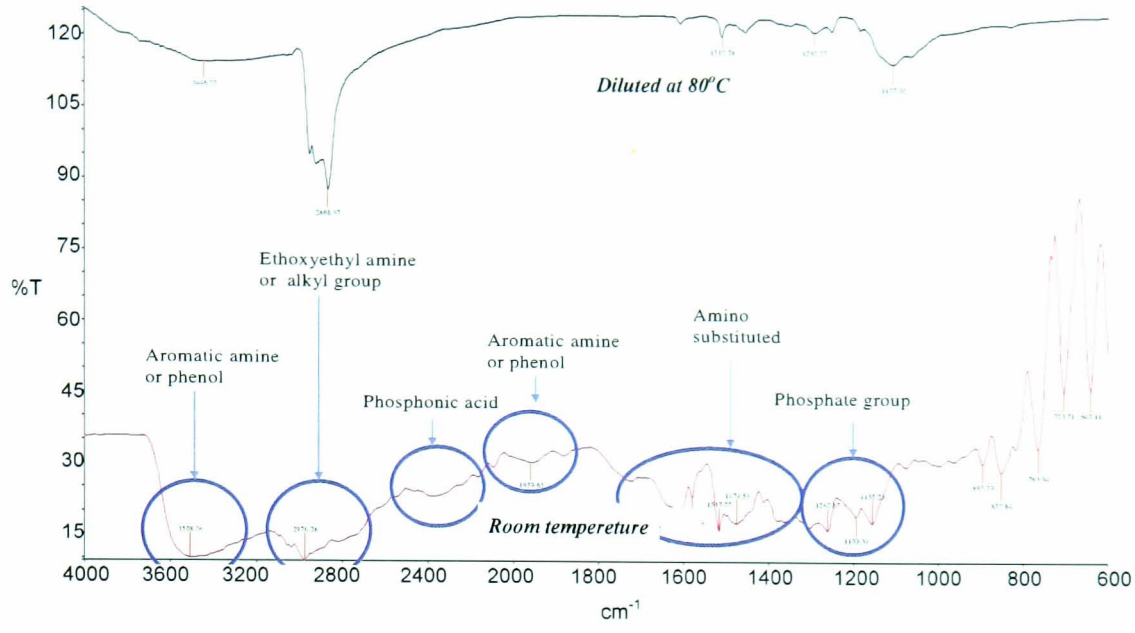

Figure 9-18: FTIR analysis on nonoxynol-6 phosphate inhibitor for different conditions.

The spectra for 25ppm, 100ppm and 200ppm specimens were taken on the surrounding film and on the artificial pits and the summary results are shown in Table 9-2. It can be seen that there were several nonoxynol-6 phosphate matching peaks on the artificial pit site and the surrounding film area for 25ppm and 100ppm specimens but nonoxynol-6 phosphate was absent on the surrounding film area for 200ppm specimens, as shown in Figure 9-19 and Figure 9-20.

Condition	**Inhibitor absorption**	
	Pit	Film
25 ppm	Yes	Yes
100 ppm	Yes	Yes
200 ppm	No	No

Table 9-2: Summary FTIR results for nonoxynol-6 phosphate inhibitor with different concentrations.

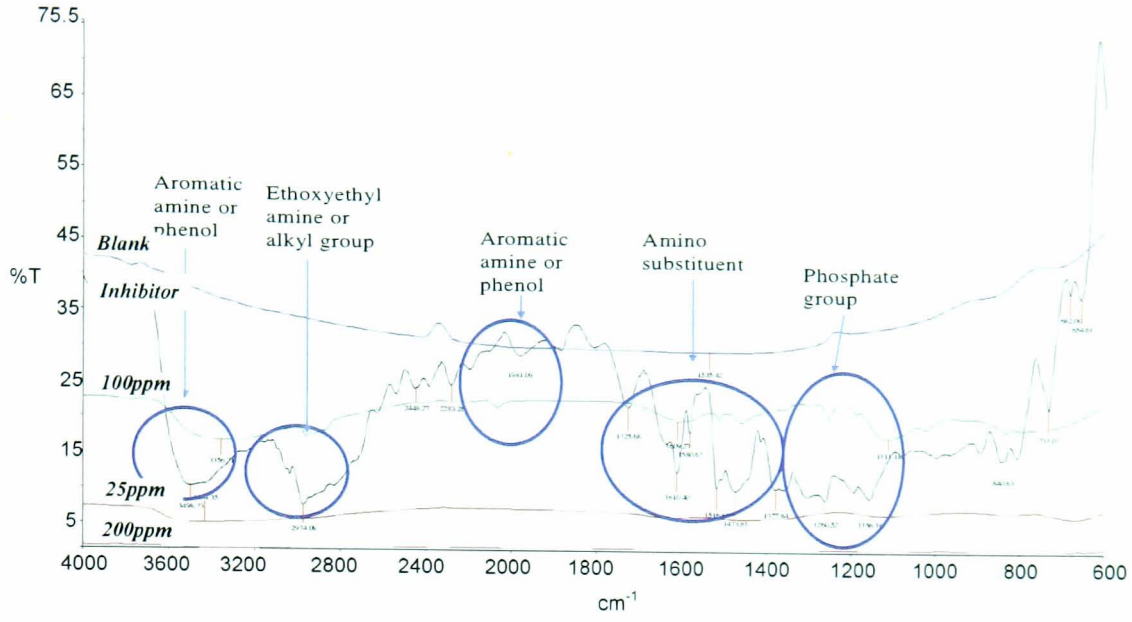

Figure 9-19: FTIR analysis on the pit site area of X65 carbon steel in 10% NaCl brine at 80°C and 10% H_2S, 90% CO_2 with different concentrations of nonoxynol-6 phosphate

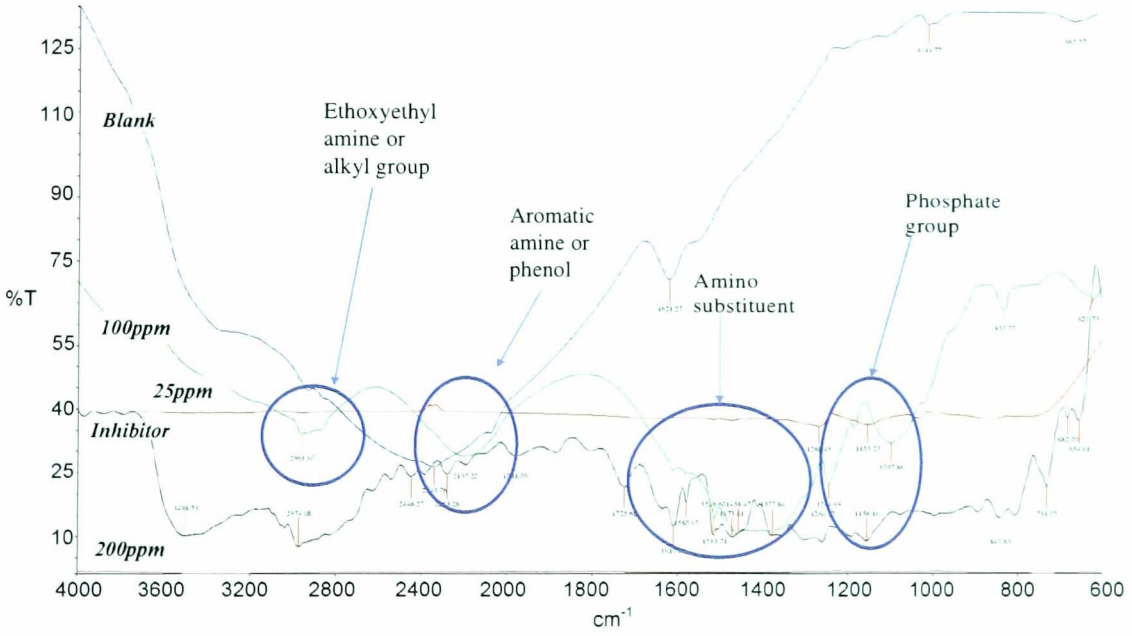

Figure 9-20: FTIR analysis on the film area of X65 carbon steel in 10% NaCl brine at 80°C and 10% H_2S, 90% CO_2 with different concentrations of nonoxynol-6 phosphate

There were strong inhibitor peaks detected in the area of the pits for 100ppm specimens, which were at around 3356 cm^{-1}, 2974 cm^{-1}, 1609 cm^{-1}, 1473 cm^{-1} and 1260cm^{-1}. For the same specimens, stronger inhibitor peaks were detected on the film

area at 2961 cm^{-1}, 1610 cm^{-1} and 1244 cm^{-1}. It can be seen that there are several matching inhibitor peaks between the pit area and the film area, which confirms that the inhibitor was present in both areas. A direct comparison between the 100ppm specimens and the blank specimen can only be made at the weak inhibitor peak area. There were strong peaks detected at 2198 and 1097cm^{-1} representing corresponding to CO_2 asymmetric stretching and polythionates respectively refers to pyrite [172, 164, 168].

There were weak inhibitor peaks detected at the pit area for the 25ppm specimen, which were at around 3498 cm^{-1}, 1473 cm^{-1}, and 1156 cm^{-1}. On the same specimens weak inhibitor peaks were detected in the film area at 1268 and 1153.23 cm^{-1}. Several matching inhibitor peaks between the pit area and the film area confirm that the inhibitor was present in both areas at 25ppm, but the lower concentration of the inhibitor affected the absorption to the surface. There is also a matching peak for pyrite found on the film area at 1030 cm^{-1}. This shows that at effective level dosing, nonoxynol-6 phosphate was found both on the pit site and the surrounding film to provide an adsorbed surfactant monolayer or bilayer with iron sulphide film on the metal surface to provide a protective film.

9.4.2 Effect of poly alkyl pyridines

Figure 9-21 shows the spectrum of the neat poly alkyl pyridines and the spectrum obtained from 100ppm poly alkyl pyridines diluted in distilled water at 80°C. It can be seen that both spectra possess several matching peaks and the spectra after being diluted still detects a strong signal and is not affected by the dilution process. A distinctively large peak is present between 2800-3500 cm-^{1}, which corresponds to the C-H stretching band, which usually refers to the aromatic amine or phenol functional group [159, 161, 182, 183, 184]. The large peak identified at 2242 cm^{-1} represents the nitrile substitute, possibly amine salts, alkynes and deuterated aliphatic [182]. The appearance of peaks around 1377 – 1472 cm^{-1} are due to carboxylate salt, which is probably due to CH_3 and CH_2 scissor [182]. The broad peaks around 1028 – 662 cm^{-1} corresponds to C-N assignment corresponding to carbonyl compound, possibly ketone, amide and aromatic aldehyde [183, 184]. Some

of the peaks cannot be conclusively assigned to a particular functional group as the inhibitor active component is just 10% mixture in methanol.

The spectra for the 25ppm, 100ppm and 200ppm specimens were taken on the surrounding film and on the artificial pits. The summary results are shown in Table 9-3. It can be seen that there were several poly alkyl pyridines with matching peaks on the artificial pit site that were absent on the surrounding film for the 100ppm and 200ppm specimens, as shown in Figure 9-22 and Figure 9-23. The bad spectra signal observed for the 25ppm specimen is due to the concentration effect and tenaciously chemisorbed inhibitors.

Condition	**Inhibitor absorption**	
	Pit	Film
25 ppm	No	No
100 ppm	Yes	No
200 ppm	Yes	No

Table 9-3: Summary FTIR results for poly alkyl pyridines inhibitor at different concentrations

Fairly strong inhibitor peaks were detected in the area of the pits for the 200ppm specimen, which were at around 2292 cm^{-1}, 1640 cm^{-1}, 1453 cm^{-1}, 1473 cm^{-1} and 1103 cm^{-1}. Weak inhibitor peaks were detected in the area of the pits area for the 100ppm specimen, which were at around 3412 cm^{-1}, 1461 cm^{-1} and 824 cm^{-1}. However, at both concentrations, 100ppm and 200ppm, poly alkyl pyridines were absent for the surrounding film.

A direct comparison between the 100ppm specimen with the blank specimen on the film area shows that a peak was detected at 3370 cm^{-1} and 1621 cm^{-1}, corresponding to H-O stretching respectively refer to mackinawite and a peak at 1011 cm^{-1} corresponding to polythionates respectively could refer to pyrite [156, 173, 172].

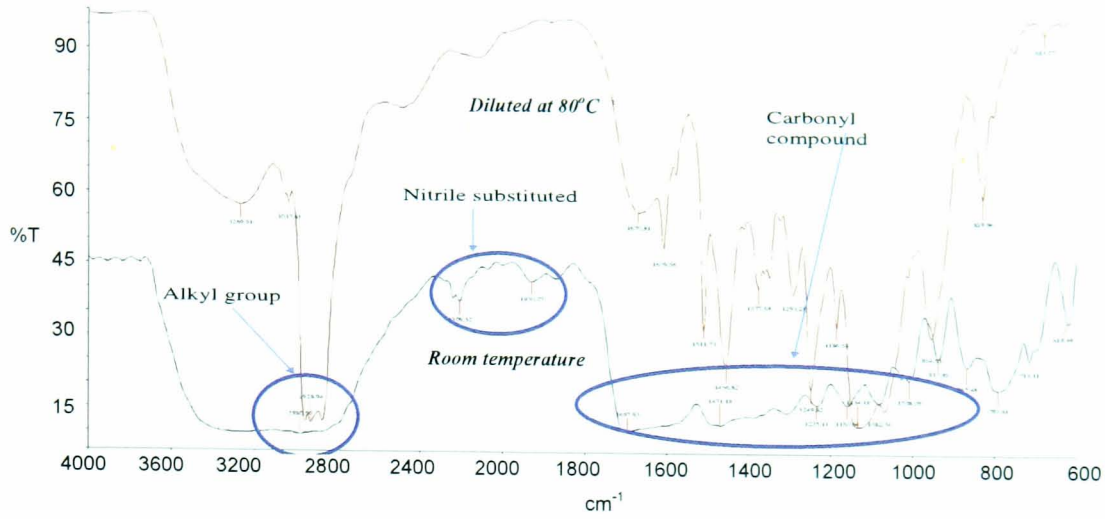

Figure 9-21: FTIR analysis of poly alkyl pyridines inhibitor in different conditions.

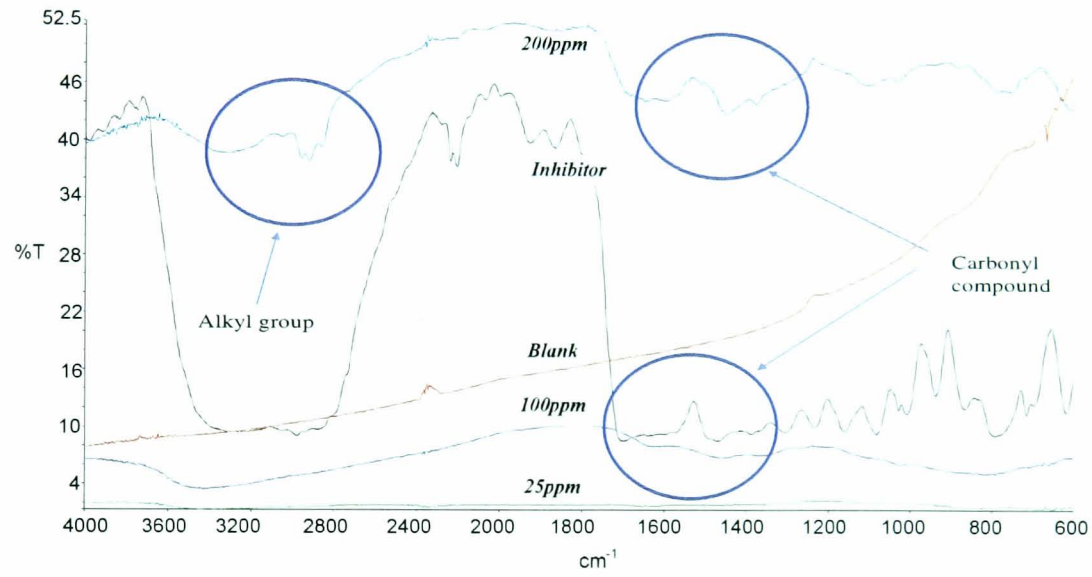

Figure 9-22: FTIR analysis on the pit site area of X65 carbon steel in 10% NaCl brine at 80°C and 10% H_2S, 90% CO_2 with different concentrations of poly alkyl pyridines.

The comparison with the 200ppm specimen shows that a peak is detected at around 3250 cm^{-1}, which could refer to $FeCO_3$ and a single peak at 2343 cm^{-1} appeared due to CO_2 asymmetric stretching [168]. A peak was detected at 1364 cm^{-1} and a single peak at 850 cm^{-1}, which only appeared on the 200ppm specimen and was absent on the inhibitor spectra and the blank spectra. It could be FeOOH with adsorbed carbonate or new film that form from the interaction between the inhibitor and the sour environment [162, 166].

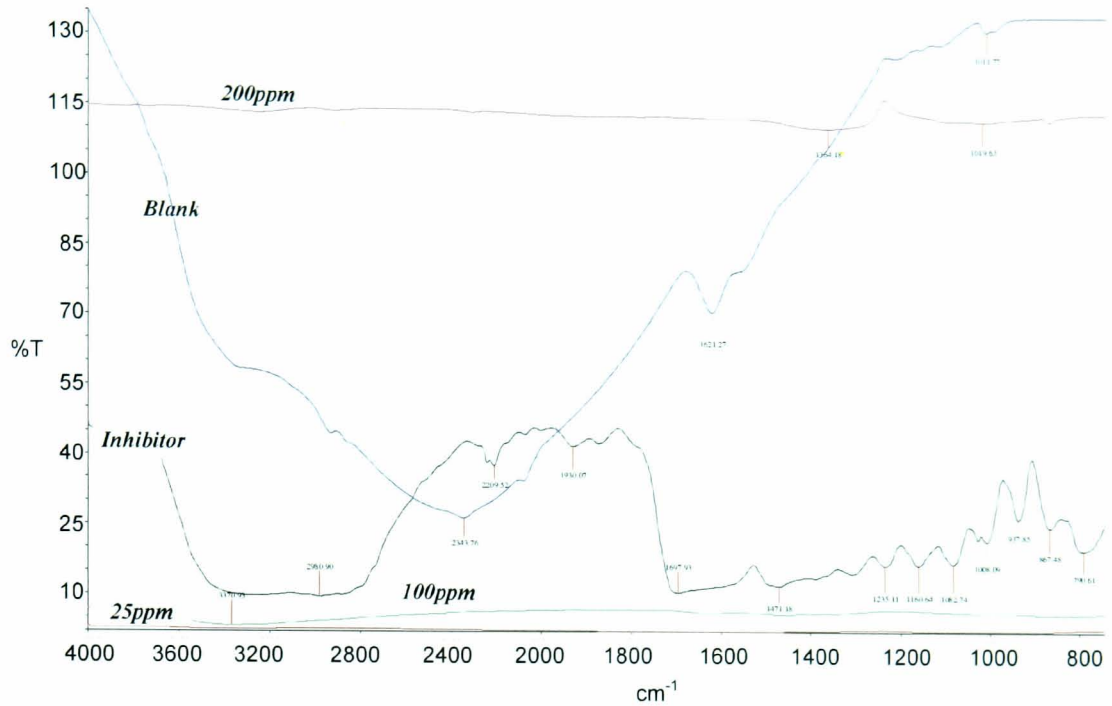

Figure 9-23: FTIR analysis on the film area of X65 carbon steel in 10% NaCl brine at 80°C and 10% H_2S, 90% CO_2 with different concentrations of poly alkyl pyridines

9.5 Summary

This chapter shows that the potentiostatic approach on artificial pits allows the artificial pit to propagate to around 31µm deep. Both nonoxynol-6 phosphate and poly alkyl pyridines inhibitors showed excellent performance to stop pit propagation if effective concentrations were applied. The *in-situ* camera observed that an iron sulphide film could cover most of the surface in 60 minutes. However, if effective concentration of inhibitor is applied, it shows that the inhibitors actually stop the formation of a black film, which could refer to iron sulphide. FTIR analysis indicates that the poly alkyl pyridines inhibitor inhibits pits by absorbing at the pit site and nonoxynol-6 phosphate inhibitor inhibits the pits by absorbing on the film.

Chapter 10 Discussion

In the previous chapters detailed characteristics of sweet and sour films followed by pitting behaviour and the effect of inhibition have been presented. In order to understand the mechanisms of inhibition on pitting, this chapter will discuss the formation of films in sweet and sour conditions that influence the localised pitting attack and the mechanisms of individual component inhibitors to mitigate pitting corrosion. This chapter is divided into three sections – section one discusses the early stages of sweet film formation and the protectiveness on the film and discusses the effect of sweet pre-corrosion under sour conditions. The second section will discuss the initiation and propagation of pitting in sweet and sour corrosion and the mechanisms of inhibitors on sweet pre-corrosion. The third section will discuss the mechanisms of pitting and its inhibition based on the *in-situ* observation technique and FTIR analysis in sweet and sour conditions.

10.1 Sweet film behaviour

In this section, there are four main parts to discuss with respect to the behaviour of the sweet film:

- X65 microstructure
- CO_2 corrosion mechanism
- Fe_3C role in localized pitting
- $FeCO_3$ film build up

The microstructure of X65 carbon steel has large pearlitic eyes areas and a ferrite phase with small grains [130]. Pitting initiation preferentially takes place in the pearlitic areas where the uncorroded Fe_3C phase is left behind from the anodic reaction in sweet corrosion [130]. The early stages of sweet corrosion start with the anodic reaction with the transfer of Fe^{2+} ion from the surface to the solution. This reaction leaves an undissolved Fe_3C component from the steel that accumulates on the surface [5, 29, 49]. Simultaneously, the cathodic reactions that take place release CO_3^{2-} ion to the solution. When the solubility limit is exceeded then the iron carbonate film precipitates. The solubility of Fe^{2+} is influenced by the pH of the solution; pH values of more than 5 have a lower solubility, which corresponds to

higher supersaturations and accelerates the precipitation process of $FeCO_3$ [5]. This will influence the time needed to reach a steady state condition in which the film growth covers all the surface, as indicated by reaching a constant corrosion rate. The types of film and the protectiveness of the film depend on whether the overall process is governed by diffusion of the metal cation or by the perceptible anion [29]. The $FeCO_3$ film will be protective if precipitation and redissolution are the majority process, which is termed soluble, however, the film will be unprotective if the diffusion in the liquid phase is predominant in which case the process is called insoluble [29].

Figure 10-1 explains that the early stage of sweet film formation at 50°C, 1%NaCl with saturated CO_2 starts with the transfer of Fe^{2+} ion from the surface to the solution and leaves undissolved Fe_3C on the surface. At 0.5 hours exposure time, AFM shows that the thickness of the film is 1.4μm thick. This is 0.7μm thicker compared to 0 hour, which leaves behind undissolved Fe_3C from the anodic reaction. This is supported by the EDX results that show that the reduction of iron content at 97.47% Fe compared to 98.19% Fe at 0 hour. Figure 6-19 shows the FIB-SEM topography image after 0.5 hours corrosion. It shows that the empty uncorroded Fe_3C phase creates a groove, which appears as a uniform attack with a rough surface. The groove will then be filled with $FeCO_3$ film and the overall predominant process will govern the protectiveness. This reaction will cause internal acidification, which will change the local pH and local water chemistry and lead to the risk of localised pitting attack. The FIB-SEM cross-section image in Figure 6-18 shows that at 0.5 hours there are some porous or unfilled regions, which lead to unprotective film.

After 1-hour exposure, there is $FeCO_3$ growth in most of the unfilled regions. However, due to the pH of around 4, the solubility of Fe^{2+} is high, which corresponds to a low supersaturation, and, therefore, an insoluble type film forms. This is shown in Figure 10-1(iii), which is supported by the AFM results that show that the film thickness is 1.5μm. It is interesting that the corrosion rate behaviour becomes constant after 1 hour, recorded at around 3 mm/yr to 4 mm/yr, which is evidence that the film reaches a steady state condition. In this condition, the film that grows is classed, as a semi protective mixed type $FeCO_3$ and Fe_3C film. However, the EDX relative percentage data shows that the iron content in the films decreased as the films grew

thicker with time. Figure 6-22 shows that after the film reached a steady state condition, the film thickness increased linearly overtime until 4 hours; conversely the iron content reduced linearly with time. Figure 6-23 shows that the linear relation between the film thickness and the iron content after 1-hour exposure time.

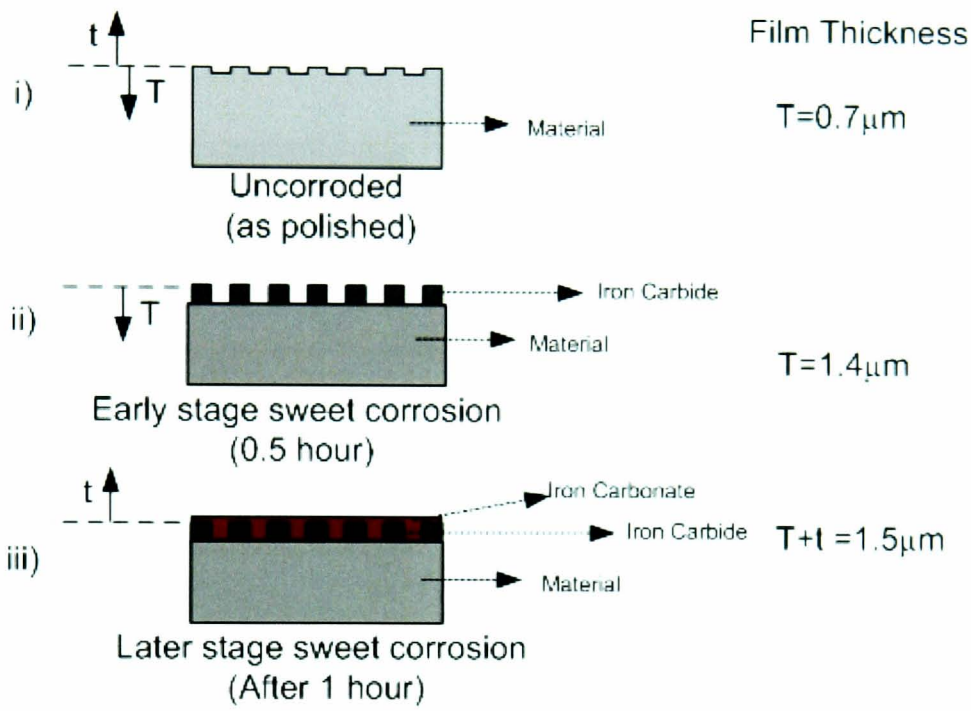

Figure 10-1: Early stage of sweet film formation.

The SEM images in Figure 6-8 show that at 4 hours the $FeCO_3$ film growth is thicker with time, which is influenced by the texture of the Fe_3C structure that it leaves on the surface. However at 8 hours, the morphology of the film is seen to change due to more $FeCO_3$ being produced on the surface compared to Fe_3C. The morphology at this stage is changing by breaking the Fe_3C structure, which is left behind and whitish flakes scattered around the surface start to develop, as shown in Figure 10-2. This type of film morphology will develop and become thicker with time.

After 24 hours of exposure time, the cross-section image in Figure 6-14 shows that the film growth is up to 23μm. Generally, the structure is not homogeneous and the content flaws and pores are typically distributed over the entire thickness, which is in agreement with the results of Schmitt et al., who obtained the same morphology

with a 40µm film thickness after 48 hours in similar experimental conditions [62]. The top view morphology in Figure 6-24 shows that the morphology of the film revealed two district phases consisting of flat dark grey regions that are porous film with scattered whitish flakes forming a film around the surface, which indicates $FeCO_3$ film and Fe_3C film. This is also supported by the XPS results, which indicate that the 2.5-hour specimen has Fe_3C and $FeCO_3$ elements on the surface.

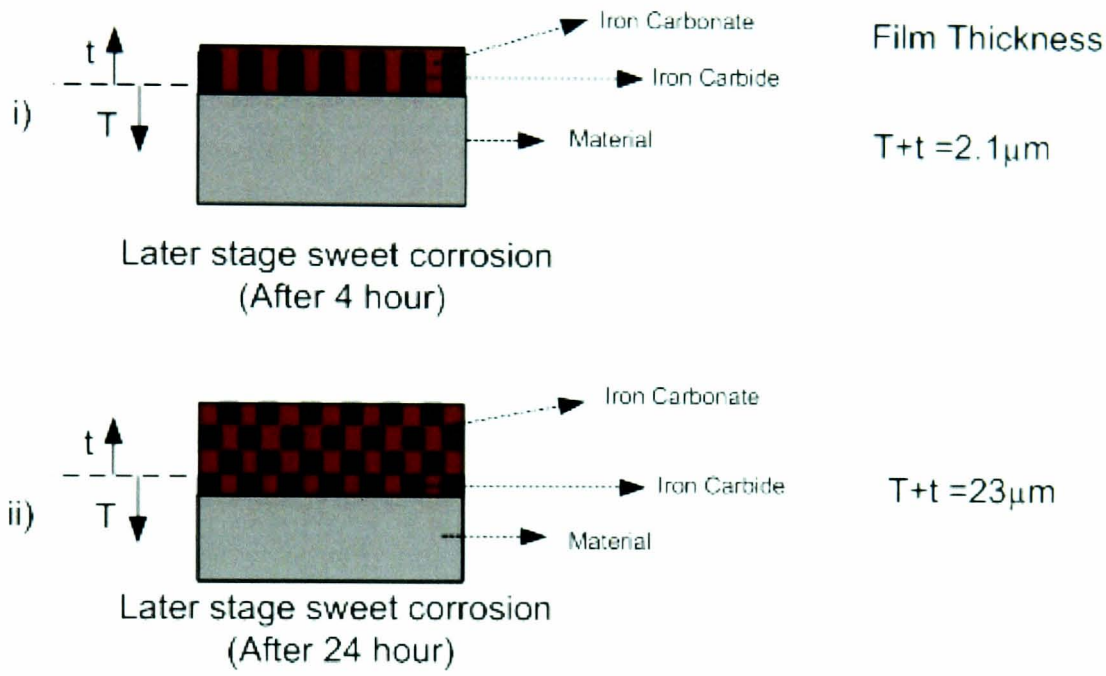

Figure 10-2: Later stage of sweet film formation

The EDX data on the whitish flakes type film are in agreement with Ruzic et al. in their studies they prove that the EDX content of the whitish flakes type film indicates a pure $FeCO_3$ type film [42]. The film thickness in these studies was measured using three different techniques FIB, SEM, AFM and cross-section SEM. The cross-section SEM technique is not very suitable to measure very thin films that are less than 2 µm, as the preparation process may damage the film, as the gap between the resin, film and substrate is very small.

10.2 Sour film behaviour

In this section, there are three main parts to discuss with respect to the sour film behaviour:

- Sour corrosion mechanism
- FeS film build up
- $FeCO_3$ and Fe_3C film in sour condition

The sour specimens were first pre-corroded in 1% sodium chloride at a constant test temperature of 50°C in CO_2 saturated solution at atmospheric pressure for 2.5 hours before being transferred to the sour experiment vessel at different temperatures. On completion of the test at Baker Hughes laboratory, the specimens were used in this study to analyse the film and understand the effect of the sweet pre-corrosion at different sour temperature exposures. From the literature, a better understanding of the mechanism of the sour film after sweet pre-corrosion and the effect on the film morphology at various temperatures in sour environments need further investigation and will be discussed in this section.

In sour environments, both iron sulphide and iron carbonate layers can form on the surface of the steel. The formation of a film on the surface is the most important factor governing the corrosion rate and depends primarily on the kinetics of the film growth [125]. Hydrogen sulphide dissolution is about three times weaker than carbonic acid, however, hydrogen sulphide gas is about three times more soluble than carbonic acid. Hence, the effect of hydrogen sulphide and carbon dioxide decreasing the solution pH is approximately the same [1, 5]. However, the level of hydrogen sulphide in the solution will determine the kinetics of the film growth. At low levels of hydrogen sulphide, it can act as a promoter of anodic dissolution through sulphide adsorption and affect the pH and increase the corrosion rate by forming iron carbonate. However, hydrogen sulphide can also reduce the corrosion rate by forming a protective iron sulphide film, as the rapid kinetics of mackinawite formation consume or complexes most of the Fe^{2+} ions produced by the corrosion reaction when the corrosion product could be iron carbonate [5, 113].

Iron sulphide formation can be either by direct solid state reaction between hydrogen sulphide gas and the steel surface or by iron precipitation [24]. The mechanism of this reaction will structure different types of iron sulphide, which results in the formation of two different layers. The first layer usually shows the presence of a very thin mackinawite film as a result of the direct reaction at the early stage of film formation. The second layer of iron sulphide will form due to the iron precipitation process and ionic conduction of S^{2-}, HS^{-}, Fe^{2+}, etc. through the semiconductive mackinawite matrix. The cathodic reaction will be supported by the conductive iron sulphide film on the other layer and the anodic dissolution of ferritic iron will process beneath the film by solid state diffusion and leave the Fe_3C phase with subsequent groove formation [24, 130]. In both cases the mechanical integrity of the growing film is weakened due to the migration of Fe^{2+}, which leaves a void at the metal interface. This undermining process can develop internal stress, which leads to film fracture causing potential localized corrosion [24, 125]. Figure 10-3 shows the mechanism of the sour film formation.

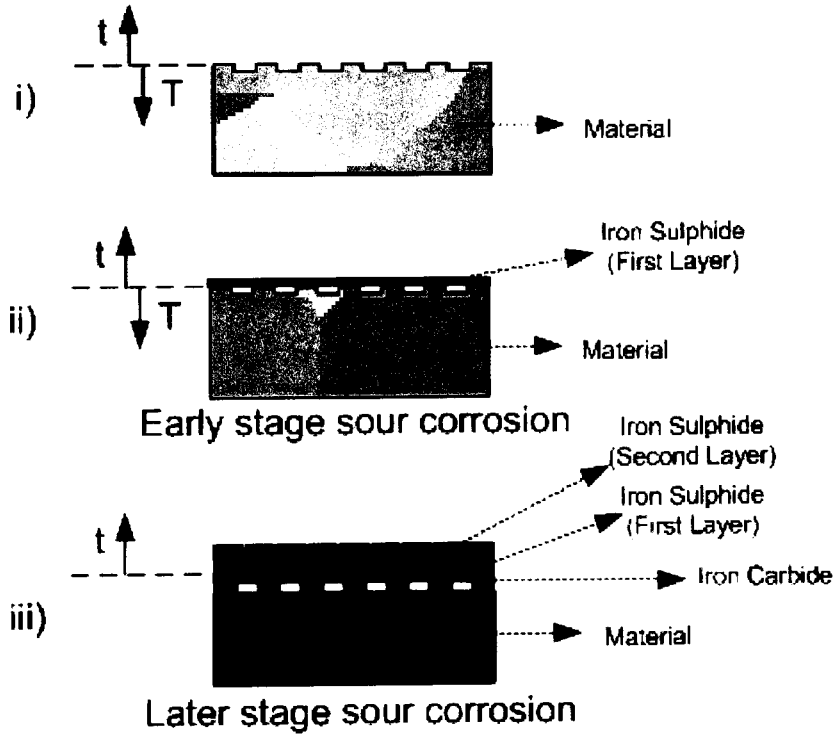

Figure 10-3: Sour corrosion film formation.

The literature has reported many types of iron sulphide that may form in sour environments – amorphous ferrous sulphide, mackinawite, cubic ferrous sulphide, smythite, greigite, pyrrhotite, troilite and pyrite [4]. The three main forms of iron sulphide that are commonly found in the field include mackinawite, which is a metastable form of FeS that forms in the presence of small amounts of hydrogen sulphide [24]. The second species is pyrrhotite, which is believed to be more thermodynamically stable than mackinawite due to the formation kinetics being much slower [24]. Pyrrhotites will form as a sour corrosion product when the iron sulphide level in the bulk fluid meets or exceeds the saturation levels [113]. The third species is pyrite, which is associated with the form at high hydrogen sulphide partial pressure [24].

Figure 6-7 shows that iron carbonate and iron carbide formed on the surface after 2.5 hours sweet pre-corrosion at 50°C, 1% NaCl. After the specimen was transferred to the sour vessel, an iron sulphide film starts forming on top of the existing iron carbonate and iron carbide. It is likely that the iron sulphide was formed by precipitation from the solution and transformation of the iron carbonate layers. Figure 6-15 to Figure 6-17 show that the morphology of the sour specimens is different at high temperatures and low temperatures. At higher temperatures the solubility of the iron sulphide increases but the solubility of the iron carbonates decreases [122]. At 90°C the morphology of the films present in the three difference layers is shown in Figure 10-4. The first layer is the existing iron mixed iron carbonate and iron carbide film formed in the pre-corrosion. The second layer is a very thin iron sulphide film, which is likely to be mackinawite formation as a result of the direct reaction between the hydrogen sulphide and the steel surface. The third layer of iron sulphide will form due to the iron precipitation process and the type of iron sulphide that forms on this layer will depend on the kinetics of the process. For the 90°C specimen, the iron sulphide layer is more likely to be mackinawite due to the EDX results, as shown in Table 10-1. Interestingly the XPS results in Table 6-5 also indicate that the Fe $2p_{3/2}$ spectrum detects a strong peak of iron sulphide and weak peak of iron carbide but not an iron carbonate peak. However, the C 1s spectrum indicates a weak peak of iron carbonate on the surface.

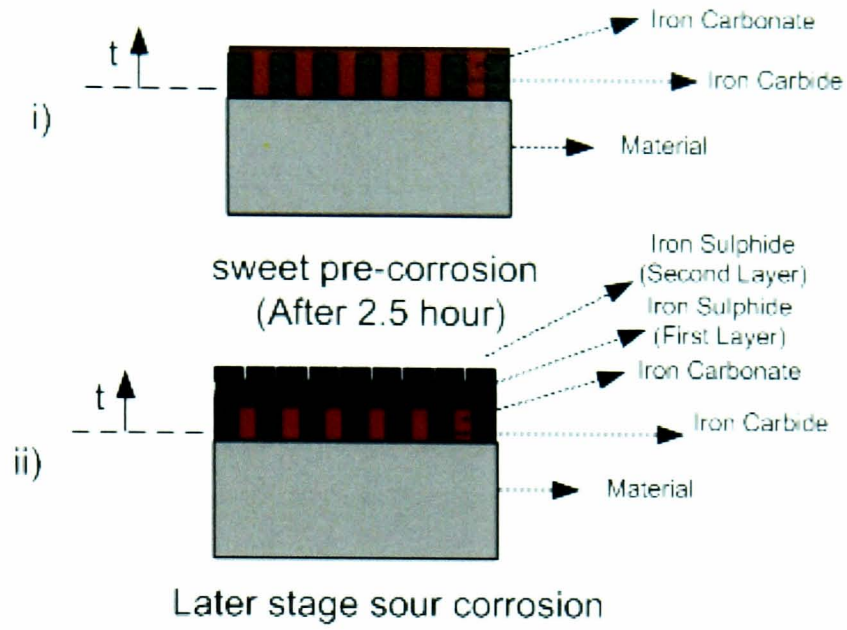

Figure 10-4: Film formation in sour environments at 90°C

Temp.	First layer	Second layer	Third layer
C %	5.2	8.6	7.4
O %	4.2	25.4	28.9
S %	0	12.7	11.2
Fe %	90.5	47.9	47.6

Table 10-1: EDX on the sour film at 90°C

At 15°C the morphology of the films also presents three different layers, as shown in Figure 10-4. However, the third layer morphology is changing due to the kinetics of the film formation changing at low temperature. The first layer is the same, consisting of the existing mix of iron carbonate and iron carbide film from the pre-corrosion. The second layer is most likely to be the same thin mackinawite film from the direct reaction process, which indicates that this process is not influenced by temperature, as shown in Table 10-2. The third layer morphology, which has a very low sulphur content and very high oxygen content most likely indicates the formation of iron carbonate film on the surface. Interestingly the XPS Fe $2p_{3/2}$ spectrum results in Table 6-5 also indicate a strong peak of iron carbonate and iron sulphide on the surface. This is considered to be due to the lower the temperature the lower the

solubility of the hydrogen sulphide and the carbonate acids have a higher solubility resulting in the formation of iron carbonate.

Temp.	First layer	Second layer	Third layer
C %	5.2	9.3	5.4
O %	4.2	21.7	34.9
S %	0	13.6	1.41
Fe %	90.5	48.8	56.8

Table 10-2: EDX analysis on the sour film at 15°C

The third sour specimen that emerged at 15°C during starting and increased the temperature during experiment to 90°C shows that the film content is more likely to be influenced by the lower temperature morphology, as shown in Table 10-3. This is supported by the SEM image in Figure 6.16. Figure 6.17 shows a small difference in film morphology. As the third layer morphology has very low sulphur content and very high oxygen content it most likely indicates the formation of iron carbonate film on the surface. However, the second layer film also has a low sulphur content but higher iron content, which is probably because the second layer film does not form a cross the entire surface thereby exposing the pre-corrosion film and iron carbide phase. This is attributed to the temperature change increasing the kinetic energy of the iron precipitation and forming iron carbonate and iron sulphide due to the rapid kinetic process.

Temp.	First layer	Second layer	Third layer
C %	5.2	5.7	3.5
O %	4.2	17.9	35.1
S %	0	1.5	0.4
Fe %	90.5	68.0	59.6

Table 10-3: EDX on the film at 15°C and to 90°C

10.3 Sweet film breakdown and pit initiation

The iron carbonate film damage and film re-growth on the steel surface may be one of the ways to initiate and propagate localized corrosion [53, 55]. It is suggested that the water chemistry, with respect to Fe^{2+} supersaturation, pH, temperature and sodium chloride concentration, influences the film dissolution and film breakdown process [55]. The specimen was immersed for 2 hours at 80°C and in 10% NaCl with saturated CO_2 to form a semi-protective film on the steel surface. Higher concentrations of sodium chloride lead to more chloride ions, which stimulate metal dissolution, especially at any particular point that is favourable for pitting initiation [3]. Han et al. also show that higher localized attack was obtained in higher NaCl concentrations [50]. After 2 hours, a mixed iron carbonate and iron carbide film was formed with a corrosion rate around 3.5 mm/yr. Then the solution of the pH was adjusted to 5.65 to reduce the solubility of Fe^{2+}, which corresponded to higher supersaturation, and, therefore, accelerated the precipitation of iron carbonate. This contributed to lowering the corrosion rate to 1.75 mm/yr [5]. During this period more compact iron carbonate film formed on top of the mixed iron carbonate and iron carbide film, as shown in Figure 7-2.

After 4 hours the 1000ppm $FeCl_2$ was added to the solution to achieve a high concentration of Fe^{2+} and increase the supersaturation of iron carbonate on the surface. The corrosion rate dropped to the range of 0.75 mm/yr, because the high supersaturation of Fe^{2+} was able to heal the damage to the iron carbonate film by re-growth of a new film layer on top of the existing iron carbonate and iron carbide. The pit propagation rate slowed after the iron carbonate film actively grew a cross the surface until 100 hours and covered around the pit area and partially covered the pits. There is no significant change in pit diameter and iron carbonate film growth between 100 hours and 150 hours. It is interesting to observe the results from the *in-situ* camera observation in Figure 7-3 on pit initiation after 5 hours at the uncorroded spot area, which propagated to 30μm in pit mouth diameter after 8 hours. Observation by the *in-situ* camera shows that the pit diameter growth is active in the first 3 hours after initiation and then the pit diameter propagation rate slows and stops at 10 hours, as shown in Figure 7-4. Figure 7-5 shows the SEM image of iron carbonate film on the surface after 150 hours. Some damage to the surface is apparent in which the film

leaves footprints of iron carbonate crystals. However, the film protectiveness in this case was not as low as 0.1 mm/yr, as reported in the literature, because the pH value at 5.65 affected the adherence and sealing porosity [5, 55]. Han et al. also showed that the solubility of $FeCO_3$ is at the saturation line between supersaturation and undersaturation at pH 5.65, 80°C and Fe^{2+} concentration at 20ppm [50]. In this film condition iron carbide is still left behind and provides local acidification, which facilitates galvanic corrosion, and, hence, promotes initiation and propagation of pitting. The structure of the mixed film plays an important role between the formation and breakdown of the protective film, which leads to localised attack. The pits initiating beneath the porous corrosion film will propagate into larger pits and the remaining corrosion film on top will completely fill the pit or be removed stepwise by flow, as shown in Figure 7-6 [55, 62].

Figure 7-11 in the results chapter shows that the pit depth measurements for the 6-hour test to 70-hour test indicated nonlinear growth. The corrosion rate reduces to 0.25 mm/yr after 6 hours and increases to around 1.25 mm/y between 30 hours and 70 hours. This corrosion rate is supported by Nesic et al. who predicted a corrosion rate of 1.6 mm/yr after 30 hours in 250ppm of $FeCl_2$, pH 5.8 at 80°C [20]. It was very interesting to discover that after 72 hours the corrosion rate dropped to 0.75 mm/yr and remained constant until the end of the experiments at 150 hours. The corrosion rate in the first 72 hours fluctuated due to the build up of the protective film and the passivation and repassivation process that takes place on the surface. It was very interesting to observe that the measured pitting depth indicated that the nonlinear growth between 30 hours and 70 hours could be due to the film build up process taking place, which promotes pitting initiation, reduces the pit propagation process and leads to corrosion rate fluctuation [194, 195]. This is supported by Cheng et al., who observed that the pit initiation stage could be indicated by the current fluctuation due to the kinetics of pit growth and repassivation of the internal surface within the pit and new deposit forming over the pit mouth [195]. This is also supported by Han et al. who indicate that localized corrosion is not propagated due to the scale formation taking place [55]. Schmitt et al. also show that the film thickness grew approximately 60μm after 50 hours and the film thickness did not change until 190 hours [62]. After 72 hours the pit depth obtained increased overtime until 150 hours and the corrosion rate is constant at 0.75 mm/yr. The magnitude of pitting is established according to

the three maximum pit depths for each set because it represents the worst-case scenario for pitting corrosion, which leads to pipeline failure. Tests with a duration of 120 hours and 150 hours were run in triplicate to better establish the trends that could differentiate inhibitor performance at various concentrations at a later stage. The pit depth difference between the maximum pit and average pit at 150 hours is around 20μm, however, the average pit depth and maximum pit depth establish a good trend for the pit propagation overtime. The measured pitting depth shows that the maximum pit depth obtained after 150 hours is 73μm and the average pit depth obtained is 53μm. The replicate pit depth is difficult to obtain, as the pitting mechanism beneath the protective corrosion layer involves the galvanic coupling between the steel and the Fe_3C left under the film, which force of acidification process and affects the local pH [29].

Figure 7-6 shows that the cross-section morphology of the film consists of a dark grey region, which is Fe_3C that is in contact with the steel surface, and a whitish flakes type film, which is $FeCO_3$ scattered and partially fills the film. A very thin layer of whitish film, which is $FeCO_3$, is also present in the outer layer of the film and isolates the total film from the water solution. Precipitation of $FeCO_3$ at the outer layer locally isolates the Fe_3C from the solution and reduces the porosity of the corrosion layer and causes an overall decrease in the corrosion rate, as shown in Figure 10-5. This leads to the formation of a protective film and explains the phenomena of the constant corrosion rate and constant film thickness between 72 hours and 150 hours. A possible explanation for pitting propagation between 70 hours and 150 hours is due to the $FeCO_3$ outer film layer isolating any disturbance in the local balance between the respective anodic and cathodic reaction. This eventually leads to possible local depletion in HCO_3^- or a decrease in the local solubility of Fe^{2+} and enhances localised reaction towards propagation activity. The argument has a good agreement with Han et al., who demonstrated that when iron carbonate is near the saturation level it will create a favourable condition for localised corrosion propagation [55]. This is supported by Jovancicevic et al. observed that potential stabilization is an indication of pit stable growth [196].

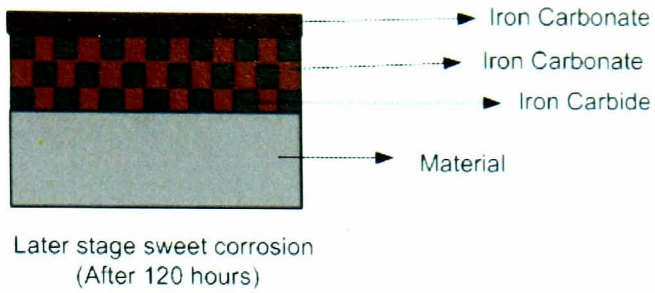

Figure 10-5: $FeCO_3$ at the outer layer locally isolating the Fe_3C from the solution

The pitting growth mechanism over time is shown in Figure 10-6. The mechanism is divided into three different zones. Zone 1, shaded green, represents the film breakdown stage. During this stage, depending on the operating condition, the formation of mixed iron carbonate and iron carbide films creates a favourable condition for pitting to initiate [3].

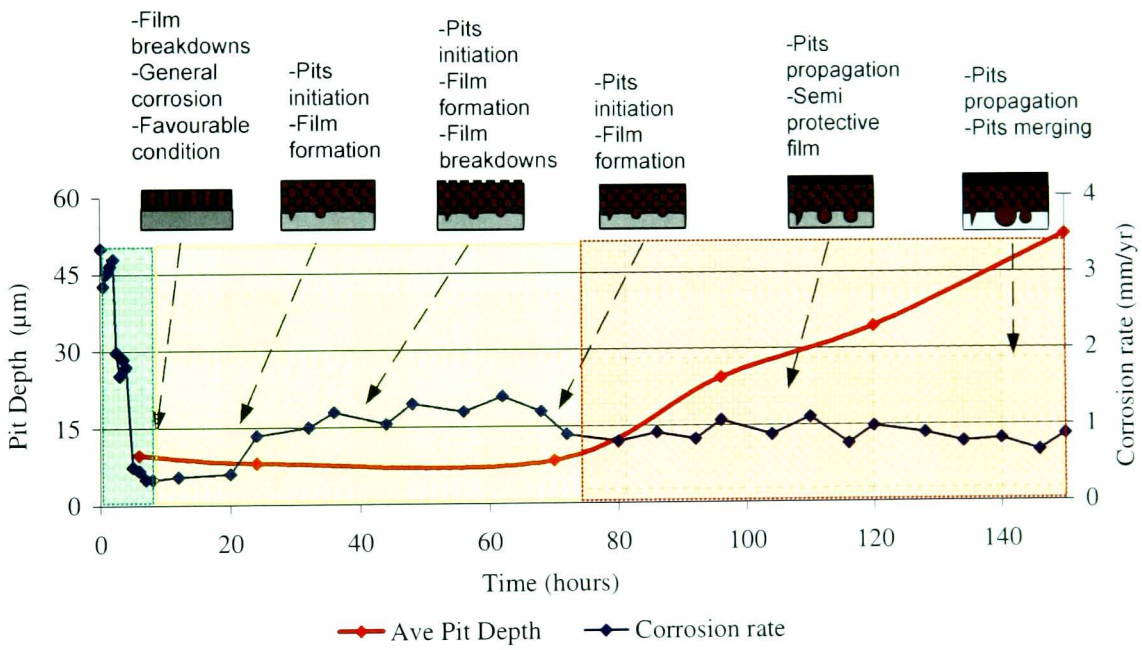

Figure 10-6: Schematic representation of pitting growth mechanism over time for X65 carbon steel in CO_2 saturated, 10% NaCl brine at 80°C, pH 5.65 and 1000ppm Fe^{2+}

During this stage, the corrosion damage is dominated by general corrosion. When the favourable condition is achieved, the pit initiation stage will start, which is represented by the yellow zone. During this stage, the film breakdown process will continue due to the kinetics of pit initiation and repassivation of the internal surface within the pit and new deposits forming over the pit mouth [195]. This process will

cause a fluctuation in the corrosion rate [194, 195]. When the semi-protective film is fully formed, the propagation stage will start, which is represented by the red zone. In this zone the corrosion rate is consistent but the pit will propagate deeper and larger over time [196].

10.4 Sour pitting behaviour

Under sour conditions, iron sulphide will precipitate on the metal surface reducing the general corrosion rate [126]. However, if iron sulphide is not fully covered the metal or iron sulphide film breaks down and there will be exposed anodic sites on the metal [126]. This will lead to a large cathodic area in the iron sulphide film, and, consequently, small anodes at breakdown locations, which will result in accelerated corrosion that may grow into pits or could also appear as a uniform attack with a rough surface [126, 130]. Figure 7-7 in the results chapter shows that pH has a significant effect in reducing the corrosion rate, which is also reported by Sun et al. [110]. Stable iron sulphide is more likely to form at pH 5.65 and as a result decreases the corrosion rate.

Increasing the Fe^{2+} concentration by adding 1000ppm of Fe^{2+} shows a contrary reaction by drastically increasing the corrosion rate to 16 mm/yr. This might be because additional Fe^{2+} ions in the solution have a direct reaction with the H_2S gas and are unable to form a protective iron sulphide film. However, there is no significant effect of pH and Fe^{2+} concentration in terms of pitting depth measurement. The main effects for pitting in these experiments were the influence of high chloride concentrations at 10% NaCl and high temperatures of 80°C. This is supported by Sun et al. who suggested that higher chloride concentrations might impair the iron sulphide scale consistency, and, consequently, cause pitting corrosion [110]. Kavarekval et al. also observed that higher temperature environments increase the pitting corrosion attack [132]. Figure 7-12 shows that increasing the exposure time generates more severe localized corrosion and deeper pits. After 4 hours exposure time the maximum pit depth recorded was around 10.2μm with a corrosion rate at 0.4 mm/yr.

After 96 hours the maximum pit depth increased to around 31μm and the average of 3 maximum pit depths is 29.8 μm with a final corrosion rate recorded at 0.3 mm/yr. These results are supported by Kavarekval et al., who reported that the pit depth increases over time and obtained a maximum pit depth of 25μm with a final corrosion rate of 0.33 mm/yr after 96 hours in 0.1% NaCl, 60°C, 0.02 bar H_2S and 1 bar CO_2 [132]. Sun et al. reported that pitting in a sour environment is a non-linear process and that the film passivation and repassivation activity will influence the pit propagation rate [129]. Kavarekval et al. reported that the pit passivation process seems to be dependent on the corrosion product precipitating within the pits [132]. Figure 7-9 shows that the iron in the film layer consists of two irregular layers of crystals in which the top layer poorly adhered to the surface and formed pit clusters [4, 130]. Kavarekval reported that the pit cluster was covered with numerous smaller pits and clusters [130]. This indicates that the pitting event takes place at the pit cluster and sustains an active pit environment at the pit mouth to propagate further and resulting consequential pit depth [133]. This is also supported by Kvarekval, by a SEM cross-section of the pit, shows that it was covered by a FeS corrosion film probably mackinawite [132]. Figure 10-7 shows the pit growth mechanism of sour pitting in sour environments. This shows that the pit will initiate at the film breakdown site and initiate the pits. Then, the film breakdown location will become small anodes and the iron sulphide film will be a large cathode, which will result in accelerated corrosion that may grow into pits [126, 130].

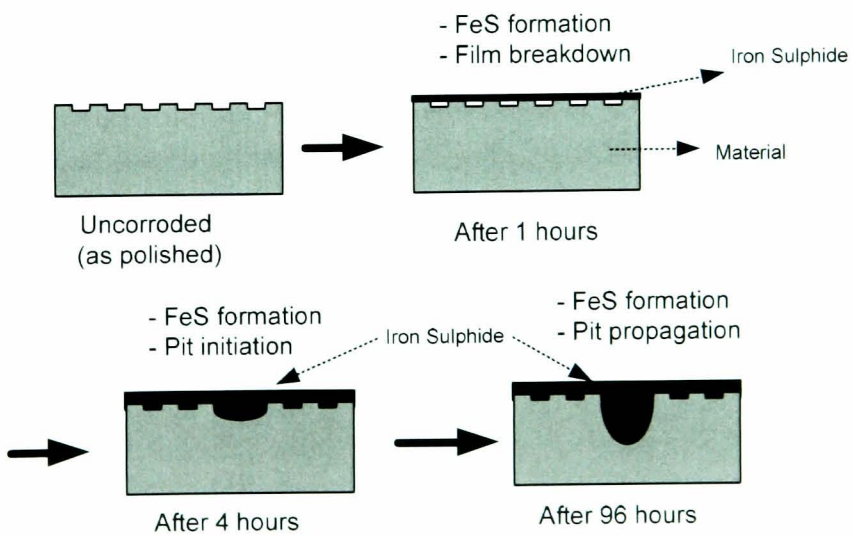

Figure 10-7: Schematic representation of pitting growth mechanism over time for X65 carbon steel in 10% H_2S 90% CO_2, 10% NaCl brine at 80°C and pH 5.65

10.5 Inhibition of pitting propagation by phosphate esters in sweet environment

Phosphate ester compounds are commonly used as an active component in the corrosion inhibitor due to its adsorption characteristics and effectiveness as an anodic corrosion inhibitor [98, 106]. Phosphate esters, in general, are used to inhibit general corrosion in the oil and gas environment, however, the synergistic effect of phosphate ester with other inhibitors have been suggested to reduce localized corrosion [106]. Most work on inhibitors has been carried out to study the inhibiting effect on the general corrosion or pitting corrosion starting from the initial stage of corrosion. However, in this present work, phosphate ester was used to study the effect on pitting propagation after 120 hours pre-corrosion. Figure 7-15, in the results chapter, shows that phosphate ester was added into the test vessel at 120 hours to stop pitting propagation. The inhibitor resulted in a small increase in the corrosion rate at lower concentrations between 10ppm to 50ppm but did not show any significant effect at higher inhibitor concentrations. This corresponds with the suggestion that the interaction between the phosphate ester and Fe^{2+} raises the corrosion rate, as the concentration of the inhibitor appears to be under the minimum value required to be adsorbed at the surface. Wong et al. shows that phosphate ester lowers the corrosion rate by preventing the growth of iron carbonate film when the concentration of phosphate ester is at least 25ppm [98]. Alink et al. and Wong et al. showed that phosphate ester forms a stronger complex with Fe^{2+} to form iron phosphate, which prevents the formation of iron carbonate layer and provides better protection to reduce further attack if applied above the minimum concentration required [98, 106].

In this test condition, the iron carbonate layer had already formed after 120 hours and adding phosphate ester at this time further affected the rate of precipitation of iron carbonate film, which affects the adsorption mechanism onto the existing film. At lower than minimum concentrations of phosphate ester, it is postulated to slow down the precipitation rate of iron carbonate and form a weak complex with Fe^{2+} resulting in a mixed reaction with less adsorption to the existing film, as shown in Figure 10-8. These types of film possibly change the film structure to increase the porosity by reducing the iron carbonate crystal structure and lead to loss of protection with consequent increase in the corrosion rate [98].

However, if the required amount of phosphate ester is applied, it will form a stronger complex with Fe^{2+} and prevent further formation of iron carbonate. The corrosion rate does not change, which could be because the existing iron carbonate film structure is still unchanged and provides the same corrosion protection. The literature shows that when phosphate ester is added after a long pre-corrosion time it may not have any effect on the corrosion rate due to the cementite layer on the surface of the steel [91, 98, 192]. It is interesting to observe that Akbar et al. also show that the inhibitor does not reduce the corrosion rate in the erosion corrosion test after pre-corrosion [197]. However, when phosphate ester is added at the beginning of the test, it shows a reduction in the corrosion rate [98]. This could be due to the phosphate ester mechanism, which forms a complex with Fe^{2+} and is transported through the porous film where it reacts with Fe^{2+} and the base metal. This is supported by Dougherty, who shows that above the threshold concentration, the inhibitor is transported to the metal surface for inhibition [198]. Further investigation would have to be carried out to study the product formed from complex Fe^{2+} and phosphate ester after long pre-corrosion.

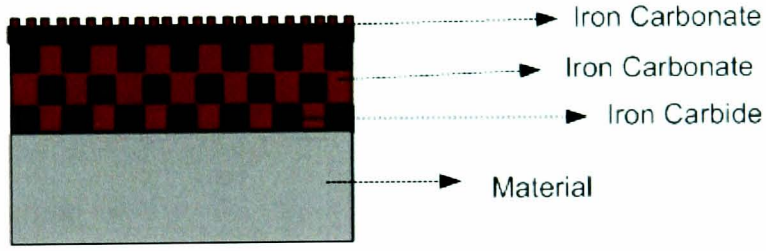

Figure 10-8: Effect of underdose of phosphate ester

Figure 7-18 in the results chapter shows that phosphate ester is able to significantly decrease and stop pitting propagation at doses above the minimum concentration required. The data show that the inhibitor works with effective performance after 25ppm. The pit depth shows a slight increase at 300ppm of inhibitor, which is postulated to be due to the higher inhibitor concentration beyond the critical value of the inhibitor concentration. Figure 10-9 compares the average pit depth and average general corrosion rate with the concentration profile and shows the phosphate ester mechanism on the concentration profile. The data show that after 75ppm the average pit depth and final corrosion rate shows the same trend.

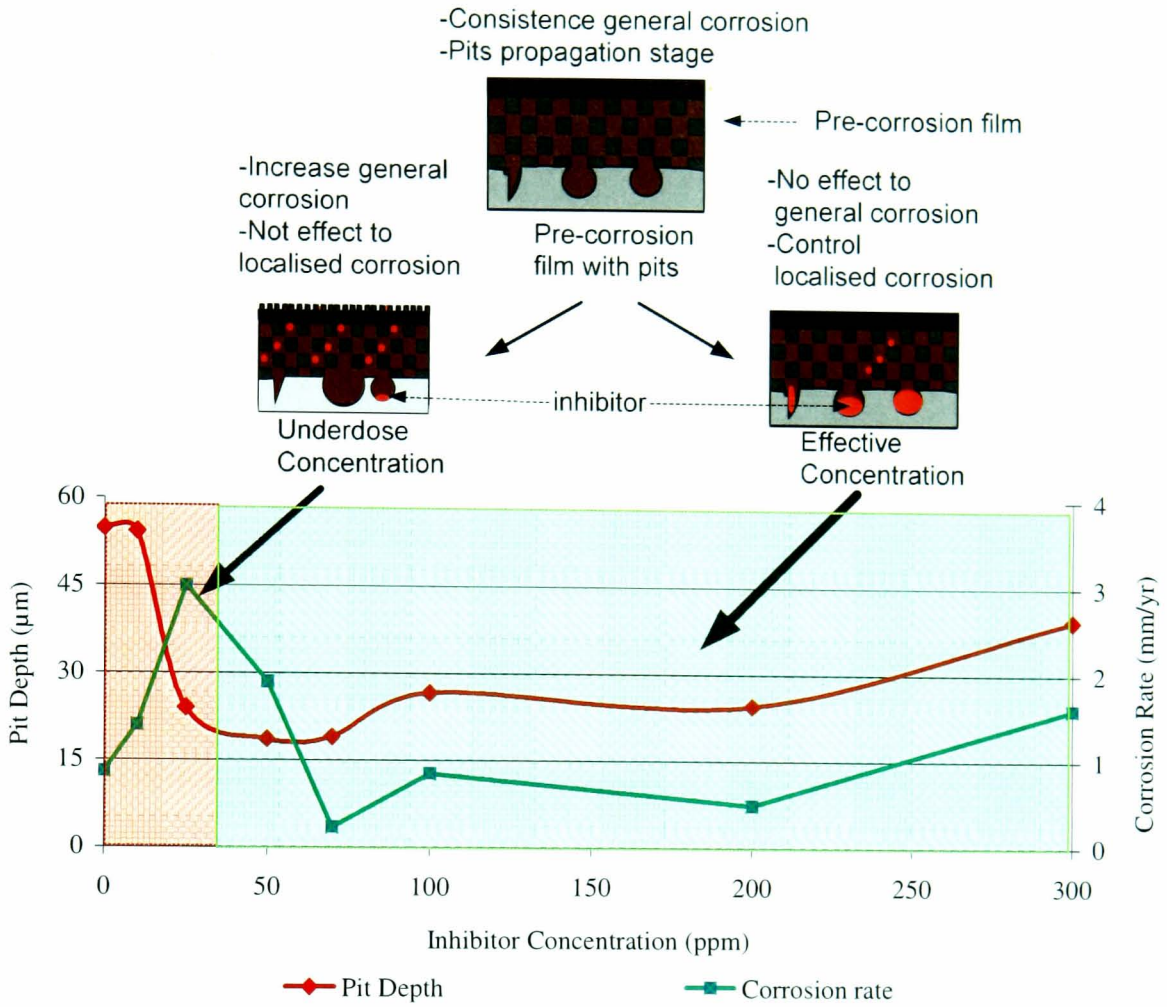

Figure 10-9: Schematic representation of phosphate ester mechanism on concentration profile on X65 carbon steel in CO_2 saturated 10% NaCl, pH 5.65, 1000ppm Fe^{2+}, at 80°C

It is interesting that, at 10ppm, the corrosion rate is still at a lower rate but produces a deep pit, which indicates that the formation of iron carbonate is still taking place on the surface and the inhibitor concentration still appears to be under the minimum value required. During this stage the inhibitor might be insufficient to transport to the metal surface to provide protection and the concentration is too low to affect the pre-corrosion layer [197, 198]. As the inhibitor concentration increases from 25ppm and 50ppm, it indicates the transition concentrations, which explain the slow rate of formation of iron carbonate due to the inhibitor transported to the metal surface. These concentrations also start forming a stronger complex between the inhibitor with Fe^{2+} by reducing the pitting propagation. The inhibitor works

effectively after 75ppm by reducing the final pit depth and does not increase the corrosion rate. During this stage the inhibitor is sufficient to transport to the metal surface to perform localised protection. It is interesting to note the relation between the pitting propagation and complexation of Fe^{2+} by phosphate ester after pre-corrosion. It is postulated that the phosphate ester is transported to the metal surface through the pre-corrosion layer to perform complexes with Fe^{2+} to form iron phosphate and is absorbed at the pitting site, which reduces the iron dissolution and prevents further pitting propagation. This is supported by Jovancicevic et al., who observed that anodic inhibitors strengthen the protective film by adsorption thereby reducing iron dissolution and lowering localised corrosion [199]. However, the adsorption behaviour of phosphate ester on the pit sites leaves the long pre-corrosion film without protection and is unable to control the general corrosion rate after long pre-corrosion.

10.6 Inhibition of pitting propagation by imidazoline in sweet environment

Extensive use of imidazoline corrosion inhibitors in oilfield applications to protect the carbon steel from general corrosion have generally been successful, however, the mechanisms of inhibition, especially with pitting, are not widely understood [42, 98, 104, 105]. In this set of experiments, imidazoline was used to study the effect on pitting propagation after 120 hours pre-corrosion. After 120 hours pre-corrosion, a mixed iron carbonate and iron carbide film had already formed and pitting had already been initiated and propagated. The effect of imidazoline was observed in terms of the corrosion rate and final pitting depth at the end of the experiments at 150 hours. Figure 7-17 in the results chapter shows a significant increase in the corrosion rate after 10ppm inhibitors were applied, however, no significant change in corrosion rate was observed for 25ppm, 50ppm, 75ppm and 100ppm.

Nevertheless, a slight decrease in corrosion rate was observed at 200ppm and 300ppm concentrations. This result is supported by the literature, which shows that imidazoline reduces the corrosion rate after a long period of pre-corrosion [65, 91, 98]. The results suggest that imidazoline interaction with iron carbonate film and

forming the imidazoline monolayer governs the mechanism to reduce the corrosion rate [65, 98]. At 10ppm inhibitor concentration, the corrosion rate increased significantly after the inhibitor was added and the improvement towards the end of the test shows that the interaction between the inhibitor, Fe^{2+}, and the existing iron carbonate film on the surface. Wong et al. and Chokshi et al. reported that in the presence of iron carbonate film, imidazoline inhibitor will interact with Fe^{2+} and create an adsorbing film to reduce the corrosion rate [65, 98]. Wong et al. reported that at concentrations above 25ppm, imidazoline prevents the growth of iron carbonate film on the surface, however, at 5ppm and 10ppm concentrations the formation of iron carbonate film continues to grow, however, it also reduces the corrosion rate [98].

In this test condition the inhibitor possibly tries to form a monolayer on the existing iron carbonate scale. However, due to the lower inhibitor concentration, the reaction mechanism with Fe^{2+} is weaker compared to the precipitation of the iron carbonate film resulting in a mixed film between the iron carbonate and imidazoline film, which reduced the corrosion towards the end of the test [65, 98, 105]. At concentrations between 25ppm and 200ppm, it is suggested that the inhibitor forms a monolayer on the existing iron carbonate film and prevents further formation of an iron carbonate film, as shown in Figure 10-10.

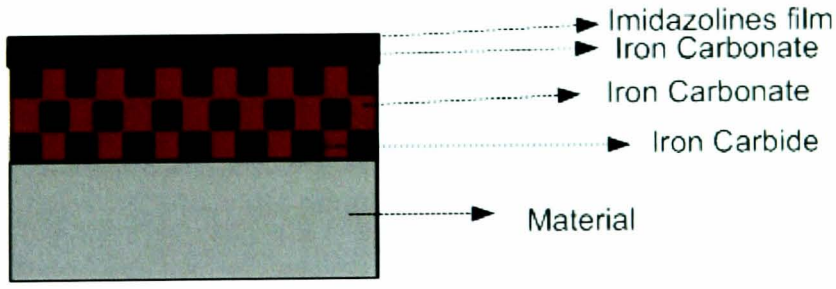

Figure 10-10: Imidazoline film

However, due to the thicker pre-corrosion film on the surface, no significant decrease in the corrosion rate was observed. This is supported by Chokshi et al., who observed that the film porosity was very similar after adding inhibitor or without inhibitor after 47 hours pre-corrosion time. Jovancicevic et al. shows that at higher inhibitor concentrations, the imidazoline film will form a thicker film with the

presence of larger micelles on the surface and lead to the formation of a bilayer [65, 105]. This explains that with 200ppm and 300ppm inhibitor the imidazoline forms a bilayer film and a thicker film resulting in a slight reduction in the corrosion rate.

Figure 7-20 in the results chapter shows that imidozoline was able to decrease and stop pitting propagation even at lower concentrations. This is supported by Jovancicevic et al., who observed that the imidazoline monolayer film formed a barrier to water and chloride ingress thereby protecting the surface [105]. In this work, it shows that the imidazoline film not only protects the surface from general corrosion but also from further pitting propagation after long pre-corrosion, as shown in Figure 10-11.

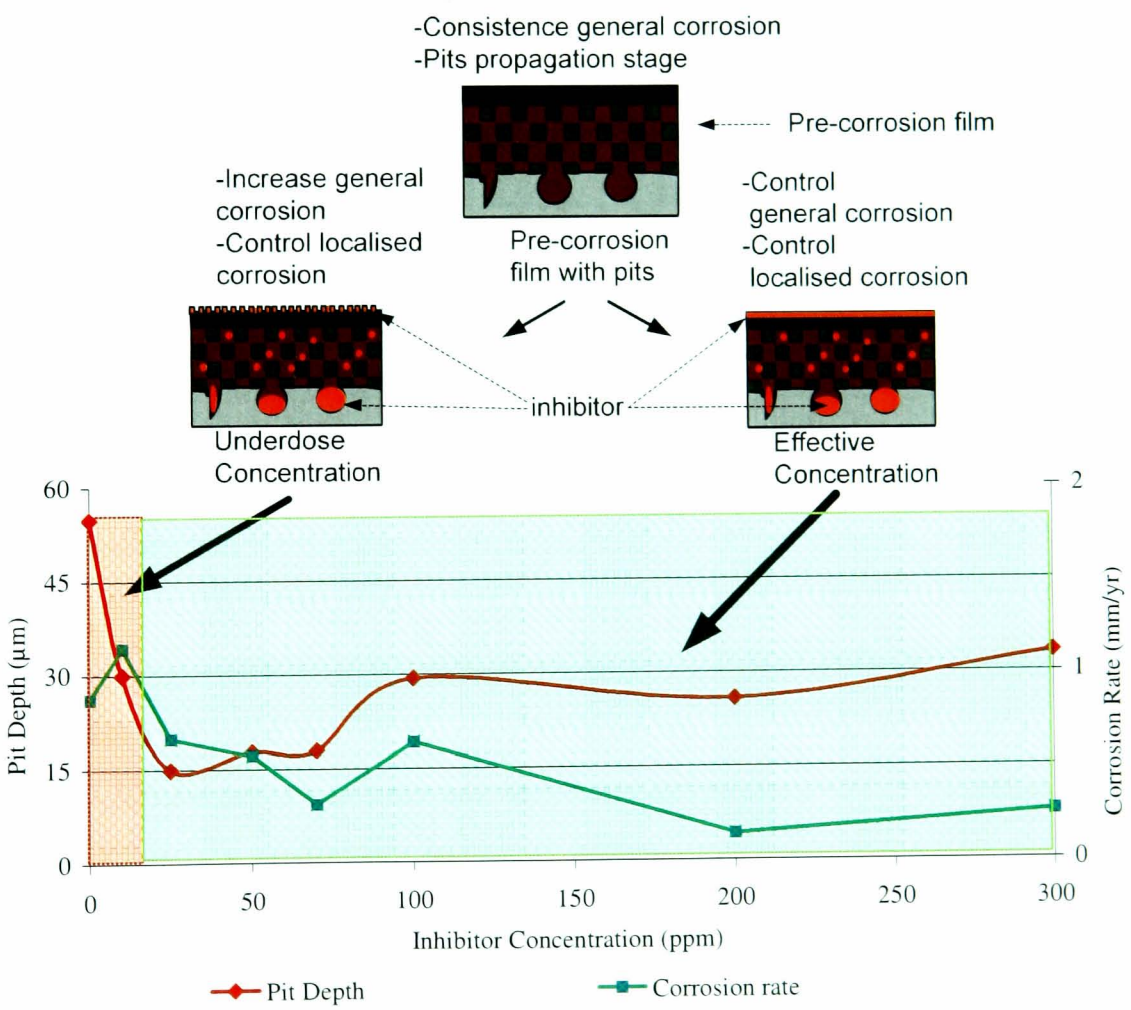

Figure 10-11: Schematic representation of imidazoline mechanism on concentration profile on X65 carbon steel in CO_2 saturated 10% NaCl, pH 5.65, 1000ppm Fe^{2+}, at 80°C

At an effective concentration, imidazoline adsorbs on the pre-corrosion film and Fe^{2+} on or near the metal surface. This is supported by Jovancicevic et al., who indicate that cathodic inhibitors adsorb onto the iron carbonate film thereby interfering with the proton reduction [199]. This is also supported by Wong et al. and Ramachandran et al., who observed that imidazoline interacts with Fe^{2+} and creates an adsorbing film on or near the metal surface [98, 200]. It is interesting to observe that at higher imidazoline concentrations, the final pit depth increases slightly even though the corrosion rate decreases. Chokshi et al. reported that the imidazoline film reduces the precipitation and supersaturation of iron carbonate to reduce the corrosion rate, however, this leads to slightly more acidic conditions on the metal surface [65]. It is postulated that at higher concentrations, a thicker bilayer film forms there by providing protection and reducing the corrosion rate, however, it leads to a more acidic environment at the metal surface, which results in slight pitting propagation [65, 105]. An alternative postulation could be that the thicker bilayer film created by the inhibitor film creates an under film localized environment that lead a favourable pitting condition. It is interesting to note that the imidazoline concentration controls the thickness of the imidazoline film layer and that thickness influences the protection mechanism to reduce the corrosion and localized attack. At lower imidazoline concentrations, the underdose effect slightly increases the corrosion rate but still provides a localised corrosion protection after long pre-corrosion. This is postulated to be due to the slow transport of imidazoline through the thicker pre-corrosion film to adsorb on the metal surface thereby causing the slow absorption of imidazoline on the pre-corrosion film.

10.7 monitoring of artificial pitting [illegible]
condition

Artificial pits made from microhardness indentation were developed with the aim of conducting preliminary laboratory testing on inhibitor assessment prior to a field trial. This artificial pit design simulated any indentation or small defect in the pipeline during the installation stage and operational stage that normally becomes a hot spot for pitting attack when the favourable conditions take place. This is supported by Chu et al., who show that pits are more likely to initiate at metallurgical discontinuities on the surface, such as grain boundaries, pearlitic colonies and banded

phases in the steel [104]. Laycock et al. also showed that pits are likely to initiate at occluded geometries because both ohmic and diffusional resistance are higher at these sites, which create a favourable condition for pitting [7]. Comparing these artificial pits with Turnbull et al.'s "pencil pit" and Nesic et al.'s "artificial pits", this artificial pit propagates naturally from the autocatalytic nature of pitting and growing in the direction of gravity compared to the existing artificial pit design by galvanic mechanisms that separate the anode and cathode [50, 69].

In this study it is difficult to monitor the growth of the pitting propagation either laterally or in depth direction due the extreme experimental condition and the nature of carbon steel pitting covering the pits with corrosion deposit. A long experiment time and higher Fe^{2+} concentration, creates a challenging environment to obtain good visibility on the pit surface. However, this *in-situ* observation technique is able to monitor the growth of the film on the surface of the pits and the reaction of the inhibitor with the film at the pit sites. This technique will be a powerful technique to observe the carbon steel pitting initiation process in shorter duration tests and observe the inhibitor effect on the pitting initiation. This technique is also very good for observing the pitting behaviour in stainless steel and other alloy materials. Comparing this *in-situ* technique with other similar observation techniques in the literature, this technique could perform at higher temperatures of up to 80°C in one single cell with a glass window without the need for a separate glass window unit in the corrosion loop [47, 78, 145, 146]. Moreover, by using this *in-situ* observation technique it is also possible to observe the early stages of iron sulphide film formation in sour conditions. Due to the blackish colour of the iron sulphide film, it is possible to observe and determine the effect of sour gas after sweet pre-corrosion using this technique.

Figure 8-1, in the results chapter, shows the formation of iron carbonate film repeating the same procedure from the previous Chapter 7 tests to reduce the corrosion rate before a potentiostatic current is applied at 100mV from OCP for 20 hours to initiate and propagate the pit. The average pit depth for the artificial pit from the three blank tests is 46.8μm and for the natural pit depth is 67.7μm. Comparing the average natural pit obtained from the potentiostatic method procedure with the natural pit growth procedure from the previous experiment shows that this method accelerates the pitting propagation process and reduces the experiment time by 85% or 6 days but

still obtains the desired pit depth. There was about 20μm difference in the average final pit depth between the artificial pit and natural pit on the surface, however, this was due to the extreme testing environment and the nature of pitting itself. One of the main benefits of the artificial pit technique is that the *in-situ* camera can monitor the surface area of the artificial pit from the early stage of the experiment until the end of the experiment. Figure 10-12 shows the *in-situ* condition of the artificial pit at the start of the experiment and before the end of the experiment. This shows that the film grows on the film as well as inside the artificial pit. This is supported by FTIR analysis in Figure 8-17, which identifies the film as iron carbonate film. However, the absorption of iron carbonate film on the artificial pit could be weaker due to the geometry and simulated film breakdown and lead to artificial pit propagation.

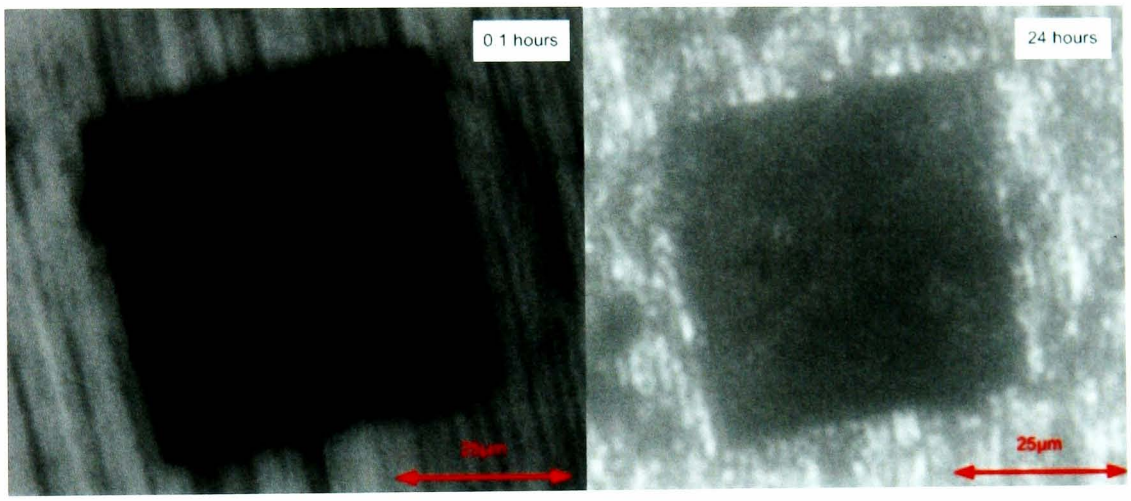

Figure 10-12: *In-situ* artificial pit surface at start of the test and after 24 hours in CO_2 saturated 10% NaCl, pH 5.65, 1000ppm Fe^{2+}, at 80°C

Using the *in-situ* observation technique it is not possible to monitor the growth of the artificial pits in lateral and depth direction because the corrosion product constituted at the edge of the pit mouth covering the cementite layer left behind and the pit propagates beneath the original corrosion film on top of the edge of the pit mouth [47, 194, 195]. Figure 10-13 shows the artificial pits growth mechanism based on the *in-situ* observation findings.

The literature shows that pitting initiation generally occurs at occluded geometry sites on the surface [7, 104]. Creating artificial pits simulates a hot spot where the pits will grow. Iimura et al. observed that the pH inside the artificial pits

dropped due to the chloride ions being concentrated within the pit [194]. Cheng et al. observed that chloride ions migrate into the inclusion site and create an occluded cavity, which causes dissolution of the metal cations [195]. Therefore, the artificial pit growth is due to the concentration of Cl^- inside the artificial pits, which continues to propagate when the deposit fills the artificial pits and creates a favourable condition for pitting growth. It is very interesting to compare the mechanism of the artificial pit and the natural pit in Figure 10-6. Although both pits experience similar conditions they propagate using two different electrochemical techniques. This shows that the artificial pit using the accelerated potentiostatic technique is able to simulate the natural pitting growth technique in a more time efficient way.

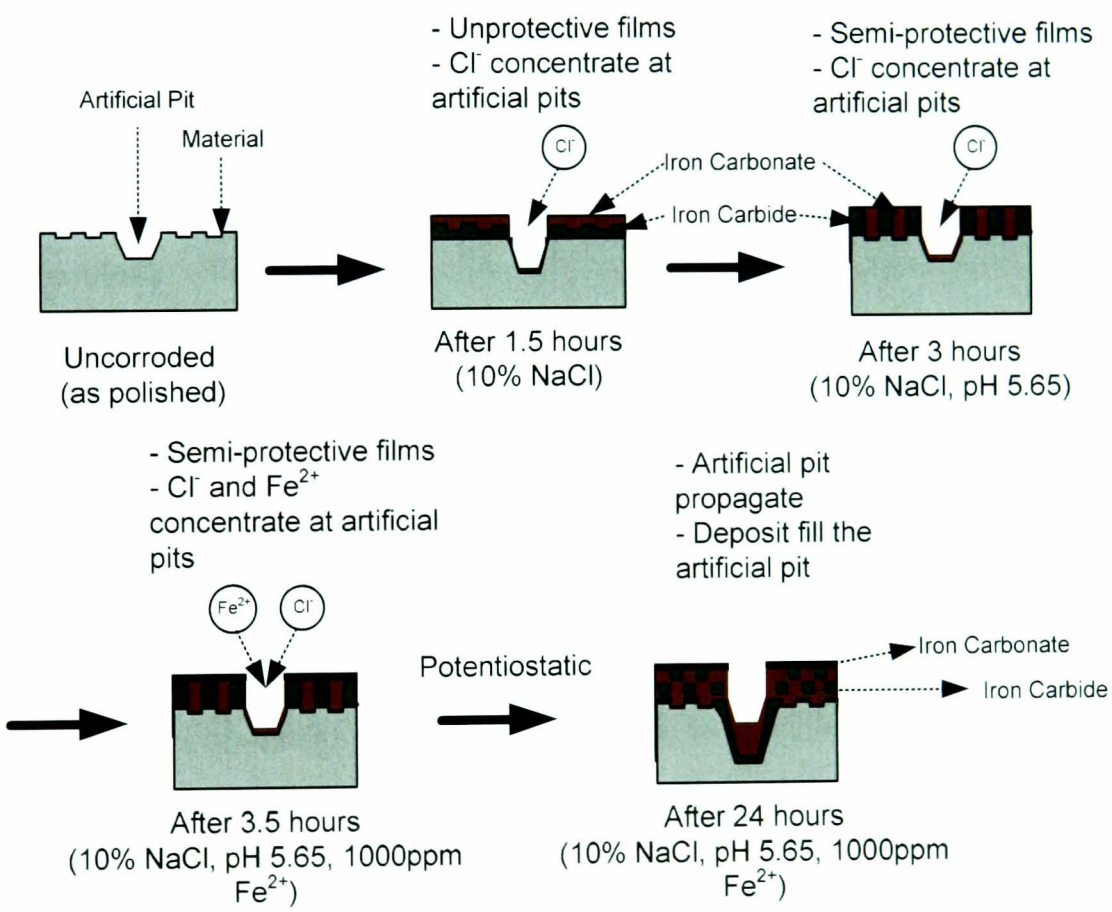

Figure 10-13: Artificial pit growth mechanism in CO_2 saturated 10% NaCl, pH 5.65, 1000ppm Fe^{2+}, at 80°C for 24 hours

10.8 The effect of phosphate ester on artificial pit growth under sweet condition

Figure 8-3 from the results chapter shows that lower concentrations of inhibitor result in higher current up to 80mA, however, when the inhibitor concentration increases there is no significant difference in the current compared with the blank specimens. It is interesting to compare the potentiostatic current behaviour with linear polarization results from the long test in Chapter 7. Both tests show the same trends with an increase in the corrosion current at lower concentrations and no significant effect in terms of corrosion current at higher concentrations. Figure 8-13 shows the difference between the maximum and average pits that grow on the surface. It shows that with a lower phosphate ester concentration, both the artificial and natural pits propagate deeper than the blank specimens, however, when the concentration increases the propagation rate slows down resulting in a reduction of pitting depth. It is interesting to note that the difference in pit depth between the artificial pit and natural pit reduce when the phosphate ester concentration increases, which indicates that both pits corresponded in the same way towards inhibitor performance. These similar trends indicate that the pitting activities and the reaction with the inhibitor are comparable between the artificial pits and the natural pits. Comparing these results with the previous long test results from Chapter 7 shows similar trends in terms of pit depth corresponding to inhibitor concentrations.

At lower phosphate ester concentrations, pit propagation is significantly higher than the blank test. It is postulated that less adsorption of the inhibitor molecules within the pit sides results in the reduction of inhibitor performance and consequential increase in the propagation activities [7]. An alternative postulation may be that at this concentration it generates an interaction from various chemistries contained in the inhibitor resulting in the nullification of the corrosion inhibitor [7]. It is interesting that the *in-situ* camera shows that at lower inhibitor concentrations, the artificial pit was covered by a black deposit and the FTIR analysis also indicated the absence of inhibitor at the artificial pits. It is clear that the reason for the pit propagation was due to the black deposit covering the pit and blocking the inhibitor from accessing the pit, which generated a localized environment that favours pit propagation activity. However, after the inhibitor concentration appears to be above the minimum value

required the propagation rate decreased because the inhibitor absorbed in the pit sites and stopped the black deposit covering up the pit there by avoiding the creation of a localised cell. This is supported by the FTIR analysis, which indicated the presence of inhibitor at the pit sides. The inhibitor molecular was absorbed in the pit sides resulting in the formation of an inhibitor film at the pit sides, which delayed the propagation of the localised cell [7]. Figure 10-14 shows the phosphate ester mechanism on the artificial pits. It shows that an effective concentration of phosphate ester is attracted to Fe^{2+} and the low pH sites inside the artificial pits form iron phosphate to provide protection against localised corrosion. However, at lower concentrations an underdose effect is observed due to the failure to transport to the pit site and react with the pre-corrosion product, which leads to the formation of a black deposit that covers the pits. Further investigation would have to be carried out to study the black deposit product formed at the pit sites during the underdose condition.

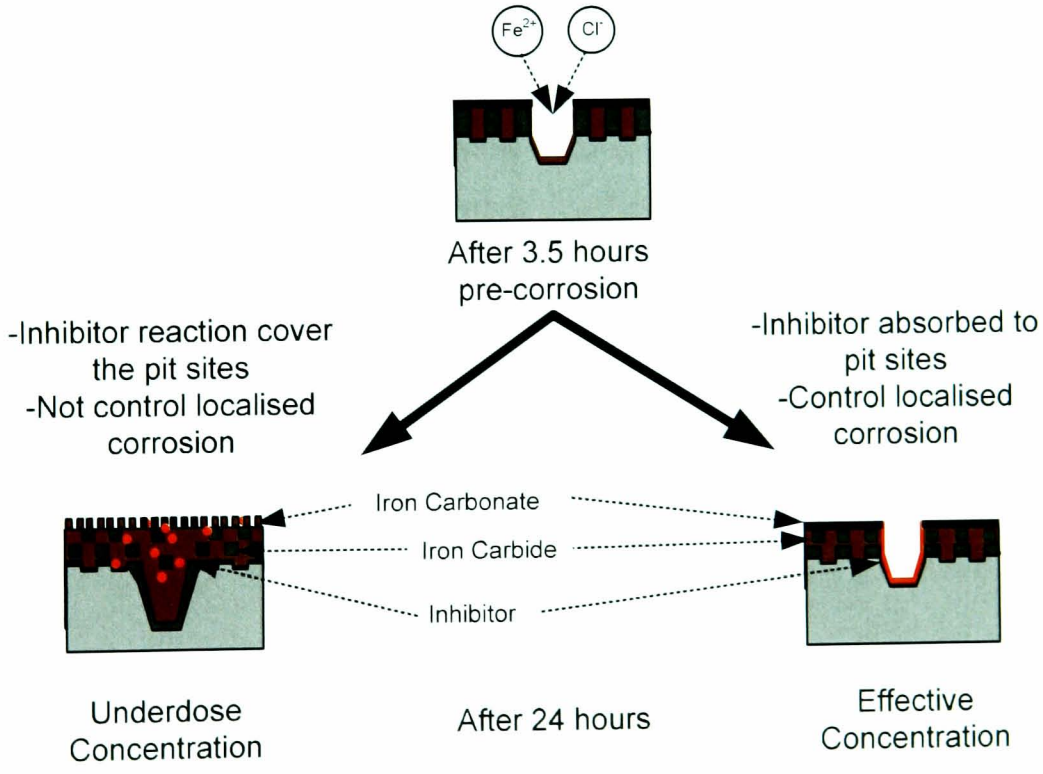

Figure 10-14: Phosphate ester mechanism in CO_2 saturated, 10% NaCl, pH 5.65, 1000ppm Fe^{2+}, at 80°C for 24 hours

10.9 The effect of imidazoline on artificial pit growth under sweet condition

Figure 8-5 from the results chapter shows that Imidazoline provides better protection to reduce the applied current, as the inhibitor concentration increases, which might be because the inhibitor protects the overall surface by forming a film of imidozaline. It is interesting to compare the potentiostatic current behaviour with the linear polarization results from the long test in Chapter 7. Both tests show the same trend, which reduces the corrosion current as the inhibitor concentration increases, which could be because the inhibitor forms a thicker film at higher concentrations. Figure 10-16 shows the difference between the maximum and average pits that grow on the surface. It shows that both artificial and natural pits propagate in the same manner and propagate deeper at higher concentrations compared to the blank specimens. This similar trend indicates that the pitting activities and the reaction with the inhibitor are comparable between the artificial pits and natural pits, which indicates that both pits corresponded in the same way towards inhibitor performance.

Comparing these results with the previous long test result from Chapter 7 shows a similar trend in terms of pit depth corresponding to inhibitor concentrations. Both results show that the inhibitor reduces the pit propagation even at lower concentrations; however, the artificial pit test shows a significant increase in pit propagation rate at higher inhibitor concentrations compared to the slight increase in the long test. It is postulated that this is due to the difference in pre-corrosion time between the tests, in that the artificial pit only has 4 hours pre-corrosion test, which corresponds to a thinner iron carbonate film. This means that at higher concentrations, imidazoline could form a thicker film to form the barrier, which leads to more acidic environments at the metal surface there by influencing the pit propagation. An alternative postulation may be because at higher concentrations it generates an overdose effect reaction within the inhibitor and Fe^{2+} resulting in the nullification of the corrosion inhibitor [7]. It is interesting that the *in-situ* camera shows that at higher inhibitor concentrations, the artificial pit was covered by the black deposit and the FTIR analysis also indicates that the absence of inhibitor at the artificial pits and the film area. It is clear that the reason for the pit propagation was due to the black deposit covering the pit and blocking the inhibitor from accessing the pit, which

generates a localized environment that favours pit propagation activity. However, if the inhibitor concentration is below the maximum values required, the inhibitor will not be absorbed on the surface and form an imidazoline film to provide protection from general corrosion attack and localised corrosion attack. This is supported by the FTIR analysis, which indicated the presence of inhibitor on the film area and at the pits site. The inhibitor molecules were adsorbed on the surface resulting in inhibitor film formation thereby delaying the propagation of localised cells [7]. Figure 10-15 shows the imidazoline mechanism on artificial pits. It shows that an effective concentration of phosphate ester is attracted to Fe^{2+} on or near the metal surface and on the film. Imidazoline will form an imidazoline monolayer, which governs the mechanism and reduces the corrosion rate [65, 98]. However, at higher concentrations an overdose effect is observed due to the thicker imidazoline film forming a barrier, which leads to more acidic environments at the metal surface, thereby influencing pit propagation.

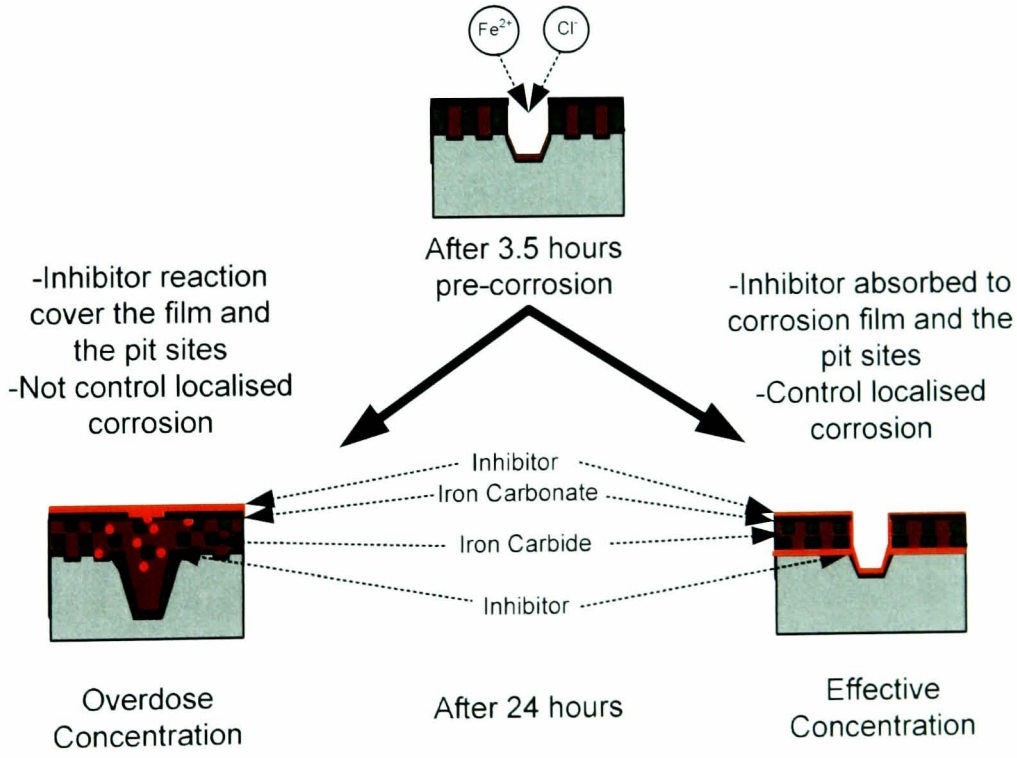

Figure 10-15: Imidazoline mechanism in CO_2 saturated, 10% NaCl, pH 5.65, 1000ppm Fe^{2+}, at 80°C for 24 hours

10.10 *In-situ* monitoring of artificial pit growth under sour condition

Artificial pit techniques with *in-situ* camera observation have been developed for sour environments to evaluate pitting corrosion inhibitor. The design for artificial pits in sour environments is similar with sweet environments using microhardness indentation. The geometry of the artificial pit affects the stability of the iron sulphide film and becomes a hot spot for film breakdown and pitting propagation [139, 141]. Marsh et al. used the artificial pit technique to evaluate inhibitor performance in a sour environment by a pre-corrosion electrode coupled through an ammeter to a larger electrode [141]. Figure 9-1 in the results chapter indicates that the formation of iron sulphide provided a protective film on the surface by reducing the corrosion rate of 1 mm/yr in the first 2.5 hours before the potentiosatic current was applied at 100mV form OCP for 20 hours to activate the artificial pit and propagate to the desired depth. Due to the lower pH and high chloride concentration, the film that forms after 2.5 hours is semi protective, poorly adherent and easily removed, which could lead to a pitting attack [135, 139, 141].

The *in-situ* camera shows in Figure 9-9 that after introducing the sour gas the blackish film gradually deposited on the sample surface and after 1 hour, the film grew over the artificial pit surface. FTIR analysis shows that the blackish film was iron sulphide film consisting of mackinawite and pyrite. After 1 hour, the observation through the glass wall showed that the solution turned black in colour, which could be because of the dissolution from the iron sulphide film due to the low solubility in water. After the 24-hour test, the average artificial pit depth was 31.6μm and the average natural pit was 34.9μm; approximately a 2.7μm difference in depth. This suggests that the average condition in the artificial pit and natural pit shows similar behaviour in propagation stability; however, the maximum natural pit on the surface reached 49.3μm due to the morphology of the iron sulphide film, which may be subject to local breakdown. This could be because the propagation process over a period of time is related to the diffusion characteristic associated with the pit depth; however, the pit depth trend is similar [141].

Figure 10-16 shows the artificial pit growth mechanism in a sour environment based on the *in-situ* observation findings. It is interesting to observe that the artificial pits in both the sweet and sour conditions start growth due to chloride ion migrating into artificial pits [195]. However, under sour conditions the quick formation of iron sulphide fills the artificial pit mouth within one hour. The propagation mechanism is different between sweet and sour pitting due to the conductive iron sulphide film. Due to the artificial pit geometry, the films that form on top of the pit mouth are not stable and lead to film breakdown. This will create a large cathodic area in the iron sulphide film, and, consequently, small anodes at the breakdown locations, which will result in accelerated corrosion that may cause the artificial pits to grow [126, 130]. It is very interesting to compare the mechanism of the artificial pits and the natural pits in the sour environment. Both pits have a similar propagation mechanism but use different electrochemical techniques. This shows that the artificial pits using the accelerated potentiostatic technique in a sour environment are able to simulate the natural pitting growth technique in a more time efficient way.

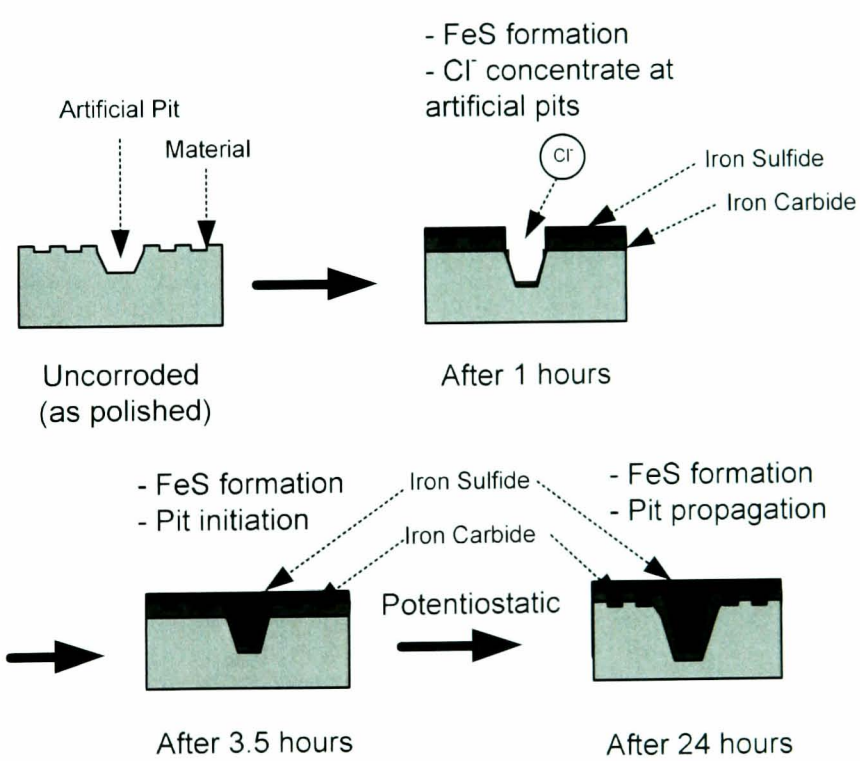

Figure 10-16: Artificial pit growth mechanism in 10% H_2S, 90% CO_2 , 10% NaCl at 80°C for 24 hours

10.11 The effect of nonoxynol-6 phosphate on artificial pit growth under sour conditions

Corrosion inhibitors are often used in sour environments to control general and localised corrosion [141, 116]. Corrosion inhibitors are adsorbed in the iron sulphide film and change the morphology and wettability of the film to provide protection to the surface [139]. The active component in the inhibitor may reduce the dissolution of scale into an aqueous environment or hinder the diffusion control led growth of iron sulphide scale or prevent spilling of the scale surface [116]. Nonoxynol-6 phosphate inhibitor belongs to the phosphate ester inhibitor type group. Figure 9-3 from the results chapter shows that inhibitors can reduce the corrosion rate gradually even at lower concentrations. This is supported by Wang et al. who show that 15ppm concentration of polyethoxylate alkyl phenol could provide protection to reduce the corrosion rate [139]. The performance of the inhibitor to reduce the corrosion rate increases as the inhibitor concentration increases; however, the pit depth analysis in Figure 9-13 shows a contradictory effect. The difference between the average and maximum pit depth is about 20μm for the natural pit at 25ppm but as the concentration increased to 100ppm and 200ppm the difference decreased significantly. This suggests that the inhibitor reaction was not very stable below the minimum concentration desired to mitigate pitting attack. The inhibitor performs at an effective concentration at 100ppm and it is interesting that the FTIR found the inhibitor element on the film area and pit area. The *in-situ* camera observation shows that the inhibitor prevents the growth of iron sulphide film on the surface and from the FTIR analysis it suggests that the inhibitor creates an inhibitor monolayer to prevent general corrosion and pitting corrosion.

However, at 200ppm inhibitor concentration, Figure 10-17 shows that the inhibitor reduces the general corrosion but promotes the propagation of pitting. It is postulated that an overdose occurs at a concentration of 200ppm, which forms a thicker bilayer film on the surface causing the sulphide film to be unstable, which is also associated with the higher current in Figure 9-5. The thicker film formation provides a better barrier to reduce the corrosion rate; however, it leads to a higher acidic environment on the metal surface, which results in pitting propagation [65, 105]. This is supported by the *in-situ* camera observation, which shows that the

solution turns milky in colour. An alternative postulation could be that at 200ppm it generates a direct interaction with H_2S gas and Fe^{2+} ion resulting in the nullification of the corrosion inhibitor function to reduce the pitting propagation.

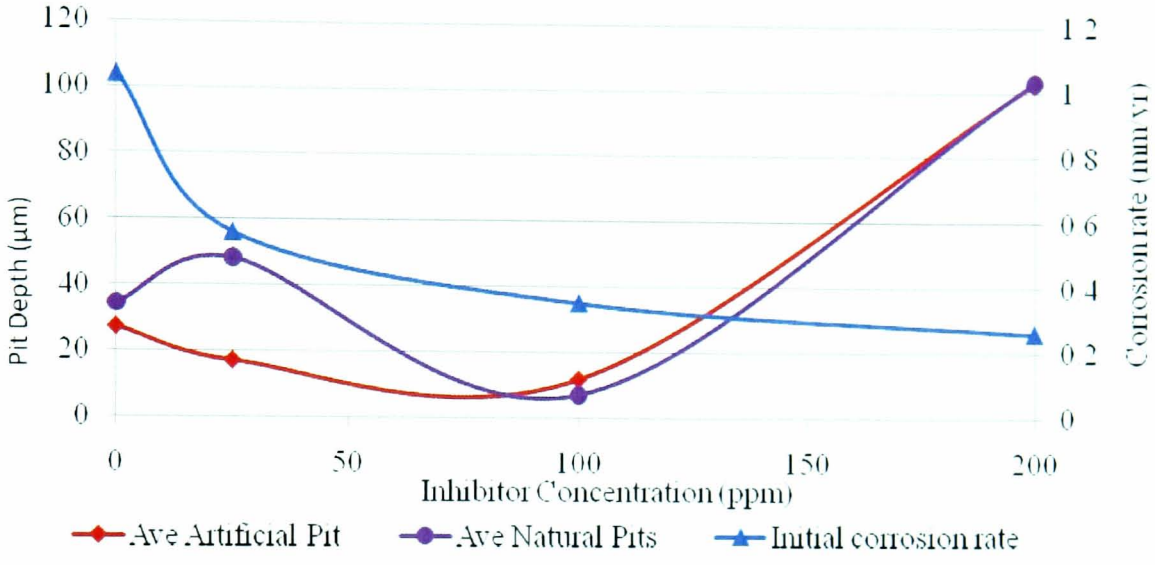

Figure 10-17: Corrosion rate and pit depth data on concentration profile for Nonoxynol-6 phosphate inhibitor on X65 carbon steel, 10% H_2S, 90% CO_2 at 80°C

This is supported by the FTIR results, which show that none of the inhibitor elements were found on the film area or pitting site. Figure 10-18 shows the nonoxynol-6 phosphate mechanism on artificial pits based on the *in-situ* observation findings.

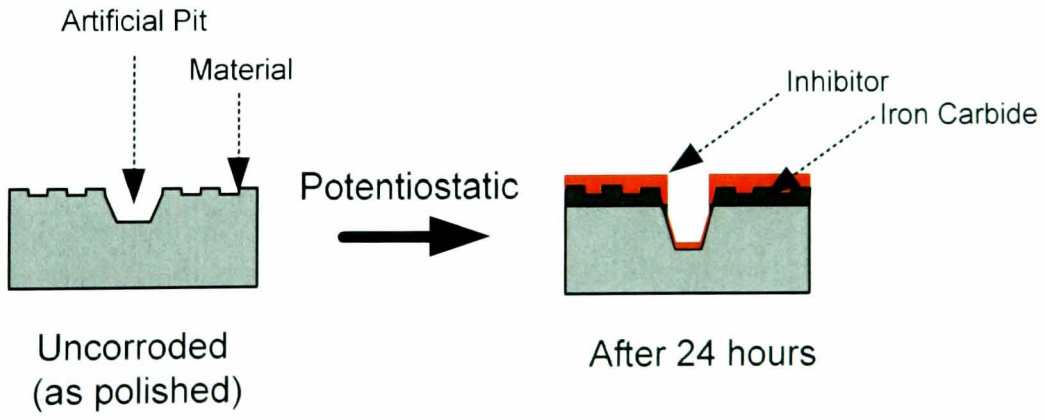

Figure 10-18: Nonoxynol-6 phosphate mechanism on X65 carbon steel, 10% H_2S, 90% CO_2 at 80°C after 24 hours

It shows that at an effective concentration, nonoxynol-6 phosphate is attracted to Fe^{2+} on or near the metal surface and on the film. Nonoxynol-6 phosphate will form a monolayer, which governs the mechanism to reduce the general corrosion and localised corrosion [65, 98]. It is very interesting to compare the nonoxynol-6 phosphate mechanism with the imidozoline mechanism in sweet environments. Nonoxynol-6 phosphate belongs to the phosphate ester group of inhibitors; however, both inhibitors show similar a mechanism in inhibiting general corrosion and localised corrosion. This shows that both inhibitors could be classed as mixed anodic/cathodic inhibitors due to their interaction with Fe^{2+} and formation of an inhibitor film at both the anodic and cathodic sites [196].

10.12 The effect of poly alkyl pyridines on artificial pit growth under sweet conditions

Poly alkyl pyridine inhibitors belong to the imidazoline type inhibitor group that was used in the sour condition. Figure 9-6 from the results chapter shows that the inhibitor could greatly reduce the corrosion rate even at lower concentrations. This is supported by Wang et al., who shows that a 15ppm concentration of imidazoline type inhibitor could reduce the risk of both a general and localised attack [139]. The performance of the inhibitor to reduce the corrosion rate increases as the inhibitor concentration increases, however, the pit depth analysis in Figure 9-15 shows that the inhibitor promotes the pit propagation if the concentration is applied below the minimum value required. A small difference between the average pit and maximum pit depth for artificial pit and natural pit suggests that the inhibitor reaction was similar across the surface. The inhibitor performed at optimum concentration at 200ppm to reduce the general corrosion rate and pitting attack, as shown in Figure 10-19. However, at 25ppm, the inhibitor only provided protection for general corrosion but not against pitting propagation. It is postulated that below the minimum concentration required the inhibitor destructively adsorbed on colloidal iron sulphide, which formed around the mouth of the pit [141]. This is supported by Marsh et al. who show that at 15ppm, the imidazoline group inhibitor only provides protection against general corrosion but provides little protection against localised corrosion [141]. Interestingly the FTIR analysis found the inhibitor element at the pit site area for 100ppm and 200ppm, however, the inhibitor was absent for 25ppm. This suggests

that above the minimum concentration, the inhibitor actually adsorbed to the pit mouth area and only formed a protective inhibitor film at the pit site. The FTIR results show that none of the inhibitor elements were found on the film surface area away from the pitting. The *in-situ* camera observation shows that the growth of iron sulphide film slows down for 100ppm and does not grow for 200ppm. This suggests that the inhibitor actually hinders the diffusion control led growth of the iron sulphide film on the surface and provides localised protection at the pit site [116].

Figure 10-20 shows the poly alkyl pyridine mechanism on artificial pits based on the findings of the *in-situ* observation. It shows that at an effective concentration, poly alkyl pyridine is attracted to Fe^{2+} and low pH sites inside the artificial pits and forms a film of inhibitor to provide protection to localised corrosion and general corrosion. It is very interesting to compare the poly alkyl pyridine mechanism with the phosphate ester mechanism in sweet environments. Poly alkyl pyridine belongs to the imidazoline group of inhibitors; however, both inhibitors show a similar mechanism. Both inhibitors inhibit the localised corrosion by blocking the anodic sites on the surface.

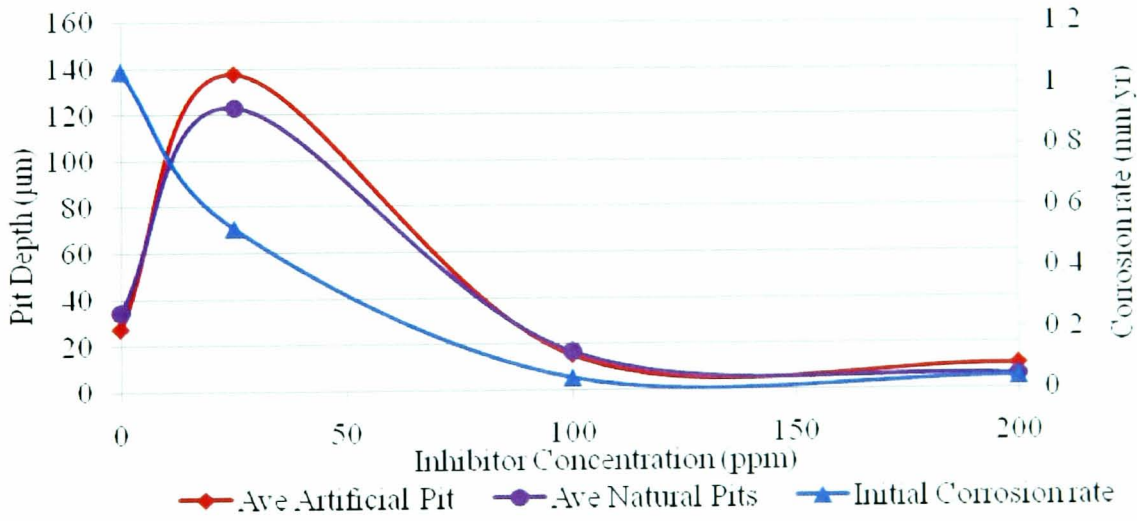

Figure 10-19: Corrosion rate and pit depth data on concentration profile for poly alkyl pyridine inhibitors on X65 carbon steel, 10% H_2S, 90% CO_2 at 80°C

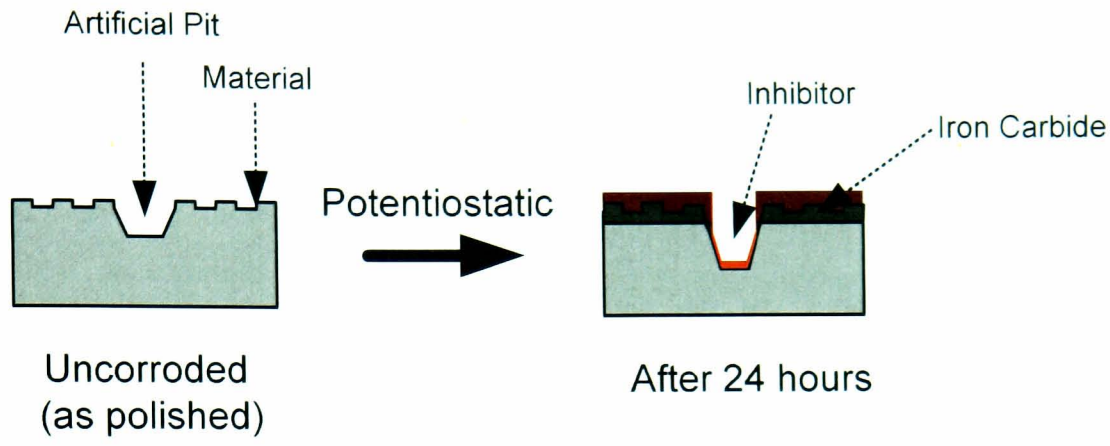

Figure 10-20: Poly alkyl pyridine mechanism on X65 carbon steel, 10% H_2S, 90% CO_2 at 80°C after 24 hours

Chapter 11 Conclusion and future work

11.1 Conclusion

An extensive study on inhibition of pitting corrosion of carbon steel X65 in sweet and sour conditions was carried out using the electrochemical technique and post-test surface analysis techniques. The mechanisms related to the pitting behaviour and inhibitor under sweet and sour conditions were identified and analysed. The interaction between the corrosion film and inhibitor play an important role in reducing and stopping pitting corrosion if the effective concentration of the inhibitor is applied to the system. These important findings are summarised in the following sections.

11.1.1 *In-situ* visualisation rig and sour rig design and setup

- An *in-situ* visualisation technique was developed to monitor the film growth and pitting process on X65 carbon steel surface under sweet and sour conditions.

- It was possible to observe the film growth and early stages of natural pit growth using an *in-situ* visualisation technique under sweet conditions. By using this technique it was also possible to observe the interaction between the corrosion inhibitor and corrosion product on the surface and at the pit site area to understand the inhibitor mechanism. However, it was not possible to monitor pitting propagation using this technique due to the extreme experimental condition and the nature of carbon steel pitting covering the pits with corrosion deposit.

- It was possible to observe the early stage of film growth using an *in-situ* visualisation technique under sour conditions. It was also possible to observe the interaction between the corrosion inhibitor and corrosion product on the surface and at the pit site area using this technique to understand the inhibitor mechanism. However, it was not possible to monitor pitting growth using this technique due the nature of the iron sulphide film covering the pits.

- A sour corrosion rig was developed and was able to perform sour corrosion experiments successfully and safely. The rig was equipped with an *in-situ* visualization technique with an option to perform normal sour experiments. This rig was also able to perform two experiments at a time and was equipped with all the necessary safety equipment.

- *In-situ* visualisation experiments and normal sour experiments were successfully performed using the sour corrosion rig to study localised corrosion behaviour for X65 carbon steel.

- The artificial pit technique developed in this study was able to propagate under sweet and sour conditions to a desired pit depth using the potentiostatic method. This technique was also able to simulate the natural pitting propagation under sweet and sour conditions with accelerated time duration.

11.1.2 Characterisation of the surface film formed from sweet and sour corrosion.

- Surface analyses of early sweet and sour corrosion products were studied using SEM, FIB/SEM, AFM, EDX and XPS, SEM and FIB/SEM.

- The morphology of sweet films were studied from 0.5 to 72 hours and it was observed that the corrosion film is denser and more compact on the external part of the film and some porous structures at the bottom of the film.

- FIB-SEM observed that at 0.5 hours the cross-section shows a good bonding between the film to the metal surface, which is denser and more compact at the film interface and some porous structures at the base of the film adjacent to the substrate.

- AFM analysis observed that the film morphology starts to become rough after 1 hour due to the iron carbonate film build up filling the gap that is left from the anodic process. SEM analysis also observed that the morphology of the

sweet film is denser and more compact on the external part of the film and some porous structures at the bottom of the film.

- XPS analysis observed that the iron carbonate component is present and grows at the external part of the sweet film followed by iron carbide growth under it to make the film semi protective.

- Under sour conditions, iron sulphide is the predominant product for the 90°C specimens and provides better protection compared to the 15°C specimens. The studies also show that both iron carbonate and iron carbide are present in the sour specimens.

- SEM analysis for the sour specimens observed that the films are composed of two different layers. The base layer deposit grows across the material interface uniformly and the second layer grows in scattered domains on the base layer.

11.1.3 Investigation of pitting corrosion in sweet and sour conditions.

- Under sweet conditions, the pitting process was studied at various times from 6 to 150 hours. Pits are able to initiate and propagate to around 66.3μm to 73.4μm depth after 150 hours. The pits under the studied test conditions did not show a consistent pit depth increase over time until 70 hours of immersing time. However, tests at 96, 120 and 150 hours show a linear increase of pitting depth over time.

- Under sour conditions, the pit depth recorded for the first 4 hours was around 8.9μm. The pit propagates to around 31.4μm depth after 96 hours exposure time.

- Pitting in sweet and sour will start propagating once the film formation reaches a steady state condition.

- Both phosphate ester and imidazoline inhibitors showed excellent performance to stop pit propagation in sweet conditions if the effective concentration is applied.

- Under the effective concentration of phosphate ester, there was no significant different effect in terms of reducing the corrosion rate due to the iron carbonate film that formed across the surface before the inhibitor was added.

- The effective concentration of imidazoline showed good performance in reducing the general corrosion rate.

11.1.4 Evaluation of inhibitor performance using artificial pit technique under sweet conditions.

- The potentiostatic approach for artificial pits was studied under the sweet conditions. It was found that it allows the artificial pit to propagate to around 48.9μm to 53.1μm after 24 hours.

- Both phosphate ester and imidazoline inhibitors showed excellent performance to stop pit propagation if the effective concentration was applied.

- *In-situ* cameras were able to observe the formation of a black deposit on the surface due to the underdose reaction of phosphate ester with the corrosion product covering the artificial pits, which resulted in a favourable condition for pits to grow. However if the effective concentration of phosphate ester inhibitor is applied, it shows that the inhibitors stop the formation of the black deposit.

- FTIR analysis is able to identify iron carbonate film on the blank specimens and detect the presence of the inhibitor on the surface after the inhibitor test. FTIR analysis reveals that phosphate ester inhibitors inhibit pits by adsorbing the inhibitor at the pit site but are absent in the surrounding film. Imidazoline

inhibitor inhibits the pits by absorbing at the pit site and in the surrounding film.

11.1.5 Evaluation of inhibitor performance using artificial pit technique under sour conditions

- The potentiostatic approach for artificial pits was studied under sour conditions. It allows the artificial pits to propagate to around 31.6μm depth after 24 hours.

- Both nonoxynol-6 phosphate and poly alkyl pyridine inhibitors showed excellent performance to stop pit propagation if the effective concentration is applied.

- Both nonoxynol-6 phosphate and poly alkyl pyridine inhibitors showed excellent performance to reduce the corrosion rate.

- The *in-situ* camera observed that an iron sulphide film could cover most of the surface in 60 minutes. However if the effective concentration of the inhibitor is applied, it shows that the inhibitors actually delay and stop the formation of the black film, which could be because of the iron sulphide.

- FTIR analysis is able to identify the iron sulphide film on the blank specimens and detect the presence of the inhibitor on the surface after the inhibitor test. The FTIR analysis reveals that the poly alkyl pyridine inhibitors inhibit pits by absorbing the inhibitor at the pit site but are absent in the surrounding film. Nonoxynol-6 phosphate inhibitor inhibits the pits by adsorbing at the pit site and in the surrounding film.

11.3 Industrial relevance

- The artificial pit technique developed in this study could be adapted to the field corrosion test coupon. This will create a hot spot on the coupon, which could provide information about general corrosion and pitting corrosion.
- Figure 11-1 shows the inhibitor selection recommendation for pitting corrosion inhibition for oil and gas X65 pipeline field application based on the findings from this study.

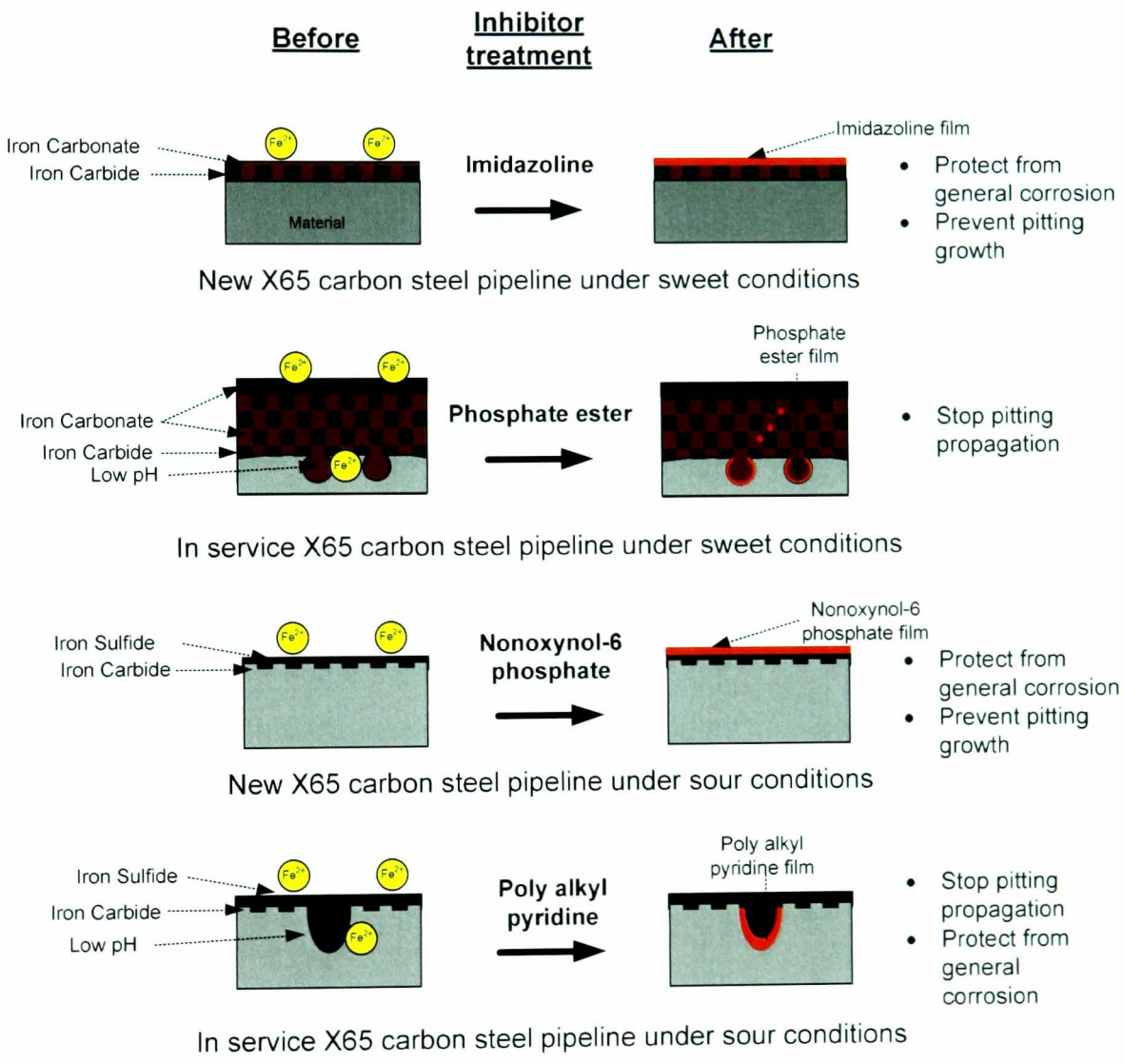

Figure 11-1: Inhibitor selection recommendation for localised corrosion inhibition for oil and gas X65 pipeline field application

11.3 Recommendations for future research

- Further mechanistic studies for corrosion and pitting corrosion inhibitors in sweet and sour conditions are able to identify the reacting species resulting from the reaction on the surface, which may comprise both corrosion products and corrosion inhibitors. A further mix of inhibitors needs to be done to observe the effect on general corrosion and pitting corrosion to study the mechanism of the action.

- The effect of pitting with the effective concentration of inhibitor is an interesting area and a very important issue in field service. Further investigation needs to be done relating to effective concentrations of inhibitor to gain a better understanding of the mechanism of failure due to this problem.

- Further corrosion research on the sweet corrosion effect on sour corrosion in X65 transmission pipeline applications is required since many sweet service pipelines on file become sour service pipelines due to oil and gas reservoir ageing. The characteristic of sour corrosion film needs comprehensive investigation to identify the various types of iron sulphide to understand the behaviour for those species towards the protectiveness of iron sulphide film and localised corrosion.

- The need for further development in *in-situ* monitoring techniques is desirable to investigate the film breakdown and pitting behaviour. *In-situ* cameras with 3D lens or 3D microscopes could identify the pit depth *in-situ*. The *in-situ* monitoring can also be combined with the Localised Corrosion Technique (LCM) developed by Baker Hughes to correlate the *in-situ* current peak with the pitting activity observed by the *in-situ* camera with time.

- The artificial pit technique can be developed further to better understand the pitting corrosion behaviour. The size of the artificial pit could be reduced to 2μm to allow for the growth in diameter. The artificial pit technique could also be used in the study of stainless steel.

References

1. Vedage H, Ramanarayanan T.A, Mumford J.D, Smith S.N, "Electrochemical growth of iron sulphide films in H_2S saturated chloride" Corrosion Vol.49 No.2 (1993) p.114-121
2. Wu.S.L, Cui.Z.D, He.F, Bai.Z.Q, Zhu.S.L, Yang.X,J "Characteristic of the surface film formed from carbon dioxide corrosion on N80 Steel" Material Letter Vol 58 (2004) p.1076-1081
3. Nesic S "Key issues related to modelling of internal corrosion of oil and gas pipelines – A review" Corrosion Science Vol 49 (2007) p.4308-4338
4. Sun.W, Nesic.S, Papavinasam.S "Kinetics of corrosion layer formation. Part 2-Iron sulphide and mixed iron sulphide/carbonate layers in carbon dioxide/hydrogen sulphide corrosion" Corrosion Vol 64. No.7(2008) p.586-599
5. Kermani M.B, Morshed A "Carbon dioxide corrosion in oil and gas production-A compendium" Corrosion Vol 59. No.8 (2003) p.659-683
6. Horsup D.I, Dunstan.T.S, Clint J.H "Breakthrough corrosion inhibitor technology for heavily foulded system" Corrosion Vol 65. No.8(2009) p.527-544
7. Moloney J.J, Mok W.Y, Gamble C.G. "Compatible corrosion and kinetic hydrate inhibitors for wet sour gas transmission lines" NACE Corrosion Conference (2009) paper 09350 p.1-23
8. Johnson.B.V, Al-Gharfi.M.J.H, Al-Harthy.A.S.M, Kompally.S.N "The use of carbon steel in highly sour oil and gas production systems" SPE 114140 (2008) p.1-9
9. Marsh.J, The.T, Ounnas.S "Corrosion management for aging pipelines-experience from the Forties Fields" SPE 114141 (2008) p.1-10
10. Koch G.H, Brongers M.P.H, Thompson N.G. "Corrosion costs and preventive strategies in United States" NACE international No. FHWA-RD-01-156 P.1-12
11. Chernov.V.Y, Makarenko.V.D, Kryzhanivskyi.E.I, Shlapak.L.S "On the causes of corrosion fracture of industrial pipeline" Material Science Vol 38. No.6 (2002) p.880-883
12. Gatlin L.W "Evaluation of inhibitor for wet, sour gas gathering system" Corrosion, May (1978) p.9-17

13. Li.D.G, Feng.Y.R, Bai.Z.Q, Zheng.M.S "Characteristics of CO_2 corrosion formed on N80 steel in stratum water with saturated CO_2" Applied Surface Science Vol 253 (2007) p.8371-8376
14. Papavinasam S, Doiron A, Revie R.W. "Model to predict internal pitting corrosion of oil and gas pipelines" Vol 66. No.3(2010) p.1-11
15. McKay S.F, Lasebikan B.A, Mok W.Y, Collins J.A, Leontieff A, Duncan G.S "Corrosion inhibition challenges in a mature subsea production facility" NACE Corrosion Conference (2009) paper 09112 p.1-42
16. J.M, Zuo.Y "Corrosion behaviour in simulated solutions within pits and crevices on carbon steel" Corrosion Engineering Vol 42 No.3 (2007) p.203-206
17. J.M, Zuo.Y "Corrosion behaviour in simulated solutions within pits and crevices on carbon steel" Corrosion Engineering Vol 42 No.3 (2007) p.203-206
18. Szyprowski.A.J "Methods of investigation on hydrogen sulphide corrosion of steel and its inhibitors" Corrosion Vol 59. No.1 (2003) p.68-81
19. Nordsveen.M, Nesic.S, Nyborg.R, Stangeland.A "A mechanistic model for carbon dioxide corrosion of mild steel in the presence of protective iron carbonate films – Part1: Theory and verification" Corrosion Vol 59. No.5 (2003) p.443-456
20. Nesic.S, Lee.K.L.J "A mechanistic modal for carbon dioxide corrosion of mild steel in the present of protective iron carbonate films – Part 3: Film growth model" Corrosion Vol 59. No.7 (2003) p.616-628
21. Stewart S, Jovancicevic V, Menendez C, Moloney J, Wamburi W. "Evaluation of a new sour gas inhibitor for field applications via localised corrosion monitoring techniques" NACE Corrosion Conference (2010) paper 10274 p.1-17
22. Velazquez, Caleyo F, Hallen J.M "Technical note: Field study – Pitting corrosion of underground pipelines related to local soil and pipe characteristic" Corrosion Vol 66. No.1 (2010) p.1-5
23. Palmer A.C, King R.A."Subsea pipeline engineering" PennWell,USA (2008) p.27-59; p.190-245
24. Singer M, Brown B, Camacho A, Nesic S. "Combined effect of carbon dioxide, hydrogen sulphide and acetic acid on bottom of the line corrosion" Corrosion Vol 67. No.1 (2011) p.1-16

25. Papavinasam S, Revie R.W, Doiron A. "Predicting corrosion of oil and gas pipelines review of corrosion science models" NACE Corrosion Conference (2005) paper 05643 p.1-14
26. Ruzic V, Veidt M, Nesic S "Protective iron carbonate films- Part 3" Corrosion Vol 62. No.8 (2007) p.758-769
27. Schmitt G, Scheepers M, Siegmund G. "Inhibition of the top of the line corrosion under stratified flow" NACE Corrosion Conference (2001) paper 01032 p.1-20
28. Amri J, Gulbrandsen E, Nogueira R.P "The effect of acid on the pit propagation in CO_2 corrosion of carbon steel" Electrochemistry communications 10 (2008) p200-203
29. Crolet J.L, Thevenot N, Nesic S "Role of conductive products in the protectiveness of corrosion layers" Corrosion Vol 54. No.3 (1998) p.194-203
30. Fontana.M.G "Corrosion engineering" McGraw Hill, New York (1986) p.1-85; p. 445-502
31. Schutze M "Corrosion and environmental degradation: Volume 1" Wiley-vch, Germany (2000) p.1-66; p.162-166; p.472-506
32. Scully.J.C "The fundamentals of corrosion" Pergamon Press, England (1990) p.54-120; p.165-176
33. Uhlig.H.H, Revie.R.W "Corrosion and corrosion control" John Wiley and Sons, Canada (1985) p.1-122
34. Marcus.P "Corrosion mechanisms in theory and practice" Marcel Dekker, New York (2002) p.1-18
35. Craig B.D "Fundamental aspect of corrosion films in corrosion science" Plenum Press, New York (1991) p.1-46; p.109-128
36. Tait.W.S "An introduction to electrochemical corrosion for practicing engineers and scientist" Paisodocs Publications, p.1-62
37. Waseda.Y, Suzuki.S "Characterization of corrosion products on steel surfaces" Springer, New York (2006) p.1-31
38. ASTM International "Standard guide for examination and evaluation of pitting Corrosion" G46-94 (2005) p.170-177
39. Jordan.M.M, Feasey N, Johnston C, Marlow D, Elrick M "Biodegradable scale inhibitor laboratory and field evaluation of green carbonate and sulphate scale

inhibitors with deployment histories in the North Sea" The Royal Society of Chemistry (2007) p.286-290

40. Sastri.V.S "Corrosion inhibitors" Wiley, New York (1998) p.567-576; p.633-645

41. Jiang.X, Zheng.Y.G, Qu.D.R, Ke.W "Effect of calcium ions on pitting corrosion and inhibition performance in CO_2 corrosion of N80 steel" Corrosion Science Vol 48 (2006) p.3091-3108

42. Ruzic V, Veidt M, Nesic S "Protective iron carbonate films- Part 1" Corrosion Vol 62. No.5 (2006) p.419-432

43. Ruzic V, Veidt M, Nesic S "Protective iron carbonate films- Part 2" Corrosion Vol 62. No.7 (2006) p.598-611

44. European Federation of Corrosion Publication " A working party on CO_2 corrosion control in oil and gas production: Design consideration edited by M.B Kermani & L.M. Smith " Institute of Materials, England (1997)

45. Waard C.D, Milliams D.E "Carbonic acid corrosion of steel" Corrosion Vol 31. No.5 (1975) p.117-181

46. Choi Y.C, Nesic S. " Corrosion behaviour of carbon steel in supercritical CO_2 – Water environments" NACE Corrosion Conference (2009) paper 09256 p.1-20

47. Nyborg R "Initiation and growth of mesa corrosion attack during CO_2 corrosion of carbon steel" NACE Corrosion Conference (1998) paper 0048 p.1-11

48. Lopez D.A, Schreiner W.H, Sanchez S.R, Simson S.N "The influence of carbon steel microstructure on corrosion layers An XPS and SEM characterization" Applied Surface Science 207 (2003) p. 69-85

49. Sun W, Nesic S "Kinetic of corrosion layer formation: Part 1-Iron carbonate layers in carbon dioxide corrosion" Corrosion Vol 64. No.4(2008) p.334-346

50. Han J, Brown B.N, Nesic S "Investigation of the galvanic mechanism for localized carbon dioxide corrosion propagation using the artificial pit technique" Corrosion Vol 66. No.90 (2010) p.1-12

51. Banas.J, Lelek-Borkowska.U, Mazurkiewicz.B, Solarski.W "Effect of CO_2 and H_2S on the composition and stability of passive film on iron alloys in geothermal water" Electrochimica Acta 52 (2007) p.5704-5714

52. Fajardo.V, Canto.C, Brown.B, Nesic.S, "Effect of Organic Acids in CO_2 Corrosion" Corrosion Conference (2007) paper 07319 p.1-18

53. Hunnik E.W.J, Pots B.F.M, Henderiksen E.L.J.A. "The formation of protective $FeCO_3$ corrosion product layers in CO_2 corrosion" Corrosion Conference (1996) paper 0006 p.1-11

54. European Federation of Corrosion Publication "Advances in corrosion control and materials in oil and gas production" IOM Communications Lts, England (1999) p.53-210

55. Han.J, Yang.Y, Brown.B, Nesic.S, "Electrochemical investigation of localised CO_2 corrosion on mild steel" Corrosion Conference (2007) Paper 07323 p.1-25

56. Sun.Y, George K, Nesic.S, "The effect of Cl^- and acetic acid on Localised CO_2 corrosion in wet gas flow" Corrosion Conference (2003) p.1-28

57. George K, Nesic S. "Electrochemical investigation and modelling of carbon dioxide corrosion of carbon steel in the presence of acetic acid" Corrosion Conference (2004) paper 04379 p.1-25

58. Neville A, Hodgkiess T . "An assessment of the corrosion behaviour of high-grade alloys in seawater at elevated temperature and under a high velocity impinging flow" Corrosion science Vol 38, No.06 (1996) p.927-956

59. Cui.Z.D, Wu.S.L, Zho.S.L, Yang.X.J "Study on corrosion properties of pipeline in simulated produced water saturated with supercritical CO_2" Applied Surface Science 252 (2006) p. 2368-2374

60. Gulbrandsen E, Kvarekval J, Miland H. "Effect of oxygen contamination on inhibition studies in carbon dioxide corrosion" Corrosion Vol 61, No.11 (2005) p.1086-1097

61. Wranglen.G "Review article on the influence of sulphide inclusions on the corrodibility of Fe and steel" Corrosion Science Vol 9 (1969) p. 586-602

62. Schmitt G, Gudde T, Strobel-Effertz E. "Fracture mechanical properties of CO_2 corrosion product scales and their relation to localized corrosion" Corrosion Conference (1996) paper 0009 p.1-21

63. Schmitt G, Mueller M, Papenfuss M. "Understanding of carbon steel from physical properties or iron carbonate scales" Corrosion Conference (1999) paper 0038 p.1-13

64. Dugstad A, Hemmer H, Seiersten M "Effect of steel microstructure on corrosion rate and protective iron carbonate film formation" Corrosion Vol 57. No.4 (2001) p. 369-378

65. Chokshi K, Sun W, Nesic S "Iron carbonate scale growth and the effect of inhibition in CO_2 corrosion of mild steel" Corrosion (2005) p.1-23

66. Romero.J.M, Villalobos.J.L, Sosa.E, Amaya.M "Localised corrosion of API X52 and API X65 pipeline steel in the presence of treated seawater used in the oil industry" Corrosion Vol 60. No.7 (2004) pg. 689-696

67. Rayment.T, Davenport.A.J, Dent.A.J, Tinnes.J.P, Wiltshira. R.J.K, Martin.C. Clark.G, Quinn.P, Mosselmans.J.F.W "Characterisation of salt films on dissolving metal surface in artificial corrisonn pits via *in-situ* synchrotron x-ray diffraction" Electrochemistry Communication Vol 10 (2008) p.855-858

68. Brown.B, Parakala.S.R, Nesic.S, "CO_2 corrosion in the presence of trace amounts of H_2S" Corrosion Conference (2004) Paper 04736 p.1-28

69. Turnbull.A, Coleman.D, Griffiths.A.J "Assessment of test methods for evaluating effectiveness of corrosion inhibitors in retarding propagation of localised corrosion" British Corrosion Journal Vol 36. No.3 (2001) p.210-214

70. Melchers.R.E "Pitting corrosion of mild steel in marine immersion environment-Part 1: Maximum pit depth" Corrosion Vol 60. No.9 (2004) p.824-836

71. Wang.X.Y, Wu.Y.S, Zhang.L, Yu.Z.Y "Atomic force microscopy and X-ray photoelectron spectroscopy study on the passive film for type 316L stainless steel" Corrosion Vol 57. No.6 (2001) p.540-546

72. Laycock.N.J, Newman.R.C "Localised dissolution kinetics, salt films and pitting potential" Corrosion Science Vol 39 No.10-11(1997) p.1771-1790

73. Chu.R, Chen.W, Wang.S.H, King.F, Jack.T.R, Fesler R.R "Microstructure dependence of stress corrosion cracking initiation in X65 pipeline steel exposed to a near-neutral pH soil environment" Corrosion Vol 60. No.3 (2004) p.275-283

74. Frankel.G.S, Sridhar.N "Understanding localised corrosion" Material Today Vol 11. No.10 (2008) p.38-44

75. Melchers.R.E "Pitting corrosion of mild steel under marine anaerobic conditions- Part 2: Maximum pit depth" Corrosion Vol 62. No.12 (2006) p.1074-1081

76. Devenport A.J, Isaacs.H.S, Bardwell.J.A, Macdaugall.B, Franckel.G.S. Schrott.A.G "*In-situ* studies of passive film chemistry using x-ray absorption spectroscopy" Corrosion Sciences Vol 35. No.1-4 (1993) p.19-25

77. Neville. A, Hodgkiess.T "Study of passive film on stainless steels and high grade nickel base alloy using x-ray photoelectron spectroscopy" British Corrosion Journal Vol.35 No.3 (2000) p.183-188

78. Gonzalez-Garcia.Y, Burstein.G.T, Gonzalez.S, Sauto.R.M "Imaging metastable pits on austenitic stainless steel *in-situ* at open circuit corrosion potential" Electrochemistry Communications Journal Vol.6 (2004) p.637-642

79. Wei.Z, Duby.P, Somasundaran.P "Inhibition of pitting corrosion by surfactants as a function of temperature" Corrosion Vol 61. No.4 (2005) p.341-347

80. Melchers.R.E "Pitting corrosion of mild steel in marine immersion environment-Part 2:Variability of maximum pit depth" Corrosion Vol 60. No.10 (2004) p.937-944

81. Melchers.R.E "Statistical characterization of pitting corrosion -Part 1: Data analysis" Corrosion Vol 61. No.7 (2005) p.655-664

82. Amri J, Gulbrandsen E, Nogueira R.P "Propagation and arrest of localized attacks in carbon steel in the presence of acetic acid" Corrosion Vol 66. No.3 (2010) p.1-7

83. Zhao.J.M, Zuo.Y "Corrosion behaviour in simulated solution within pits and crevices on carbon steel" Corrosion Engineering Vol 42 No.3 (2007) p.203-206

84. Cui.N, Qiao.L.J, Lou.J.L, Chovelli.S "Pitting of carbon steel with banded microstructure in chloride solution" British Corrosion Journal Vol 35. No.3 (2000) p.210-215

85. Menendez C.M, Jovancicevic V "Novel approach for assessing inhibitor performance against localized corrosion" Corrosion Conference (2003) Paper 03374 p.1-14

86. Joosten M.W, Johnsen T, Dugstad A, Walmann T, Jossang T, Meakin P, Feder J. "*In-situ* observation of localized CO_2 corrosion" Corrosion Conference (1994) Paper 3 p.1-14

87. Xiao Y, Nesic S. "A stochastic prediction model of localised CO_2 corrosion" Corrosion Conference (2005) Paper 05057 p.1-12

88. Issacs H.S. "The localized breakdown and repair of passive surface during pitting" Corrosion Science Vol.29 No. 2/3 (1989) p.313-323

89. Katano.Y, Miyata.K, Shimizu.H, Isogai.T "Predictive model for pit growth on underground pipes" Corrosion Vol 59. No.2 (2003) p.155-161

90. Foss M, Gulbrandsen E "CO_2 corrosion inhibition and oil wetting of carbon steel with ferric corrosion products" Corrosion Conference (2009) Paper 09563 p.1-17

91. Foss M, Gulbrandsen E, Sjoblom J "Interaction of carbon dioxide corrosion inhibitors with corrosion product deposit" Corrosion Conference (2008) Paper 08343 p.1-19

92. Marcus.P "Oil field chemicals" Marcel Dekker, New York (2002) p.82-102

93. Rostami A, Nasr-El-Din H.A "Review of corrosion inhibitors used in well stimulation" SPE 121726 (2009) p.1-17

94. Marco R.D, Durnie W, Jefferson A, Kinsella B "Surface analysis of adsorbed carbon dioxide corrosion inhibitors" Corrosion Vol 57. No.1 (2001) p.9-18

95. Iannuzzi M, Frankel G.S. "Mechanisms of corrosion inhibition of AA2024-T3" Corrosion Vol 49 (2007) p.2371-2391

96. Jiang.X, Zheng.Y.G, Ke.W "Corrosion Inhibitor performance for CO_2 corrosion of N80 steel under static and flowing condition" Corrosion Vol 61. No.4 (2005) p.326-334

97. Ergun.M, Akcay.L "Investigation of pitting potential of carbon steel using experimental design method" British Corrosion Journal Vol 37. No.3 (2002) p.235-238

98. Wong J.E, Park N. "Further investigation on the effect of corrosion inhibitor actives on the formation of iron carbonate on carbon steel" Corrosion Conference (2009) Paper 09569 p.1-31

99. Wong J.E, Park N. "Effect of corrosion inhibitor active components on the growth of iron carbonate scale under CO_2 conditions" Corrosion Conference (2008) Paper 08345 p.1-25

100. Tsui K, Wong J.E, Park N. "Effect of corrosion inhibitor active components on corrosion inhibitor in a sweet environments" Corrosion Conference (2010) Paper 10326 p.1-24

101. Menendez C.M, Jovancicevic V "Quantitative analysis of localized corrosion in the presence of corrosion inhibitors" Corrosion Conference (2007) Paper 07619 p.1-15

102. Meng Q, Jovancicevic V "Electrochemical evaluation of CO_2 corrosion inhibitors in high turbulence multiphase flow" Corrosion Conference (2008) Paper 08625 p.1-14

103. Jiang X, Nesic S "The effect of electrode size on electrochemical noise measurements and the role of chloride on localized CO_2 corrosion of mild steel" Corrosion Conference (2009) Paper 09575 p.1-16

104. Bhargava G, Ramanarayanam T.A, Gouzman I, Abelev E, Bernasek S.L "Inhibition of iron corrosion by imidazoline: An electrochemical and surface science study" Corrosion Vol 65. No.5 (2009) p.308-317

105. Jovancicevic, Ramachandran S, Prince P "Inhibition of carbon dioxide corrosion of mild steel by imidazolines and their precursors" Corrosion Vol 55. No.5 (1999) p.449-455

106. Alik B, Outlaw B, Jovancicevic V, Ramachandran S, Campbell S "Mechanism of CO_2 corrosion inhibition by phosphate esters" Corrosion Conference (1999) Paper 37 p.1-19

107. Hay.M.G "Fitness for purpose material testing for sour gas services – An overview" Corrosion Vol 57. No.3 (2001) p.236-252

108. Nesic S, Li H, Huang J, Sormaz D "An open source mechanistic model for CO_2/H_2S corrosion of carbon steel" Corrosion Conference (2009) Paper 09572 p.1-19

109. Smith S.N, Joosten M.W "Corrosion of carbon steel by H_2S in CO_2 containing oilfield environments" Corrosion Conference (2006) Paper 06115 p.1-25

110. Sun W, Pugh D.V, Smith S.N, Ling S, Pacheco J.L, Franco R.J "A parametric study of sour corrosion of carbon steel" Corrosion Conference (2010) Paper 10278 p.1-19

111. Haung H.H, Tsai W.T, Lee J.T. "Electrochemical behaviour of A516 carbon steel in solution containing hydrogen sulphide" Corrosion Vol.52 No.9 (1996) p.708-713

112. Heuer.J.K, Stubbins.J.F. "An XPS characterization of $FeCO_3$ films from CO_2 Corrosion" Corrosion Science Vol.41 (1999) pg.1231-1243

113. Smith S.N, Pacheco J.L "Prediction of corrosion in slightly sour environments" Corrosion Conference (2002) Paper 02241 p.1-15

114. Ren C, Liu D, Bai Z, Li T "Corrosion behaviour of oil tube steel in stimulant solution with hydrogen sulphide and carbon dioxide" Material Chemistry and Physice 93 (2005) p.305-309

115. Ma.H, Cheng.X, Li.G, Chen.S, Quan.Z, Zhao.S,Niu.L "The influence of hydrogen sulphide on corrosion of iron under different conditions" Corrosion Science Vol 42 (1999) p.1669-1683

116. Ramachandran S, Ward M.B, Bartip K.A "Molecular modelling of corrosion or iron in H_2S environments" Corrosion Conference (2002) Paper 02240 p.1-13

117. Zea.L, Jepson.P, Kumar.R "Role of pressure and reaction time on corrosion control of H_2S scavenger" SPE 114175 (2008) p.1-4

118. Brown.B, Nesic.S, "CO_2/H_2S Corrosion under scale forming conditions" Corrosion Conference (2005) paper 05625 p.1-29

119. Videm.K, Kvarekval.J "Corosion of carbon steel in carbon dioxide saturated solutions containing small amounts of hydrogen sulphide" Corrosion Vol 51. No.4 (1995) p.260-269

120. Pugh D.V, Asher S.L, Cai J, Sisak J "Top-of-line corrosion mechanism for sour wet gas pipelines" Corrosion Conference (2009) Paper 09285 p.1-15

121. Kvarekval J, Dugstad A "Corrosion mitigation with pH stabilisation in slightly sour gas/condensate pipelines" Corrosion Conference (2006) Paper 06645 p.1-15

122. Kvarekval J, Nyborg R, Seiersten M "Corrosion product films on carbon steel in semi sour CO_2/H_2S enviromets" Corrosion Conference (2002) Paper 02296 p.1-17

123. Place M.C, Lewis R "25 years of successful corrosion inhibition of Mississippi's deep sour gas production" Corrosion Conference (2002) Paper 02282 p.1-10

124. Smith J.S, Miller J.D.A "Nature of sulphides and their corrosive effect on ferrous metals: a review" British Corrosion Journal Vol 10. No.3 (1975) p.136-143

125. Sun W, Nesic "A mechanistic model of uniform hydrogen sulphide/carbon dioxide corrosion of mild steel" Corrosion Vol 65. No.5 (2009) p.291-307

126. Jenkins A "The application of corrosion inhibitors to prevent localized corrosion in a sour oilfield" Corrosion Conference (2010) Paper 10330 p.1-11

127. Svenningsen G, Palencsar A, Kvarekval J "Investigation of iron sulphide layer growth in aqueous H_2S/CO_2 environments" Corrosion Conference (2009) Paper 09359 p.1-15

128. Omar I.H, Gunaltum Y M, Kvarekval J, Dugstad A "H_2S corrosion of carbon steel under simulated Kashagan field conditions" Corrosion Conference (2005) Paper 05300 p.1-15
129. Sun H, Blumer D, Davis J "Pit propagation of carbon steel in sour conditions" Corrosion Conference (2010) Paper 10282 p.1-11
130. Kavarekval J "Morphology of localised corrosion attacks in sour environments" Corrosion Conference (2007) Paper 07659 p.1-10
131. Kavarekval J, Dustad A "Pitting corrosion in CO_2/H_2S containing glycol solution under flowing conditions" Corrosion Conference (2005) Paper 05631 p.1-18
132. Kavarekval J, Dustad A "Pitting corrosion mechanisms on carbon steel in sour glycol/water mixtures" Corrosion Conference (2004) Paper 04737 p.1-15
133. Moloney J.J, Mok W.Y, Menendez C.M. "*In-situ* assessment of pitting corrosion and its inhibition using a localized corrosion monitoring technique" Corrosion Vol 66. No.6(2010) p.1-18
134. Steward S, Menendez C, Jovancicevic V "New corrosion inhibitor evaluation approach for highly sour service conditions" Corrosion Conference (2009) Paper 09360 p.1-13
135. Park N.G, Morello L, Abriam G "Understanding inhibition of sour system with water soluble corrosion inhibitors" Corrosion Conference (2009) Paper 09362 p.1-23
136. Sastri V.S, Elboujdaini M, Brown J.R, Perumareddi J.R "Surface analysis of inhibitor films formed in hydrogen sulphide medium" Corrosion Vol 52. No.6 (1996) p.447-452
137. Sastri V.S, Perumareddi J.R "Selection of corrosion inhibitors for use in sour media" Corrosion Vol 50. No.6(1994) p.432-437
138. Schmitt G, Saleh A.O "Evaluation of environmentally friendly corrosion inhibitors for sour service" Corrosion Conference (2000) Paper 00335 p.1-13
139. Wang H, Wylde J "Corrosion inhibitor development for slight sour environment with oxygen intrusion issue" Corrosion Conference (2010) Paper 10275 p.1-21
140. Obeyesekere N, Haraghi A, Chen L, Zhou S, Abayarathna D "Enviromrntally friendly corrosion inhibitors for sweet and sour gas corrosion" Corrosion Conference (2004) Paper 04733 p.1-29

141. March J, Palmer J.W, Newman R.C "Evaluation of inhibitor performance for protection against localized corrosion" Corrosion Conference (2002) Paper 02288 p.1-15

142. Turnbull A, McCarthey L.N, Zhou S, "A model to predict the evolution of pitting corrosion and pit to crack transition incorporating statistically distributed input parameters" Corrosion Science Vol 48. (2006) p.2084-2105

143. Hinds G, Turnbull A "Novel multi-electrode test method for evaluating inhibition of underdeposit corrosion – Part 1: Sweet conditions" Corrosion Vol 66. No.4 (2010) p.1-10

144. Hinds G, Turnbull A "Novel multi-electrode test method for evaluating inhibition of underdeposit corrosion – Part 2: Sour conditions" Corrosion Vol 66. No.5 (2010) p.1-6

145. Euvrard.M, Filiatre.C, Crauaz.E "A cell to study *in-situ* electrocrystsllizstion of calcium carbonate" Journal of Crystal Growth Vol 216 (2000) p.466-474

146. Schmitt G, Feinen S "Effect of anions and cations on the pit initiation in CO_2 corrosion of iron and steel" Corrosion Conference (2000) Paper 00001 p.1-11

147. Fonseca.L, Perex-Murane.F, Calaza.C, Santander.J, Figueras.E, Gracia.I, Cane.C, Mareno.M, Marco.S "Thermal AFM: a Thermopile case study" Ultramiscopy Vol 101. (2004) p.153-159

148. Bursteun.G.T, Moloney. J.J "Cyclic thermammetry" electrochemistry communication Vol 6. (2004) p.1037-1041

149. Cui N, Ma H.Y, Luo J.L, Chiovelli S "Use of scanning reference electrode technique for characterizing pitting and general corrosion of carbon steel in natural media" Electrochemistry communications No. 3 (2001) p.716-721

150. Trethewey K.R, Sargeant D.A, Marsh D.J, Tamimi A.A "Applications of the scanning reference electrode technique to localised corrosion" Corrosion Science Vol 35 No. 1-4 (1993) p.127-134

151. Vignal V, Krawiec H, Heintz O, Oltra R "The use of local electrochemical behaviour and pitting corrosion of stainless steels" Electrochimica acta Vol 52 (2007) p.4994-5001

152. Malayoglu U, Neville A, Beamson G "Characterization of the passive film on HIPed Stellite 6 alloy using x-ray photoelectron spectroscopy" Material science and engineering(2005) p.91-101

153. Sakai Y, Lijima Y, Asakawa D, Hiraoka K "XPS depth profiling of polystyrene etched by electrospray droplet impact" Surface and interface analysis (2010) Vol. 42, p.658-661

154. Wang C, Neville "Understanding inhibitor action on components of erosion, corrosion and their interaction in CO_2 containing slurries" SPE 87511 (2004) p.1-9

155. Souza V.A.D, Neville A "Corrosion mechanisms and electrochemical behaviour of thermal sprat coatings (WC-Cr-Ni and WCCrC)" Corrosion Conference (2002) Paper 02180 p.1-11

156. Baird T, Campbell K.C, Holliman P.J, Hoyle R, Stirling D, Williams B.P "Structural and morphological studies of iron sulphide" J.Chems Soc. Faraday Trans, 92(3) (1996) p.445-450

157. Kurosawa K, Li H.L, Ujihira Y, Nomura K "Characterization of carbonitrided and oxidized layer on low carbon steel by conversion electron Mossbauer spectrometry, X-ray diferractometry and X-ray photoelectrons spectrometry" Corrosion Vol 55. No.3 (1999) p.238-247

158. Bozzini B, Mele C, Romanello V "An *in-situ* FTIR evaluation of candidate organic corrosion inhibitor for carbon steel in contact with alkaline aqueous solution" Material and Corrosion Vol 58 No.5. (2007) p.362-368

159. Durnie W.H, Kinsella B.J, De Marco R, Jefferson A "A study of the adsorption of commercial carbon dioxide corrosion inhibitor formulations" Applies Electrochemistry Vol. 31 (2001) p.1221-1226

160. Campbell S, Jovancicevic V "Corrosion inhibitor film formation studied by ATR-FTIR" Paper No. 0484, Corrosion/1999 NACE, (1999) p.1-12

161. Sharma L, Kimura T "FTIR investigation into the miscible interaction in new material for optical devices" Polymer for Advanced Technologies Vol. 14 (2003) p.392-399

162. Legrand L, Savoye S, Chausse A, Messina R "Study of oxidation product formed on iron in solutions containing bicarbonate/carbonate" Electrochimica Acta 46 (2000) p.111-117

163. Murphy R, Lammers K, Smirnov A, Schoonen M.A.A, Strongin D.R "Ferrihydrite phase transformation in the presence of aqueous sulphide and supercritical CO_2" Chemical geology 271 (2010) p.26-30

164. Otiz R, Marquez O.P, Marqyez J, Gutierrez C "FTIR spectroscopy study of electrochemical reduction of CO_2 on various metal electrodes in methanol" Electroanalytical chemistry 390 (1995) p.99-107

165. Blengino J.M, Keddam J, P "Physico-chemical characterization of corrosion layers formed in iron in a sodium carbonate-bicarbonate containing environment" Corrosion science Vol 37. No.4 (1995) p.621-634

166. Savoye S, Legrand L, Sagon G "Experimental investigation on iron corrosion products formed in bicarbonate/carbonate containing solution at 90°C" Corrosion science Vol 43. (2001) p.2049-2064

167. Reig F.B, Adelantado J.G.G, Moreno M.C.M.M "FTIR quantitative analysis of calcium carbonate and silica mixture using the constant ratio method application to geological sample" Talanta 85 (2002) p.811-821

168. Gardella J.A, Jiang D, Mckenna W.P, Eyring E.M "Application of FTIR/PAS to surface and corrosion phenomena" App. Of surface science 15 (1983) p.69-49

169. Romero M, Marquez R, Gonzalez M "Use of FTIR *in-situ* technique to evaluate MIC by SRB" Corrosion Conference (2007) Paper 07531 p.1-10

170. Wang Z, Shui H, Zhang D, Gao J "A comparison of FeS, FeS+S and solid super acid catalytic properties for coal hydro-liquefaction" Fuel 86 (2007) p.835-842

171. Neal A, Techkarnjanaruk S, "Iron sulphides and sulphur species produced at hematite surface in the presence of sulphide reducing bacteria" Geochimica acta Vol 52 No. 2 (2001) p.223-235

172. Chernyshova I.V "An *in-situ* FTIR study of galena and pyrite oxidation in aqueous solution" Jor. Of. Elactroanalytical chemistry 558 (2003) p.83-98

173. Cldeira C.L, Ciminelli VST, Diias A, Osseo-Asare K " Pyrite oxidation in alkaline solutions nature of the product layer" Int. Jor. Miner process 72 (2003) p.373-386

174. OSHA Hydrogen Sulphide Safety [Online][Accessed 10 March 2008] Available from <htpp://www.osha.gov/dts/sltc/chemicalsamples/data/CH_246800>

175. European Federation of Corrosion Publication "Guidelines on materials requirements for carbon and low alloys steels for H_2S-containing environments in oil and gas production" Maney Publishing (2002) p.1-55

176. API Committee "API recommended practices for conducting oil and gas production operation involving hydrogen sulphide" API RP 55 (1983) p.1-22

177. Moulder.J.F, Stickle.J.F, Sobol.P.E, Bomben.K.D "Handbook of x-ray photoelectron spectroscopy" Perkin-Elmer Corporation, Eden Prairie, Minnesota (1995)

178. Watt J.F, Wolstenholme.J "An introduction to surface analysis by XPS and AES" Wiley, England (2003) p.1-14; p.59-78

179. Briggs.D "Practical Surface Analysis by Auger and x-ray photoelectron spectroscopy" John Wiley and Sons, England (1983) p.6-13; p.181-214

180. Jenkins. R "An introduction to x-ray spectrometry " Heyden, New York (1974) p.1-6

181. Li S.J, Yumoto H,Shimotomai M, Ishihara M "Effects of the power of electron shower and substrate bias on the synthesis of cementite films" Thin Solid films 345 (1999) p. 23-28

182. ASTM E1078-02 "Standard guide for specimen preparation and mounting in surface analysis" ASTM international, USA (2002) p.1-9

183. ASTM E1523-03 "Standard guide to charge control and charge referencing techniques in x-ray photoelectron spectroscopy" ASTM international, USA (2003) p.1-6

184. ASTM E996-04 "Standard practice for reporting data in auger electron spectroscopy and x-ray photoelectron spectroscopy" ASTM international, USA (2004) p.1-3

185. ASTM E995-04 "Standard guide for background subtraction techniques in auger electron spectroscopy and x-ray photoelectron spectroscopy" ASTM international, USA (2004) p.1-4

186. Degen.I.A "Table of characteristic group frequencies for the interpretation of infrared and raman spectra" Acolyte, England (1997) p.1-93

187. Nyquist R.A "Interpreting infrared , raman and nuclear magnetic resonance spectra Vol 2" Acedemic press, London (2001), p.231-350

188. Nyquist R.A "Interpreting infrared , raman and nuclear magnetic resonance spectra Vol 1" Acedemic press, London (2001), p.31-164

189. ASTM E1421-99 "Standard practice for describing and measuring performance of fourier transform mid-infrared (FT-MIR) spectrometers: level zero and level one test" ASTM international, USA (2009) p.258-269

190. Baker Hughes proprietary information.

191. Crolet J.L, Thevenot N, Dugstad A "Role of free acetic acid on the CO_2 corrosion of steel" Corrosion Conference (1999) Paper 24 p.1-16

192. Gulbrandsen. E, Nesic S, Stangeland A, Burchardt T "Effect of pre-corrosion on the performance of inhibitor for CO_2 corrosion of carbon steel" Corrosion Conference (1998) Paper 13 p.1-20

193. Mok W.Y, Dougherty J, Jovancicevic V "Potentiostatic electrochemical noise for corrosion monitoring general and localized corrosion" Corrosion Conference (2002) Paper 02335 p.1-12

194. Limura A, Takahashi K "Growth model and on-line measurement of pitting corrosion on carbon steel" Corrosion Conference (1996) Paper 343 p.1-11

195. Cheng Y.F, Luo J.L "Metastable pitting of carbon steel under potentiostatic control" Journal of the electrochemistry society Vol.146, no.3 (1999) p.970-976

196. Jovancicevic V, Hartwick D "A new electrochemical approach for evaluation of corrosion inhibitors in neutral aqueous solutions" Corrosion Conference (1997) Paper 0281 p.1-20

197. Akbar A, Hu X, Neville A, Wang C "The influence of flow rate and inhibitor on the protective layer under erosion corrosion conditions using rotating cylinder electrode" Corrosion Conference (2011) Paper 11274 p.1-12

198. Dougherty J.A "Controlling CO_2 corrosion with inhibitors" Corrosion Conference (1998) Paper 015 p.1-15

199. Jovancicevic V, Ahn Y.S, Dougherty J, Alink B "CO_2 corrosion inhibition by sulphur containing organic compounds" Corrosion Conference (2000) Paper 0007 p.1-18

200. Ramachandran S, Jovancicevic V "Molecular modelling of the inhibition of mild steel carbon dioxide corrosion by imidazolines" Corrosion science Vol 55. (1999) p.259-267

Appendix

Appendix A: Operation and emergency procedure of sour rigs

1) Standard laboratory procedure should be observed whilst working in the laboratory.
2) Prior to the start of any testing involving H_2S gas, a notice must be given to the project supervisor, laboratory technician and one other member of the research group, this is to ensure that an appropriate and immediate response be taken in the case of a H_2S alarm.
3) Extreme care must be taken and a personal H_2S safety alarm must be carried and switched on when entering the laboratory.
4) The alarm should be set to activate when the H_2S concentration inside the fume cupboard is more then 10ppm or if the H_2S concentration is more then 5ppm in the laboratory area.
5) A sign "H_2S Test in Progress" must be displayed on the Laboratory entrance doors throughout the duration of the test.
6) When the H_2S alarm is activated, the laboratory should be evacuated immediately. The cause of the alarm should be determined by checking the information displayed on the control box mounted outside the laboratory.
7) A shut down valve should be automatically activated to cut off the H_2S supply when the limit set for the alarm is reached.
8) It is considered safe to re-enter the laboratory when the control box outside the laboratory registers the H_2S level as being less than 1ppm.
9) The "Reset" on the control box is pressed once to deactivate the alarm
10) Pressing the "Reset" a second time re-energises the automatic shut down valve to allow gas to pass through.
11) The H_2S gas supply is turned off using the valve on top of the cylinder.
12) All leaks should be made good if it is safe to do so.

Appendix B: Helium pressure test procedure for sour rig

1) Check that all parts of the equipment are safe and ready to use.
2) Test the pipeline (not experiment vessel) at 0.8 bar with helium and hold the pressure for 10 minutes to check the connection.
3) Increase the test pressure to 1 bar to check the blow off valve is operating.
4) Finish the 1 bar helium pressure test and release the pressure
5) Fill the vessel with test solution.
6) Mount the specimen on the specimen holder
7) Insert test electrodes and test the electrode assembly in the vessel.
8) Check the O-ring position
9) Seal the test vessel.
10) Start the helium pressure test at 0.08 bar. Test the system with helium for 15 minutes. (Both inlet and outlet valves must be open to allow gas to flow through the vessel and scrubber units but close the final exit valve to trap the pressure at 0.08 bar).
11) Observe any gas and solution leaking.
12) Observe the pressure gauge to make sure that the gauge remains constant and that there is no leaking..
13) Increase the test pressure to 0.1 bar to check the blow off valve is operating.
14) Finish the 0.1 bar helium pressure test.
15) Start the helium flow test. Test the system with helium for 15 minutes. (Both inlet and outlet valves must be open to allow gas to flow through the vessel and scrubber.
16) Observe any gas and solution leaking
17) Observe the pressure gauge to make sure there is no trapped pressure.
18) Finish the helium flow test.

Appendix C: Cleaning the scrubber procedure for sour rig

1) Switch on the heater and stirrer unit.
2) Allow the vessel to heat to 30°C.
3) Purge the vessel with N_2 and the outlet gas should be routed to the scrubber unit for at least 60 minutes.
4) Stop the N_2 purging and slightly open the vent valve on top of the vessel lid and inject the H_2S scavenger and close back the valve.
5) Purge the vessel with N_2, again for at least 15 minutes.
6) Stop purging and carefully check the presence of any residual H_2S in the vessel using the alarm. If any appreciative amount of H_2S, more then 5ppm, is present close the valve and return to step 4.
7) Loosen the lid clip.
8) Lift the lid carefully from the vessel.
9) Empty the vessel. Dispose of the solution into a designated container. (The solution in the container should be treated by additional H_2S scavenger and mixed with water to remove any H_2S in the solution prior to final disposal).